Imperial College London

Fabry-Pérot Resonators in Guided-Wave Media

Attique Dawood

A thesis submitted in partial fulfilment of the requirements for the

Degree of Doctor of Philosophy of Imperial College London
and the
Diploma of Imperial College London

Supervisor
Prof. Stepan Lucyszyn

Co. Supervisor
Dr. Oleksiy Sydoruk

Electrical and Electronic Engineering Department
Imperial College London
January, 2020

Copyright ©

The copyright of this thesis rests with the author. Unless otherwise indicated, its contents are licensed under a Creative Commons Attribution-Non Commercial 4.0 International Licence (CC BY-NC).

Under this licence, you may copy and redistribute the material in any medium or format. You may also create and distribute modified versions of the work. This is on the condition that: you credit the author and do not use it, or any derivative works, for a commercial purpose.

When reusing or sharing this work, ensure you make the licence terms clear to others by naming the licence and linking to the licence text. Where a work has been adapted, you should indicate that the work has been changed and describe those changes.

Please seek permission from the copyright holder for uses of this work that are not included in this licence or permitted under UK Copyright Law.

Declaration of Originality

I hereby certify that I am the sole author of this dissertation and that, to the best of my knowledge, this thesis does not infringe upon any copyright or proprietary rights and any material from other resources that has been used is appropriately acknowledged.

Attique Dawood

Table of Contents

Page

Table of Contents v

Acknowledgements xi

Abstract xiii

List of Figures xv

List of Tables xxxiii

List of Abbreviations xxxv

List of Symbols xxxvii

1 Current Research Trends in THz Technology **1**

1.1 Terahertz Technology 1

1.2 Plasmonics 2

1.3 Bulk Plasmon-Polaritons 3

1.4 Surface Plasmon-Polaritons as Surface Waves on a Metal 5

1.5 Plasmons in 2-DES 8

1.6 FDTD Technique 9

1.6.1 Modelling Approach 11

1.7 FDTD Modelling of Lossy Spherical Resonators 13

1.7.1 FDTD Results 16

1.8 Acknowledgements 17

References 18

2 Travelling Waves, Pseudo Waves and Power Waves **21**

2.1 Introduction 21

2.2 Lossy Materials and Components 23

2.3 The Transmission Line Model and Telegraphers' Equations 26

2.4 Transmission Line Modelling of Waveguides 27

2.5 Travelling Waves, Pseudo Waves and Power Waves 30
2.6 Voltage-Wave and Power-Wave Reflection Coefficients 32
2.7 Generalised Two-Port Network 32
2.8 Generalised n-Port S- and S_p-Parameters 34
2.9 Interconversion Between Two-Port S, Z, Y, h, ABCD and T Parameters 36
2.10 Cascading 38
2.11 Renormalisation of Scattering Parameters 40
2.12 Conversion Between S- and S_p-Parameters 44
2.13 Example: Two-Layer Media as Two-Port Network 45
2.14 Example: Three-Layer Media as Two-Port Network 46
2.15 Example: Signal Flow Graph Analysis of Three-Layer Media 49
2.16 Example: Zero-Order Power Propagation Model for Lossy Three-layer Media 52
2.17 Conclusion 55
2.18 Acknowledgements 55
References 56

3 Modelling Lossy Resonators **59**
3.1 Introduction 59
3.2 General Solution of a Symmetric Fabry-Pérot Resonator 60
3.3 Eigenvalue Solution of a Lossy Fabry-Pérot Resonator 63
3.3.1 Example: Lossy Three-Media Fabry-Pérot Resonator 64
3.3.2 Example: The 'Inverse' Three-Media Fabry-Pérot Resonator 68
3.4 Conclusion 71
3.5 Acknowledgements 71
References 75

4 Excitation of 'Open-Box' Modes in Dielectric-Filled MPRWG **77**
4.1 Introduction 77
4.2 Analytical Variational Modelling (M1) 78
4.3 Field-Based Analytical Modelling of Dielectric-Filled MPRWG 81
4.4 Numerical Modelling of Dielectric-Filled MPRWG (M5) 84
4.5 Analytical Field-Based Q-Factor Modelling 86
4.6 Open-Box Mode Resonance Modelling 87

4.6.1 Qualitative Excitation of Open-Box Mode Resonances With a Frequency-Domain Solver . . . 90
4.6.2 Open-Box Mode Resonance Field Plots From Eigenmode Solver . . . 96
4.6.3 Analytical Modelling of Open-Box Mode Resonances . . . 96
4.7 Conclusion . . . 102
4.8 Acknowledgements . . . 103
References . . . 104

5 Excitation of Fabry-Pérot Eigenmodes in Dielectric-Filled Waveguides 105
5.1 Introduction . . . 105
5.2 Fabry-Pérot Eigenmodes in Parallel-Plate Waveguide . . . 106
5.2.1 Theory . . . 106
5.2.2 Results . . . 109
5.3 Fabry-Pérot Eigenmodes in Circular Waveguide . . . 111
5.3.1 Theory . . . 111
5.3.2 Results . . . 116
5.4 Conclusion . . . 117
5.5 Acknowledgements . . . 122
References . . . 123

6 An S-Parameter Renormalisation Technique for Resolving Ambiguities 125
6.1 Introduction . . . 125
6.2 Spectroscopic Extraction of Dielectric Properties Using Graphical Method . . . 126
6.3 Spectroscopic Extraction of Dielectric Properties Using Renormalisation Method . . . 129
6.4 Modelling Comparison With NRW Approach . . . 132
6.5 Measurement Noise Resilience Analysis . . . 141
6.6 Estimation of VNA S/N . . . 146
6.7 Conclusion . . . 151
6.8 Acknowledgements . . . 151
References . . . 153

7 THz Spectroscopy Using Surface Plasmon Excitation 155
7.1 Introduction . . . 155
7.2 Dispersion Modelling . . . 156
7.3 Planar Media Reflection/Transmission Approach . . . 158

7.4 Full Wave Simulation Using *COMSOL Multiphysics*® and FDTD . . . 163
7.4.1 Full-Wave Simulation Results . . . 169
7.5 Spectroscopy of Material Sample . . . 172
7.6 Conclusions . . . 172
7.7 Acknowledgements . . . 177
References . . . 178

8 Full-wave Modelling of THz Frequency Plasmons in 2-DES 179
8.1 Introduction . . . 179
8.2 Device Structure and Modelling Considerations . . . 181
8.2.1 Excitation and Ports . . . 183
8.2.2 Meshing . . . 184
8.3 Comparison with Experiments: Gate-Modulation Signals . . . 185
8.4 Beyond Experiment: Transmission, Reflection, Absorption and Field Profiles . . . 188
8.5 Comparison with Experiments: Magnetoplasmons . . . 191
8.6 Improving Device Performance . . . 194
8.7 Modelling Losses in the Device Structure . . . 198
8.7.1 Modelling 2-DES Edge Losses . . . 198
8.7.2 Modelling Substrate Losses . . . 198
8.7.3 Modelling Losses in Ohmic Contacts . . . 198
8.8 Conclusions . . . 201
8.9 Acknowledgements . . . 201
References . . . 202

9 Conclusions 205

A Fundamental Forces and Maxwell's Equations 209
A.1 Fundamental Forces . . . 209
A.2 Maxwell's Equations . . . 209
A.3 Complex Phasor Form of Maxwell's Equations and Classical Skin Effect Model . . . 210

B Effective Complex Dielectric Function and Refractive Index 213

C Drude Model 215

D The Equation of Plane Wave in Unbounded Medium 217

E Electric Field Reflection and Transmission Coefficients Due to a Plane Wave Reflection and Transmission at an Interface Between Two Media **219**

F Plane Wave Reflection and Transmission For Planar Three-Layer Media **223**

G MATLAB Code to Compute Coplanar Waveguide Mode Profile **227**

H Two-port network conversions between S, Z, Y, h, ABCD and T parameters **230**

I MATLAB Code to Compute Fabry-Pérot Eigenmodes in Parallel-Plate Waveguide **234**

References 236

Acknowledgements

Firstly, I would like to thank my supervisor Prof. Stepan Lucyszyn for his continuous encouragement, support and guidance throughout the duration of my stay at Imperial College London. I found the door to his office always open for any discussion on any difficulty I was facing. He would regularly check upon my progress and have a chat with anything I needed help with, while always suggesting new ideas and avenues to explore. The most important aspect of his supervision was the countless hours I spent in his office, while he would go through each and every word of the drafts I submitted to him. This was an excellent learning opportunity for me, as I learned how to do many things related to research first hand from him. The most important skill I developed under supervision was paying attention to detail and not take things for granted.

I would also like to thank my co. supervisor Dr. Oleksiy Sydoruk for his support and guidance, especially in the early stage of my PhD. I had countless meetings and discussions with him regarding the direction of my PhD research. One of his qualities I want to mention is his ability to suggest very clear and concise solutions to some of the problems and difficulties I faced and that greatly helped me. The most important aspect of his supervision were the journal clubs, where I learned from him how to analyse and extract useful information from published papers.

I would also want to acknowledge the helpful discussions I had with Dr. William Otter and want to thank my co-authors Nick Ridler and Dr. Jingye Sun, whose contributions were invaluable. Among administration staff I want to thank Teresa Carbajo Garcia who welcomed me on my first day at college and showed me around, Jay Sahote for helping me with placing orders and Susan Brace for all the support relating to different administrative matters. A special mention and thanks to Dr. Sergey Siaber who was my closest friend at college.

Finally and most importantly, I would like to thank my parents and family for their continuous support during the course of my stay in London.

Abstract

The objective of this thesis is to study Fabry-Pérot resonators in transmission lines and waveguides. Transmission lines and waveguides may be referred to as guided-wave media. A Fabry-Pérot resonator is the simplest form of resonator occurring frequently in coupled guided-wave structures, for example dielectric-filled waveguides, lasers, plasmonic waveguides etc. In this thesis, analytical as well as numerical approaches have been adopted to model different resonator problems. Analytical solutions of Maxwell's equations, derived from first principles, are used whenever possible. The commercially available finite-element-based electromagnetic solver *COMSOL Multiphysics*® has been used throughout the course of this work for numerical full-wave modelling. In addition, a finite difference time-domain (FDTD) code was also developed for numerical full-wave modelling.

This thesis consists of eight chapters. The first chapter is a review of current trends in THz technology and plasmonics, with a brief description of the FDTD technique and how FDTD can be used to model surface plasmon polaritons.

Chapter 2 is an overview of scattering parameters in relation to travelling waves, pseudo waves and power waves. Several useful results have been derived in this chapter including, direct formulas for renormalisation of conventional (S-) and power (S_p-)scattering parameters for a two-port network; conversion between S- and S_p-parameters for a multi-port network; and direct formulas for interconversion between S, Z, Y, h, ABCD and T parameters for a two-port network with arbitrary port reference impedances.

Chapter 3 deals with challenges in modelling lossy resonant structures by considering the example of a lossy one-dimensional resonator as the walls of the resonator are transformed from perfect electric conductor (PEC) to free space.

Chapter 4 discusses excitation of Fabry-Pérot eigenmodes in 3-D printed dielectric samples when placed in a waveguide as observed by authors of a recently published paper.

Chapter 5 presents a rigorous analysis of Fabry-Pérot eigenmode excitation in dielectric filled parallel-plate and circular waveguides.

Chapter 6 reviews an S-parameter renormalisation technique for resolving ambiguities in re-

flectance and transmittance relationships of a two-port network, from noisy measurements. The technique was introduced in a recently published paper. Furthermore, a method for estimation of vector network analyser (VNA) output signal-to-noise ratio is also discussed.

Chapter 7 introduces a THz spectroscopy technique based on surface plasmon excitation. Several modelling approaches have been used to model the spectroscopic response of a high resistivity Si slab under a Si prism when surface plasmons are excited on the Si slab using the attenuated total reflection (ATR) scheme. The intended experimental set-up was modelled using different techniques including; dispersion modelling, analytical planar media reflection/transmission modelling from first principles using Maxwell's equations and full-wave numerical modelling using the FDTD technique and *COMSOL Multiphysics*® frequency domain solver.

Chapter 8 is on modelling plasmon propagation in two-dimensional electron system (2-DES) channels in the presence of a magnetic field. The experimental results published by a recent study were modelled using *COMSOL Multiphysics*® and the transmission of the proposed device was computed for the first time, which revealed that the device was too lossy. Based on the simulated results, a new device structure was proposed which could reduce transmission losses by 20 dB.

List of Figures

1.1 Dispersion plot of frequency against wavenumber showing the dispersion curves of surface plasmon polaritons (red) and bulk plasmons (blue). The bound surface plasmons only exist below the plasma frequency while the radiative and bulk plasmons cannot propagate below plasma frequency. Also, the existence of modes to the left of the light line can be excited by an incident electromagnetic wave while the bound surface plasmons on the right of the light line can only be excited using special techniques. 4

1.2 Surface plasmon polariton as surface wave on a dielectric/metal boundary. The electromagnetic field decays along the y-direction away from $y = 0$ interface but propagates along the $+x$-direction. Here, $\varepsilon_{r1} > 0$ and $\varepsilon_{r2} < 0$. 6

1.3 Attenuated total reflection configurations for excitation of surface plasmon polaritons where the incident wave undergoes total internal reflection at the bottom side of prism where the evanescent fields extending out of the bottom face can excite surface plasmon polaritons: (a) in the Otto configuration, a metallic slab is placed underneath the bottom side of prism separated by an air gap or dielectric in between with surface plasmons excitation on the top of metal slab; and (b) in the Kretschmann configuration, there is no gap between metal and prism with surface plasmons excitation underneath the metal. 7

1.4 Structure of a high electron mobility transistor (HEMT). An GaAs/AlGaAs heterostructure is created by depositing a layer of AlGaAs on top of GaAs substrate resulting in an inversion layer of free electrons at the junction between GaAs and AlGaAs creating a two-dimensional electron system (2-DES). The concentration of electrons in the 2-DES can be manipulated by applying a voltage to the gate on top of AlGaAs layer. Ohmic contacts at the ends of the 2-DES can be used to couple energy in and out of the HEMT. 9

1.5 Arrangement of electric (filled circles and triangles) and magnetic field (hollow circles and triangles) nodes, separated by half spatial steps, in 2-D finite difference time-domain (FDTD) scheme: (a) transverse magnetic or TM_z arrangement with magnetic field oriented normal to the FDTD grid; and (b) transverse electric or TE_z arrangement with electric field oriented normal to the FDTD grid. Figure redrawn from Schneider [23]. 10

1.6 Dispersion relations for air–2-DES–air, GaAs–2-DES–GaAs and air–2-DES–GaAs. The exact curves were obtained from theory. The FDTD curves correspond to a thin 3-D channel which can effectively model a 2-DES. An increase in frequency requires a corresponding decrease in thickness of 3-D channel to better model a 2-DES. . . . 13

1.7 Finite different time-domain simulated field distributions showing 2-D plasmon excitation at 200 GHz, corresponding to roughly one full wavelength, on a two-dimensional electron system (2-DES) channel that is 30 μm wide and 90 μm long on a GaAs substrate with air on top: (a) top view showing longitudinal field pattern on the 2-DES channel, coplanar waveguide sections and location of source; and (b) side view of field pattern on the 2-DES channel. 14

1.8 Finite different time-domain simulated field distributions showing 2-D plasmon excitation at 200 GHz, corresponding to roughly one full wavelength, on a two-dimensional electron system (2-DES) channel that is 160 μm wide and 90 μm long on a GaAs substrate with air on top: (a) top view showing longitudinal field pattern on the 2-DES channel with clearly visible 2-D and edge plasmons, coplanar waveguide sections and location of source; and (b) side view of field pattern on the 2-DES channel. 14

1.9 Steady-state electric field distribution on a gold nanosphere of radius 40 nm from 3-D FDTD simulation. The gold nanosphere was excited by an incident x-polarised electromagnetic wave having a wavelength of 600 nm. 15

1.10 Comparison of complex eigenfrequency response from FDTD simulations with data from perturbation model [19] of a spherical cavity resonator of radius 150 μm with conducting walls. The conductivity of resonator walls was swept over a range of values from 10^{-6} S/m (very lossy) to 10^{8} S/m (almost ideal resonator). 15

2.1 Lumped-element model of transmission line. 27

2.2 Cross-section of a metal-pipe rectangular waveguide of dimensions $a \times b$ showing the vertical integration path at $x = a/2$ to obtain V_0 from (2.23). 30

2.3 A one-port network consisting of a transmission line of characteristic impedance Z_0 and length L connecting a source V_S, with source impedance Z_S, terminated with a load Z_L. With incident waves a_1 on the transmission line, the impedance mismatch at the load results in reflected waves b_1 on a terminated transmission line. Z_{ref} is the reference impedance at the load ($z = 0$) looking into the transmission, which is Z_0 for travelling waves. 31

2.4 Illustration of a generalised two-port network. The scattering parameters of a two-port network relate the output wave quantities b_i at Port i in terms of input wave quantities a_i. Where, Z_{0i} and Z_{refi} are, respectively, the characteristic impedance of transmission line and reference impedance at Port i, given $i = 1, 2$. 33

2.5 Graphical illustration of relationships between voltage (S-) and power (S_p-) scattering parameters. Double red arrows represent renormalisation of S- or S_p-parameters with respect to a certain reference impedance. Double green arrows show equivalence relationships, where real-referenced S_p-parameters either reduce to pseudo waves or travelling waves. Blue double arrows show a generalised conversion between S- and S_p-parameters. The measurement domain consists of real-referenced S- or S_p-parameters which are the actual powers measured by instruments. 36

2.6 Cascading two-port networks: (a) conventional approach where individual networks have a common reference port impedance; (b) cascading is possible if connecting ports of two networks have the same reference port impedance; (c) overall S-parameters are with respect to reference port impedance of input and output ports of individual networks, respectively, and; (d), (e) cascading is not possible if interconnecting ports of individual networks have different reference port impedances. 41

2.7 Plane wave reflection and transmission at the interface between two planar lossy media. The reflected and transmitted electric fields are related to the incident electric fields by the Fresnel reflection and transmission coefficients, respectively. 47

2.8 Incident and reflected fields in three-layer media. As and Bs are, respectively, reflected and transmitted fields in a given medium. Here, the reference plane for coefficients A_3 is the plane $z = l$, while all other coefficients are referenced with respect to the $z = 0$ plane. There are no reflected waves in medium ③. 48

2.9 Plot of S-parameters of 1-D Fabry-Pérot resonator with $\sigma_① = \sigma_③ = 100$ S/m based on the conventional and power wave definitions, respectively. With conventional complex-referenced S-parameters, the insertion and return loss exceed 0 dB, however, the S_p-parameter response shows that the total energy is conserved. Frequencies at S-parameter resonant peaks are also indicated. 50

2.10 Signal flow graph illustration of 1-D Fabry-Pérot resonator of width l. Each node represents an equation given by the sum of inputs minus the sum of outputs. There are no incident waves at Port 2, therefore, Γ_{12} and T_{12} can be ignored. The total reflection and transmission coefficients can be computed from algebraic manipulation of resultant node equations. 51

2.11 Heuristic engineering approach for the power propagation model with an arbitrary lossy surrounding medium: (top) illustrating individual contributions; (bottom) illustrating Fabry-Pérot reflections. A large black arrow shows the total incident power at the left interface. Some of the incident power is reflected back, determined by the reflectance $\mathcal{R}_{11}$, while some of it is transmitted $\mathcal{T}_{21} = 1 - \mathcal{R}_{11}$. The attenuation constant α, which is non-zero for a lossy medium, determines the losses as the incident wave travels from left interface to the right. At the right interface, again some of the power is reflected back inside, while some of it is transmitted. The sum of individual reflections (and transmissions) give the total reflected (and transmitted) power. Figure redrawn from Sun and Lucyszyn [12]. 53

3.1 Incident and reflected fields in three-layer media. As and Bs are, respectively, reflected and transmitted fields in a given medium. Here, the reference plane for fields with coefficient A_3 is the plane $z = l$, while all other fields are referenced with respect to the $z = 0$ plane. There are no reflected waves in medium ③. 61

3.2 Plot of complex eigenfrequency components f_0' and f_0'' as a function of bulk DC conductivity of resonator walls $\sigma_①$: (a) comparison of the fundamental mode obtained from theory and *COMSOL Multiphysics*® eigenmode solver, which shows that the *COMSOL Multiphysics*® eigenmode solver does not converge to correct solution for $\sigma_① < 30$ S/m as the fundamental transforms into static mode; (b) transformation of next higher order mode with $m = 2$ into fundamental mode with $m = 1$ as the resonator becomes very lossy; and (c) first five modes with fundamental mode indicated by thick line plots. The higher order modes tend to transform into the next lower mode as the resonator becomes very lossy. 66

3.3 Plot of unloaded Q-factors $Q_u(|\omega_0|)$ and $Q_u(\omega_0')$ against bulk DC conductivity of resonator walls $\sigma_{①}$: (a) fundamental mode obtained from theory and *COMSOL Multiphysics®* eigenmode solver, which shows that the *COMSOL Multiphysics®* eigenmode solver does not converge to correct solution for $\sigma_{①} < 30$ S/m and also displays a disagreement with theory for $\sigma_{①} > 10^4$ S/m due to sensitive nature of quality factor relationship given by (3.12) and (3.13); (b) next higher order mode with $m = 2$ suggesting that (3.13) is more useful for computing quality factor; and (c) first five modes with fundamental mode indicated by thick line plots. 67

3.4 Plot of S-parameters of 1-D Fabry-Pérot resonator with $\sigma_{①} = \sigma_{③} = 100$ S/m based on the conventional and power wave definitions, respectively. With conventional complex-referenced S-parameters, the insertion and return loss exceed 0 dB, however, the S_p-parameter response shows that the total energy is conserved. Frequencies at S-parameter resonant peaks are also indicated. 68

3.5 Plot of return loss ($20\log_{10}|S_{11}|$) in the complex frequency plane with $\sigma_{①} = 100$ S/m. The poles of return loss zero indicated by red dots are the complex eigenfrequencies, while zeros indicated by blue dots correspond to the spectral location of ideal modes on the $Im\{\tilde{f}\} = 0$ line. Notice, however, that the resonator medium itself is lossless; indicated by the close proximity of zeros to the $Im\{\tilde{f}\} = 0$ line. 69

3.6 Plot of insertion loss ($20\log_{10}|S_{21}|$) as a function of bulk DC conductivity. A decrease in Q-factor can be observed from the broadening of resonances as $\sigma_{①} \to 0$; and convergence of resonances, at return loss zero frequencies, as $\sigma_{①} \to \infty$. 70

3.7 Visual summary of the response of the lossy Fabry-Pérot resonator with a line scatter plot of the complex eigenfrequencies in the complex frequency plane with selected spot values of bulk DC conductivity. The fundamental mode is indicated with spot values of bulk DC conductivity. The higher order modes tend to transform into the next lower mode as the resonator becomes lossy. 70

3.8 Plot of complex eigenfrequency components f_0' and f_0'' as a function of bulk DC conductivity of resonator $\sigma_②$: (a) comparison of fundamental mode obtained from theory and *COMSOL Multiphysics*® eigenmode solver showing the limitation of the *COMSOL Multiphysics*® eigenmode solver to give correct solution only for a certain range of values of $\sigma_②$. Furthermore, the solution for fundamental mode by the *COMSOL Multiphysics*® eigenmode solver incorrectly tries to converge to next higher mode with $m = 2$. (b) Next higher order mode with $m = 2$; and (c) first five modes with fundamental mode indicated by thick line plots. 72

3.9 Plot of unloaded Q-factors $Q_u(|\omega_0|)$ and $Q_u(\omega_0')$ against bulk DC conductivity of resonator walls $\sigma_①$: (a) fundamental mode obtained from theory and *COMSOL Multiphysics*® eigenmode solver, which shows that the *COMSOL Multiphysics*® eigenmode solver does not converge to correct solution for $\sigma_① < 30$ S/m and also displays a disagreement with theory for $\sigma_① > 10^4$ S/m due to sensitive nature of quality factor relationship given by (3.12) and (3.13); (b) next higher order mode with $m = 2$ suggesting that (3.13) is more useful for computing quality factor; and (c) first five modes with fundamental mode indicated by thick line plots. 73

3.10 Plot of S-parameters of the inverse Fabry-Pérot resonator with $\sigma_② = 20$ S/m based on the conventional and power wave definitions, respectively. Due to the resonator medium itself being lossy and dominant, the S-parameter response shows a broadening of resonances. The resonator almost acts like an absorber at higher frequencies, with return loss less than -20 dB and insertion loss close to 10 dB at 1.5 THz. 74

3.11 Plot of return loss ($20\log_{10}|S_{11}|$) in the complex frequency plane with $\sigma_① = 20$ S/m. The poles of return loss zero indicated by red dots are the complex eigenfrequencies, while zeros indicated by blue dots correspond to the spectral location of ideal modes on the $Im\{\tilde{f}\} = 0$ line. The shift of zeros well above the $Im\{\tilde{f}\} = 0$ line indicates the resonator medium is also lossy. 74

4.1 Illustration of an ideal dielectric-filled metal-pipe rectangular waveguide of dimensions $a \times b$. The length of the dielectric sample is l while the air-filled sections are of length l_{air}. In any section, As and Bs are the incident and reflected fields, respectively. Figure redrawn from Sun *et al.* [1]. 82

4.2 Normalised power responses for fused deposition modelling (FDM) 3-D printed acrylonitrile butadiene-styrene (ABS) Samples #1 and #2 filling the standard WR-90 quarter-wavelength thru line waveguide. The spectral location of open-box mode resonances are indicated and appear as sharp spikes in the measured response. Figure redrawn from Sun *et al.* [1]. 89

4.3 Photomicrographs of an FDM 3-D printed ABS sample under test with nominal 100 μm layer height and 100% infill printer settings: (a) top layer x-y plane view; (b) top layer x-y plane close-in view; (c) bottom layer x-y plane view of a corner; (d) bottom layer x-y plane close-in view; and (e) vertical build x-z plane view. Figure reproduced from Sun *et al.* [1]. 91

4.4 Numerical modelling of open-box mode excitation for Sample #1 with bulk dielectric constant and loss tangent of 2.541 and 8.188×10^{-4}, respectively, from M3 [1] using up-scaled geometry corresponding to the FDM 3-D-printed ABS sample: (a) 3-D contour plot of dielectric constant $\varepsilon_r(x, y, x)$ on the surface of simulated dielectric sample in *COMSOL Multiphysics*®, with $l_{air} = l$; and (b) resulting S-parameters showing open-box mode resonances at 10.11, 11.16 and 12.05 GHz. 93

4.5 Numerical modelling of open-box mode excitation for Sample #1 with dielectric constant and loss tangent of 2.3284 and 19.148×10^{-4}, respectively, from M3 using coarse meshing: (a) 3-D coarse meshing of the complete structure illustrated in Fig. 4.1, with $l_{air} = l$; and (b) resulting S-parameters showing open-box mode resonances at 10.17, 11.15 and 12.18 GHz. Figure reproduced from Sun *et al.* [1]. 94

4.6 Illustration of layer-by-layer fused deposition modelling (FDM) 3-D printing of acrylonitrile butadiene-styrene (ABS) sample showing a 90° shift in angle for alternating layers. The ABS is deposited as molten filaments oriented at 45° relative to the sides of the sample and compressed to form several layers of a structure resembling a woodpile. 95

4.7 Longitudinal top-down cross-sectional view of the rectangular metal-pipe rectangular waveguide showing the dielectric-filled, air-filled and perfectly matched layer (PML) sections in the waveguide. Two slit ports were defined at the ends of the air-filled sections with excitation at Port 1. The ports were specified to compute scattering parameters for the dominant TE_{10} mode. Since the ports defined in *COMSOL Multiphysics*® do not coincide with the actual measurement reference planes, S-parameters obtained from *COMSOL Multiphysics*® must be de-embedded to give the correct S-parameters at the specified measurements reference planes. 97

4.8 Plot of (a) return loss and insertion loss; and (b) absorptance of the dielectric-filled metal-pipe rectangular waveguide operating in the dominant TE_{10} mode having dimensions $a = 22.86$ mm, $b = 10.16$ mm and dielectric section of length $l = 9.626$ mm; with dielectric constant $\varepsilon'_{reff②} = 2.3284$ and loss tangent $\tan\delta_{e②} = 19.1480 \times 10^{-4}$ of the filled in-homogeneous and anisotropic dielectric medium. Dotted lines in (a) show the ideal response computed from theory, while the solid lines show the simulated response from the *COMSOL Multiphysics*® frequency domain solver. The spectral location of box-mode resonances can be clearly seen in (b), with the predicted open-box mode resonance frequencies within 0.01 GHz compared to those computed from theory and eigenmode solver for Sample #1, given in Table 4.2. 98

4.9 Numerically simulated E_y-field plot for TE_{201} open-box mode at $f_{201} = 10.074$ GHz for Sample #1 with dielectric constant loss tangent of 2.3284 and 19.148×10^{-4}, respectively, from M3. Figure reproduced from Sun *et al.* [1]. 99

4.10 Numerically simulated E_x-field plot for TE_{011} open-box mode at $f_{011} = 11.144$ GHz for Sample #1 with dielectric constant loss tangent of 2.3284 and 19.148×10^{-4}, respectively, from M3. Figure reproduced from Sun *et al.* [1]. 99

4.11 Numerically simulated field plots for TE_{111} open-box mode at $f_{111} = 12.046$ GHz for Sample #1 with dielectric constant loss tangent of 2.3284 and 19.148×10^{-4}, respectively, from M3: (a) E_y-field; and (b) E_x-field. Figure reproduced from Sun *et al.* [1]. 100

5.1 Illustration of an ideal dielectric-filled parallel-plate waveguide of width a. The length of the dielectric-filled section is l while the air-filled sections are of length l_{air}. In any section, As and Bs are the complex coefficients associated with the incident and reflected fields, respectively. 108

5.2 Plot of (a) return loss and insertion loss; and (b) absorptance of the dielectric-filled parallel-plate waveguide, operating in the dominant TE_1 mode, with width $a = 22.86$ mm and dielectric section of length $l = 9.626$ mm; with dielectric constant $\varepsilon'_{reff②} = 2.325$ and loss tangent $\tan\delta_{e②} = 19.73 \times 10^{-4}$ of the filled in-homogeneous and anisotropic dielectric medium. Dotted lines in (a) show the ideal response computed from theory, while the solid lines show the simulated response from the *COMSOL Multiphysics*® frequency domain solver. The spectral location of box-mode resonances can be clearly seen in (b), with the predicted box-mode resonance frequencies within 0.02 GHz compared to those computed from theory and eigenmode solver, given in Table 5.1. 112

5.3 Numerically simulated E_y-field plot for the even TE_{11} Fabry-Pérot eigenmode at $f_{11} = 5.6096$ GHz for the parallel-plate waveguide. The field lines extend well outside the boundaries of the dielectric, while the mode exists well below the cut-off frequency of air-filled waveguide. 113

5.4 Numerically simulated E_x-field plot for the odd TM_{11} Fabry-Pérot eigenmode at $f_{11} = 6.1412$ GHz for the parallel-plate waveguide. The field lines extend well outside the boundaries of the dielectric, while the mode exists well below the cut-off frequency of air-filled waveguide. 113

5.5 Numerically simulated E_y-field plot for the even TE_{21} Fabry-Pérot eigenmode at $f_{21} = 10.092$ GHz in the X-band for the parallel-plate waveguide. 114

5.6 Numerically simulated E_x-field plot for the odd TM_{21} Fabry-Pérot eigenmode at $f_{21} = 10.899$ GHz in the X-band for the parallel-plate waveguide. 114

5.7 Illustration of an ideal dielectric-filled circular waveguide of radius r_a. The length of the dielectric-filled section is l while the air-filled sections are of length l_{air}. In any section, As and Bs are the complex coefficients associated with the incident and reflected fields, respectively. 115

5.8 Plot of (a) return loss and insertion loss; and (b) absorptance of the dielectric-filled circular waveguide, operating in the dominant TE_{11} mode, with waveguide radius $r_a = 11.415$ mm and dielectric section of length $l = 9.626$ mm; with dielectric constant $\varepsilon'_{reff②} = 2.325$ and loss tangent $\tan\delta_{e②} = 19.73 \times 10^{-4}$ of the filled inhomogeneous and anisotropic dielectric medium. Dotted lines in (a) show the ideal response computed from theory, while the solid lines show the simulated response from the *COMSOL Multiphysics*® frequency domain solver. The spectral location of box-mode resonances can be clearly seen in (b), with the predicted box-mode resonance frequencies within 0.01 GHz compared to those computed from theory and eigenmode solver, given in Table 5.3. 118

5.9 Numerically simulated field plots for TE_{111} Fabry-Pérot eigenmode at $f_{111} = 6.4224$ GHz, obtained from *COMSOL Multiphysics*® for a dielectric-filled circular waveguide: (a) E_r-field; (b) E_ϕ-field. The mode exists well below the cut-off frequency of the waveguide. 119

5.10 Numerically simulated E_r-field plot for the odd TM_{101} Fabry-Pérot eigenmode at $f_{101} = 8.8134$ GHz, obtained from *COMSOL Multiphysics*® eigenmode solver for a dielectric-filled circular waveguide. 120

5.11 Numerically simulated E_ϕ-field plot for TE_{121} Fabry-Pérot eigenmode at $f_{121} = 9.8512$ GHz, obtained from *COMSOL Multiphysics*® eigenmode solver for a dielectric-filled circular waveguide. 121

5.12 Numerically simulated E_ϕ-field plot for TE_{101} Fabry-Pérot eigenmode at $f_{101} = 11.97$ GHz, obtained from *COMSOL Multiphysics*® eigenmode solver for a dielectric-filled circular waveguide. 121

6.1 Individual solutions in $n - \kappa$ space at 8.2 GHz from (a) ideal noiseless measurements emulated with $\tilde{n}_{ideal} = 1.5248 - j0.001468$ (set equal to $\tilde{n}$(11.08 GHz) from Sample #1 associated with Fabry-Pérot resonance modelling with the *variational* method); and (b) real noisy measurements for Sample #1, having $\tilde{n}_{extracted} = 1.5265 - j0.002281$ (corresponding to a dielectric constant and loss tangent of 2.330 and 29.89×10^{-4}, respectively). Figure redrawn from Sun *et al.* [2]. 127

6.2 Extracted values for dielectric constant and loss tangent (in 0.1 GHz steps) using the manual Graphical approach with l- and $2l$-stages for Samples #1 and #2. Figure reproduced from Sun *et al.* [2]. 129

6.3 Port reference impedances plotted on impedance Smith chart normalised to $Z^{air}_{TE10}(\omega)$ for the 3-D printed Sample #1 [2]. Blue crosses represent purely real impedances, while green asterisks represent complex impedances on the $1 \pm jx$ circle: (a) 8.2 GHz; (b) 11.08 GHz; (c) 12.4 GHz. Figure redrawn from Sun *et al.* [2]. 131

6.4 Port reference impedance plotted against frequency normalised to $Z^{air}_{TE10}(\omega)$ for the 3-D printed Sample #1 [2], corresponding to recommended data set: (a) $Re\{Z_T(\omega)/Z^{air}_{TE10}(\omega)\}$ corresponding to the $r \pm j0$ line; (b) $Im\{Z_T(\omega)/Z^{air}_{TE10}(\omega)\}$ corresponding to the $1 \pm jx$ circle. Figure redrawn from Sun *et al.* [2]. 131

6.5 Contour plots for common log of summations of the right-hand sides for (6.3)–(6.5), (6.8)–(6.9) and (6.12)–(6.13) for 3-D printed Sample #1 [2] at 9 GHz without renormalisation: (a) side view; (b) top view with solid black lines showing the target value $\tilde{n}$(11.08 GHz) and dotted black lines showing the extracted value. Figure reproduced from Sun *et al.* [2]. 133

6.6 Contour plots for common log of summations of the right-hand sides for (6.3)–(6.5), (6.8)–(6.9) and (6.12)–(6.13) for the 3-D printed Sample #1 [2] at 9 GHz with renormalisation: (a) side view; (b) top view with solid black lines showing the target value $\tilde{n}$(11.08 GHz) and dotted black lines showing the extracted value. Figure reproduced from *Sun et al.* [2]. 134

6.7 Extracted values for dielectric constant and loss tangent (in 0.01 GHz steps) using automated Renormalisation technique with $l/2$-, l-, $2l$-stages and shorted l-stage: (a) without impedance renormalisation; and (b) with impedance renormalisation. The spectral location of sharp spikes correspond to the 'open-box' mode resonances which affect the extracted values of dielectric constant and loss tangent. Without impedance renormalisation (a), abrupt changes in dielectric constant can be observed, most notably at the Fabry-Pérot resonance frequency, due to ambiguities. With renormalisation (b), however, the extracted responses are much smoother and not affected by the Fabry-Pérot resonance. Figure reproduced from *Sun et al.* [2]. 135

6.8 Extracted relative (effective permittivity and permeability) values using the Nicolson-Ross-Weir (in 0.01 GHz steps) and automated Renormalisation approaches: (a) real part of relative values for Sample #1; (b) loss tangent for Sample #1; (c) real part of relative values for Sample #2; and (d) loss tangent for Sample #2. Figure reproduced from Sun *et al.* [2]. 142

6.9 Noise sensitivity for a hypothetical dielectric sample having a fixed dielectric constant $\varepsilon'_{reff} = 2.31$ and loss tangent $\varepsilon''_{reff}/\varepsilon'_{reff} = 20 \times 10^{-4}$ (with $n_{Target} = 1.51987$ and $\kappa_{Target} = 1.52 \times 10^{-3}$ at 9 GHz) inserted into the simulated thru section of waveguide modelled at 9 GHz using the *variational* method: (a) Original NRW; (b) Modified NRW; and (c) Renormalisation method. Figure reproduced from Sun *et al.* [2]. . . . 147

6.10 Normalised *measurement* RMS error vector magnitudes from Fig. 6.9 for different methodologies. Figure reproduced from Sun *et al.* [2]. 148

6.11 Measured $|S_{21}|$ for the air-filled 9.626 mm long thru line section of MPRWG, with its running average and extracted random noise components. Figure reproduced from Sun *et al.* [2]. 150

7.1 Frequency versus normalised wavenumber dispersion plots of surface plasmon polaritons (SPP) for n-type Si samples with resistivities: (a) 10 Ωcm; (b) 1 Ωcm; and (c) 0.1 Ωcm. The dispersion curves were computed using (1.8), where the dielectric was assumed to be air with Si sample underneath. The surface plasmon frequency f_{sp} is also indicated for the three samples, which is also the limiting value as the wavenumber increases. SPPs are excited where the dispersion curves, for glass and SPPs on Si, intersect. The dotted lines below and above the SPP dispersion curve, respectively, represent the odd and even SPP modes on a Si slab of thickness 525 μm, which were numerically computed using (3.32) and (3.33). 157

7.2 Frequency versus normalised wavenumber dispersion plots of surface plasmon polaritons (SPP) for n-type Si samples with resistivities: (a) 10 Ωcm; (b) 1 Ωcm; and (c) 0.1 Ωcm. The dispersion curves were computed using (1.8), where the dielectric was assumed to be air with Si sample underneath. The surface plasmon frequency f_{sp} is also indicated for the three samples, which is also the limiting value as the wavenumber increases. SPPs are excited where the dispersion curves, for Si prism and SPPs on Si slab, intersect. The dotted lines below and above the SPP dispersion curve, respectively, represent the odd and even SPP modes on a Si slab of thickness 525 μm, which were numerically computed using (3.32) and (3.33). 159

7.3 The Otto attenuated total reflection (ATR) scheme, for excitation of surface plasmon polaritons (SPP), depicted as a planar media reflection/transmission problem. The incident transverse electromagnetic (TEM) waves in the prism medium undergo total internal reflection at the side of prism adjacent to the gap between the prism and Si slab. The evanescent fields in the gap can have a wavenumber, parallel to the interface, that can excite SPPs on the surface of Si slab as shown by the red arrow. The Si slab is backed by air or free space. In the *COMSOL Multiphysics*® frequency domain solver, the incident TEM waves are excited at Port 1 with the specified incident angle θ_{inc}. The simulation domain at the top and bottom are truncated in Floquet boundary conditions, with the k_y and k_{xi} wavenumbers for the Floquet boundary computed from (E.6) and (E.7) for any medium i, respectively. 161

7.4 Plot of return loss $20\log_{10}|S_{11}|$ of the planar media problem depicted in Fig. 7.3, against frequency and gap between the prism and Si slab d_{gap} for the 10 Ωcm Si sample with $\theta_{inc} = 45°$: (a) analytical method; and (b) *COMSOL Multiphysics*® frequency domain solver. The odd (left) and even (right) mode surface plasmon excitations can be seen as sharp contours in the return loss plot. The return loss reaches a minimum for the odd and even modes close to $d_{gap} = 415$ μm and $d_{gap} = 270$ μm, respectively. 164

7.5 Comparison of return loss $20\log_{10}|S_{11}|$ plotted against frequency obtained from analytical method and *COMSOL Multiphysics*® simulation with gap between the prism and Si slab set as $d_{gap} = 415$ μm. The response shows odd (left) and even (right) mode surface plasmon modes excited on a Si slab of thickness 525 μm and 10 Ωcm resistivity. The *COMSOL Multiphysics*® response is shifted towards higher frequencies by about 0.15 GHz compared to the analytical method. 165

7.6 Plot of analytically computed return loss $20\log_{10}|S_{11}|$ against frequency and angle of incidence with $d_{gap} = 415$ μm. The response shows odd (left) and even (right) mode surface plasmon modes excited on a Si slab of thickness 525 μm and 10 Ωcm resistivity.165

7.7 H_z magnetic field distributions of surface plasmons polaritons obtained from *COMSOL Multiphysics*® simulations for Si prism and 10 Ωcm Si slab at: (a) 103 GHz and; (b) 104.1 GHz. Odd and even mode surface plasmon excitations can be seen in (a) and (b), respectively, on both sides of the Si slab. 166

7.8 Contour plot of return loss $20\log_{10}|S_{11}|$ against frequency, and gap between the prism and Si slab d_{gap}, for the 1 Ωcm Si sample with $\theta_{inc} = 45°$. The optimal surface plasmon excitation occurs close to $d_{gap} = 160$ μm, where the return loss is minimum. 167

7.9 Comparison of return loss $20\log_{10}|S_{11}|$ plotted against frequency obtained from analytical method and *COMSOL Multiphysics*® simulation with gap between the prism and Si slab set as $d_{gap} = 160$ μm and $\theta_{inc} = 45°$. The predicted surface plasmon excitation from both methods is close to 341.8 GHz on a Si slab of thickness 525 μm and 1 Ωcm resistivity. 167

7.10 Analytically computed return loss $20\log_{10}|S_{11}|$ plotted against angle of incidence and frequency with $d_{gap} = 160$ μm. The return loss is minimum close to $\theta_{inc} = 45°$ corresponding to optimal surface plasmon excitation. The response tends to sharpen as θ_{inc} is increased. 168

7.11 H_z magnetic field distributions of surface plasmon polaritons (SPP) obtained from *COMSOL Multiphysics*® simulations for Si prism and 1 Ωcm Si sample at 341.8 GHz. The excited SPPs reside on the surface of Si slab close to the prism. For analytical calculations, the Si slab can be approximated, in this case, as a semi-infinite media. . 168

7.12 Simulated geometry showing prism, Si slab, ports and perfectly matched layer (PML) boundaries. A Ricker wavelet with a Gaussian profile is excited at Port 1, while Port 2 is used to record the transmitted fields. The evanescent component of the incident fields at the diagonal side of the prism excite surface plasmon polaritons on the Si slab. The whole simulation domain is terminated in PMLs to absorb any radiated fields. 170

7.13 Non-uniform triangular meshing scheme used in *COMSOL Multiphysics*® with $d_{gap} = 415$ μm: (a) fully meshed geometry; (b) zoomed view of lower part of prism and Si slab. As seen in the zoomed view (b), the meshing is finest inside the prism, gap and the Si slab. 171

7.14 Rectangular meshing scheme used in FDTD with $d_{gap} = 415$ μm: (a) fully meshed geometry; (b) zoomed view of lower part of prism and Si slab. With, rectangular meshing elements, the diagonal side of the prism and Si slab are approximated as a sawtooth. 171

7.15 Effective return loss $20\log_{10}|S_{11}^{eff}|$ from full-wave *COMSOL Multiphysics*® and finite-difference time domain simulations for the 10 Ωcm Si slab with $d_{gap} = 415$ μm. The response from both solvers show odd and even excitation of surface plasmons close to 103 and 104 GHz, respectively. 173

7.16 Effective return loss $20\log_{10}|S_{11}^{eff}|$ from *COMSOL Multiphysics*® and FDTD simulations for 1 Ωcm Si slab with $d_{gap} = 160$ μm. Unlike, analytical results, both full-wave solvers show two resonances in the observed response roughly centred around 342 GHz. 173

7.17 Analytically computed response $20\log_{10}|S_{11}|$ of a 750 μm thick test material having dielectric constant between 2.30 and 2.35 with 1 Ωcm Si slab. The surface plasmon resonance shifts by approximately 0.08 GHz if the dielectric constant changes by 0.01. 174

7.18 Analytically computed response $20\log_{10}|S_{11}|$ of a 300 μm thick test material having dielectric constant between 2.30 and 2.35 with 10 Ωcm Si slab. The surface plasmon resonance shifts by approximately 0.35 GHz if the dielectric constant changes by 0.01. 174

7.19 Effective return loss $20\log_{10}|S_{11}^{eff}|$ from full wave *COMSOL Multiphysics*® simulations for 10 Ωcm Si slab with $d_{gap} = 750$ μm. The surface plasmon resonance shifts by approximately 0.08 GHz if the dielectric constant changes by 0.01. 175

7.20 Effective return loss $20\log_{10}|S_{11}^{eff}|$ from full wave FDTD simulations for 10 Ωcm Si slab with $d_{gap} = 750$ μm. The surface plasmon resonance shifts by approximately 0.08 GHz if the dielectric constant changes by 0.01. 175

7.21 Effective return loss $20\log_{10}|S_{11}^{eff}|$ from full wave *COMSOL Multiphysics*® simulations for 1 Ωcm Si slab with $d_{gap} = 300$ μm. The surface plasmon resonance shifts by approximately 0.35 GHz if the dielectric constant changes by 0.01. 176

7.22 Effective return loss $20\log_{10}|S_{11}^{eff}|$ from full wave FDTD Multiphysics simulations for 1 Ωcm Si slab with $d_{gap} = 300$ μm. The surface plasmon resonance shifts by approximately 0.35 GHz if the dielectric constant changes by 0.01. 176

8.1 (a) Schematic side view of a 2-DES device used in experiments. The device geometry is inspired by the field-effect transistor; (b) Micrograph (adapted from Wu *et al.* [1]); and (c) schematic top view of the device used in experiments by Wu *et al.* The complex device geometry requires three-dimensional modelling. Figure reproduced from Dawood *et al.* [2]. 180

8.2 The transverse electric field profile of the even coplanar waveguide (CPWG) mode numerically computed from Laplace's equation, using a finite-difference scheme and method of relaxation. The thick black lines denote perfect electric conductor (PEC) boundaries and the CPWG conductors in the transverse plane. The lower half (shaded grey region) is GaAs substrate with the upper half (white region) is air. Fields are stronger in the GaAs region compared to air due to dielectric constant of GaAs being greater than air. With the even CPWG mode, the side conductors or ground planes of the CPWG must be maintained at the sample potential while the centre conductor is at a different potential. This is ensured by connecting the outer ground planes with the bounding PEC box. 184

8.3 Meshed model in *COMSOL Multiphysics*® illustrating the non-uniform meshing scheme with cubic elements. Along the longitudinal direction, meshing is finest in the gated region, while the ungated 2-DES and coplanar waveguide sections have coarse meshing. Along the vertical direction meshing is finest close to the 2-DES and AlGaAs layer with a total of 8 meshing elements in the z-direction. Along the y-direction, meshing is finest at the edges of the 2-DES. 185

8.4 (a) Measured gate modulation signals (data taken from Wu *et al.* [1]), compared with *COMSOL Multiphysics*® models having with $\tau = 33$ ps (b) and with $\tau = 7$ ps (c). The lower value of τ provides better agreement with experiment. The dashed lines show positions of plasmon resonances calculated by a two-dimensional modal technique. Figure reproduced from Dawood *et al.* [2]. 186

8.5 (a) Modelled true transmission ($20\log_{10}|S_{21}|$) for a range of gate voltages; and (b) transmission, reflection and absorption at a gate voltage of -2 V in the device. The absorption and reflection dominate, and the transmission does not exceed -25 dB. The spectral location of resonances are indicated with the transmission plot in (b). Figure reproduced from Dawood *et al.* [2]. 189

8.6 Distributions of the longitudinal component of the electric field on the 2-DES. The frequencies correspond to the transmission peaks in Fig. 8.5. The left panels present the top view, the right panels present the field calculated along a line across the middle of the 2-DES. The first three resonances appear to be predominantly longitudinal excitations; the last two-resonances show transverse excitations and excitations at the edges of the 2-DES. Figure reproduced from Dawood *et al.* [2]. 190

8.7 (a) Measured (data taken from Wu *et al.*[4]); and (b) simulated gate-modulation signals for magneto-plasmons. The dashed lines are the predicted resonances from the 2-D modal technique. The red line indicates the cyclotron frequency. Theory and experiment agree for features between 100 and 300 GHz. Figure reproduced from Dawood *et al.* [2]. 192

8.8 Simulated true transmission ($20\log_{10}|S_{21}|$) from *COMSOL Multiphysics*® frequency domain solver for the same structure. The dashed lines show positions of the resonances predicted by the 2-D modal technique. Figure reproduced from Dawood *et al.* [2]. 193

8.9 Top view of the device with improved characteristics. A shorter overall length reduces absorption in the 2-DES channel (shaded red), whereas, connecting the gate and the ground planes of the coplanar waveguides provides better coupling between the 2-DES and the waveguides. Figure reproduced from Dawood *et al.* [2]. 195

8.10 Simulated transmission (a) as a function of gate voltage; and (b) the transmission, reflection, and absorption characteristics at a gate voltage of -2 V for the device of Fig. 8.9. At 164 GHz, the transmission is around -3 dB, and the insertion loss is below -15 dB. Figure reproduced from Dawood *et al.* [2]. 196

8.11 Longitudinal component of the electric field on the 2-DES at the three transmission peaks shown in Fig. 8.10 at 164, 272 and 393 GHz. The left panels present the top view, the right panels present the field calculated along a line across the middle of the 2-DES. At all frequencies, only longitudinal plasmons are excited. Figure reproduced from Dawood *et al.* [2]. 197

8.12 Lossy τ profile in the transverse direction along the 2-DES channel. The 2-DES lies at $-15 < y < 15$ μm. The profile introduces edge losses in the 2-DES channel. 199

8.13 Plot of gate modulation signal with the lossy profile shown in Fig. 8.12. The dashed lines show predicted resonances from the 2-D modal technique. Adding edge losses broadens the resonances obtained from simulation. 199

8.14 Plot of gate modulation signal with substrate losses and $\tau = 33$ ps. The dashed lines show predicted resonances from the 2-D modal technique. With substrate losses, the resonances obtained from simulation are broadened. 200

8.15 Plot of gate modulation signal taking into account ohmic losses in contacts with $\tau = 33$ ps. The dashed lines show predicted resonances from the 2-D modal technique. Some of the resonances are broadened while some sharp resonances can also be observed. 200

C.1 Forces on an electron in the presence of electric field. $\mathbf{E}$ is an externally applied electric field, $e\mathbf{E}$ is the force on electron due to $\mathbf{E}$, $m\mathbf{v}/\tau$ is the damping force and $md\mathbf{v}/dt$ is the resultant force. 215

E.1 Illustration of transverse electromagnetic (TEM) wave obliquely incident at an interface between two media making an angle θ_{inc} with the normal: (a) transverse electric (TE or s-polarisation); and (b) transverse magnetic (TM or p-polarisation). The coefficients A_i are the amplitudes of incident transverse field components in medium i while, the coefficients B_i are the amplitudes of reflected transverse field components in medium i. 220

F.1 Illustration of transverse electromagnetic (TEM) wave obliquely incident on a planar three-layer media making an angle θ_{inc} with the normal: (a) transverse electric (TE or s-polarisation); and (b) transverse magnetic (TM or p-polarisation). The coefficients A_i are the amplitudes of incident transverse field components in medium i while, the coefficients B_i are the amplitudes of reflected transverse field components in medium i. The slab is of thickness l. 226

List of Tables

2.1 Transformation relationship between voltage, current and pseudo waves. 39

2.2 Transformation relationship between voltage, current and power waves. 39

2.3 Summary of exact equations for two-media and one- or two-port modelling. 47

2.4 Summary of theoretical bounds for coefficients and parameters with positive resistances. 50

3.1 Comparison of numerically computed eigenfrequencies of the lossy 1-D resonator with ideal case. Resonator length is $l = 300$ μm with bulk DC conductivity of resonator wall being 100 S/m. The computed absolute value of complex eigenfrequency $|\tilde{f}_0|$ corresponds to the spectral location of peaks of S_{21} in Fig.3.4. The ideal response corresponds to the spectral location of dips of S_{11} in Fig.3.4. 69

4.1 Fabry-Pérot resonance simulation results with numerical modelling M5. Table reproduced from Sun *et al.* [1]. 88

4.2 Open-box mode resonance frequencies (and associated mode Q-factors) spectroscopically measured and predicted using numerical eigenmode solver and field-based analytical solutions. Table reproduced from Sun *et al.* [1]. 101

5.1 Fabry-Pérot eigenmodes (and associated mode Q-factors) computed using analytical field-based solutions and numerical eigenmode solver for the parallel-plate waveguide shown in Fig. 5.1. 111

5.2 Numerical values of p_{mn} and p'_{mn} for selected mn mode numbers for the respective TM and TE modes in a circular waveguide. Table reproduced from Pozar [7]. 117

5.3 Fabry-Pérot eigenmodes (and associated mode Q-factors) in a circular waveguide computed using analytical field-based solutions and numerical eigenmode solver for the CWG (Fig. 5.7). 120

6.1 NRW extracted X-band dielectric properties for all ABS samples reported by Deffenbaugh *et al.* [4]. Table reproduced from *Sun et al.* [2]. 136

6.2 Summary of dielectric properties for ABS extracted using various strategies. Table reproduced from Sun *et al.* [2]. 143
6.3 X-band averages of dielectric constant extracted using various strategies. Table reproduced from Sun *et al.* [2]. 144
6.4 Worst-case normalised *measurement* peak error vector magnitudes from Fig. 6.9 for different methodologies. Table reproduced from Sun *et al.* [2]. 148
6.5 Upper-bound *Measurement* $S/N|_{\mathrm{db}}$ summary for the calibrated Agilent E8364 PNA Network Analyzer calibrated in waveguide at X-band. Table reproduced from Sun *et al.* [2]. 150

7.1 Physical parameters of available n- and p-type heavily doped Si samples. Data reproduced from Otter [1]. 158

8.1 Dimensions used in simulations (see Fig. 8.1). Table reproduced from Dawood *et al.* [2].182

H.1 Conversion from S to Z, Y, h, ABCD and T parameters. 230
H.2 Conversion from Z to S, Y, h, ABCD and T parameters. 231
H.3 Conversion from Y to S, Z, h, ABCD and T parameters. 231
H.4 Conversion from h to S, Z, Y, ABCD and T parameters. 232
H.5 Conversion from ABCD to S, Z, Y, h and T parameters. 232
H.6 Conversion from T to S, Z, Y, h and ABCD parameters. 233
H.7 Conversion between two-port S- and $\mathrm{S_p}$-parameters. 233

List of Abbreviations

2-DES	2-Dimensional Electron System
ABS	Acrylonitrile Butadiene Styrene
AC	Alternating Current
ADE	Alternate Differential Equation
ATR	Attenuated Total Reflection
AWGN	Additive White Gaussian Noise
CCIM	Complex Conjugate Impedance Matching
CPU	Central Processing Unit
CPWG	Coplanar Waveguide
CWG	Circular Waveguide
DC	Direct current
EIA	Electronics Industries Alliance
EM	Electromagnetic
EVM	Error Vector Magnitude
FDM	Fused Deposition Modelling
FDTD	Finite Difference Time-Domain
FTIR	Fourier-Transform Infrared
IEEE	Institute of Electrical and Electronic Engineers
IF	Intermediate Frequency
GHz	Gigahertz
HEMT	High Electrom Mobility Transistor
HIPS	High Impact Polystyrene
MOSFET	Metal Oxide Semiconductor Field Effect Transistor
MPRWG	Metal-Pipe Rectangular Waveguide
MW	Microwave
NPL	National Physical Laboratory
NRW	Nicolson-Ross-Weir
PBC	Periodic Boundary Condition
PEC	Perfect Electric Conductor
PPWG	Parallel-Plate Waveguide
SI	International System of Units
PIMMS	Primary Impedance Microwave Measurement System
PMC	Perfect Magnetic Conductor
PML	Perfectly Matched Layer
PNA	Performance Network Analyser
RAM	Random Access Memory
RMS	Root Mean Square
SEM	Scanning Electron Microscope

SNR	Signal-to-Noise Ratio
SPP	Surface Plasmon Polariton
TDS	Time Domain Spectrometer
TE	Transverse Electric
TEM	Transverse Electromagnetic
THz	Terahertz
TM	Transverse Magnetic
TRL	Thru/Reflect/Line
VNA	Vector Network Analyser

List of Symbols

Greek Symbols

α	attenuation constant	Np/m
β	phase constant	rad/m
β_0	phase constant in free space	rad/m
γ	propagation constant	rad/m
$\breve{\gamma}$	collision frequency	1/s
γ_{10}	propagation constant of TE_{10} mode in MPRWG	rad/m
γ_{10}^{air}	propagation constant of TE_{10} mode in air-filled MPRWG	rad/m
γ_c	propagation constant at cut-off frequency of fundamental mode in waveguide	rad/m
γ_{cmn}	propagation constant at cut-off frequency of mn mode in waveguide	rad/m
γ_g	guided-wave propagation constant	rad/m
γ_{ud}	propagation constant in unbound dielectric medium	rad/m
$\mathit{\Gamma}$	electric field reflection coefficient	dimensionless
$\widetilde{\mathit{\Gamma}}$	voltage reflection coefficient	dimensionless
$\mathit{\Gamma}_p$	power reflection coefficient	dimensionless
$\breve{\Delta}$	duty cycle	dimensionless
$\tan\delta$	loss tangent	dimensionless
$\tan\delta_e$	electric loss tangent	dimensionless
ε_0	permittivity of free space	F/m
ε	permittivity (real)	F/m
$\tilde{\varepsilon}$	permittivity (complex)	F/m
ε_{ox}	dielectric constant of material between 2DES and gate	dimensionless
ε_r	relative permittivity (real)	dimensionless
$\tilde{\varepsilon}_r$	relative permittivity (complex)	dimensionless
ε_r'	real part of complex relative permittivity	dimensionless
ε_r''	imaginary part of complex relative permittivity	dimensionless
$\varepsilon_{r\infty}$	high frequency relative permittivity	dimensionless
ε_{rbulk}	bulk relative permittivity of an anisotropic/non-homogeneous dielectric	dimensionless
ε_{reff}'	real part of effective complex relative permittivity	dimensionless
ε_{reff}''	imaginary part of effective complex relative permittivity	dimensionless
ε_s	dielectric constant of substrate	dimensionless
ζ	TM or TE scalar	dimensionless
η	intrinsic impedance	Ω
$\acute{\eta}$	TM or TE intrinsic impedance	Ω
η_0	intrinsic impedance of free space	Ω

θ_{inc}	incident angle	rad
κ	extinction coefficient	dimensionless
λ	wavelength	m
λ_0	wavelength in free space	m
λ_c	wavelength at cut-off frequency of fundamental mode in waveguide	m
λ_{cmn}	wavelength at cut-off frequency of mn mode in waveguide	m
λ_g	wavelength in waveguide	m
λ_{ud}	wavelength in unbound dielectric medium	m
μ	permeability (real)	H/m
$\tilde{\mu}$	permeability (complex)	H/m
μ_0	permeability of free space	H/m
μ_r	relative permeability (real)	dimensionless
$\tilde{\mu}_r$	relative permeability (complex)	dimensionless
μ_r'	real part of complex relative permeability	dimensionless
μ_r''	imaginary part of complex relative permeability	dimensionless
ν_{AWGN}	additive white Gaussian noise	dimensionless
ν_{noise}	noise signal	dimensionless
$\nu_{noiseless}$	noiseless signal	dimensionless
ν_{noisy}	signal with noise	dimensionless
ξ	ratio of dielectric-filled wave impedance to air-filled wave impedance of MPRWG	dimensionless
ρ_0	Fresnel reflection coefficient with first medium being free space	dimensionless
ρ_{11}	Fresnel reflection coefficient (general two-media)	dimensionless
ρ_V	volume charge density	C/m^3
σ	intrinsic bulk conductivity	S/m
σ_{2D}	AC 2-D Drudé conductivity	S
σ_{error}	RMS error in extraction process	dimensionless
τ	relaxation time	s
τ_{20}	Fresnel transmission coefficient with first medium being free space	dimensionless
τ_{21}	Fresnel transmission coefficient (general two-media)	dimensionless
τ_g	differential-phase group delay	s
ω	angular frequency	rad/s
ω_c	angular cut-off frequency of fundamental mode in waveguide	rad/s
ω_{cmn}	angular cut-off frequency of mn mode in waveguide	rad/s
ω_{fp}	angular frequency at Fabry-Pérot resonance	rad/s
ω_p	angular plasma frequency	rad/s

Latin Uppercase Letters

$\mathcal{A}$	absorptance	dimensionless
B	magnetic flux density	Wb/m^2
D	electric flux density	C/m^2
E	electric field	V/m
E_0	amplitude of electric field	V/m
E_t	transverse electric field	V/m

E_z	longitudinal electric field	V/m
H	magnetic field	A/m
H_t	transverse magnetic field	A/m
H_z	longitudinal of magnetic field	A/m
I	current	A
I^+	forward current (wave)	A
I^-	backward/reverse current (wave)	A
I_0	current coefficient	A
I_j	current at Port j	A
J	electric current density	A/m^2
J_m	magnetic current density	V/m^2
P	complex propagation factor in Nicolson-Ross-Weir method	dimensionless
P_{av}	average power	W
P_i	incident average power	W
P_{noise}	RMS of noise signal	dimensionless
$P_{reference}$	RMS of noiseless signal	dimensionless
P_r	reflected average power	W
P_t	transmitted average power	W
Q_0	Q-factor of unbound dielectric	dimensionless
Q_{0e}	electric component of Q-factor	dimensionless
Q_{0e}	magnetic component of Q-factor	dimensionless
Q_L	loaded Q-factor	dimensionless
Q_U	unloaded Q-factor	dimensionless
Q_c	Q-factor contribution from conductive losses	dimensionless
Q_d	Q-factor contribution from dielectric losses	dimensionless
Q_e	Q-factor contribution from radiative losses	dimensionless
R	resistance	Ω
$\mathcal{R}$	reflectance	dimensionless
$\mathcal{R}_{MEAS}$	reflectance from measurements	dimensionless
$\mathcal{R}^{CAS}$	reflectance of $2l$-stage cascaded network	dimensionless
$\mathcal{R}^{CAS}_{MEAS}$	reflectance of $2l$-stage cascaded network from measurements	dimensionless
$\mathcal{R}^{HALF}$	reflectance of $l/2$-stage network	dimensionless
$\mathcal{R}^{HALF}_{MEAS}$	reflectance of $l/2$-stage network from measurements	dimensionless
$\mathcal{R}^{PEC}$	reflectance at input Port 1 with Port 2 shorted	dimensionless
$\mathcal{R}^{PEC}_{MEAS}$	reflectance at input Port 1 with Port 2 shorted from measurements	dimensionless
S^{PEC}_{11}	voltage/pseudo-wave reflection coefficient at input Port 1 with Port 2 shorted	dimensionless
S^{eff}_{11}	effective voltage/pseudo-wave reflection coefficient	dimensionless
S^{PEC}_{11SIM}	simulated voltage/pseudo-wave reflection coefficient at input Port 1 with Port 2 shorted	dimensionless
S_{jiMEAS}	voltage/pseudo-wave transmission coefficient with input Port i and output Port j from measurements	dimensionless
S_{jiSIM}	simulated voltage/pseudo-wave transmission coefficient with input Port i and output Port j	dimensionless
S^{CAS}_{jiSIM}	voltage/pseudo-wave transmission coefficient with input Port i and output Port j of $2l$-stage cascaded network	dimensionless
S^{HALF}_{jiSIM}	voltage/pseudo-wave transmission coefficient with input Port i and output Port j of $l/2$-stage network	dimensionless
S_{ji}	voltage/pseudo-wave transmission coefficient with input Port i and output Port j	dimensionless

S_{ji}^{CAS}	voltage/pseudo-wave transmission coefficient with input Port i and output Port j of $2l$-stage cascaded network	dimensionless
S_{jj}	voltage/pseudo-wave reflection coefficient at Port j	dimensionless
S_{pji}	power-wave transmission coefficient with input Port i and output Port j	dimensionless
S_{pjj}	power-wave reflection coefficient at Port j	dimensionless
T	electric field transmission coefficient	dimensionless
T_p	power transmission coefficient	dimensionless
$\mathcal{T}$	transmittance	dimensionless
$\mathcal{T}^{CAS}$	transmittance of $2l$-stage cascaded network	dimensionless
$\mathcal{T}_{MEAS}^{CAS}$	transmittance of $2l$-stage cascaded network from measurements	dimensionless
$\mathcal{T}^{HALF}$	transmittance of $l/2$-stage network	dimensionless
$\mathcal{T}_{MEAS}^{HALF}$	transmittance of $l/2$-stage network from measurements	dimensionless
$\mathcal{T}_{MEAS}$	transmittance from measurements	dimensionless
V	voltage	V
V^+	forward or incident voltage wave	V
V^-	backward or reflected voltage wave	V
V_0	voltage coefficient	V
V_g	gate voltage	V
V_j	voltage at Port j	V
W	stored energy in a resonator	J
W_E	stored magnetic energy in a resonator	J
W_M	stored magnetic energy in a resonator	J
Z_0	characteristic impedance of a transmission line	Ω
Z_0^{air}	characteristic impedance of air-filled MPRWG	Ω
Z_L	load impedance	Ω
Z_S	source impedance	Ω
Z_T	reference port impedance of MPRWG	Ω
Z_{TE10}	wave impedance of TE_{10} mode	Ω
$Z_{TE\mathrm{mn}}$	wave impedance of $\mathrm{TE}_{\mathrm{mn}}$ mode	Ω
$Z_{TE\mathrm{mn}}^{air}$	wave impedance of $\mathrm{TE}_{\mathrm{mn}}$ mode in air-filled waveguide	Ω
$Z_{TM\mathrm{mn}}$	wave impedance of $\mathrm{TM}_{\mathrm{mn}}$ mode	Ω
Z_{ref}	reference impedance	Ω
Z_{refj}	reference impedance at Port j	Ω
Z_s	surface impedance	Ω

Latin Lowercase Letters

$\underrightarrow{a}$	incident travelling wave or pseudo wave	$\mathrm{V}/\Omega^{1/2}$
a_j	incident voltage wave at Port j	$\mathrm{V}/\Omega^{1/2}$
a_{pj}	incident power wave at Port j	$\mathrm{V}/\Omega^{1/2}$
$\underleftarrow{b}$	reflected travelling wave or pseudo wave	$\mathrm{V}/\Omega^{1/2}$
b_j	reflected voltage wave at Port j	$\mathrm{V}/\Omega^{1/2}$
b_{pj}	reflected power wave at Port j	$\mathrm{V}/\Omega^{1/2}$
c	speed of light in vacuum	m/s
d_{gap}	gap between prism and Si sample	m
e	charge on electron	C

e_t	transverse electric field component	V/m
e_z	longitudinal electric field component	V/m
f	frequency	1/s
$\tilde{f}_0$	complex eigenfrequency	1/s
f_0'	real part of complex eigenfrequency	1/s
f_0''	imaginary part of complex eigenfrequency	1/s
f_c	cut-off frequency of fundamental mode in waveguide	1/s
f_{cm0}	cut-off frequency of mn mode in waveguide	1/s
f_{fp}	Fabry-Pérot resonance frequency	1/s
f_I	resonant frequency of fundamental mode of an ideal resonator	1/s
f_m	resonant frequency of $\mathrm{m}^{\mathring{th}}$ mode of an ideal resonator	1/s
$\tilde{f}_{mnp}$	complex resonance frequency of mnp eigenmode	1/s
f_p	plasma frequency	1/s
h_t	transverse magnetic field component	A/m
h_z	longitudinal magnetic field component	A/m
k	wavenumber	radians/m
k_0	wave number in free space	radians/m
k_c	wavenumber at cut-off frequency of fundamental mode in waveguide	radians/m
k_{cmn}	wavenumber at cut-off frequency of mn mode in waveguide	radians/m
k_g	guided-wave wavenumber	radians/m
$\check{k}_j$	voltage-wave scalar coefficient at Port j	$\mathrm{V}/\Omega^{1/2}$
k_p	plasma wave number	radians/m
$\check{k}_{pj}$	power-wave scalar coefficient at Port j	$\mathrm{V}/\Omega^{1/2}$
k_{ud}	wavenumber in unbound dielectric medium	radians/m
l	longitudinal length of Fabry-Pérot resonator in guided-wave media	m
l_{air}	longitudinal length of air-filled sections of waveguide	m
l_p	spatial length of a period	m
l_{side}	length of shorter side of right-angled 45° prism	m
m	mass	kg
m	also used as integer mode number	dimensionless
m^*	effective mass of electron	kg
m_e	mass of electron	kg
n	refractive index (real)	dimensionless
n	also used as integer mode number	dimensionless
n_{2D}	number of charges per unit area	$1/\mathrm{m}^2$
n_{3D}	number of charges per unit volume	$1/\mathrm{m}^3$
$\tilde{n}$	refractive index (complex)	dimensionless
$\tilde{n}_{Target}$	target value of complex refractive index	dimensionless
$\tilde{n}_{extracted}$	extracted complex refractive index	dimensionless
$\tilde{n}_{ideal}$	extracted value of complex refractive index under noiseless scenario	dimensionless
n_φ	number of Fabry-Pérot resonance	dimensionless
p_0	average power coefficient	W
r	position	m
t	time	s
$t_{channel}$	quasi-2D channel thickness	m
v	velocity	m/s

Chapter 1

Current Research Trends in Terahertz Technology

1.1 Terahertz Technology

Several different definitions of the 'terahertz' (THz) band in the electromagnetic spectrum can be found in the open literature. Sun *et al.* [1] have reviewed some of these definitions of the THz band, which are used in different contexts. According to Sun *et al.* [1], "the THz band may loosely refer to the electromagnetic spectrum between 0.1–10 THz. This region is sometimes referred to as the "THz Gap", where the performance of conventional electronic (photonic) devices fall off with increasing frequency (decreasing wavelength). Over time, this technology gap continues to shrink; leading to the International Telecommunications Union (ITU)-designated spectral range from 0.3–3 THz (also known as the submillimeter-wave band). With reference to heterodyne receivers, frequencies> 3 THz are sometimes referred to as "super-THz". For optics and photonics, the International Organisation for Standardisation quote the far infrared (FIR) as being from 0.3–6 THz and mid-infrared (MIR) from 6–100 THz. When dealing with Earth systems, the FIR can be defined as THz frequencies below 20 THz; while in spectroscopy, the FIR extends from 0.3–30 THz and MIR from 30–120 THz" [1].

The THz band remained untapped for a long time and research in this spectral range was mainly confined to radio astronomy and spectroscopy [2]. Recently, there has been an increased interest in the THz band, due to saturation of the electromagnetic spectrum and also due to the potential for higher bandwidth communications. Nowadays, the electromagnetic spectrum has become a precious commodity. Therefore, efficient utilisation of the electromagnetic spectrum is necessary in order to accommodate growing demands of wireless communication systems and electrical devices. Current

communication systems operating at microwave frequencies up to a few gigahertz (GHz) offer data rates up to gigabit per second. Communication systems operating at THz frequencies will increase current data rates by an order of magnitude up to terabits per second.

The THz band has also attracted a lot of attention from researchers in the last 10–15 years due to some unique qualities of the THz radiation. In metals and metal-like materials like semi-conductors, THz plasma waves can be confined to very small spaces [3] and become extremely sensitive to physical conditions like temperature [4]. This can be exploited in the development of high resolution imaging, highly sensitive sensors and detectors, switches and the fabrication of extremely small-scale devices. THz radiation is non-ionising and this property is especially of interest in the field of medical imaging for detection of cancers and tumours [5].

One difficulty faced by researchers, is a lack of THz sources that can generate adequate levels of power required for communication. This has led researchers to development of THz sources based on quantum cascade lasers [6], resonant tunnelling diodes [7] and optically pumped lasers [8].

Despite difficulties in the development of THz technology, researchers have successfully demonstrated several novel applications of THz radiation [9]. For example, successful treatment of cancer in rats [9], 3-D printed tunable THz components [10], inspection of artwork [11] and bank notes [12], estimating layer thickness of tablets [13] and paint [14], detection of concealed weapons [15], airport security [16] and imaging of burn wounds [17].

Advances in THz technology is accompanied with a need to accurately model prototype THz devices using analytical and numerical techniques. These techniques can be classified as either rigorous or non-rigorous. Rigorous techniques give an exact solution subject to certain parameters, while non-rigorous methods give an approximate solution based on certain assumptions. Among numerical techniques, commercial solvers offer the best modelling tools but setting up these solvers correctly is often not trivial. For example, intuitive choice of certain parameters may result in unexpected results [18] due to undocumented assumptions by the solver. Also, there are certain limitations, beyond which, these solvers do not guarantee accurate results as in the case of lossy resonators [19].

1.2 Plasmonics

The Greeks, as far back as the 4^{th} century, were familiar with the changing colours of glass when gold or silver particles were suspended in it. This concept was used in the construction of stained glass windows to develop beautiful patterns and works of art. It is now well understood that the changing colours of stained glass windows is due to the surface plasmon excitation when light

interacts with the suspended gold or silver nanoparticles.

Surface plasmons are EM wave, which propagate along the interface or the surface of a metal. The wavelength of these surface waves can be up to 10–100 times shorter than the free space wavelength. The confinement of waves in a small space (as surface plasmons) opens up a wide range of possible applications for reducing device size.

The study of surface plasmons, known as plasmonics, has been around for quite a while but only recently, there has been an increasing interest in plasmonics in the THz band. With integrated electronic devices nearing their speed and bandwidth limitations [3], a promising solution is to replace these devices with EM waves operating in the near-infrared or beyond near-infrared due to the higher bandwidth available, as the operating frequency increases. But these EM waves can only propagate in a medium with dimensions comparable to the wavelength of EM wave, due to diffraction limit [4]. This places a restriction on the fabricated device size, which is much greater than the fabricated device size of current electronic devices in use. As an example, for signals employing near-infrared wavelength of about 1500 nm (200 THz) the minimum dimensions required for propagation is much larger than dimensions of smallest electronic devices in use [9], which are typically in the order of 10–100 nm.

During the recent decade, a lot of research work has been carried out in order to utilise plasmonics in different areas. Efforts are ongoing to develop something called a 'plasmonster' or a plasmonic transistor. Such a device would result in phenomenal data rates while, at the same time, the device size would also be comparable to the size of current electronic devices in use.

A particular application of plasmonics is in the treatment of cancer. Experiments carried out on rats have shown that extremely small dielectric nano-particles coated with silver can attach themselves to the cancer cells when injected in the blood stream of rats. When infrared light was used to illuminate these particles, thereby raising their temperature, the cancer cells were killed. Thus, such rats were cured of cancer [9].

1.3 Bulk Plasmon-Polaritons

The wavenumber of a plane wave propagating through the bulk of a metal is given by,

$$k = \frac{\omega}{c}\sqrt{\mu_r \tilde{\varepsilon_r}\left(\omega\right)} \tag{1.1}$$

where, $\varepsilon_{r\tilde{e}ff}\left(\omega\right)$ is the frequency-dependent effective relative permittivity given by Drude model. For the lossless case with $\varepsilon_r = 1$ and $\mu_r = 1$, the wavenumber from (C.10) is,

$$k = \frac{\omega}{c}\sqrt{1 - \frac{\omega_p^2}{\omega^2}} \tag{1.2}$$

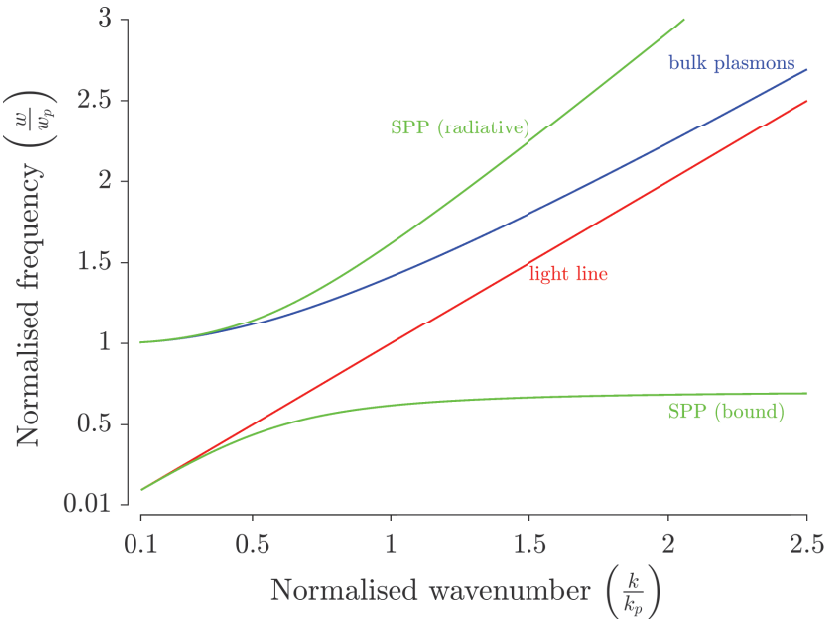


Figure 1.1: Dispersion plot of frequency against wavenumber showing the dispersion curves of surface plasmon polaritons (red) and bulk plasmons (blue). The bound surface plasmons only exist below the plasma frequency while the radiative and bulk plasmons cannot propagate below plasma frequency. Also, the existence of modes to the left of the light line can be excited by an incident electromagnetic wave while the bound surface plasmons on the right of the light line can only be excited using special techniques.

The dispersion of bulk plasmon-polaritons is plotted in Fig. 1.1 with respect to normalised wavenumber k/k_p and normalised frequency ω/ω_p, where $k_p = \omega_p/c$.

1.4 Surface Plasmon-Polaritons as Surface Waves on a Metal

Surface plasmon-polaritons (SPP) are waves due to collective oscillation of electrons on the surface of a metal (or plasma). They are similar to water waves on the surface of a pond if one throws a stone into water. SPPs are excited when electromagnetic waves are incident from a medium of positive permittivity onto a medium of negative permittivity under the right conditions. This is a common scenario in the case of certain metals, like gold and silver, which exhibit negative permittivity in a broad frequency spectrum.

Surface plasmons are excited when a wave from medium 1 is incident onto medium 2 (such as a metal), with $\varepsilon_{r2} > -\varepsilon_{r1}$ [20] as shown in Fig. 1.2. It can be shown that the component of wave along the interface (k_x) is real and the component of wave normal to the interface, say k_y, is complex. The electromagnetic field in a surface wave decays along both $+y$- and $-y$-directions, but propagates along x. The wave is described by the following field expressions [20],

$$H_z = \begin{cases} Ae^{-(jk_x x - \kappa_{y2} y)} & y \leq 0 \\ Ae^{-(jk_x x + \kappa_{y1} y)} & y > 0 \end{cases} \tag{1.3}$$

$$E_x = \begin{cases} \dfrac{\kappa_{y2}}{j\omega\varepsilon_{eff2}} Ae^{-(jk_x x - \kappa_{y1} y)} & y \leq 0 \\ \dfrac{-\kappa_{y1}}{j\omega\varepsilon_{eff1}} Ae^{-(jk_x x + \kappa_{y1} y)} & y > 0 \end{cases} \tag{1.4}$$

$$E_y = \begin{cases} \dfrac{k_{x2}}{\omega\varepsilon_{eff2}} Ae^{-(jk_x x - \kappa_{y2} y)} & y \leq 0 \\ \dfrac{k_{x1}}{\omega\varepsilon_{eff1}} Ae^{-(jk_x x + \kappa_{y1} y)} & y > 0 \end{cases} \tag{1.5}$$

where,

$$k_x^2 = k_1^2 + \kappa_{y1}^2 = k_2^2 + \kappa_{y2}^2 \tag{1.6}$$

which imposes the following condition,

$$-\frac{\kappa_{y1}}{\varepsilon_{eff1}} = \frac{\kappa_{y2}}{\varepsilon_{eff2}} \tag{1.7}$$

which leads to,

$$k_x = \frac{\omega}{c}\sqrt{\frac{\varepsilon_{r1}\varepsilon_{r2}}{\varepsilon_{r1} + \varepsilon_{r2}}} \tag{1.8}$$

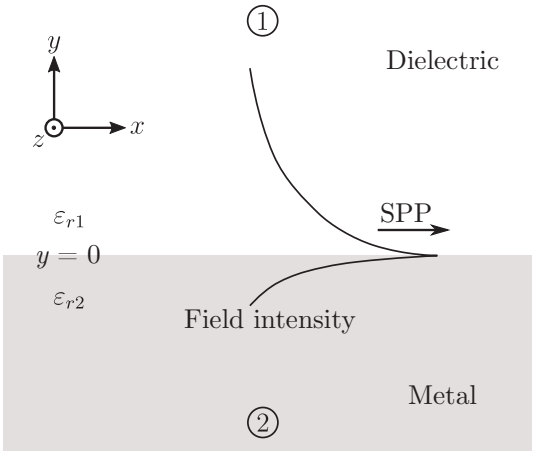


Figure 1.2: Surface plasmon polariton as surface wave on a dielectric/metal boundary. The electromagnetic field decays along the y-direction away from $y = 0$ interface but propagates along the $+x$-direction. Here, $\varepsilon_{r1} > 0$ and $\varepsilon_{r2} < 0$.

and,

$$k_{yi} = \frac{\omega}{c}\sqrt{\frac{\varepsilon_{ri}^2}{\varepsilon_{r1} + \varepsilon_{r2}}} \tag{1.9}$$

where, $jk_{yi} = \kappa_{yi}$. The subscript i is either 1 for air/dielectric or 2 for metal.

A beam of light incident on a metal cannot excite surface plasmons under ordinary circumstances. This is because the wavenumber of light is less than the wavenumber of SPP, which lies parallel to the surface of metal. The wavenumber of incident beam must increase so as to provide a parallel component of wavenubmer that matches with the wavenumber of SPP. One technique is to use attenuated total reflection (ATR) of the incident beam such that the required wavenumber is provided by the evanescent component of electric field on the side where total internal reflection takes place.

There are two ATR configurations for exciting surface plasmon polaritons, Otto and Kretschmann configurations; which are named after the respective scientists who proposed them. These two configurations are shown in Fig. 1.3. In the Otto configuration, a material which can exhibit negative permittivity at frequencies of interest, like a metal, is placed underneath a prism with a gap (filled with dielectric) between the metal and the prism. A beam of light incident on the prism undergoes total internal reflection if the angle of incidence is greater than the critical angle of prism. The evanescent fields due to ATR on the bottom side of the prism interact with the metal and excite surface plasmons on the upper surface of the metal. In the Kretschmann configuration, there is no gap between the prism and metal, while surface plasmons are excited on the lower surface of the metal.

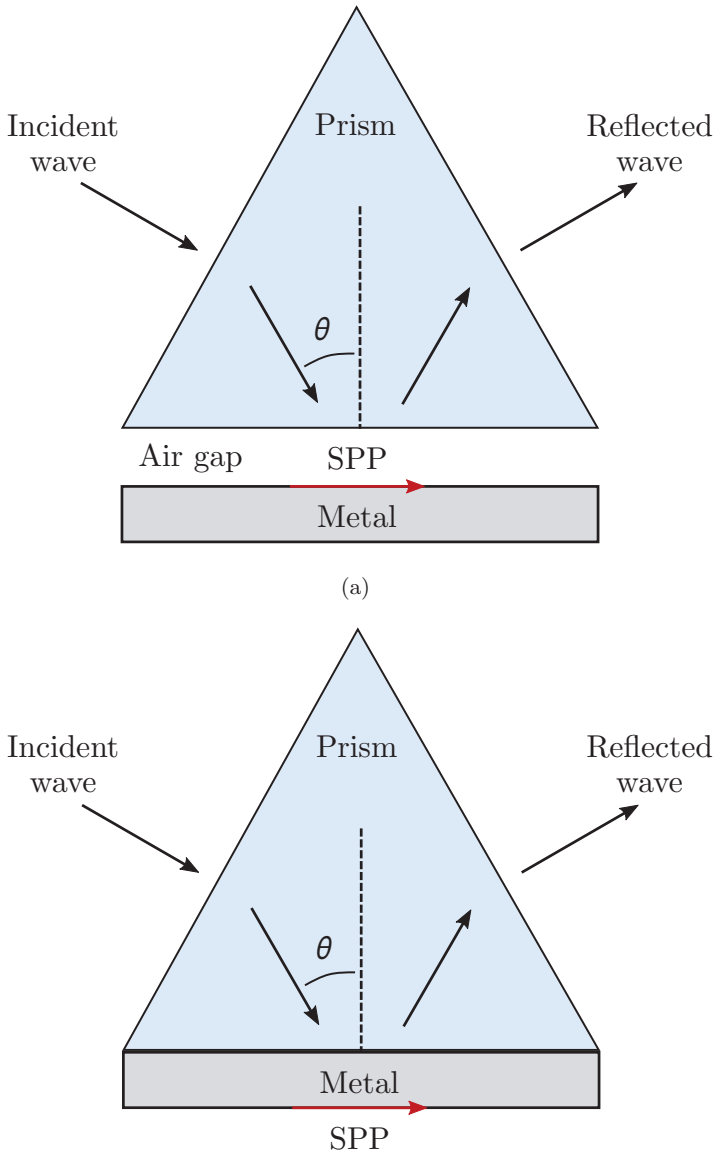


Figure 1.3: Attenuated total reflection configurations for excitation of surface plasmon polaritons where the incident wave undergoes total internal reflection at the bottom side of prism where the evanescent fields extending out of the bottom face can excite surface plasmon polaritons: (a) in the Otto configuration, a metallic slab is placed underneath the bottom side of prism separated by an air gap or dielectric in between with surface plasmons excitation on the top of metal slab; and (b) in the Kretschmann configuration, there is no gap between metal and prism with surface plasmons excitation underneath the metal.

1.5 Plasmons in Two-Dimensional Electron System (2-DES)

A two-dimensional electron system or 2-DES for short is modelled as a sea of electrons that are free to move in two dimensions, while they remain tightly confined in the third dimension. A 2-DES can also be described as a sheet of electrons.

The earliest 2-DES experiments were carried out in liquid helium. Nowadays, experiments utilising 2-DESs are mostly carried out using semiconductor devices. In metal oxide field effect transistors (MOSFETS), 2-DES is created underneath the gate due to an inversion layer of electrons that are confined to the oxide layer. 2-DES can also be created at the interface between the junction of two different materials, as in the case of heterostructures used in high electron mobility transistors (HEMT). An illustration of a GaAs/AlGaAs heterostructure is shown in Fig. 1.4, where AlGaAs is deposited on a GaAs substrate. A 2-DES inversion layer is created at junction between the deposited AlGaAs and the GaAs substrate. Ohmic contacts are located at either end of the structure and a metallic gate is shown above the AlGaAs layer. An electric potential applied at the gate will result in a change of concentration of the 2-DES electrons directly underneath the gate.

Surface plasmon-polaritons can be excited in 2-DES, where they are also known as 2-D plasmons. 2-D plasmons can be excited using either a grating coupler on top of 2-DES or by coupling electromagnetic energy using a waveguide.

The dispersion relation of 2-D plasmons in a 2-DES surrounded by an homogeneous medium of dielectric constant ε_r is well known and given by [21],

$$k = \frac{2\omega^2 \varepsilon_r \varepsilon_0 m^*}{e^2 n_{2D}} \tag{1.10}$$

Here, ω is the angular frequency, ε_r is the relative dielectric constant of the medium surrounding the 2-DES, m^* is the effective mass of electron, e is charge on electron and n_{2D} is the 2-D electron density. If the surrounding media are different then ε_r is the effective dielectric constant of surrounding media, which is defined as $\varepsilon_r = \varepsilon_{reff} = (\varepsilon_{r1} + \varepsilon_{r2})/2$.

The dispersion relation of gated 2-D plasmons satisfies the following relationship [22],

$$\omega^2 = k \frac{e^2 n_{2D}}{m^*} \frac{1}{\varepsilon_s + \varepsilon_{ox} \coth(kd)} \tag{1.11}$$

where, ε_s is the dielectric constant of substrate underneath 2-DES, ε_{ox} is the dielectric constant of the material between 2-DES and gate, k is the wave number of 2-D plasmons and d is the distance between 2-DES and gate.

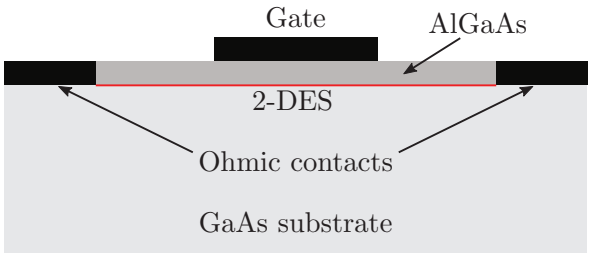


Figure 1.4: Structure of a high electron mobility transistor (HEMT). An GaAs/AlGaAs heterostructure is created by depositing a layer of AlGaAs on top of GaAs substrate resulting in an inversion layer of free electrons at the junction between GaAs and AlGaAs creating a two-dimensional electron system (2-DES). The concentration of electrons in the 2-DES can be manipulated by applying a voltage to the gate on top of AlGaAs layer. Ohmic contacts at the ends of the 2-DES can be used to couple energy in and out of the HEMT.

1.6 Finite Difference Time-Domain Technique

Finite difference time-domain (FDTD) is a popular numerical technique, which can be used to solve Maxwell's equations. It was originally proposed by Yee in 1966 [24]. FDTD is a rigorous time-domain technique that is conceptually simple and easy to implement. In FDTD, the problem space is discretised as a grid (known as Yee grid) and each grid point is assigned material parameters. In the Cartesian coordinate system, the x, y and z components of electric and magnetic fields in an FDTD grid are located at half space- and time-steps from each other.

In a 2-D FDTD scheme, only three field components are required. The two possible arrangement of field components in a 2-D FDTD grid are known as TM_z or TE_z. In TM_z arrangement, the magnetic field is oriented along the z-direction normal to the FDTD grid, with the electric field components along x and y direction parallel to the FDTD grid. Similarly, in TE_z arrangement, z component of electric is normal to the FDTD grid, while x and y components of magnetic field are parallel to the grid.

Arrangement of electric and magnetic field nodes in the 2-D grid set at half spatial steps as shown in Figs. 1.5(a) and 1.5(b) for the TM_z and TE_z schemes, respectively. The algorithm works by defining initial field quantities or specifying sources in the grid and is then advanced in time using discrete time steps. At each time step, future values of field quantities are computed from past values using Maxwell's equations.

The main strength of the FDTD technique is in its ability to model arbitrary structures because assigning material parameters is straightforward. The main drawback is that FDTD is inherently

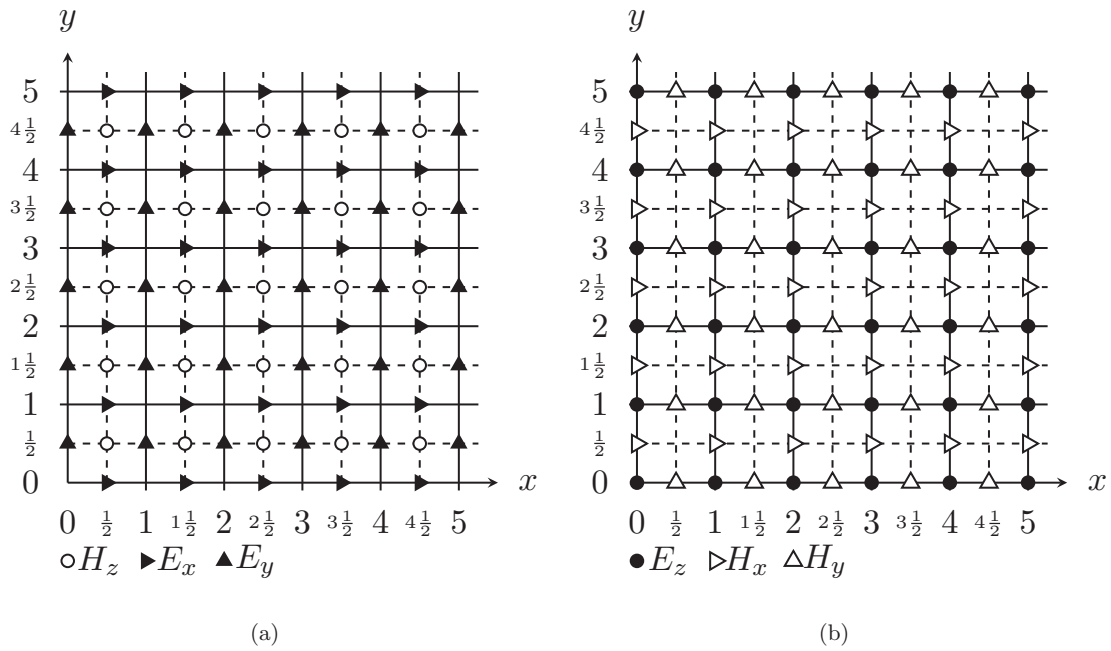


Figure 1.5: Arrangement of electric (filled circles and triangles) and magnetic field (hollow circles and triangles) nodes, separated by half spatial steps, in 2-D finite difference time-domain (FDTD) scheme: (a) transverse magnetic or TM_z arrangement with magnetic field oriented normal to the FDTD grid; and (b) transverse electric or TE_z arrangement with electric field oriented normal to the FDTD grid. Figure redrawn from Schneider [23].

a time-domain method and does not work well for frequency-domain problems involving resonant structures. Also, compared to frequency-domain methods, error in the FDTD grid is compounded as the simulation evolves in time. Here, FDTD has been used to model surface plasmon excitation for THz spectroscopy and 2-D surface plasmon excitation in 2-DES channels. This section describes the modelling approach.

1.6.1 Modelling Approach

The motion of electrons in a 2-DES can be described by the Drude model. The conventional alternating differential equation (ADE) method can be used to model Drude materials using FDTD ([25], [26]). In the ADE method, the expression for permittivity (and/or permeability) is replaced with the frequency dependent permittivity based on the Drude's dispersion model for metals, which can then be used to calculate the E-field from D-field (and H-field from B-field, if permeability is also dispersive) at alternate time steps in the FDTD algorithm. In these methods, however, the presence of DC current cannot be taken into account, since the current terms are not present and are handled implicitly.

An alternative approach is to express the current terms explicitly as shown in the following derivation. A separate solver running in parallel with the FDTD algorithm can solve for contributions due to DC current at each time step. Ampere and Faraday's laws in differential form are,

$$\nabla \times \mathbf{H} = \mathbf{J} + \varepsilon_0 \frac{\partial \mathbf{E}}{\partial t} \tag{1.12}$$

$$\nabla \times \mathbf{E} = \mathbf{J}_m - \mu_0 \frac{\partial \mathbf{H}}{\partial t} \tag{1.13}$$

where, $\mathbf{J}$ and $\mathbf{J}_m$ are electric and magnetic current densities, respectively. $\mathbf{J}$ can be expressed as,

$$\mathbf{J} = en_{3D}\mathbf{v} \tag{1.14}$$

where, en_{3D} is the charge on n_{3D} charges and,

$$\frac{\partial \mathbf{v}}{\partial t} = \frac{e}{m_e}\mathbf{E} \tag{1.15}$$

represents the Drude model. Solving this set of equations would give the same result as the ADE Drude model implementation. Writing the above equations in steady-state frequency-domain,

$$\nabla \times \mathbf{H} = \mathbf{J} + j\omega\varepsilon_0\mathbf{E} \tag{1.16}$$

$$\nabla \times \mathbf{E} = -j\omega\mu_0\mathbf{H} \tag{1.17}$$

$$\mathbf{J} = en_{3D}\mathbf{v} \tag{1.18}$$

$$j\omega\mathbf{v} = \frac{e}{m_e}\mathbf{E} \tag{1.19}$$

$$\mathbf{J} = \frac{e^2 n_{3D}}{j\omega m_e}\mathbf{E} \tag{1.20}$$

Substituting (1.20) in (1.16),

$$\nabla \times \mathbf{H} = \frac{e^2 n_{3D}}{j\omega m_e}\mathbf{E} + j\omega\varepsilon_0\mathbf{E}$$

This simplifies to,

$$\nabla \times \mathbf{H} = j\omega\left(\varepsilon_0 - \frac{e^2 n_{3D}}{\omega^2 m_e}\right)\mathbf{E} \tag{1.21}$$

which is the Drude model. The following set of FDTD equations based on above model can be used to run the simulation,

$$J_{mk}^{\ n} = J_{mk}^{\ n-1} + \Delta t\mu_o\omega_{pm}^2 H_k^{n-\frac{1}{2}} \tag{1.22}$$

$$H_k^{n+\frac{1}{2}} = H_k^{n-\frac{1}{2}} + \frac{\Delta t}{\mu}\left(-\nabla \times \mathbf{E}^n + J_{mk}^{\ n}\right) \tag{1.23}$$

$$J_{k+\frac{1}{2}}^{n+\frac{1}{2}} = J_{k+\frac{1}{2}}^{n-\frac{1}{2}} + \Delta t\varepsilon_o\omega_p^2 E_{k+\frac{1}{2}}^n \tag{1.24}$$

$$E_{k+\frac{1}{2}}^{n+1} = E_{k+\frac{1}{2}}^n + \frac{\Delta t}{\varepsilon}\left(\nabla \times \mathbf{H}^{n+\frac{1}{2}} - J_{k+\frac{1}{2}}^{n+\frac{1}{2}}\right) \tag{1.25}$$

The Courant stability condition must be satisfied to ensure that the FDTD simulation does not become unstable. The Courant stability condition imposes a constraint on maximum time step Δt based on the smallest grid discretisation Δ. The Courant stability condition can be expressed as,

$$c\frac{\Delta t}{\Delta} \leq 1 \tag{1.26}$$

or,

$$\Delta t \leq \frac{\Delta}{c} \tag{1.27}$$

where, c is speed of light, Δ is the smallest grid discretisation and Δt is the time step. A 2-D FDTD code with the TM_z scheme was developed to model different variations of ungated 2-DES channel. The different configurations included air above and below the 2-DES channel, GaAs above and below the 2-DES channel and an air–2-DES–GaAs hybrid structure. The physical parameters of the simulation were chosen to allow comparison with the experimental device from Sydoruk *et al.* [27]. The dispersion curves obtained from fast Fourier transform (FFT) of the steady-state FDTD simulation. The comparison of dispersion relations obtained from FDTD and theory is shown in Fig. 1.6 which shows excellent agreement between FDTD and theory at frequencies less than 0.5 THz. Afterwards code for a 3-D FDTD solver was developed, which simulated plasmon excitation on 2-D ungated channel terminated at both ends with coplanar waveguides. The 2-D channel was 30 μm wide and 60 μm long and placed on a GaAs substrate with air above it. The

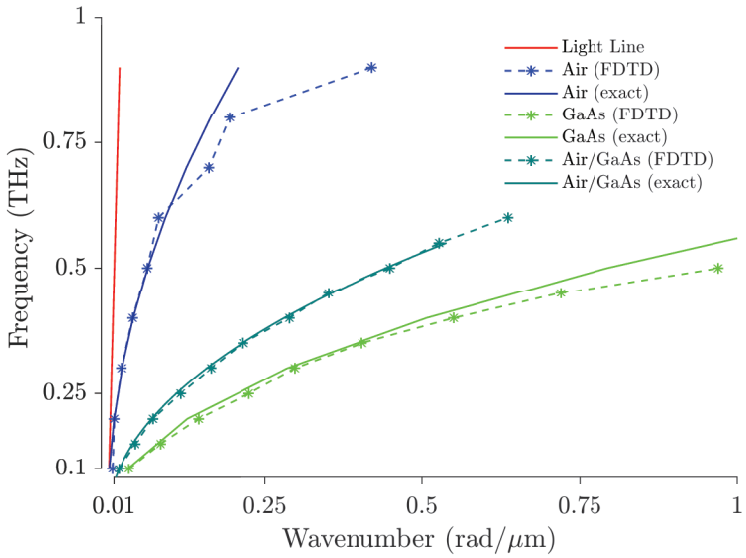
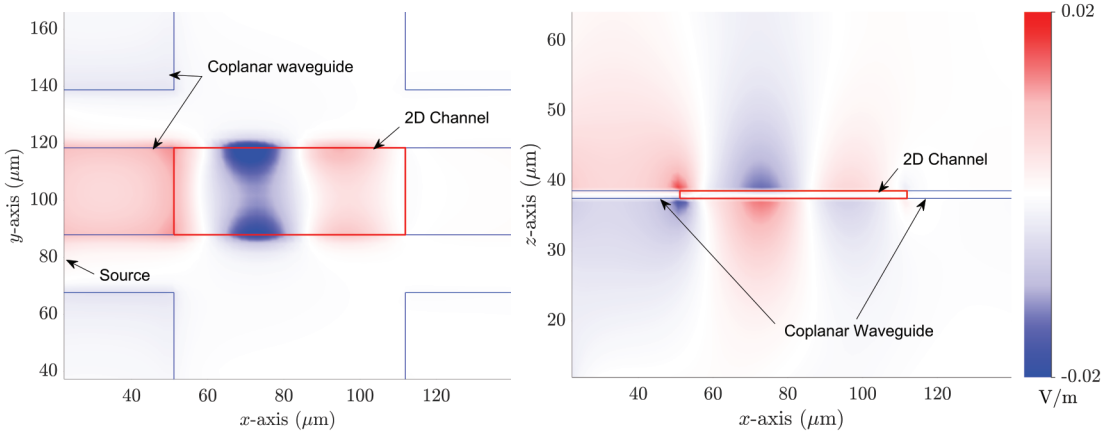


Figure 1.6: Dispersion relations for air–2-DES–air, GaAs–2-DES–GaAs and air–2-DES–GaAs. The exact curves were obtained from theory. The FDTD curves correspond to a thin 3-D channel which can effectively model a 2-DES. An increase in frequency requires a corresponding decrease in thickness of 3-D channel to better model a 2-DES.

channel itself was modelled as a 3-D slab of finite thickness using Drude permittivity where the 3-D plasma electron density was $n_{3D} = n_{2D}/t_{channel} = 3.1 \times 10^{15}$ cm^{-3}. Here, n_{2D} is the 2-D electron density, which was taken following the experiments from [28] as 6.5×10^{11} cm^{-2}. The thickness was $t = 2.1$ μm which not only reduced the simulation time but also yielded the correct dispersion curves as seen in Fig. 1.6 [27]. Figure. 1.7 shows the distribution of the transverse electric field at 200 GHz, which shows roughly one complete wavelength of 2-D plasmons on the 2-DES channel. 2-D and 3-D edge-plasmon excitation on the 2-D channel can be clearly seen. Figure 1.8 shows plasmon modes on a channel that is 160 μm wide and 90 μm long. Excitation of 2-D plasmons can be better visualised on a wider channel. Figure 1.9 shows FDTD simulated steady-state field distribution on a gold nanosphere of 40 nm radius when subject to an incident wave of wavelength $\lambda = 400$ nm. The incident wave was polarised in the x-direction and excited localised plasmons on the surface of the nanosphere.

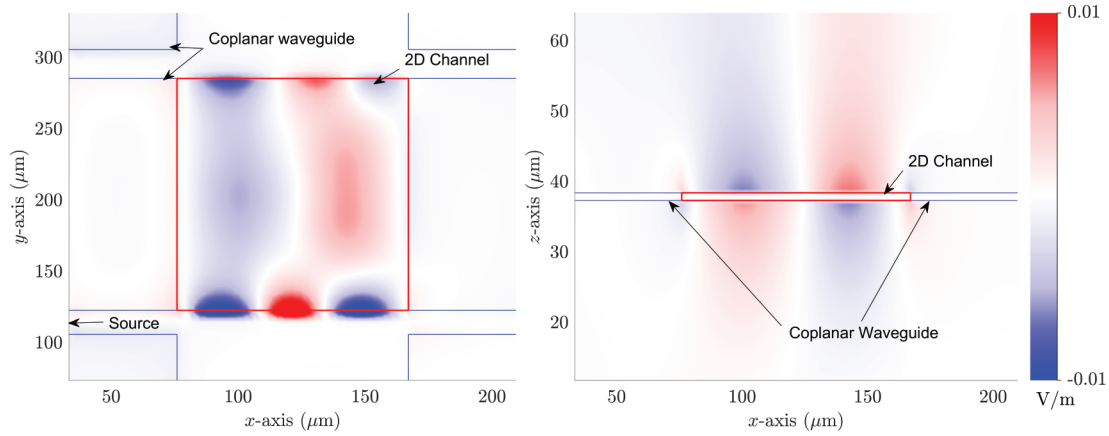
1.7 FDTD Modelling of Lossy Spherical Resonators

As demonstrated by Papantonis and Lucyszyn [19], commercial electromagnetic solvers are not able to model the simplest of resonator geometries, like a sphere, when the cavity walls have low



(a) (b)

Figure 1.7: Finite different time-domain simulated field distributions showing 2-D plasmon excitation at 200 GHz, corresponding to roughly one full wavelength, on a two-dimensional electron system (2-DES) channel that is 30 μm wide and 90 μm long on a GaAs substrate with air on top: (a) top view showing longitudinal field pattern on the 2-DES channel, coplanar waveguide sections and location of source; and (b) side view of field pattern on the 2-DES channel.



(a) (b)

Figure 1.8: Finite different time-domain simulated field distributions showing 2-D plasmon excitation at 200 GHz, corresponding to roughly one full wavelength, on a two-dimensional electron system (2-DES) channel that is 160 μm wide and 90 μm long on a GaAs substrate with air on top: (a) top view showing longitudinal field pattern on the 2-DES channel with clearly visible 2-D and edge plasmons, coplanar waveguide sections and location of source; and (b) side view of field pattern on the 2-DES channel.

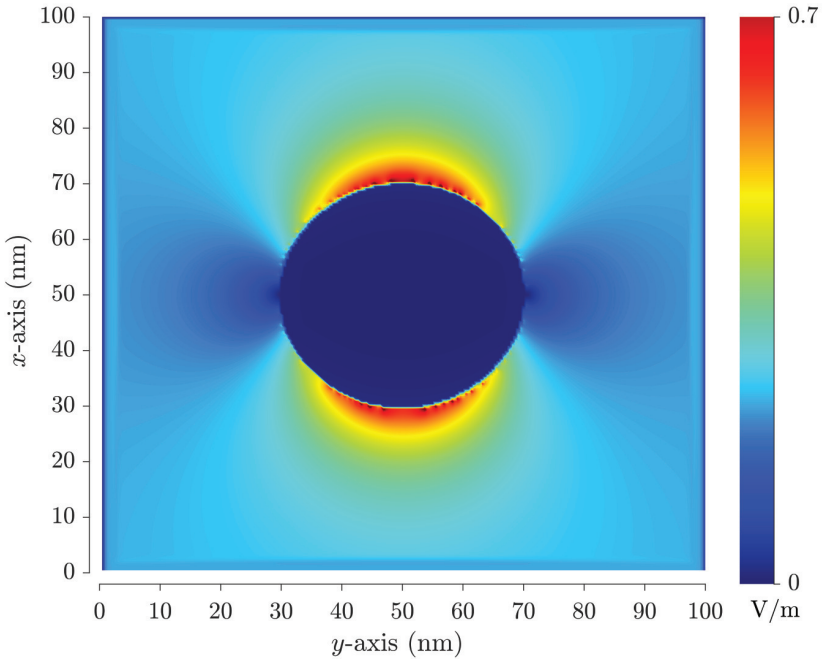


Figure 1.9: Steady-state electric field distribution on a gold nanosphere of radius 40 nm from 3-D FDTD simulation. The gold nanosphere was excited by an incident x-polarised electromagnetic wave having a wavelength of 600 nm.

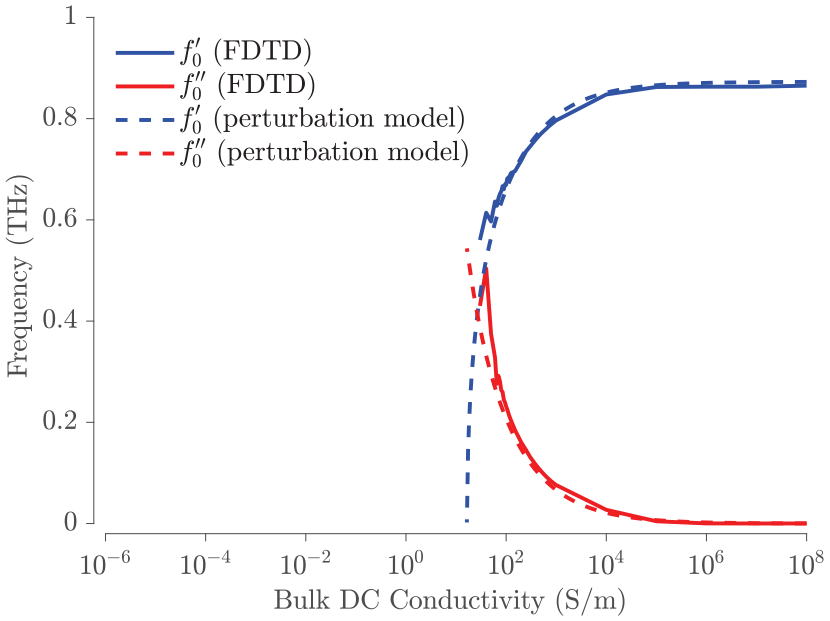


Figure 1.10: Comparison of complex eigenfrequency response from FDTD simulations with data from perturbation model [19] of a spherical cavity resonator of radius 150 μm with conducting walls. The conductivity of resonator walls was swept over a range of values from 10^{-6} S/m (very lossy) to 10^{8} S/m (almost ideal resonator).

intrinsic conductivity. Papantonis and Lucyszyn [19] provide an exact analytical solution to the spherical cavity problem when the walls of the cavity are transformed from PEC to free space. In addition, they have compared the exact solution with the results obtained from different commercial numerical solvers.

Papantonis and Lucyszyn [19] have only used frequency domain solvers to compare their results for the lossy spherical resonator with the analytical theory they developed. An in-house-developed FDTD code was used to model the lossy spherical resonator by Papantonis and Lucyszyn [19] in order to investigate the performance of a time-domain solver in predicting the eigenfrequency response of a lossy structure. The spherical resonator can be excited in two ways; either a single sinusoidal signal that is sufficiently close to the mode that is of interest, or a wideband Gaussian pulse which should contain frequencies of the modes of interest.

For the first case, the sinusoidal source was left turned on for some time so that initial transients have died down. Then the source was turned off gradually so as not to excite any spurious fields. The real and imaginary parts of the complex eigenfrequency can be obtained from frequency and decay, respectively, of the recorded time domain signal after the source has turned off. This method has the advantage of single mode excitation and avoids exciting any unwanted modes.

A wideband Gaussian pulse can excite multiple modes at the same time and, whenever multi-mode excitation is desired this is the preferred method of excitation. The Gaussian signal must contain frequencies of interest at which the eigenmode excitation is desired. The excited signal is then recorded and a Fourier transform of this time-domain signal will then show peaks at resonant frequencies.

In order to obtain the complex eigenfrequencies, the resonator must be excited with a signal that is close to the desired eigenmode frequency, which in this case can be taken as the fundamental mode frequency of TM_{011}, given by 0.8728 THz [19] corresponding to half wavelength in the radial . Spurious modes can also be excited if the excitation frequency is sufficiently close to these unwanted modes.

1.7.1 FDTD Results

FDTD simulations were run for a sphere of radius $r = 150$ μm and complex eigenfrequencies were obtained from the recorded time domain signal for different values of bulk DC conductivity of resonator walls. As an example, with $\sigma = 1$ kS the decaying field strength is plotted at the centre of the sphere as the sinusoidal source is gradually turned off from $t = 27$ ps to $t = 31$ ps. From this, the complex frequency was calculated as $\tilde{f}_0 = 0.8 + j0.066897$ THz ($|\tilde{f}_0| = 0.8027$ THz), where

$\tilde{f}_0 = f_0' + jf_0''$ and $f_0' = 0.8$ THz with $f_0'' = 0.066897$ THz, which is comparable to the actual value of $\tilde{f}_0 = 0.805 + j0.065$ [19]. Fig. 1.10 compares eigenfrequencies obtained from FDTD simulations with the perturbation model (data from [19]). While FDTD correctly predicts the eigenfrequency response for $\sigma > 100$ S/m, its accuracy decreases rapidly as the resonator becomes very lossy $\sigma < 100$ S/m. With a very lossy resonator, fields inside the resonator rapidly decay and noise quickly dominates the time-domain response.

1.8 Acknowledgements

Prof. Stepan Lucyszyn and Dr. Oleksiy Sydoruk provided much need guidance and direction throughout the literature review stage. The FDTD modelling of plasmons was done under the supervision of Dr. Oleksiy Sydoruk, who also suggested the alternate current based FDTD Drude model presented in Section 1.6.1. FDTD modelling of lossy spherical resonator was done under the supervision of Prof. Stepan Lucyszyn, who also provided the data for the perturbation model ([19]) for comparison with the FDTD results.

References

[1] J. Sun, F. Hu, and S. Lucyszyn, "Predicting atmospheric attenuation under pristine conditions between 0.1 and 100 THz," *IEEE Access*, vol. 4, pp. 9377–9399, 2016.

[2] T. G. Phillips and J. Keene, "Submillimeter astronomy (heterodyne spectroscopy)," *Proc. IEEE*, vol. 80, no. 11, pp. 1662–1678, 1992.

[3] D. K. Gramotnev and S. I. Bozhevolnyi, "Plasmonics beyond the diffraction limit," *Nat. Photonics*, vol. 4, no. 2, pp. 83–91, 2010.

[4] E. Ozbay, "Plasmonics: Merging photonics and electronics at nanoscale dimensions," *Science*, vol. 311, no. 5758, pp. 189–193, 2006.

[5] M. Tonouchi, "Cutting-edge terahertz technology," *Nat. Photonics*, vol. 1, no. 2, pp. 97–105, 2007.

[6] R. A. Lewis, "A review of terahertz sources," *J. Phys. D: Appl. Phys.*, vol. 47, no. 37, p. 374001, 2014.

[7] K. Zhong, W. Shi, D. Xu, P. Liu, Y. Wang, J. Mei, C. Yan, S. Fu, and J. Yao, "Optically pumped terahertz sources," *Science China Technological Sciences*, pp. 1–18, 2017.

[8] E. Wasige, K. H. Alharbi, A. Al-Khalidi, J. Wang, A. Khalid, G. C. Rodrigues, and J. Figueiredo, "Resonant tunnelling diode terahertz sources for broadband wireless communications," in *Terahertz, RF, Millimeter, and Submillimeter-Wave Technology and Applications X*, vol. 10103, p. 101031J, International Society for Optics and Photonics, 2017.

[9] H. A. Atwater, "The promise of plasmonics," *Scientific American*, vol. 296, no. 4, pp. 56–62, 2007.

[10] W. J. Otter and S. Lucyszyn, "Hybrid 3-D-printing technology for tunable THz applications," *Proc. IEEE*, vol. 105, pp. 756–767, Apr. 2016.

[11] K. Fukunaga, I. Hosako, Y. Ogawa, and S. Hayashi, "THz spectroscopy for art conservation science," in *2007 Joint 32nd International Conference on Infrared and Millimeter Waves and the 15th International Conference on Terahertz Electronics*, pp. 678–679, IEEE, 2007.

[12] J. Sun, F. Hu, Z. Wang, and S. Lucyszyn, "Banknote characterization using a thermal infrared 'THz torch' spectrometer," in *2015 Asia-Pacific Microwave Conference (APMC)*, vol. 2, pp. 1–3, IEEE, 2015.

[13] M. Chakraborty, P. Bawuah, N. Tan, T. Ervasti, P. Pääkkönen, J. A. Zeitler, J. Ketolainen, and K.-E. Peiponen, "On the correlation of effective terahertz refractive index and average surface roughness of pharmaceutical tablets," *J. Infrared, Millimeter, and Terahertz Waves*, vol. 37, no. 8, pp. 776–785, 2016.

[14] K. Su, Y.-C. Shen, and J. A. Zeitler, "Terahertz sensor for non-contact thickness and quality measurement of automobile paints of varying complexity," *IEEE Trans. THz Sci. Technol.*, vol. 4, no. 4, pp. 432–439, 2014.

[15] R. Knipper, A. Brahm, E. Heinz, T. May, G. Notni, H.-G. Meyer, A. Tünnermann, and J. Popp, "THz absorption in fabric and its impact on body scanning for security application," *IEEE Trans. THz Sci. Technol.*, vol. 5, no. 6, pp. 999–1004, 2015.

[16] A. D. van Rheenen and M. W. Haakestad, "Robust identification of concealed dangerous substances by spectral correlation of terahertz transmission images," *IEEE Trans. THz Sci. Technol.*, vol. 5, no. 3, pp. 438–444, 2015.

[17] N. Bajwa, S. Sung, D. B. Ennis, M. C. Fishbein, B. Nowroozi, D. Ruan, A. Maccabi, J. Alger, M. A. S. John, W. S. Grundfest, *et al.*, "Terahertz imaging of cutaneous edema: Correlation with magnetic resonance imaging in burn wounds," *IEEE Trans. Biomed. Eng.*, vol. 64, no. 11, pp. 2682–2694, 2017.

[18] E. Episkopou, S. Papantonis, W. J. Otter, and S. Lucyszyn, "Defining material parameters in commercial EM solvers for arbitrary metal-based THz structures," *IEEE Trans. THz Sci. Technol.*, vol. 2, no. 5, pp. 513–524, 2012.

[19] S. Papantonis and S. Lucyszyn, "Lossy spherical cavity resonators for stress-testing arbitrary 3D eigenmode solvers," *PIER*, vol. 151, pp. 151–167, 2015.

[20] R. B. Schasfoort and A. J. Tudos, *Handbook of surface plasmon resonance*. Royal Society of Chemistry, 2008.

[21] K. Linghua, Y. Baorong, and H. Xiwei, "Dispersion relations of longitudinal plasmons in one, two and three dimensional electron gas of metals," *Plasma Sci. Technol.*, vol. 9, no. 5, p. 519, 2007.

[22] S. J. Allen, D. C. Tsui, and R. A. Logan, "Observation of the two-dimensional plasmon in silicon inversion layers," *Phys. Rev. Lett.*, vol. 38, pp. 980—983, 1977.

[23] J. B. Schneider, *Understanding the Finite Difference Time-Domain Method*. `www.eecs.wsu.edu/~schneidj/ufdtd`, 2010.

[24] K. Yee, "Numerical solution of inital boundary value problems involving Maxwell's equations in isotropic media," *IEEE Trans. Antennas Propag.*, vol. 14, pp. 302–307, May 1966.

[25] Y. Zhao and J. Liu, "FDTD for hydrodynamic electron fluid Maxwell equations," in *Photonics*, vol. 2, pp. 459–467, Multidisciplinary Digital Publishing Institute, 2015.

[26] A. Dawood, "Finite difference time-domain modelling of metamaterials: GPU implementation of cylindrical cloak," *Advanced Electromagnetics*, vol. 2, no. 2, pp. 10–17, 2013.

[27] O. Sydoruk, J. Wu, A. Mayorov, C. Wood, D. Mistry, and J. Cunningham, "Terahertz plasmons in coupled two-dimensional semiconductor resonators," *Phys. Rev. B*, vol. 92, no. 19, p. 195304, 2015.

[28] J. Wu, A. S. Mayorov, C. D. Wood, D. Mistry, L. Li, W. Muchenje, M. C. Rosamond, L. Chen, E. H. Linfield, A. G. Davies, *et al.*, "Excitation, detection, and electrostatic manipulation of terahertz-frequency range plasmons in a two-dimensional electron system," *Sci. Rep.*, vol. 5, 2015.

Chapter 2

Travelling Waves, Pseudo Waves and Power Waves

2.1 Introduction

Electromagnetic energy can be transferred from one point to another using either wireless of guided-wave structures. Guided-wave structures can be categorised as either transmission lines or waveguides; however, unless stated specifically, the term *'transmission line'* will implicitly include waveguides. In transmission line theory, the lumped-element model of transmission line is a general representation of any transmission line and can be mathematically expressed as the telegraphers' equations. The solution of telegraphers' equations are total voltage and current on the transmission line. The total voltage and current are expressed as the sum of incident (or forward) and reflected (or backward) voltage and current waves, respectively. The term *voltage wave* is originally a reference to the actual incident and reflected travelling voltage waves obtained as solutions to the telegraphers' equations. The ratio of voltage-to-current in any direction is the characteristic impedance of the transmission line.

In waveguide theory, Maxwell's equations can be used to obtain the forward and backward propagating modes, which are the solutions expressed in terms of electric and magnetic fields. The ratio of transverse electric and magnetic fields at a particular location on the transverse plane is known as the wave impedance at that specific location.

The transverse electric and magnetic fields for a waveguide mode can also be expressed in terms of voltage and current waves, respectively, subject to certain constraints. For example, the ratio of voltage-to-current waves for forward propagating modes [1] is defined as the characteristic impedance of the waveguide operating in a particular mode, such that the power carried by the mode is obtained

from the voltage and current quantities defined in circuit theory. This is important when treating waveguides (and networks containing waveguide components) as transmission lines, and for when interconnecting a waveguide with a transmission line. For example, within an air-filled coaxial cable operating in the dominant transverse electromagnetic (TEM) wave mode, voltages and currents are uniquely defined; giving only one value of characteristic impedance for its specific dimensions. This is not the case for non-TEM wave modes, where different integration paths for the voltages and currents give different results and so characteristic impedance can change. For any guided-wave structure, commonly used definitions (e.g., power-voltage, power-current and current-voltage) for characteristic impedance are available in literature [1], [2].

Travelling waves, formally expressed as linear combination of total voltage and current on the transmission line, are meant to simplify power calculations. In their simplest form, travelling waves are essentially normalised/scaled voltage waves and may be represented as the ratio of incident or reflected voltage waves to the square root of the characteristic impedance of the transmission line. The incident and reflected powers on a lossless transmission line can be conveniently computed from the magnitude squared of incident and reflected travelling waves, respectively.

Travelling waves can have a *reference* impedance, which may be different from the characteristic impedance of its guided-wave structure. In this case, the travelling waves are referred to as *pseudo* waves [1], because they are no longer the actual voltage waves on the transmission line.

Pseudo wave formulation is useful where, choosing a suitable reference impedance, can simplify analysis. For example, with a dispersive transmission line, where its characteristic impedance changes significantly over the frequency band of interest, a convenient approach is to adopt a constant real value of reference impedance for the purpose of measurements. A change in reference impedance is known as *renormalisation*.

Both travelling waves and pseudo waves have the same dimensions. It should be noted that pseudo waves are more general and travelling waves can be obtained from pseudo wave formulation by simply equating the reference impedance as the characteristic impedance. Another wave formulation found in the open literature [3], [4] is that of *power* waves, which is mostly used in circuit theory, as it is useful for maximum power transfer in complex conjugate-matched networks. It should be noted that travelling, pseudo and power waves are all expressed in terms of units of normalised voltage; travelling waves or pseudo waves may be referred to as voltage waves, to distinguish them from power waves.

Due to the different definitions associated with travelling, pseudo and power waves, the conversion formulas derived for different network parameters (e.g., S, Z, Y, h, ABCD and T) will also be

different. For example, as highlighted by Marks and Williams [5], the conversion formulas derived by Frickey [6] (and more recently by Reveyrand [7]), for the two-port interconversion between S, Z, Y, h, ABCD and T parameters, assume Youla's power wave definition [3]. As a result, the highly cited work of Frickey [6] is not valid for pseudo waves. Moreover, even well-known circuit simulators, like PSpice may implement conversions based on Youla's definition of power waves, by default, as shown by a PSpice given by Frickey [6] and pointed out by Marks and Williams in [5]. AWR Microwave Office is another example of a popular software package where the nature of the conversions is not specified.

In general, a (sub-)system is designed to have a common reference impedance (e.g., 50 Ω). However, individual sub-circuits may be designed to have specific complex port termination impedances (e.g., low noise amplifiers with optimal input impedance and complex conjugate impedance matching (CCIM) at the output port; high gain amplifiers with simultaneous-CCIM at both input and output ports; and power amplifiers with optimal output impedance and CCIM at the input port). The complete circuit may then incorporate impedance matching networks to transform to real terminating impedances. For this case, the voltage and power wave based definitions can be used interchangeably. However, modern monolithic microwave integrated circuit [8] design approaches try to minimise the unwanted effects of parasitics and amount of expensive real-estate needed for implementing on-chip impedance matching. As a result, with complex port impedances, network parameter conversion requires the correct definition.

Direct conversion formulas for two-port networks, using the voltage-wave definition, have been previously reported by Cooman [9], based on the approach by Ferrero and Pirola [10], but these assume a common complex reference impedance for both ports. For completeness, using the same approach outlined by Cooman [9] and Ferrero *et al.* [10], the conversions for two-port networks having arbitrary port termination reference impedances are included here.

2.2 Lossy Materials and Components

Lossy materials and their use in passive lumped-element components have attracted a great deal of attention from the microwave community. However, this is not the case for passive guided-wave components. This is because, in general, modern engineered (sub-)systems are designed to attain maximum efficiency, which includes the use of low loss materials. Moreover, at certain frequencies, natural structures (e.g., from biological tissue, down to cellular organisms and even sub-atomic structures) can be modelled as lossy electromagnetic resonators [11]. Conversely, in applications where materials are heated deliberately (e.g., microwave drying) or inadvertently (e.g., microwave

dosimetry) loss mechanisms still need to be characterised.

For this reason, even the treatment of a single boundary, between two arbitrary lossy materials, is generally not considered in most standard textbooks. This is due to the mathematical rigour needed, leading to the assumption of at least one of the materials being lossless. As a result, a common misconception is that the magnitude of the reflection coefficient (and transmission coefficient with a two-port network) of the voltage-wave scattering (S-)parameters cannot exceed unity. While this is true for real impedances, it may not be the case when both impedances are complex.

Arbitrarily lossy one-port systems include propagating modes, antennas and resonators. Their feed or simulation/measurement reference impedance can also be represented by a complex number. Here, with complex reference impedance, the feed (associated with a material or guided-wave component) is lossy. Alternatively, an amplifier will have complex terminating impedance(s), as an example of a two-port system.

Another confusion may arise from using power definitions (e.g., reflectance and transmittance) derived from a zero-order voltage-wave (e.g., Fresnel reflection and transmission) coefficients [12], for a simple two-media boundary problem. This is because the magnitude of the Fresnel reflection coefficient $|\rho_{11}|$ can be greater than unity when both media are lossy, whereas, that for the Fresnel transmission coefficient $|\tau_{21}|$ can be greater than unity even when both media are lossless.

A two-port network, which can represent a three-material system, is one example of a more general multi-port network. Here, S-parameters can have more than one reference impedance assigned to the various ports. With a multi-port network, the S-parameters define a unitary matrix, which inherently satisfies the principle of conservation of energy; this being one of the advantages of using S-parameters. Therefore, while this unitary upper bound exists for a common reference impedance that is purely real, the magnitude of any S-parameter can exceed unity (even for a passive system) when just one reference impedance is complex and so the unitary matrix condition is lost.

In Section 2.14, a 1-D cavity resonator is presented by a three-material system, having lossy terminations, giving a complex natural resonance frequency. The complex-referenced S-parameters give important insight into the resonance frequencies of this lossy system. Also, it is shown that complex referenced S-parameters cannot be directly used to compute reflectance and transmittance; requiring conversion from S- to S_p-parameters. To this end, expressions for direct interconversion between S- and S_p-parameters are given for two-port networks. Also, direct conversion formulas are given for the renormalisation of two-port S- and S_p-parameters.

Power reflectance and transmittance cannot exceed unity for a passive system, in order to obey

the principle of conservation of energy [12],[13]. This will be demonstrated later. With frequency- and space-domain spectroscopy, reflectance and transmittance are equal to the magnitude squared of the voltage-wave reflection and transmission coefficients, respectively, with S-parameters having reference impedances that must be purely real (e.g., the intrinsic impedance of free space with measurements performed in free space [12], characteristic impedance with lossless transmission lines and wave impedance with lossless waveguide media [13]). However, in reality, all real transmission lines are lossy, therefore, when measurements are with respect to the characteristic impedance of a transmission line (or wave impedance of waveguide), e.g., as in TRL calibration, the measured S-parameters have a reference impedance which is complex. It is important to use S_p-parameters in this case for computing power.

As early as the 1960s, the microwave engineers working with reference transmission lines having losses were familiar with the voltage-wave reflection coefficient exceeding unity when the reference port impedances were complex. Here, power reflectance no longer equals the magnitude squared of the voltage-wave reflection coefficient. In 1961, Youla [3] introduced the concept of power waves in circuit theory. Later in 1965, Kurokawa [4] introduced power waves and power-wave S_p-parameters in waveguide theory. This was picked-up by others, for example Marks and Williams [1]. Recently, Amakawa [16] reviewed voltage and power waves, with examples of power waves used in filter design. While power waves are useful for power calculations they have certain undesirable properties. For example, the Smith chart cannot be used with power waves [1]. Also, the cascading condition for S_p-parameters require that interconnecting ports of cascaded networks have reference port impedances that are mutually conjugates. This is counter-intuitive to the well-known cascading condition for S-parameters which requires interconnected ports of cascaded networks to have the same reference port impedance. It is common for S-parameters to have a single reference impedance implicitly satisfying the cascading condition. Where complex-referenced S-parameters are desired, the optimal approach for computing power is to convert S-paramters to S_p-parameters. In this work, generalised formulas for conversion between S- and S_p-parameters for a multi(n)-port network are given.

Conversion of S-parameters referenced from one set of reference impedances to another set, is known as matrix renormalisation [17]. Although, matrix renormalisation of either S- or S_p-parameters for generalised n-port networks has been discussed in earlier papers [1], [4], [16], [17]; these formulas appear as matrix relationships and not straightforward to implement. Closed-form expressions for renormalisation of S- and S_p-parameters of two-port networks are given, which are convenient when dealing with two-port networks.

2.3 The Transmission Line Model and Telegraphers' Equations

The lumped-element transmission line model shown in Fig. 2.1 is the generalised representation of a transmission line. Application of circuit analysis leads to the telegraphers' equations,

$$\frac{d^2V(z)}{dz^2} - \gamma^2 V(z) = 0 \tag{2.1}$$

and,

$$\frac{d^2I(z)}{dz^2} - \gamma^2 I(z) = 0 \tag{2.2}$$

These are wave equations in one variable and solutions are the incident and reflected voltage and current waves on the transmission line. The total voltage and current on the line are,

$$V(z) = V^+e^{-\gamma z} + V^-e^{\gamma z} \tag{2.3}$$

and,

$$I(z) = I^+e^{-\gamma z} + I^-e^{\gamma z} \tag{2.4}$$

where, $V(z)$ and $I(z)$ are the frequency domain root-mean-square (RMS) voltage and current on the line. Here, $\gamma = \alpha + j\beta$ is the complex propagation constant for the transmission line, where $V^+e^{-\gamma z}$ and $V^-e^{\gamma z}$ are the incident and reflected voltage waves, respectively; and $I^+e^{-\gamma z}$ and $I^-e^{\gamma z}$ are the incident and reflected current waves, respectively. At $z = 0$,

$$V = V^+ + V^- \tag{2.5}$$

$$I = I^+ + I^- \tag{2.6}$$

The ratio of voltage and current waves in the same direction is defined as the characteristic impedance of the transmission line.

$$Z_0 = \frac{V^+}{I^+} = -\frac{V^-}{I^-} \tag{2.7}$$

where, current can be expressed as,

$$I = \frac{1}{Z_0}(V^+ - V^-) \tag{2.8}$$

The ratio of reflected and incident voltage waves is known as the *voltage reflection coefficient* and is similar to the electric field reflection coefficient,

$$\widetilde{\Gamma} = \frac{V^-}{V^+} \tag{2.9}$$

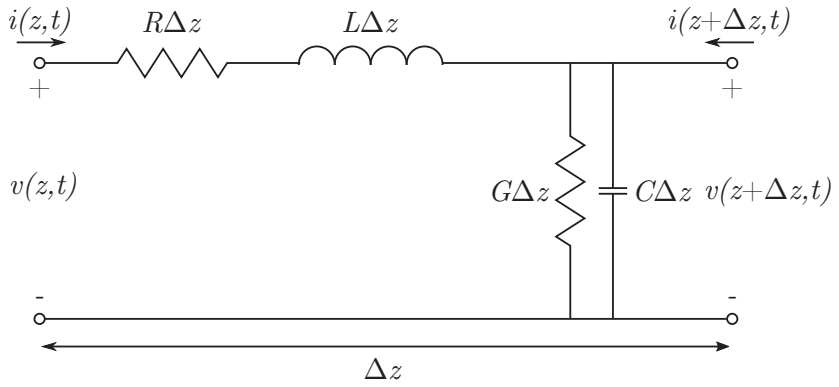


Figure 2.1: Lumped-element model of transmission line.

2.4 Transmission Line Modelling of Waveguides

Waveguides are capable of transporting energy in the form of electromagnetic waves (EM) by guiding these EM waves along the longitudinal direction which is the direction of propagation. Common examples of waveguides are coaxial cable, metal-pipe rectangular waveguides (MPRWG), optical fibre, microstrip, stripline, etc. Analysis of waveguides usually assumes a uniform waveguide cross-section along the length of the guide as it simplifies analysis. Analysis is done by solving Maxwell's equations for electric and magnetic field components in the transverse cross-sectional plane subject to boundary conditions imposed by the waveguide structure. The solutions are known as modes of the waveguide and classified as TEM, TE, TM or quasi-TEM. TEM modes have no component of electric or magnetic field along the propagation direction. In TE and TM modes, the electric and magnetic fields, respectively, have a component along the direction of propagation; and in quasi-TEM mode, which is a hybrid of TE and TM modes, the components of electric and magnetic fields along propagation direction are so small that they are usually neglected to simplify analysis. Coaxial cable or any two-conductor waveguide structure supports only TEM modes, while single conductor waveguides like MPRWG support TE or TM modes only. Microstrip and striplines support a hybrid of TE and TM modes known as quasi-TEM modes.

Except for TEM modes, voltages and currents are not well-defined for modes in a waveguide and, therefore, suitable definitions of voltages and currents as functions of electric and magnetic field must be adopted. Voltages and currents may be obtained from electric and magnetic fields by defining integration paths in the transverse plane.

The Maxwell's equations in waveguides can be reduced to a two-dimensional Helmholtz equation

of the form,

$$\left(\frac{\partial}{\partial x^2}+\frac{\partial}{\partial y^2}-\gamma_c^2\right)A_z=0 \tag{2.10}$$

where, $\mathbf{A}_z(x,y,z)=A_z\hat{z}=\mathbf{a}_z(x,y)e^{-\gamma z}$ is either the electric or magnetic field component along propagation direction depending on TM or TE mode, γ_c is the cut-off propagation constant given by,

$$\gamma_c^2=\gamma_{ud}^2-\gamma_g^2 \tag{2.11}$$

where, γ_{ud} is the propagation constant in an unbound dielectric medium and γ_g is the guided-wave propagation constant. The solution of (2.10) is of the form,

$$\mathbf{E}(x,y,z)=[\mathbf{E}_t(x,y)+\mathbf{e}_z(x,y)e^{-\gamma z}] \tag{2.12}$$

$$\mathbf{H}(x,y,z)=[\mathbf{H}_t(x,y)+\mathbf{h}_z(x,y)e^{-\gamma z}] \tag{2.13}$$

where, $\mathbf{E}(x,y,z)$ and $\mathbf{H}(x,y,z)$ are the complex phasor RMS electric and magnetic fields, respectively; with $\mathbf{E}_t(x,y)$ and $\mathbf{H}_t(x,y)$ being the transverse components of electric and magnetic fields, respectively. The transverse fields can be expressed as linear combinations of forward and backward propagating fields as,

$$\mathbf{E}_t(x,y,z)=\mathbf{e}_t(x,y)\left[C^+e^{-\gamma z}+C^-e^{\gamma z}\right] \tag{2.14}$$

and,

$$\mathbf{H}_t(x,y,z)=\mathbf{h}_t(x,y)\left[C^+e^{-\gamma z}-C^-e^{\gamma z}\right] \tag{2.15}$$

where, C^+ and C^- are constants. Equations (2.14) and (2.15) can be expressed as linear combinations of voltages and currents,

$$\mathbf{e}_t(x,y)\left[C^+e^{-\gamma z}+C^-e^{\gamma z}\right]=\frac{\mathbf{e}_t(x,y)}{V_0}\left[V^+e^{-\gamma z}+V^-e^{\gamma z}\right]=\frac{\mathbf{e}_t(x,y)}{V_0}V(z) \tag{2.16}$$

and,

$$\mathbf{h}_t(x,y)\left[C^+e^{-\gamma z}-C^-e^{\gamma z}\right]=\frac{\mathbf{h}_t(x,y)}{I_0}\left[I^+e^{-\gamma z}-I^-e^{\gamma z}\right]=\frac{\mathbf{h}_t(x,y)}{I_0}I(z) \tag{2.17}$$

where, the choice of $V(z)$ and $I(z)$ dependent on constants V_0 and I_0. The complex power carried by a mode is given by the integration of the Poynting vector over the cross-sectional area of the waveguide,

$$P(z)=\int_S \mathbf{E}_t\times\mathbf{H}_t^*\cdot d\mathbf{S} \tag{2.18}$$

The constants V_0 and I_0 may be chosen such that,

$$P(z)=V(z)I^*(z)=\frac{V(z)I^*(z)}{V_0I_0^*}\int_S \mathbf{e}_t\times\mathbf{h}_t^*\cdot d\mathbf{S} \tag{2.19}$$

Equation (2.19) imposes the constraint,

$$V_0 I_0^* = p_0 = \int_S \mathbf{e}_t \times \mathbf{h}_t^* \cdot d\mathbf{S} \tag{2.20}$$

where, the real or average power is given by,

$$P_{av} = Re\{P(z)\} \tag{2.21}$$

The characteristic impedance of the waveguide, when only the forward propagating mode is present, is then defined as [1],

$$Z_0 \equiv \frac{V_0}{I_0} = \frac{|V_0|^2}{p_0^*} = \frac{p_0}{|I_0|^2} \tag{2.22}$$

Although the choice of V_0 and I_0 is arbitrary, usually one of these constants is chosen independently and the other is determined using the constraints imposed by (2.18)–(2.20). The constants V_0 and I_0 may be obtained using the well-known integration relationships,

$$V_0 = -\int_a^b \mathbf{e}_t \cdot d\mathbf{l} \tag{2.23}$$

and,

$$I_0 = \oint_L \mathbf{h}_t \cdot d\mathbf{l} \tag{2.24}$$

Standard definitions of characteristic impedance in the open literature are power-voltage, power-current and voltage-current. With the power-voltage definition, characteristic impedance may be obtained by first using (2.23) selecting appropriate end points for the integral in (2.23) to obtain V_0; and then using $Z_0 = |V_0|^2/p_0^*$ from (2.22) such that the power relationship in (2.20) is satisfied. With the power-current definition, I_0 is first obtained using (2.24) and then $Z_0 = p_0/|I_0|^2$ from (2.22) is applied such that (2.20) holds. With the voltage-current definition both V_0 and I_0 may be selected independently. For example, using the power-voltage definition, characteristic impedance of a MPRWG of dimensions $a \times b$ operating in the dominant TE_{10} mode is,

$$Z_0 = \frac{2b}{a} Z_{TE10} \tag{2.25}$$

where, $Z_{TE10} = E_t/H_t$ is the wave impedance of TE_{10} mode. The tntegration path for V_0 is shown in Fig. 2.2. The NI AWR Microwave Office provides an option to choose from power-voltage, voltage-current or a normalised characteristic impedance when a transition between MPRWG and coaxial section is desired [18].

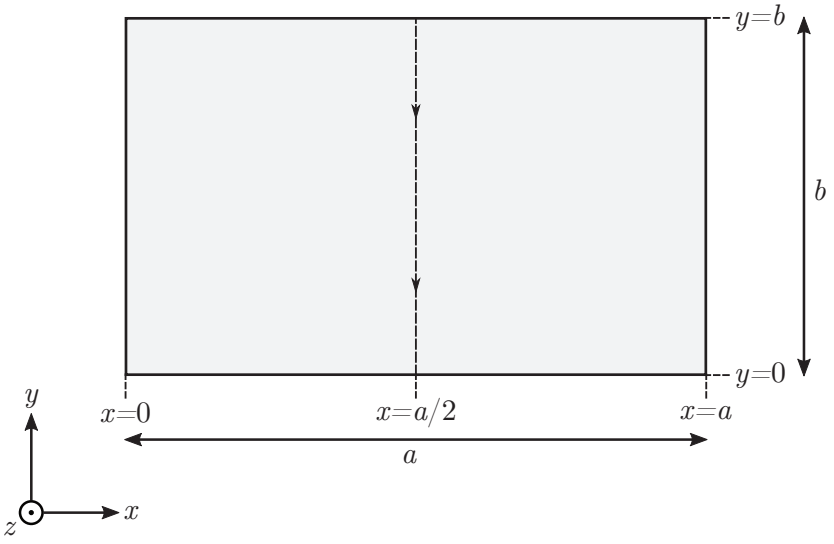


Figure 2.2: Cross-section of a metal-pipe rectangular waveguide of dimensions $a \times b$ showing the vertical integration path at $x = a/2$ to obtain V_0 from (2.23).

2.5 Travelling Waves, Pseudo Waves and Power Waves

A one-port structure can be represented as a transmission line of length L having characteristic impedance Z_0 terminated with load Z_L at $z = 0$ and a source impedance Z_S at $z = -L$ as shown in Fig. 2.3. Travelling waves are defined as scaled incident and reflected voltage waves (2.5),

$$a_1 = \frac{V_1^+}{\sqrt{Re\{Z_0\}}} = \frac{1}{2\sqrt{Re\{Z_0\}}}(V_1 + Z_0 I_1) \tag{2.26}$$

$$b_1 = \frac{V_1^-}{\sqrt{Re\{Z_0\}}} = \frac{1}{2\sqrt{Re\{Z_0\}}}(V_1 - Z_0 I_1) \tag{2.27}$$

where, a_1 and b_1 are the incident and reflected travelling waves. The average power carried by forward and backward propagating modes from (2.19) for a lossless transmission line are given by,

$$P_{av}^+ = Re\{V_1^+ I_1^{+*}\} = \frac{|V_1^+|^2}{Re\{Z_0\}} = |a_1|^2 \tag{2.28}$$

$$P_{av}^- = Re\{V_1^- I_1^{-*}\} = \frac{|V_1^-|^2}{Re\{Z_0\}} = |b_1|^2 \tag{2.29}$$

It can be observed from (2.26)–(2.29) that travelling waves are defined such that the average power in incident and reflected waves are given by the magnitude squared of incident and reflected travelling waves, respectively. This fact highlights the usefulness of travelling waves with lossless transmission lines. Moreover, travelling waves can be directly measured as they are only scaled version of actual waves on the transmission line. If the characteristic impedance is complex, the

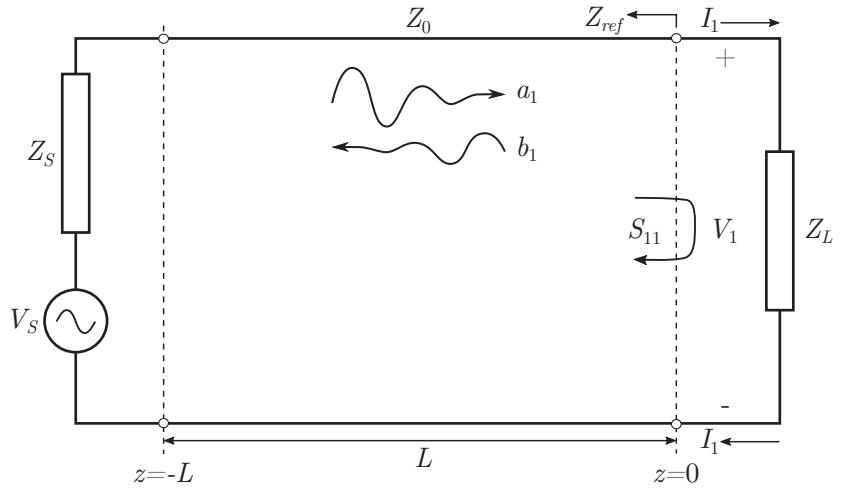


Figure 2.3: A one-port network consisting of a transmission line of characteristic impedance Z_0 and length L connecting a source V_S, with source impedance Z_S, terminated with a load Z_L. With incident waves a_1 on the transmission line, the impedance mismatch at the load results in reflected waves b_1 on a terminated transmission line. Z_{ref} is the reference impedance at the load ($z = 0$) looking into the transmission, which is Z_0 for travelling waves.

total average power at any reference point on the transmission line can be calculated from (2.19), (2.26) and (2.27) as,

$$P_{av}(z) = |a_1|^2 + |b_1|^2 + 2Im\{a_1 b_1^*\}\frac{Im\{Z_0\}}{Re\{Z_0\}} \tag{2.30}$$

In Fig. 2.3, Z_{ref} is the reference impedance looking into the transmission line at the load which is $Z_{ref} = Z_0$ for travelling waves. A change in reference impedance tells us what would happen to the original travelling waves on the transmission line. For this purpose, pseudo waves are defined which are fictitious in nature but allows analysis with respect to a certain 'reference' impedance of our choice. Pseudo waves for a one-port are defined as,

$$a_1 = \frac{\sqrt{Re\{Z_{ref}\}}}{2|Z_{ref}|}(V_1 + Z_{ref} I_1) \tag{2.31}$$

$$b_1 = \frac{\sqrt{Re\{Z_{ref}\}}}{2|Z_{ref}|}(V_1 - Z_{ref} I_1) \tag{2.32}$$

where a_1 and b_1 are incident and reflected pseudo waves. As in the case of travelling waves, average incident and reflected powers are given by the magnitude squared of incident and reflected pseudo waves, respectively, if the reference impedance is real. Where characteristic impedance is complex, a real reference impedance may be used to find average powers from pseudo wave formulation.

The third type of wave under discussion in this section is the power wave and its purpose is to compute average power or for conjugate matching of cascaded networks. Unlike travelling waves

and pseudo waves, power waves always give correct average power even if the reference impedance is complex. For a one-port system, power waves are defined as,

$$a_{p1} = \frac{1}{2\sqrt{Re\{Z_{ref}\}}}(V_1 + Z_{ref}I_1) \tag{2.33}$$

$$b_{p1} = \frac{1}{2\sqrt{Re\{Z_{ref}\}}}(V_1 - Z^*_{ref}I_1) \tag{2.34}$$

2.6 Voltage-Wave and Power-Wave Reflection Coefficients

Consider the one-port system shown in Fig. 2.3 having a single scattering or S-parameter, S_{11}, which in this case, is the voltage-wave reflection coefficient at the load ($z = 0$) defined as,

$$S_{11} = \frac{Z_L - Z_{ref}}{Z_L + Z_{ref}} = \frac{b_1}{a_1} \tag{2.35}$$

where, b_1 and a_1 are the reflected and incident travelling waves or pseudo waves and can be generally referred to as just voltage waves. With $Z_{ref} = Z_0$,

$$S_{11} = \frac{Z_L - Z_0}{Z_L + Z_0} \tag{2.36}$$

The concept of a voltage-wave reflection coefficient follows from the fact that if the characteristic impedance of the transmission line and the load impedance are matched then there will be no reflected voltage waves on the transmission line. It should be noted that (2.35) is a more general definition of voltage reflection coefficient, to that defined earlier in (2.9), and is applicable to travelling waves or pseudo waves even though it is referred to as a 'voltage-wave' reflection coefficient.

A power reflection coefficient [16] may be defined in terms of power delivered to the load, which will be maximum when the characteristic impedance and load impedance are conjugately matched, i.e., $Z_0 = Z^*_L$. The power reflection coefficient can be defined as,

$$S_{p11} = \frac{Z_L - Z^*_0}{Z_L + Z_0} = \frac{b_{p1}}{a_{p1}} \tag{2.37}$$

where, b_{p1} and a_{p1} are the reflected and incident power waves at the load, respectively.

2.7 Generalised Two-Port Network

A generalised two-port network is shown in Fig. 2.4. Ports 1 and 2 are connected to transmission lines with characteristic impedances Z_{01} and Z_{01}, respectively; with Z_{ref1} and Z_{ref2} the reference port impedances at Port 1 and 2, respectively. The reference impedances may or may not be equal

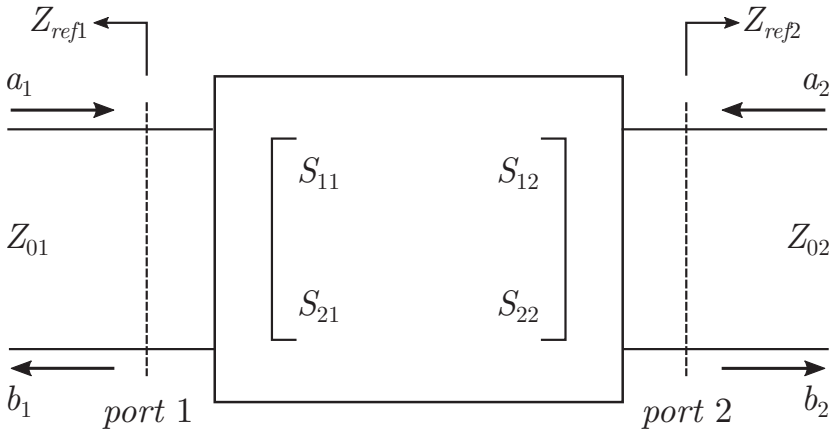


Figure 2.4: Illustration of a generalised two-port network. The scattering parameters of a two-port network relate the output wave quantities b_i at Port i in terms of input wave quantities a_i. Where, Z_{0i} and Z_{refi} are, respectively, the characteristic impedance of transmission line and reference impedance at Port i, given $i = 1, 2$.

to the characteristic impedances of the transmission lines. Here, a_n and b_n are, respectively, the incident and reflected voltage waves at Port $n = 1, 2$. The scattering matrix or S-matrix for this two-port network is defined by the following two equations,

$$b_1 = S_{11}a_1 + S_{12}a_2 \tag{2.38}$$

$$b_2 = S_{21}a_1 + S_{22}a_2 \tag{2.39}$$

In matrix form,

$$\begin{bmatrix} b_1 \\ b_2 \end{bmatrix} = \begin{bmatrix} S_{11} & S_{12} \\ S_{21} & S_{22} \end{bmatrix} \begin{bmatrix} a_1 \\ a_2 \end{bmatrix} \tag{2.40}$$

or,

$$\mathbf{b} = \mathbf{S}\mathbf{a} \tag{2.41}$$

Similarly, the power scattering parameters can be defined by,

$$b_{p1} = S_{p11}a_{p1} + S_{p12}a_{p2} \tag{2.42}$$

$$b_{p2} = S_{p21}a_{p1} + S_{p22}a_{p2} \tag{2.43}$$

In matrix form,

$$\begin{bmatrix} b_{p1} \\ b_{p2} \end{bmatrix} = \begin{bmatrix} S_{p11} & S_{p12} \\ S_{p21} & S_{p22} \end{bmatrix} \begin{bmatrix} a_{p1} \\ a_{p2} \end{bmatrix} \tag{2.44}$$

or,

$$\mathbf{b}_p = \mathbf{S}_p\mathbf{a}_p \tag{2.45}$$

2.8 Generalised n-Port Voltage-Wave and Power-Wave Scattering Parameters

For an n-port network, given an input Port i and output Port j, voltage waves a_i and b_j are defined as [1], [16],

$$a_i = \check{k}_i \left(V_i + Z_{refi} I_i\right) \tag{2.46}$$

$$b_j = \check{k}_j \left(V_j - Z_{refj} I_j\right) \tag{2.47}$$

where,

$$\check{k}_k = \frac{\sqrt{Re\left\{Z_{refk}\right\}}}{2\left|Z_{refk}\right|} \tag{2.48}$$

is the scaling factor for pseudo waves. For travelling waves the scaling factor is,

$$\check{k}_k = \frac{1}{2\sqrt{Re\left\{Z_{0k}\right\}}} \tag{2.49}$$

The generalised S-parameter for an n-port network is defined as the ratio of reflected waves at Port j to incident waves at Port i with all other input ports matched. Mathematically,

$$S_{ji(Z_{refj}, Z_{refi})} = \left.\frac{b_j}{a_i}\right|_{a_{k\neq i}=0} \tag{2.50}$$

where, the subscript of $S_{ji(Z_{refj}, Z_{refi})}$ indicates Z_{refj} and Z_{refi} as the reference impedances at output Port j and input Port i, respectively. For any Port i, a_i and b_i are known as travelling waves if $Z_{refi} = Z_{0i}$; otherwise they may be referred to as pseudo waves or the more common terminology of simply voltage waves. Pseudo waves are fictitious in nature but are useful when S-parameters may need to be expressed with respect to a certain reference impedance. As an example, the microwave community has adopted 50 Ω as the universally accepted reference impedance, as it is a good compromise between losses per unit length (minimum at 77 Ω) and power handling (maximum at 30 Ω) of a coaxial line [19].

Given input Port i and output Port j, if reference port impedances are real, i.e. $Z_{refi} = R_{refi}$ and $Z_{refi} = R_{refi}$; then average reflected and transmitted powers at Ports i and j relative to average incident power at input Port i are,

$$\frac{P_r}{P_i} = \left|S_{ii(R_{refi}, R_{refi})}\right|^2 \tag{2.51}$$

and,

$$\frac{P_t}{P_i} = \left|S_{ji(R_{refj}, R_{refi})}\right|^2 \tag{2.52}$$

The S-parameters of an n-port lossless device with real reference impedances, make up a unitary matrix **S** which satisfies the energy conservation relationship,

$$\sum_{j=1}^{n} \left| S_{ji\left(R_{refj}, R_{refi}\right)} \right|^2 = 1 \tag{2.53}$$

If reference port impedances are complex, then (2.51) and (2.52) are not valid and the unitary condition is no longer satisfied. In this case, the concept of power waves is useful. For an n-port network, given input Port i and output Port j, power waves a_{pi} and b_{pi} are defined as [2], [3], [4], [16],

$$a_{pi} = \check{k}_{pi} \left(V_i + Z_{refi} I_i \right) \tag{2.54}$$

$$b_{pj} = \check{k}_{pj} \left(V_j - Z^*_{refj} I_j \right) \tag{2.55}$$

where, the scaling factor is,

$$\check{k}_{pk} = \frac{1}{2\sqrt{Re\left\{Z_{refk}\right\}}} \tag{2.56}$$

The generalised S_p-parameters for an n-port network are defined as,

$$S_{pji\left(Z_{refj}, Z_{refi}\right)} = \left. \frac{b_{pj}}{a_{pi}} \right|_{a_{pk \neq i} = 0} \tag{2.57}$$

The average reflected and transmitted powers at Ports i and j, relative to the average incident power at Port i are given by,

$$\frac{P_r}{P_i} = \left| S_{pii\left(Z_{refi}, Z_{refi}\right)} \right|^2 \tag{2.58}$$

and,

$$\frac{P_t}{P_i} = \left| S_{pji\left(Z_{refj}, Z_{refi}\right)} \right|^2 \tag{2.59}$$

The unitary condition for S_p-parameters is always satisfied for an n-port lossless network with complex reference port impedances.

$$\sum_{j=1}^{n} \left| S_{pji\left(Z_{refj}, Z_{refi}\right)} \right|^2 = 1 \tag{2.60}$$

Notice that, (2.58)–(2.60) reduce to (2.51)–(2.53) if reference port impedances are real. Figure 2.5 presents a visual summary of relationships between different types of scattering parameters. The S- and S_p-parameters occupy the left and right half of the graphic, respectively. The measurement domain represents measured real powers with a network analyser and are usually referenced with respect to a real reference port impedance. The equivalence of real-referenced S- and S_p-parameters is indicated with green double arrows. Renormalisation among S- or S_p-parameters with respect to generalised reference impedances Z_{ref} and Z'_{ref} is shown with red double arrows. Conversions between S- and S_p-parameters is indicated by a blue double arrow.

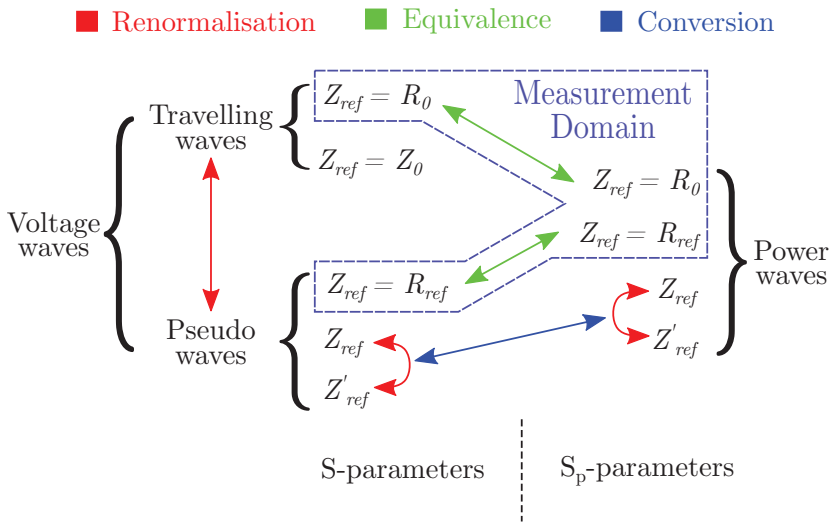


Figure 2.5: Graphical illustration of relationships between voltage (S-) and power (S_p-) scattering parameters. Double red arrows represent renormalisation of S- or S_p-parameters with respect to a certain reference impedance. Double green arrows show equivalence relationships, where real-referenced S_p-parameters either reduce to pseudo waves or travelling waves. Blue double arrows show a generalised conversion between S- and S_p-parameters. The measurement domain consists of real-referenced S- or S_p-parameters which are the actual powers measured by instruments.

2.9 Interconversion Between Two-Port S, Z, Y, h, ABCD and T Parameters

In this section, a general procedure is outlined for interconversion between different network parameters of a two-port network. In addition, direct conversion formulas for interconversion between S, Z, Y, h, ABCD and T parameters of a two-port network are derived which hold for arbitrary reference port impedances. Definitions of two-port network parameters used in this thesis are as follows:

S-parameters

$$b_1 = S_{11}a_1 + S_{12}a_2 \tag{2.61}$$

$$b_2 = S_{21}a_1 + S_{22}a_2 \tag{2.62}$$

Z-parameters

$$V_1 = Z_{11}I_1 + Z_{12}I_2 \tag{2.63}$$

$$V_2 = Z_{21}I_1 + Z_{22}I_2 \tag{2.64}$$

Y-parameters

$$I_1 = Y_{11}V_1 + Y_{12}V_2 \tag{2.65}$$

$$I_2 = Y_{21}V_1 + Y_{22}V_2 \tag{2.66}$$

h-parameters

$$V_1 = h_{11}I_1 + h_{12}V_2 \tag{2.67}$$

$$I_2 = h_{21}I_1 + h_{22}V_2 \tag{2.68}$$

ABCD-parameters

$$V_1 = AV_2 - BI_2 \tag{2.69}$$

$$I_1 = CV_2 - DI_2 \tag{2.70}$$

T-parameters

$$a_1 = T_{11}b_2 + T_{12}a_2 \tag{2.71}$$

$$b_1 = T_{21}b_2 + T_{22}a_2 \tag{2.72}$$

Following the treatment of Cooman [9], assume the given network parameters for conversion are represented by the matrix system,

$$\mathbf{B} = \mathbf{WA} \tag{2.73}$$

where, $\mathbf{B}$ is a vector containing output variables, $\mathbf{W}$ is the matrix of network parameters, and $\mathbf{A}$ is a vector containing input variables. The desired network parameters are represented by the matrix system,

$$\mathbf{B}^{\mathrm{N}} = \mathbf{W}^{\mathrm{N}}\mathbf{A}^{\mathrm{N}} \tag{2.74}$$

where, the superscript N represents variables of the new system. The goal is to find a transformation matrix $\mathbf{X}$ such that the following holds true,

$$\begin{bmatrix} \mathbf{B}^{\mathrm{N}} \\ \mathbf{A}^{\mathrm{N}} \end{bmatrix} = \begin{bmatrix} \mathbf{X}_{11} & \mathbf{X}_{12} \\ \mathbf{X}_{21} & \mathbf{X}_{22} \end{bmatrix} \begin{bmatrix} \mathbf{B} \\ \mathbf{A} \end{bmatrix} \tag{2.75}$$

After some algebraic manipulations, it can be shown that [9],

$$\mathbf{W}^{\mathrm{N}} = (\mathbf{X}_{11}\mathbf{W} + \mathbf{X}_{12})(\mathbf{X}_{21}\mathbf{W} + \mathbf{X}_{22})^{-1} \tag{2.76}$$

The transformation matrix $\mathbf{X}$ can be obtained using (2.75), which can then be used in (2.76) to the find the desired set of network parameters. As an example, if a transformation from S-parameters to ABCD-parameters is required then,

$$\begin{bmatrix} \mathbf{B}^{\mathrm{N}} \\ \mathbf{A}^{\mathrm{N}} \end{bmatrix} = \begin{bmatrix} V_1 \\ I_1 \\ V_2 \\ -I_2 \end{bmatrix} \tag{2.77}$$

and,

$$\begin{bmatrix} \mathbf{B} \\ \mathbf{A} \end{bmatrix} = \begin{bmatrix} b_1 \\ b_2 \\ a_1 \\ a_2 \end{bmatrix} \tag{2.78}$$

The transformation matrix $\mathbf{X}$ is,

$$\begin{bmatrix} \frac{1}{\check{k}_1} & 0 & \frac{1}{\check{k}_1} & 0 \\ -\frac{1}{\check{k}_1 Z_{ref1}} & 0 & \frac{1}{\check{k}_1 Z_{ref1}} & 0 \\ 0 & \frac{1}{\check{k}_2} & 0 & \frac{1}{\check{k}_2} \\ 0 & \frac{1}{\check{k}_2 Z_{ref2}} & 0 & -\frac{1}{\check{k}_2 Z_{ref2}} \end{bmatrix} \tag{2.79}$$

Using, (2.76), the following matrix equation is obtained,

$$\begin{bmatrix} A & B \\ C & D \end{bmatrix} = \left(\begin{bmatrix} \frac{1}{\check{k}_1} & 0 \\ -\frac{1}{\check{k}_1 Z_{ref1}} & 0 \end{bmatrix} \mathbf{S} + \begin{bmatrix} \frac{1}{\check{k}_1} & 0 \\ \frac{1}{\check{k}_1 Z_{ref1}} & 0 \end{bmatrix} \right) \left(\begin{bmatrix} 0 & \frac{1}{\check{k}_2} \\ 0 & \frac{1}{\check{k}_2 Z_{ref2}} \end{bmatrix} \mathbf{S} + \begin{bmatrix} 0 & \frac{1}{\check{k}_2} \\ 0 & -\frac{1}{\check{k}_2 Z_{ref2}} \end{bmatrix} \right) \tag{2.80}$$

which can be solved to obtain ABCD-parameters in terms of S-parameters. Tables 2.1 and 2.2 include transformation relationship between voltage, current, voltage waves and power waves. Two-port direct conversion formulas for interconversion between S, Z, Y, h, ABCD and T network parameters are given in Appendix H.

2.10 Cascading

Smaller networks can be cascaded to build larger networks. The overall response of a cascaded network can be easily computed using ABCD- or T-parameters of individual networks by simple matrix multiplication. Given n networks cascaded in series, the overall ABCD- or T-parameters can be computed using,

$$[ABCD]_{overall} = [ABCD]_1 [ABCD]_2 [ABCD]_3 ... [ABCD]_n \tag{2.81}$$

Table 2.1: Transformation relationship between voltage, current and pseudo waves.

Parameters	a_j	b_j	V_j	I_j
a_j	1	0	$\check{k}_j$	$\check{k}_j Z_{refj}$
b_j	0	1	$\check{k}_j$	$-\check{k}_j Z_{refj}$
V_j	$\frac{1}{2\check{k}_j}$	$\frac{1}{2\check{k}_j}$	1	0
I_j	$\frac{1}{2\check{k}_j Z_{refj}}$	$-\frac{1}{2\check{k}_j Z_{refj}}$	0	1

Table 2.2: Transformation relationship between voltage, current and power waves.

Parameters	a_{pj}	b_{pj}	V_j	I_j
a_{pj}	1	0	$\check{k}_{pj}$	$\check{k}_{pj} Z_{refj}$
b_{pj}	0	1	$\check{k}_{pj}$	$-\check{k}_{pj} Z^*_{refj}$
V_j	$\frac{Z^*_{refj}}{2\check{k}_{pj} Re\{Z_{refj}\}}$	$\frac{Z_{refj}}{2\check{k}_{pj} Re\{Z_{refj}\}}$	1	0
I_j	$\frac{1}{2\check{k}_{pj} Re\{Z_{refj}\}}$	$-\frac{1}{2\check{k}_{pj} Re\{Z_{refj}\}}$	0	1

where, $[ABCD]_n$ is the ABCD-parameter matrix of n^{th} cascaded network. When using T-parameters,

$$\mathbf{T}_{overall} = \mathbf{T}_1\mathbf{T}_2\mathbf{T}_3...\mathbf{T}_n \tag{2.82}$$

where, $\mathbf{T}_n$ is the T-parameter matrix of n^{th} network in cascade. It should be noted that, with matrix multiplication the order of multiplication is important when using (2.81) or (2.82).

Quite often, the response of individual networks is known in terms of S-parameters. In this case, application of (2.81) or (2.82) requires a conversion of individual S-parameters to ABCD- or T-parameters; and another conversion back to S-parameters for the overall response. It should be noted that the difference between ABCD- and T-parameters is that, ABCD-parameters are expressed in terms of voltages and currents while T-parameters are expressed in terms of waves. ABCD-parameters are a popular choice with circuits while T-parameters may be preferred with microwave networks.

When cascading networks it must be ensured that interconnected ports of individual networks must have the same reference port impedance. As shown in Fig. 2.6(a), the conventional approach is to have a common reference port impedance for all individual networks (Z_{ref1} in Fig. 2.6(a)) with the overall response $\mathbf{S}_{(Z_{ref1},Z_{ref1})}$. It is also possible to cascade two-port networks where reference port impedances might be different, with the condition, that interconnected ports of different networks must have the same reference port impedance, as shown in Figs. 2.6(b) and (c). The resulting overall S-parameters are transparent to interconnections and only depend on the input and output reference port impedances, as shown by the overall responses $\mathbf{S}_{(Z_{ref1},Z_{ref1})}$ and $\mathbf{S}_{(Z_{ref1},Z_{ref2})}$ in Figs. 2.6(b) and (c), respectively. With matched reference port impedances, signal flow graph theory can also be used to analyse cascaded networks. Cascading is not possible if interconnected ports have different reference port impedances as illustrated in Figs. 2.6(d) and (e). With S_p-parameters, however, the cascading condition requires that interconnected ports of individual networks have port networks impedances which are conjugates of each other. Therefore, cascading is not intuitive when working with S_p-parameters and may only be desirable in certain situations, like maximum power transfer.

2.11 Renormalisation of Scattering Parameters

S-parameters of an n-port network alone cannot completely describe the network. The S-parameters must be accompanied with an $n \times 1$ vector specifying reference port impedance at each port. A change in reference impedance at any port will result in a new set of S-parameters. This is known as renormalisation of S-parameters. In this section, direct conversion formulas for renormalisation

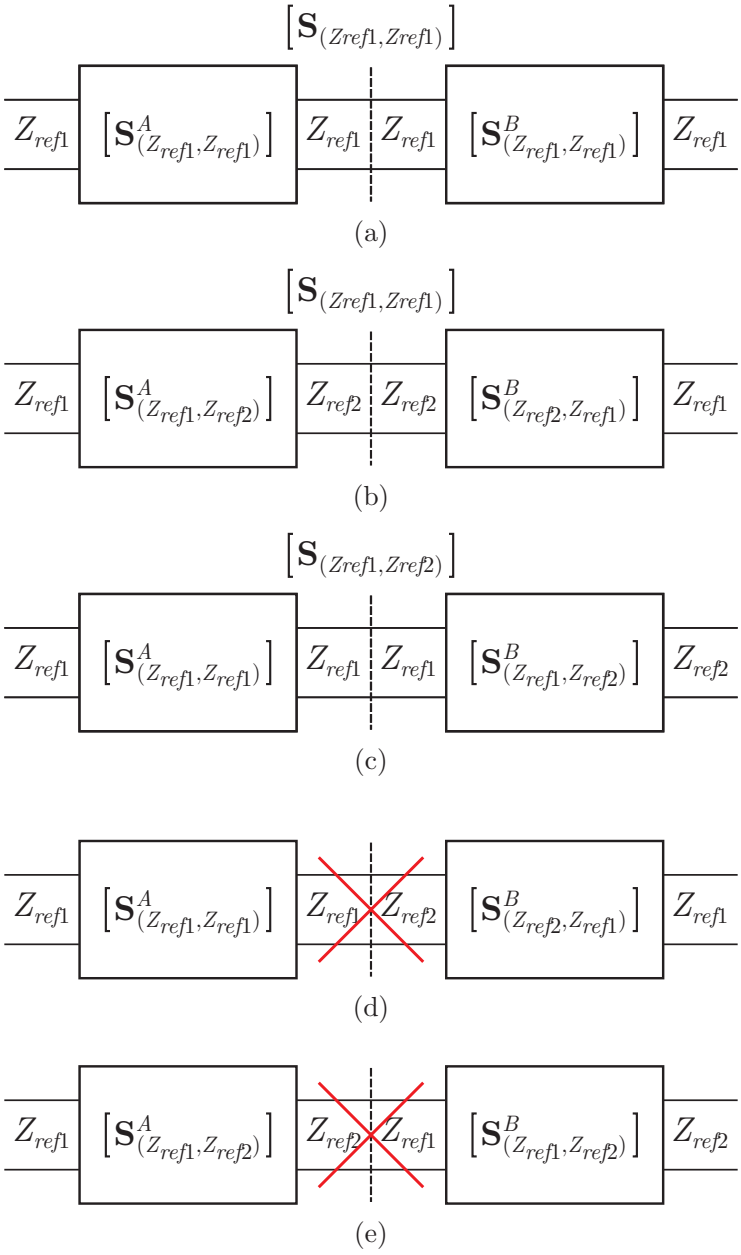


Figure 2.6: Cascading two-port networks: (a) conventional approach where individual networks have a common reference port impedance; (b) cascading is possible if connecting ports of two networks have the same reference port impedance; (c) overall S-parameters are with respect to reference port impedance of input and output ports of individual networks, respectively, and; (d), (e) cascading is not possible if interconnecting ports of individual networks have different reference port impedances.

of S- and S_p-parameters are presented.

It is convenient to have a common reference port impedance for all ports when processing S-parameter data of a multi-port network. For example, in the microwave community, 50 Ω is adopted as a universally accepted standard reference impedance for sharing S-parameter data. Where reference port impedance is not mentioned with S-parameter data, it is generally understood that the common reference port impedance is either 50 Ω or the characteristic impedance of the transmission line.

When performing measurements, the characteristic impedance of a transmission line at a port is often chosen as the reference port impedance. For example, with MPRWG measurements performed using the thru-reflect-line (TRL) calibration technique [13] for a MPRWG operating in dominant TE_{10} propagating mode, the reference impedance of measured S-parameters is the wave impedance Z_{TE10} of TE_{10} mode. The choice of reference port impedance is implicit with TRL technique.

Sun *et al.* [13] have recently demonstrated a novel technique for extraction of dielectric properties by using several sets of renormalised S-parameters to eliminate ambiguities in the solution space. Renormalisation of S-parameters can also be used to analyse and refine measurement data as demonstrated in [20].

Given a set of S-parameters $S_{ji\left(R_{refj},R_{refi}\right)}$ with reference port impedances Z_{refi} and Z_{refj} at Ports i and j, respectively; the renormalised set of S-parameters can be denoted as $S'_{ji\left(R'_{refj},R'_{refi}\right)}$ where, Z'_{refi} and Z'_{refj} are the new reference port impedances at Ports i and j, respectively. Conversion from $S_{ji\left(R_{refj},R_{refi}\right)}$ to $S'_{ji\left(R'_{refj},R'_{refi}\right)}$ can be done using the following matrix relationship [1], [4], [20],

$$\mathbf{S}' = \mathbf{Q}^{-1}\left(\mathbf{S}-\Gamma\right)\left(\mathbf{I}-\Gamma\mathbf{S}\right)^{-1}\mathbf{Q} \tag{2.83}$$

where, $\mathbf{S}$ is the original S-parameter matrix, $\mathbf{S}'$ is the renormalised S-parameter matrix, $\mathbf{I}$ is the identity matrix, $\mathbf{Q}$ is the diagonal matrix with entries,

$$Q_{kk} = \sqrt{\frac{Re\{Z_{refk}\}}{Re\{Z'_{refk}\}}}\left|\frac{Z'_{refk}}{Z_{refk}}\right|\frac{2Z_{refk}}{Z'_{refk}+Z_{refk}} \tag{2.84}$$

Γ is a diagonal matrix with entries,

$$\Gamma_{kk} = \frac{Z'_{refk}-Z_{refk}}{Z'_{refk}+Z_{refk}} \tag{2.85}$$

For a two-port network, the following direct conversion formulas can be used for renormalisation of S-parameters,

$$S'_{11\left(Z'_{ref1},Z'_{ref1}\right)} = \frac{\Gamma_{22}S_{12}S_{21}+\left(1-\Gamma_{22}S_{22}\right)\left(S_{11}-\Gamma_{11}\right)}{\left(1-\Gamma_{11}S_{11}\right)\left(1-\Gamma_{22}S_{22}\right)-\Gamma_{11}\Gamma_{22}S_{12}S_{21}} \tag{2.86}$$

$$S'_{12(Z'_{ref1},Z'_{ref2})} = \frac{Q_{22}\Gamma_{11}S_{12}\left(S_{11}-\Gamma_{11}\right)+Q_{22}S_{12}\left(1-\Gamma_{11}S_{11}\right)}{\left(1-\Gamma_{11}S_{11}\right)\left(1-\Gamma_{22}S_{22}\right)-\Gamma_{11}\Gamma_{22}S_{12}S_{21}} \tag{2.87}$$

$$S'_{21(Z'_{ref2},Z'_{ref1})} = \frac{Q_{11}\Gamma_{22}S_{21}\left(S_{22}-\Gamma_{22}\right)+Q_{11}S_{21}\left(1-\Gamma_{22}S_{22}\right)}{\left(1-\Gamma_{11}S_{11}\right)\left(1-\Gamma_{22}S_{22}\right)-\Gamma_{11}\Gamma_{22}S_{12}S_{21}} \tag{2.88}$$

$$S'_{22(Z'_{ref2},Z'_{ref2})} = \frac{\Gamma_{11}S_{12}S_{21}+\left(1-\Gamma_{11}S_{11}\right)\left(S_{22}-\Gamma_{22}\right)}{\left(1-\Gamma_{11}S_{11}\right)\left(1-\Gamma_{22}S_{22}\right)-\Gamma_{11}\Gamma_{22}S_{12}S_{21}} \tag{2.89}$$

A similar conversion can be used to renormalise S_p-parameters given by [4],

$$\mathbf{S}'_p = \mathbf{W}^{-1}\left(\mathbf{S}_p-\check{\Gamma}^{[*]}\right)\left(\mathbf{I}-\check{\Gamma}\mathbf{S}_p\right)^{-1}\mathbf{W}^{[*]} \tag{2.90}$$

where, $\mathbf{S}_p$ is the original S_p-parameter matrix, $\mathbf{S}'_p$ is the renormalised S_p-parameter matrix, $\mathbf{I}$ is the identity matrix, $\mathbf{W}$ is a diagonal matrix with entries,

$$W_{kk} = \sqrt{\left|\frac{Re\left\{Z'_{refk}\right\}}{Re\left\{Z_{refk}\right\}}\right|}\frac{Z_{refk}+Z^*_{refk}}{Z'^*_{refk}+Z_{refk}} \tag{2.91}$$

$\check{\Gamma}$ is a diagonal matrix with entries,

$$\check{\Gamma}_{kk} = \frac{Z'_{refk}-Z_{refk}}{Z'_{refk}+Z^*_{refk}} \tag{2.92}$$

A $[*]$ superscript indicates matrix complex conjugate transpose, which can be computed by taking the conjugate of all the entries of a matrix and then interchanging rows and columns, while a superscript $*$ indicates complex conjugate.

For a two-port network, the following direct conversion formulas can be used for renormalisation of S_p-parameters,

$$S'_{p11(Z'_{ref1},Z'_{ref1})} = \frac{W^*_{11}W_{22}\check{\Gamma}_{22}S_{p12}S_{p21}+W^*_{11}W_{22}\left(1-\check{\Gamma}_{22}S_{p22}\right)\left(S_{p11}-\check{\Gamma}^*_{11}\right)}{W_{11}W_{22}\left[\left(1-\check{\Gamma}_{11}S_{p11}\right)\left(1-\check{\Gamma}_{22}S_{p22}\right)-\check{\Gamma}_{11}\check{\Gamma}_{22}S_{p12}S_{p21}\right]} \tag{2.93}$$

$$S'_{p12(Z'_{ref1},Z'_{ref2})} = \frac{|W_{22}|^2 S_{p12}\left(1-\check{\Gamma}_{11}S_{p11}+\check{\Gamma}_{11}\left(S_{p11}-\check{\Gamma}^*_{11}\right)\right)}{W_{11}W_{22}\left[\left(1-\check{\Gamma}_{11}S_{p11}\right)\left(1-\check{\Gamma}_{22}S_{p22}\right)-\check{\Gamma}_{11}\check{\Gamma}_{22}S_{p12}S_{p21}\right]} \tag{2.94}$$

$$S'_{p12(Z'_{ref2},Z'_{ref1})} = \frac{|W_{11}|^2 S_{p21}\left(1-\check{\Gamma}_{22}S_{p22}+\check{\Gamma}_{22}\left(S_{p22}-\check{\Gamma}^*_{22}\right)\right)}{W_{11}W_{22}\left[\left(1-\check{\Gamma}_{11}S_{p11}\right)\left(1-\check{\Gamma}_{22}S_{p22}\right)-\check{\Gamma}_{11}\check{\Gamma}_{22}S_{p12}S_{p21}\right]} \tag{2.95}$$

$$S'_{p22(Z'_{ref2},Z'_{ref2})} = \frac{W_{11}W^*_{22}\check{\Gamma}_{11}S_{p12}S_{p21}+Q_{11}Q^*_{22}\left(1-\check{\Gamma}_{11}S_{p11}\right)\left(S_{p22}-\check{\Gamma}^*_{22}\right)}{Q_{11}Q_{22}\left[\left(1-\check{\Gamma}_{11}S_{p11}\right)\left(1-\check{\Gamma}_{22}S_{p22}\right)-\check{\Gamma}_{11}\acute{\Gamma}_{22}S_{p12}S_{p21}\right]} \tag{2.96}$$

2.12 Conversion Between Voltage-Wave and Power-Wave Scattering Parameters

Sometimes it is convenient to convert S-parameters to S_p-parameters and vice versa. In this section, generalised n-port expressions for conversion between S- and S_p-parameters are derived. From (2.46) and (2.54),

$$a_{pi} = \frac{|Z_{refi}|}{Re\{Z_{refi}\}} a_i \tag{2.97}$$

Similarly, from (2.47) and (2.55),

$$b_{pj} = \frac{|Z_{refj}|}{Re\{Z_{refj}\}} \frac{V_j - Z^*_{refj} I_j}{V_j - Z_{refj} I_j} b_j \tag{2.98}$$

Dividing (2.98) by (2.97) and using (2.50),

$$S_{pji(Z_{refj}, Z_{refi})} = \frac{b_{pj}}{a_{pi}} = \frac{|Z_{refj}|\, Re\{Z_{refi}\}}{|Z_{refi}|\, Re\{Z_{refj}\}} \frac{V_j - Z^*_{refj} I_j}{V_j - Z_{refj} I_j} S_{ji(Z_{refj}, Z_{refi})} \tag{2.99}$$

For $i \neq j$, the definition in (2.57) implies that there are no incident waves at Port j or,

$$a_{pj} = \frac{1}{2\sqrt{Re\{Z_{refj}\}}} V_j + Z_{refj} I_j = 0 \tag{2.100}$$

Solving for I_j,

$$I_j = -\frac{V_j}{Z_{refj}} \tag{2.101}$$

Substituting (2.101) in (2.99),

$$S_{pji(Z_{refj}, Z_{refi})} = \left.\frac{b_{pj}}{a_{pi}}\right|_{a_{pk\neq i}=0} = \frac{1}{2} \frac{|Z_{refj}|\, Re\{Z_{refi}\}}{|Z_{refi}|\, Re\{Z_{refj}\}} \left(1 + \frac{Z^*_{refj}}{Z_{refj}}\right) S_{ji(Z_{refj}, Z_{refi})} \tag{2.102}$$

where, (2.102) is only valid when $i \neq j$. For $i = j$, making use of (2.54), (2.55) and (2.57) to get,

$$S_{pjj(Z_{refj}, Z_{refj})} = \left.\frac{b_{pj}}{a_{pj}}\right|_{a_{pk\neq j}=0} = \frac{V_j - Z^*_{refj} I_j}{V_j + Z_{refj} I_j} \tag{2.103}$$

From, (2.46), (2.47) and (2.50),

$$S_{jj(Z_{refj}, Z_{refj})} = \left.\frac{b_j}{a_j}\right|_{a_{k\neq j}=0} = \frac{V_j - Z_{refj} I_j}{V_j + Z_{refj} I_j} \tag{2.104}$$

From this, I_j can be written in terms of V_j as,

$$I_j = \frac{V_j}{Z_{refj}} \frac{1 - S_{jj(Z_{refj}, Z_{refj})}}{1 + S_{jj(Z_{refj}, Z_{refj})}} \tag{2.105}$$

Substituting the expression for I_j in (2.103),

$$S_{pjj(Z_{refj}, Z_{refj})} = \left.\frac{b_{pj}}{a_{pj}}\right|_{a_{pk\neq j}=0} = \frac{V_j - Z^*_{refj} I_j}{V_j + Z_{refj} I_j} \tag{2.106}$$

and,

$$S_{pjj(Z_{refj},Z_{refj})} = \frac{b_{pj}}{a_{pj}}\bigg|_{a_{pk\neq j}=0} = \frac{1}{Z_{refj}}\left(S_{jj(Z_{refj},Z_{refj})} Re\left\{Z_{refj}\right\} + Im\left\{Z_{refj}\right\}\right) \tag{2.107}$$

which is valid when $i = j$. With real reference port impedances, right hand sides of both (2.102) and (2.107) reduce to $S_{pji(R_{refj},R_{refi})} = S_{ji(R_{refj}R_{refi})}$ and $S_{pjj(R_{refj},R_{refj})} = S_{jj(R_{refj},R_{refj})}$, respectively.

2.13 Example: Two-Layer Media as Two-Port Network

When a TEM plane wave is normally incident at the interface between two semi-infinite planar lossy media as shown in Fig. 2.7, the given incident, reflected and transmitted electric and magnetic fields are,

$$\mathbf{E}_i = E_0 e^{-\gamma_1 z}\hat{x} \tag{2.108}$$

$$\mathbf{H}_i = \frac{E_0}{\eta_1} e^{-\gamma_1 z}\hat{y} \tag{2.109}$$

$$\mathbf{E}_r = \rho_{11} E_0 e^{\gamma_1 z}\hat{x} \tag{2.110}$$

$$\mathbf{H}_r = -\rho_{11}\frac{E_0}{\eta_1} e^{\gamma_1 z}\hat{y} \tag{2.111}$$

$$\mathbf{E}_t = \tau_{21} E_0 e^{-\gamma_2 z}\hat{x} \tag{2.112}$$

$$\mathbf{H}_t = \tau_{21}\frac{E_0}{\eta_2} e^{-\gamma_2 z}\hat{y} \tag{2.113}$$

where,

$$\rho_{11} = \frac{\eta_2 - \eta_1}{\eta_2 + \eta_1} \tag{2.114}$$

and,

$$\tau_{21} = \frac{2\eta_2}{\eta_2 + \eta_1} \tag{2.115}$$

Here, E_0 is the RMS amplitude of electric field in V/m; $\gamma_i = jk_i = \alpha_i + j\beta_i$ is the propagation constant in medium i; $\eta_i = \sqrt{\tilde{\mu}_{effi}/\tilde{\varepsilon}_{effi}}$ is the intrinsic impedance of medium i with, $\tilde{\mu}_{effi}$ and $\tilde{\varepsilon}_{effi}$ the complex permeability and permittivity, respectively, of medium i; ρ_{11} and τ_{21} are the Fresnel reflection and transmission coefficients. A superscript $*$ indicates complex conjugate.

The reflected and transmitted powers can be computed using S_p-parameters by treating the problem as a two-port network. With $Z_{ref1} = Z_{ref2} = \eta_1$, it is clear that $S_{11} = 0$ and $S_{21} = 1$. By letting $Z_{ref1} = \eta_1$ and $Z_{ref2} = \eta_2$, the interface can be thought of as a two-port network which is simply a buffer zero length with phase $j\phi = 0$ ($e^{j\phi} = 1$).

At $z = 0$, the two-port network voltage and currents terms may be identified as: At Port 1 with $Z_{ref1} = Z_{01} = \eta_1$, $V_1^+ \to E_0$, $V_1^- \to \rho_{11}E_0$, $I_1^+ \to E_0/\eta_1$, $I_1^- \to -\rho_{11}E_0/\eta_1$, $V_1 = V_1^+ + V_1^- =$

$E_0(1+\rho_{11})$, $I_1 = I_1^+ + I_1^- = E_0(1-\rho_{11})/\eta_1$. At Port 2 with $Z_{ref2} = Z_{02} = \eta_2$, $V_2^+ \to 0$, $V_2^- =\to \tau_{21}E_0$, $I_2^+ \to 0$, $I_2^- \to -\tau_{21}E_0/\eta_2$, $V_2 = V_2^+ + V_2^- = \tau_{21}E_0$, $I_2 = I_2^+ + I_2^- = -\tau_{21}E_0/\eta_2$. Using the definition of voltage waves (2.46)–(2.47),

$$a_1 = \frac{1}{2}\frac{\sqrt{Re\{\eta_1\}}}{|\eta_1|}V_1 + \eta_1 I_1 = \frac{\sqrt{Re\{\eta_1\}}}{|\eta_1|}E_0 \tag{2.116}$$

$$b_1 = \frac{1}{2}\frac{\sqrt{Re\{\eta_1\}}}{|\eta_1|}V_1 - \eta_1 I_1 = \frac{\sqrt{Re\{\eta_1\}}}{|\eta_1|}\rho_{11}E_0 \tag{2.117}$$

$$a_2 = \frac{1}{2}\frac{\sqrt{Re\{\eta_2\}}}{|\eta_2|}V_2 + \eta_2 I_2 = 0 \tag{2.118}$$

$$b_2 = \frac{1}{2}\frac{\sqrt{Re\{\eta_2\}}}{|\eta_2|}V_2 - \eta_2 I_2 = \frac{\sqrt{Re\{\eta_2\}}}{|\eta_2|}\tau_{21}E_0 \tag{2.119}$$

The S-parameters are,

$$S_{11} = \left.\frac{b_1}{a_1}\right|_{a_2=0} = \rho_{11} = \frac{\eta_2 - \eta_1}{\eta_2 + \eta_1} \tag{2.120}$$

$$S_{21} = \left.\frac{b_2}{a_1}\right|_{a_2=0} = \frac{|\eta_1|\sqrt{Re\{\eta_2\}}}{|\eta_2|\sqrt{Re\{\eta_1\}}}\tau_{21} = \frac{|\eta_1|\sqrt{Re\{\eta_2\}}}{|\eta_2|\sqrt{Re\{\eta_1\}}}\frac{2\eta_2}{\eta_2+\eta_1} \tag{2.121}$$

Here, $S_{11} = \rho_{11}$. Using (2.102) and (2.107),

$$S_{p11} = \frac{\eta_2 - \eta_1^*}{\eta_2 + \eta_1} \tag{2.122}$$

$$S_{p21} = \left(1 + \frac{\eta_2^*}{\eta_2}\right)\frac{\sqrt{Re\{\eta_1\}}}{\sqrt{Re\{\eta_2\}}}\tau_{21} = \frac{2\sqrt{Re\{\eta_1\}}\sqrt{Re\{\eta_2\}}}{\eta_2+\eta_1} \tag{2.123}$$

Depending on whether reference port impedances are real or complex, for a two-port network, the following are true: (i) if reference port impedances Z_{ref1} and Z_{ref2} are both real then voltage and power scattering parameters are equal ($S_{11} = S_{p11}$ and $S_{21} = S_{p21}$). In this case, the normalised reflected and transmitted powers are given by reflectance and transmittance as $\mathcal{R} \equiv P_r/P_i = |S_{11}|^2 = |S_{p11}|^2$, and $\mathcal{T} \equiv P_t/P_i = |S_{21}|^2 = |S_{p21}|^2$; (ii) if one of the reference impedances is complex, then S- and S_p-parameters are not equal ($S_{11} \neq S_{p11}$ and $S_{21} \neq S_{p21}$). Also, $\mathcal{R} \equiv P_r/P_i = |S_{11}|^2 = |S_{p11}|^2$ but transmittance is given by $\mathcal{T} = |S_{p21}|^2 \neq |S_{21}|^2$; and (iii) if both reference port impedances are complex then $\mathcal{R} = |S_{p11}|^2$ and $\mathcal{T} = |S_{p21}|^2$.

2.14 Example: Three-Layer Media as Two-Port Network

In this section, a 1-D resonant cavity with lossy walls is presented which demonstrates that complex-referenced S-parameters cannot be directly used to compute reflectance and transmittance. Consider the three-layer media shown in Fig. 2.8 which is essentially a symmetric Fabry-Pérot cavity resonator of width $l = 300$ μm, corresponding to one full wavelength at 1 THz for an ideal resonator. The

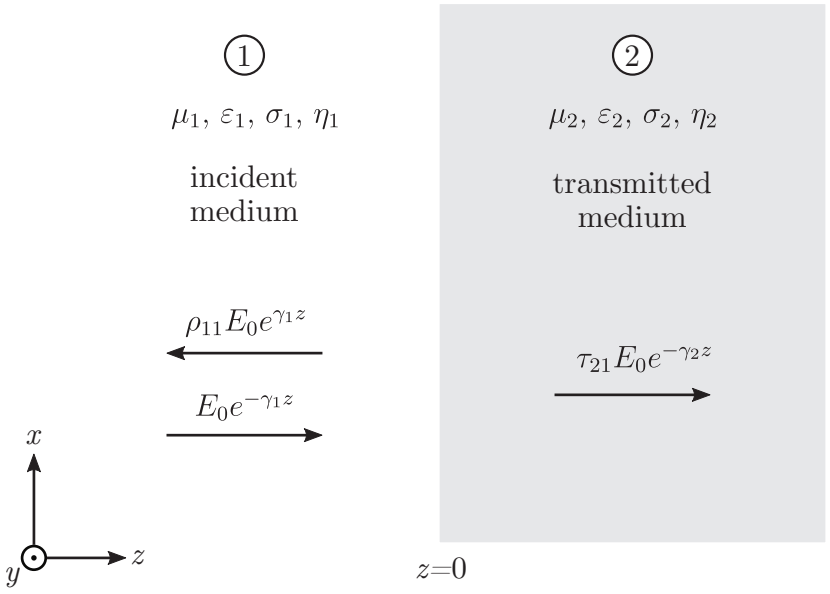


Figure 2.7: Plane wave reflection and transmission at the interface between two planar lossy media. The reflected and transmitted electric fields are related to the incident electric fields by the Fresnel reflection and transmission coefficients, respectively.

Table 2.3: Summary of exact equations for two-media and one- or two-port modelling.

Parameter	One-port Model	Two-port Model	
	$Z_{ref} \equiv \eta_1$	$Z_{ref1} \equiv \eta_1$ $Z_{ref2} \equiv \eta_1$	$Z_{ref1} \equiv \eta_1$ $Z_{ref2} \equiv \eta_2$
ρ_{11}	$\frac{\eta_2-\eta_1}{\eta_2+\eta_1}$	-	-
τ_{21}	$\frac{2\eta_2}{\eta_2+\eta_1}$	-	-
S_{11}	ρ_{11}	0	ρ_{11}
S_{21}	-	1	$\frac{\lvert\eta_1\rvert\sqrt{Re\{\eta_2\}}}{\lvert\eta_2\rvert\sqrt{Re\{\eta_1\}}}\tau_{21}$
S_{p11}	$\frac{\eta_2-\eta_1^*}{\eta_2+\eta_1}$	0	$\frac{\eta_2-\eta_1^*}{\eta_2+\eta_1}$
S_{p21}	-	1	$\frac{2\sqrt{Re\{\eta_1\}Re\{\eta_2\}}}{\eta_2+\eta_1}$
$\mathcal{R}$	$\lvert S_{p11}\rvert^2$	$\lvert S_{p11}\rvert^2 = 0$	$\lvert S_{p11}\rvert^2$
$\mathcal{T}$	-	$\lvert S_{p21}\rvert^2 = 1$	$\lvert S_{p21}\rvert^2$

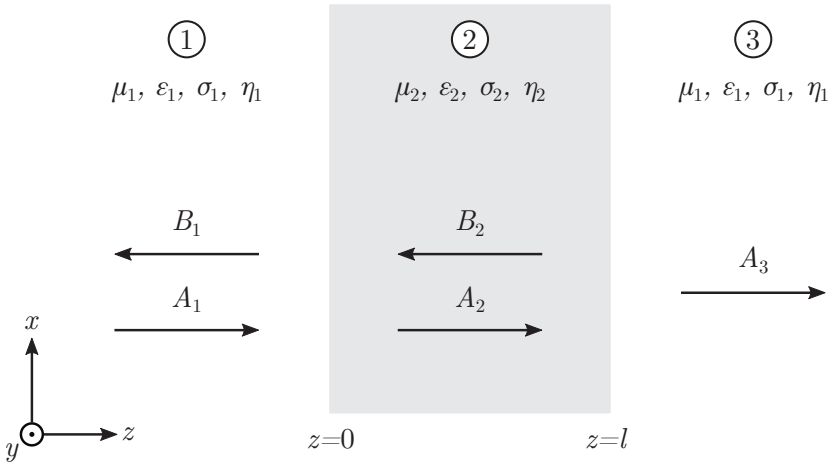


Figure 2.8: Incident and reflected fields in three-layer media. As and Bs are, respectively, reflected and transmitted fields in a given medium. Here, the reference plane for coefficients A_3 is the plane $z = l$, while all other coefficients are referenced with respect to the $z = 0$ plane. There are no reflected waves in medium ③.

biven material parameters are: $\mu_1 = \mu_2 = \mu_3 = 1$, $\varepsilon_1 = \varepsilon_2 = \varepsilon_3 = 1$, $\sigma_1 = \sigma_3 = 100$ S/m and $\sigma_2 = 0$. With these parameters, the resonator can be considered as a lossless two-port network with lossy feed and complex reference impedances $Z_{ref1} = Z_{ref2} = \eta_1$. Assuming the case of TEM incidence, the forward and backward propagating electric and magnetic fields can be written as,

$$E_{x1} = A_1 e^{-\gamma_1 z} + B_1 e^{\gamma_1 z} \tag{2.124}$$

$$H_{y1} = \frac{1}{\eta_1}\left(A_1 e^{-\gamma_1 z} - B_1 e^{\gamma_1 z}\right) \tag{2.125}$$

$$E_{x2} = A_2 e^{-\gamma_2 z} + B_2 e^{\gamma_2 z} \tag{2.126}$$

$$H_{y2} = \frac{1}{\eta_2}\left(A_2 e^{-\gamma_2 z} - B_2 e^{\gamma_2 z}\right) \tag{2.127}$$

$$E_{x3} = A_3 e^{-\gamma_3 (z-l)} \tag{2.128}$$

$$H_{y3} = \frac{1}{\eta_3} A_3 e^{-\gamma_3 (z-l)} \tag{2.129}$$

where the propagation constant is given by,

$$\gamma_i = j\omega\sqrt{\tilde{\mu}_{effi}\tilde{\varepsilon}_{effi}} \quad \text{with} \quad i = 1, 2, 3 \tag{2.130}$$

with, $\gamma_3 = \gamma_1$, ω is the angular frequency in radian/s, $\tilde{\mu}_{effi}$ is the effective complex permeability of medium i which is set as the permeability of free space (μ_0) here, $\tilde{\varepsilon}_{effi}$ is the effective complex permittivity of medium i given by,

$$\tilde{\varepsilon}_{effi} = \varepsilon_0 \tilde{\varepsilon}_{reffi} = \varepsilon_0(\varepsilon_{ri} - j\frac{\sigma_i}{\omega\varepsilon_0}) \tag{2.131}$$

where, ε_0 is the dielectric constant of free space, ε_{ri} is the dielectric constant or relative permittivity, σ_i is the intrinsic DC bulk conductivity in S/m and η_i is the intrinsic impedance of medium i in Ω.

Boundary conditions require tangential components of electric and magnetic fields to be continuous across the interface at $z = 0$ and at $z = l$. Setting $E_{x1}(z = 0) = E_{x2}(z = 0)$, $H_{y1}(z = 0) = H_{y2}(z = 0)$, $E_{x2}(z = l) = E_{x3}(z = l)$ and $H_{y2}(z = l) = H_{y3}(z = l)$, the following characteristic matrix system is obtained,

$$\begin{bmatrix} 1 & 1 & -1 & -1 & 0 \\ \eta_2 & -\eta_2 & -\eta_1 & \eta_1 & 0 \\ 0 & 0 & e^{-\gamma_2 l} & e^{\gamma_2 l} & -1 \\ 0 & 0 & \eta_1 e^{-\gamma_2 l} & -\eta_1 e^{\gamma_2 l} & -\eta_2 \end{bmatrix} \begin{bmatrix} A_1 \\ B_1 \\ A_2 \\ B_2 \\ B_3 \end{bmatrix} = \begin{bmatrix} 0 \\ 0 \\ 0 \\ 0 \end{bmatrix} \tag{2.132}$$

Setting A_1 equal to unity, the S-parameters can be obtained as,

$$S_{11} = \frac{B_1}{A_1} = \frac{\left(1 - e^{-2\gamma_2 l}\right)\left(1 - \frac{\eta_1}{\eta_2}\right)\left(1 + \frac{\eta_1}{\eta_2}\right)}{\left(1 + \frac{\eta_1}{\eta_2}\right)^2 - e^{-2\gamma_2 l}\left(1 - \frac{\eta_1}{\eta_2}\right)^2} \tag{2.133}$$

$$S_{21} = \frac{A_3}{A_1} = \frac{4\frac{\eta_1}{\eta_2} e^{-\gamma_2 l}}{\left(1 + \frac{\eta_1}{\eta_2}\right)^2 - e^{-2\gamma_2 l}\left(1 - \frac{\eta_1}{\eta_2}\right)^2} \tag{2.134}$$

Figure 2.9 shows a plot of S-parameters, S_p-parameters and S-parameters with reference port impedances set to 50 Ω. The S-parameters with common complex reference port impedance η_1 do not satisfy the energy conservation relationship, i.e., $|S_{11}|^2 + |S_{21}|^2 \neq 1$, which is expected. On the other hand, S_p-parameters and 50 Ω-referenced S-Parameters satisfy energy conservation, i.e., $|S_{p11}|^2 + |S_{p21}|^2 = |S_{11(50\ \Omega)}|^2 + |S_{21(50\ \Omega)}|^2 = 1$. The theoretical bounds for coefficients and parameters, assuming positive resistances, are summarised in Table 2.4.

2.15 Example: Signal Flow Graph Analysis of Three-Layer Media

The three-layer media Fabry-Pérot resonator shown in Fig. 2.8 can be modelled as a two-port network with the intrinsic impedance of flanking media as the terminating reference port impedances. This two-port network can be analysed using a signal flow graph to obtain a system of algebraic equations which can be solved for electric field reflection and transmission coefficients of the resonant two-port network. The complex eigenfrequencies can then be obtained from the poles of the reflection coefficient S_{11}.

Since the resonator walls are lossy the network has to be terminated at input and output ends with complex-referenced impedances. It is important to note that since reference impedances for

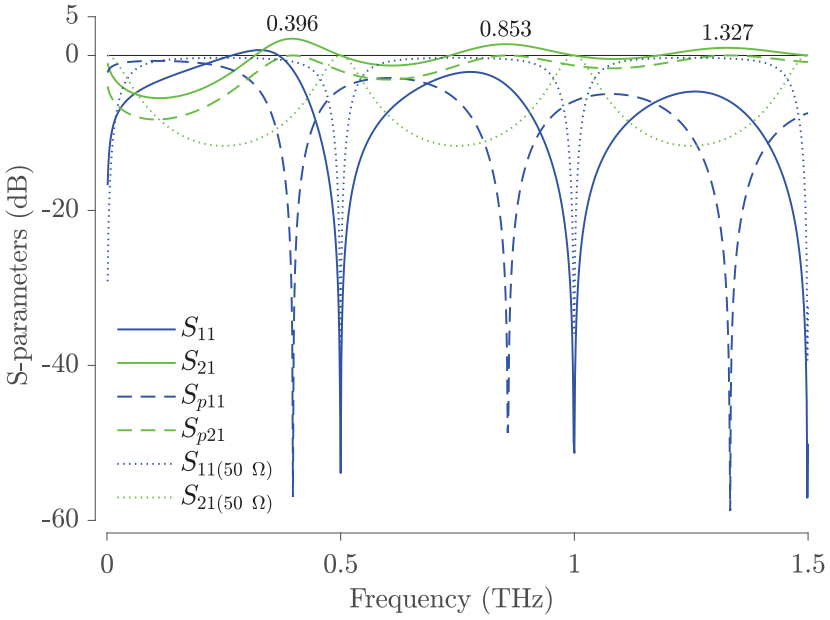


Figure 2.9: Plot of S-parameters of 1-D Fabry-Pérot resonator with $\sigma_① = \sigma_③ = 100$ S/m based on the conventional and power wave definitions, respectively. With conventional complex-referenced S-parameters, the insertion and return loss exceed 0 dB, however, the S_p-parameter response shows that the total energy is conserved. Frequencies at S-parameter resonant peaks are also indicated.

Table 2.4: Summary of theoretical bounds for coefficients and parameters with positive resistances.

Primary Reference Medium (feed)	Secondary Test Medium (network)	Two-media (one-port)			Three-media (two-port)				Power Parameters	
		Fresnel Coefficients		Power S_p-parameter	Voltage-wave S-parameters		Power S_p-parameter			
		$\lvert\rho_{11}\rvert$	$\lvert\tau_{21}\rvert$	$\lvert S_{p11}\rvert$	$\lvert S_{11}\rvert$	$\lvert S_{21}\rvert$	$\lvert S_{p11}\rvert$	$\lvert S_{p21}\rvert$	$\mathcal{R} = \lvert S_{p11}\rvert^2$	$\mathcal{T} = \lvert S_{p21}\rvert^2$
Lossless	Lossless	≤ 1	$\lessgtr 1$	≤ 1	≤ 1	≤ 1	≤ 1	≤ 1	$\lvert\rho_{11}\rvert^2,\ \lvert S_{11}\rvert^2 \leq 1$	$\lvert S_{21}\rvert^2 \leq 1$
Lossless	Lossy	≤ 1	$\lessgtr 1$	≤ 1	≤ 1	≤ 1	≤ 1	≤ 1	$\lvert\rho_{11}\rvert^2,\ \lvert S_{11}\rvert^2 \leq 1$	$\lvert S_{21}\rvert^2 \leq 1$
Lossy	Lossless	≤ 1	$\lessgtr 1$	≤ 1	$\lessgtr 1$	$\lessgtr 1$	≤ 1	≤ 1	$\lvert\rho_{11}\rvert^2 \leq 1$	≤ 1
Lossy	Lossy	$\lessgtr 1$	$\lessgtr 1$	≤ 1	$\lessgtr 1$	$\lessgtr 1$	≤ 1	≤ 1	≤ 1	≤ 1

input and output ports are complex, reflected and transmitted powers, therefore, cannot simply be obtained by taking the square of the absolute of reflection and transmission coefficients; i.e., $|S_{11}|^2$ and $|S_{21}|^2$ do not represent reflected and transmitted powers any more. The signal flow graph shown in Fig. 2.10 shows a 1-D resonator as a two-port network. The resonator itself is modelled as a transmission line which contributes a phase of $\gamma_2 l$. Here, γ_2 is the propagation constant in the resonator and l is the width of resonator. a_i is the incident wave at port i while b_i is the reflected wave at port i. Port 1 is the incident port while the transmitted signal is obtained at Port 2 with the assumption that there are no incident waves at Port 2, i.e., $a_2 = 0$. The two-port network is assumed to be reciprocal. The normal Fresnel reflection and transmission coefficients (Γ_{nm} and T_{nm}) are defined here as,

$$\Gamma_{nm} = \frac{\eta_m - \eta_n}{\eta_m + \eta_n} = \rho_{nn} \tag{2.135}$$

and,

$$T_{nm} = \frac{2\eta_m}{\eta_m + \eta_n} = \tau_{mn} \tag{2.136}$$

Where η_2 is the intrinsic impedance of the resonator medium and η_1 of the medium flanking the resonator. The node variables x_1–x_4 can be expressed as,

$$x_1 = T_{12}a_1 + \Gamma_{21}x_2 \tag{2.137}$$

$$x_2 = e^{-\gamma_2 l}x_4 \tag{2.138}$$

$$x_3 = e^{-\gamma_2 l}x_1 \tag{2.139}$$

and,

$$x_4 = \Gamma_{21}x_3 \tag{2.140}$$

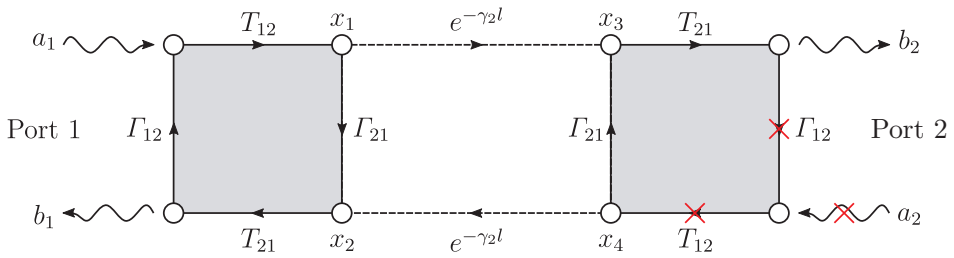


Figure 2.10: Signal flow graph illustration of 1-D Fabry-Pérot resonator of width l. Each node represents an equation given by the sum of inputs minus the sum of outputs. There are no incident waves at Port 2, therefore, Γ_{12} and T_{12} can be ignored. The total reflection and transmission coefficients can be computed from algebraic manipulation of resultant node equations.

with,

$$b_1 = \Gamma_{12} a_1 + T_{21} x_2 \tag{2.141}$$

and,

$$b_2 = T_{21} x_3 \tag{2.142}$$

Now,

$$\begin{aligned} T_{12} a_1 &= x_1 - \Gamma_{21} x_2 \\ &= e^{\gamma_2 l} x_3 - \Gamma_{21} e^{-\gamma_2 l} x_4 \\ &= e^{\gamma_2 l} x_3 - \Gamma_{21}^2 e^{-\gamma_2 l} x_3 \end{aligned} \tag{2.143}$$

and,

$$\begin{aligned} T_{12} T_{21} a_1 &= e^{\gamma_2 l} b_2 - \Gamma_{21} e^{-\gamma_2 l} b_2 \\ &= b_2 \left(e^{\gamma_2 l} - \Gamma_{21} e^{-\gamma_2 l} \right) \end{aligned} \tag{2.144}$$

The overall electric field reflection and transmission coefficients of the Fabry-Pérot resonator are then expressed as,

$$\Gamma = \frac{b_1}{a_1} = \frac{T_{12} T_{21} \Gamma_{21} e^{-2\gamma_2 l} + \Gamma_{12} \left(1 - \Gamma_{21}^2 e^{-2\gamma_2 l} \right)}{1 - \Gamma_{21}^2 e^{-2\gamma_2 l}} \tag{2.145}$$

and,

$$T = \frac{b_2}{a_1} = \frac{T_{12} T_{21} e^{-\gamma_2 l}}{1 - \Gamma_{21}^2 e^{-2\gamma_2 l}} \tag{2.146}$$

2.16 Example: Zero-Order Power Propagation Model for Lossy Three-layer Media

The three-layer media is considered a canonical problem in classical electromagnetic textbooks. However, in many textbooks like; Born and Wolf [14], and Macleod [15]; reflectance (and transmittance) is defined as the square of absolute of the electric field reflection (or transmission) coefficient, with the implicit assumption that at least one medium at any interface is lossless[1]. However, when two lossy media are considered with a common boundary, the conventional definition of power reflectance (and transmittance) is not valid.

Consider the zero-order power propagation model in a recently published paper by Sun and Lucyczyn [12] shown in Fig. 2.11, which uses a heuristic approach for computing the reflected and transmitted powers through a planar material (medium) of given thickness l; where, P_i, P_r and P_t

[1]Valid only if total reflectance (or transmittance) are expressed in terms of Fresnel reflection coefficients only, by replacing $\mathcal{T}_0$ with $1 - \mathcal{R}_0$; otherwise, both media must be lossless.

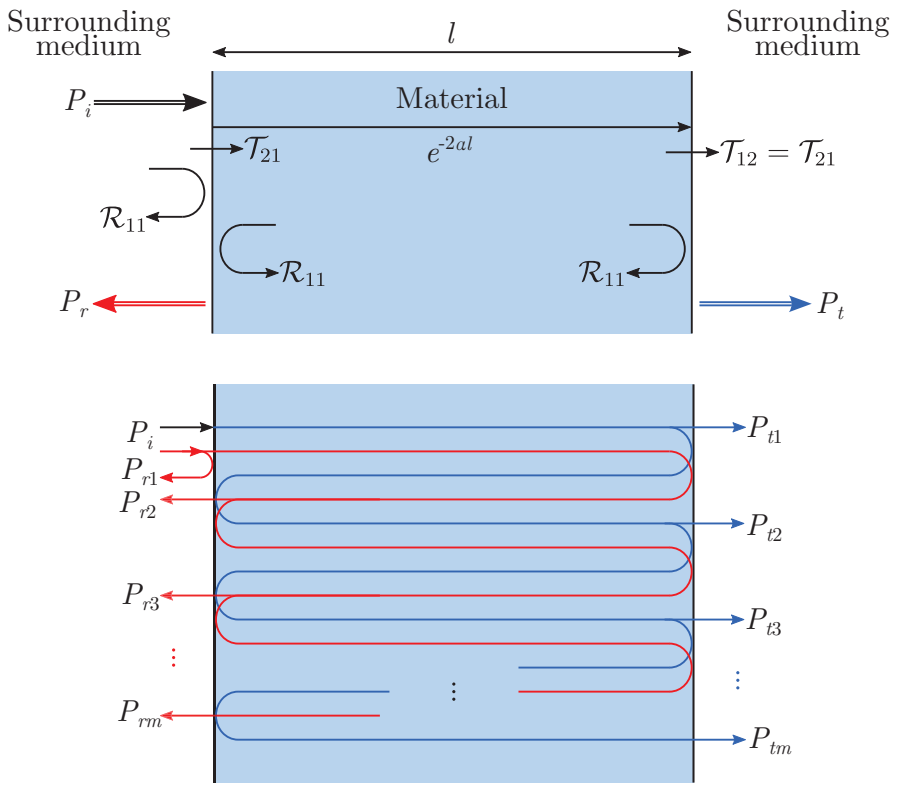


Figure 2.11: Heuristic engineering approach for the power propagation model with an arbitrary lossy surrounding medium: (top) illustrating individual contributions; (bottom) illustrating Fabry-Pérot reflections. A large black arrow shows the total incident power at the left interface. Some of the incident power is reflected back, determined by the reflectance $\mathcal{R}_{11}$, while some of it is transmitted $\mathcal{T}_{21} = 1 - \mathcal{R}_{11}$. The attenuation constant α, which is non-zero for a lossy medium, determines the losses as the incident wave travels from left interface to the right. At the right interface, again some of the power is reflected back inside, while some of it is transmitted. The sum of individual reflections (and transmissions) give the total reflected (and transmitted) power. Figure redrawn from Sun and Lucyszyn [12].

are the total incident, reflected and transmitted powers, respectively. The intrinsic impedance of the surrounding medium and material sample are η_1 and η_2, respectively. Sun and Lucyszyn [12] have assumed the surrounding medium as free space, with the implication that the common reference port impedance is η_0, which is the impedance of free space. Sun and Lucyszyn [12] express the reflectance and transmittance purely in terms of Fresnel reflection coefficients, so their power propagation model is valid if at least one medium is lossless at any boundary, however, if both media at any boundary are lossy then the proposed power propagation model by Sun and Lucyszyn [12] is no longer valid. Based on the concept of power waves, a simple correction is proposed here so that the model is valid for lossy media.

From Sun and Lucyszyn [12], the overall reflectance is given by,

$$\mathcal{R} = \frac{P_r}{P_i} \approx \frac{\sum_{m=1}^{\infty} P_{rm}}{P_i} = \left[1 + \frac{(1-\mathcal{R}_0)^2 \mathcal{T}_0^2}{1-(\mathcal{R}_0\mathcal{T}_0)^2}\right]\mathcal{R}_0 \tag{2.147}$$

where, the overall transmittance is,

$$\mathcal{T} = \frac{P_t}{P_i} \approx \frac{\sum_{m=1}^{\infty} P_{tm}}{P_i} = \frac{(1-\mathcal{R}_0)^2}{1-(\mathcal{R}_0\mathcal{T}_0)^2}\mathcal{T}_0 \tag{2.148}$$

Here, the zero-order approximation for reflectance, with free space as reference, is defined by Sun and Lucyszyn [12] as,

$$\mathcal{R}_0 = |\rho_0|^2 \tag{2.149}$$

where, $\rho_0 = (\eta_2 - \eta_0)/(\eta_2 + \eta_0) = (1-\tilde{n})/(1+\tilde{n})$ is the Fresnel reflection coefficient at the interface between free space and material sample, where free space and material sample are denoted by subscripts 0 and 2, respectively; $\tilde{n} = n - j\kappa$ is the complex refractive index of the material sample; η_2 is the intrinsic impedance of material sample; and η_0 is the intrinsic impedance of free space. If the surrounding medium is lossy then reflectance must be defined in terms of a power reflection coefficient as,

$$\mathcal{R}_{11} = \left|\frac{\eta_2 - \eta_1^*}{\eta_2 + \eta_1}\right|^2 \tag{2.150}$$

Notice that $\mathcal{R}_{11} = \mathcal{R}_0$ if at least medium is lossless. Transmittance is given by,

$$\mathcal{T}_{21} = \left|\left(1 + \frac{\eta_2^*}{\eta_2}\right)\frac{\sqrt{Re\{\eta_1\}}}{\sqrt{Re\{\eta_2\}}}\tau_{21}\right|^2 = \left|\frac{2\sqrt{Re\{\eta_1\}}\sqrt{Re\{\eta_2\}}}{\eta_2 + \eta_1}\right|^2 \tag{2.151}$$

where, $\tau_{21} = 2\eta_2/(\eta_2+\eta_1)$ is the Fresnel transmission coefficient at the left interface; the surrounding medium and material sample are denoted by subscripts 1 and 2, respectively. Using the power wave definition of reflectance and transmittance from (2.150) and (2.151), respectively, (2.147) and (2.148) can now be modified as,

$$\mathcal{R} = \frac{P_r}{P_i} \approx \frac{\sum_{m=1}^{\infty} P_{rm}}{P_i} = \left[1 + \frac{(1-\mathcal{R}_{11})^2 \mathcal{T}_{21}^2}{1-(\mathcal{R}_{11}\mathcal{T}_{21})^2}\right]\mathcal{R}_{11} \tag{2.152}$$

and,

$$\mathcal{T} = \frac{P_t}{P_i} \approx \frac{\sum_{m=1}^{\infty} P_{tm}}{P_i} = \frac{\left(1 - \mathcal{R}_{11}\right)^2}{1 - \left(\mathcal{R}_{11}\mathcal{T}_{21}\right)^2}\mathcal{T}_{21} \tag{2.153}$$

where, $\mathcal{R}_{11}$ and $\mathcal{T}_{21}$ are given by (2.150) and (2.151), respectively. Equations (2.152) and (2.153) can be used to compute reflectance and transmittance for lossy media. The same correction can be applied to any textbook result to get the correct power reflectance and transmittance when considering lossy media.

2.17 Conclusion

The concepts of voltage waves (including travelling waves and pseudo waves), power waves and characteristic impedance in microwave theory have been reviewed. Generalised formulas for n-port conversion between S- and S_p-parameters have been derived from first principles. The cascading condition for interconnecting two-port networks has been discussed with reference to S- and S_p-parameters. Direct conversion formulas for renormalisation of S- and S_p-parameters for two-port networks have also been presented. In addition, formulas for direct interconversion between S, Z, Y, h, ABCD and T parameters of a two-port network with arbitrary reference impedances have been derived. Finally, the concept of S_p-parameters has been applied to two-media and three-media one- and two-port networks to highlight the usefulness of S_p-parameters in computing power when reference port impedances may be complex.

2.18 Acknowledgements

The work presented in this chapter was done under the supervision of Prof. Stepan Lucyszyn, who provided helpful feedback and suggested improvements which were invaluable to the work presented in this chapter.

References

[1] R. B. Marks and D. F. Williams, "A general waveguide circuit theory," *J. Res. Nat. Inst. Stand. Technol.*, vol. 97, no. 5, pp. 533–562, 1992.

[2] D. F. Williams, B. K. Alpert, U. Arz, D. K. Walker, and H. Grabinski, "Causal characteristic impedance of planar transmission lines," *IEEE Trans. Adv. Packag.*, vol. 26, no. 2, pp. 165–171, 2003.

[3] D. Youla, "On scattering matrices normalized to complex port numbers," *Proc. Inst. Radio Engineers*, vol. 49, no. 7, p. 1221, 1961.

[4] K. Kurokawa, "Power waves and the scattering matrix," *IEEE Trans. Microw. Theory Techn.*, vol. 13, pp. 194–202, Mar. 1965.

[5] R. B. Marks, D. F. Williams, and D. Frickey, "Comments on" Conversions between S, Z, Y, h, ABCD, and T parameters which are valid for complex source and load impedances"[with reply]," *IEEE Trans. Microw. Theory Techn.*, vol. 43, no. 4, pp. 914–915, 1995.

[6] D. A. Frickey, "Conversions between S, Z, Y, H, ABCD, and T parameters which are valid for complex source and load impedances," *IEEE Trans. Microw. Theory Techn.*, vol. 42, no. 2, pp. 205–211, 1994.

[7] T. Reveyrand, "Multiport conversions between S, Z, Y, h, ABCD, and T parameters," in *2018 International Workshop on Integrated Nonlinear Microwave and Millimetre-wave Circuits (INMMIC)*, pp. 1–3, IEEE, 2018.

[8] Lucyszyn, *Microwave measurements*, ch. RFIC and MMIC measurement techniques, pp. 217–262. London, U.K.: IET, 3rd ed., Oct. 2007.

[9] A. Cooman, "Conversions between electrical network representations," *arXiv preprint arXiv: 1607.03642*, 2016.

[10] A. Ferrero and M. Pirola, "Generalized mixed-mode S-parameters," *IEEE Trans. Microw. Theory Techn.*, vol. 54, no. 1, pp. 458–463, 2006.

[11] S. Papantonis and S. Lucyszyn, "Lossy spherical cavity resonators for stress-testing arbitrary 3D eigenmode solvers," *PIER*, vol. 151, pp. 151–167, 2015.

[12] J. Sun and S. Lucyszyn, "Extracting complex dielectric properties from reflection-transmission mode spectroscopy," *IEEE Access*, vol. 6, pp. 8302–8321, Mar. 2018.

[13] J. Sun, A. Dawood, W. J. Otter, N. M. Ridler, and S. Lucyszyn, "Microwave characterization of low-loss FDM 3-D printed ABS with dielectric-filled metal-pipe rectangular waveguide spectroscopy," *IEEE Access*, vol. 7, pp. 95455–95486, July 2019.

[14] M. Born and E. Wolf, *Principles of optics: electromagnetic theory of propagation, interference and diffraction of light*. Elsevier, 2013.

[15] A. Macleod, *Thin-film optical filters*. CRC press, 2001.

[16] S. Amakawa, "Scattered reflections on scattering parameters –Demystifying complex-referenced S parameters–," *IEICE Trans. Electron.*, vol. 99, no. 10, pp. 1100–1112, 2016.

[17] S. Lucyszyn, V. Magnier, H. Reader, and I. Robertson, "Ultrawideband measurement of multiple-port MMICs using nonideal test fixtures and a 2-port ANA," *IEE Proc. Science Meas. Techn.*, vol. 139, pp. 235–242, Sept. 1992.

[18] Ideal Coaxial-Rectangular Waveguide Transition (TE10): COAXRWG_TE10. Accessed: 31 Oct. 2019. [Online]. Available: `https://awrcorp.com/download/faq/english/docs/elements/COAXRWG_TE10.htm`.

[19] Why Fifty Ohms? Accessed: 28 Feb. 2020. [Online]. Available: `https://www.microwaves101.com/encyclopedias/why-fifty-ohms`.

[20] Application note – Accurate measurements in almost any impedance environment. Accessed: 13 Mar. 2018. [Online]. Available: `https://dl.cdn-anritsu.com/en-us/test-measurement/files/18s/Application-Note/11410-00284B.pdf`.

Chapter 3

Modelling Lossy Resonators

3.1 Introduction

When THz electromagnetic waves encounter a good conductor most of the energy is reflected while a very small portion of the wave propagates inside the conductor, which quickly decays due to conductive losses. A cavity with metallic walls can trap electromagnetic energy inside it as electromagnetic waves reflect off the metal walls and remain trapped inside for a long time. The electromagnetic energy inside decays over time via conductive losses when electromagnetic fields interact with walls. There is also constructive and destructive interference of waves and the amplitude of waves inside the cavity dramatically increases at certain frequencies. Such frequencies are known as resonant frequencies and the cavity is known as a metal-wall cavity-resonator.

Electromagnetic resonators became a subject of interest in the 1930s when the first metallic waveguides were developed. These waveguides have now been studied for well over a hundred years and they have been extensively used in different electrical applications because of their ability to operate at fixed resonant frequencies. The resonant frequencies depend on the size and shape of the resonator in addition to the dielectric properties of the resonator and the surrounding medium. Traditionally, resonators with metallic walls have been employed to achieve low-losses resulting in high quality factors (Q-factor) at the frequency of operation. The theory for such low-loss cavity resonators is well established and research in this area was mostly confined to studying high Q resonators.

For highly lossy resonators, traditional theoretical techniques such as the perturbation theory and even eigenmode solvers employed by commercial software packages fail to give correct results, as shown by Papantonis and Lucyszyn [1] who studied spherical resonators with conducting walls and developed the theory for exact analytical solution to the lossy spherical resonator problem as the

conducting walls are transformed from PEC to free space [1]. Wolff further presented a generalised analytic solution for three-layer spherical resonator [2]–[3].

When two resonators are brought close together to within a certain distance, they start to interact. This interaction results in the exchange of electromagnetic energy, a phenomenon known as electromagnetic-coupling, resonator-coupling or coupling for short. Coupling results in detuning of the original resonant frequencies and a new set of coupled resonant frequencies arise. At these resonant frequencies, the exchange of electromagnetic energy is strongest. Coupling between two resonators is described by a dimensionless quantity known as a coupling coefficient, which typically varies between 0 and 1. It denotes the amount of electromagnetic energy exchanged between the resonators.

3.2 General Solution of a Symmetric Fabry-Pérot Resonator

A Fabry-Pérot resonator is formed when a medium of finite width is flanked on either sides by different media which is essentially a three-media problem. The Fabry-Pérot resonator is symmetrical if the flanking media have the same material parameters, and asymmetric otherwise. The Fabry-Pérot resonator is able to trap electromagnetic energy inside it due to the partial reflection of electromagnetic waves from resonator boundaries. The reflections are due to material parameter discontinuity at the boundaries. The general form of the solution for a symmetric Fabry-Pérot resonator formed of consecutive planar media is presented here. Consider Fig. 3.1 where a wave is incident on the interface at $z = 0$ and l being the length of the resonator. Under steady-state harmonic excitation, there will be forward and backward electromagnetic plane waves, with As representing the complex amplitude coefficients for the forward waves and Bs representing the backward waves. There are no reflected waves in medium ③, where the reference plane for coefficient $A_③$ is $z = l$ as indicated by the shift $z - l$ while the rest of the coefficients are referenced with respect to the $z = 0$ plane. Boundary conditions at $z = 0$ and at $z = l$ require that the tangential components of electric and magnetic fields be continuous. Application of boundary conditions will result in the following generalised characteristic matrix system for a symmetric Fabry-Pérot resonator, following the development of Chapter 2,

$$\begin{bmatrix} a & a & -b & -b & 0 \\ c & -c & -d & d & 0 \\ 0 & 0 & be^{-\varphi} & be^{\varphi} & -a \\ 0 & 0 & de^{-\varphi} & -de^{\varphi} & -c \end{bmatrix} \begin{bmatrix} A_① \\ B_① \\ A_② \\ B_② \\ A_③ \end{bmatrix} = \begin{bmatrix} 0 \\ 0 \\ 0 \\ 0 \end{bmatrix} \tag{3.1}$$

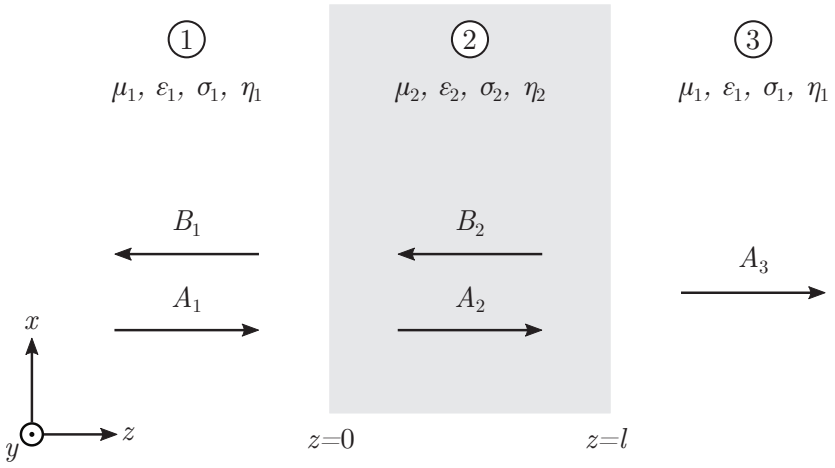


Figure 3.1: Incident and reflected fields in three-layer media. As and Bs are, respectively, reflected and transmitted fields in a given medium. Here, the reference plane for fields with coefficient A_3 is the plane $z = l$, while all other fields are referenced with respect to the $z = 0$ plane. There are no reflected waves in medium ③.

where, the coefficients $B_①$, $A_②$, $B_②$ and $A_③$ can be obtained in terms of $A_①$ as,

$$\frac{B_①}{A_①} = \frac{\left(1 - e^{-2\varphi}\right)(1-\zeta)(1+\zeta)}{(1+\zeta)^2 - e^{-2\varphi}(1-\zeta)^2} \tag{3.2}$$

$$\frac{A_②}{A_①} = \frac{-2\varsigma(1+\zeta)}{(1+\zeta)^2 - e^{-2\varphi}(1-\zeta)^2} \tag{3.3}$$

$$\frac{B_②}{A_①} = \frac{-2\varsigma e^{-2\varphi}(1-\zeta)}{(1+\zeta)^2 - e^{-2\varphi}(1-\zeta)^2} \tag{3.4}$$

$$\frac{A_③}{A_①} = \frac{4\zeta e^{-\varphi}}{(1+\zeta)^2 - e^{-2\varphi}(1-\zeta)^2} \tag{3.5}$$

where φ is the complex phase term and,

$$\zeta = \frac{ad}{bc} \tag{3.6}$$

with,

$$\varsigma = \frac{a}{b} \tag{3.7}$$

The S-parameters of the Fabry-Pérot resonator can be defined as,

$$S_{11} \equiv \left.\frac{B_①}{A_①}\right|_{B_③=0} \rightarrow B_① \quad \text{with} \quad A_① = 1 \tag{3.8}$$

and,

$$S_{21} \equiv \left.\frac{A_③}{A_①}\right|_{B_③=0} \rightarrow A_③ \quad \text{with} \quad A_① = 1 \tag{3.9}$$

Lossy resonators are characterised by their complex natural frequency [1],

$$\tilde{f}_0 = f_0^{'} + j f_0^{''} = \frac{\tilde{\omega}_0}{2\pi} \tag{3.10}$$

where, f_0' is the damped or undriven resonant frequency, also called natural frequency, and f_0'' denotes loss, where ω_0 is the angular complex eigenfrequency. For ideal resonator without any losses, $f_0'' = 0$ and $\tilde{f}_0 = f_0'$. The unloaded Q-factor is defined as,

$$Q_u(\omega, t) = \omega \frac{W(t)}{P_{loss}(t)} \tag{3.11}$$

where, the Q-factor for lossy resonators is given by [1],

$$Q_u(|\omega_0|) = \frac{|\tilde{\omega}_0|}{2\omega_0''} = \frac{|\tilde{f}_0|}{2f_0''} \tag{3.12}$$

or,

$$Q_u(\omega_0') = \frac{\omega_0^{'}}{2\omega_0''} = \frac{f_0^{'}}{2f_0''} \tag{3.13}$$

where, (3.12) is normally used for driven or steady-state response, while (3.13) is usually used for undriven or eigenmode response.

The complex natural frequency or the eigenfrequency response can be obtained by setting $A_① = 0$ in (3.2), provided $B_① \neq 0$, to obtain,

$$(1+\zeta)^2 - e^{-2\varphi}(1-\zeta)^2 = 0 \tag{3.14}$$

The solution of (3.14) results in an infinite number of solutions which are either designated as even or odd modes depending on corresponding symmetry of the electric field. The respective even and odd modes can be obtained by solving the following equations for complex eigenfrequencies,

$$(1+\zeta) + e^{-\varphi}(1-\zeta) = 0 \quad \text{Even modes} \tag{3.15}$$

$$(1+\zeta) - e^{-\varphi}(1-\zeta) = 0 \quad \text{Odd modes} \tag{3.16}$$

The coefficients for eigenmodes are obtained by setting $A_① = 0$ in (3.1) and solving for $A_②$, $B_②$ and $A_③$ in terms of $B_①$, where $B_①$ is normally set to unity.

$$A_② = -\frac{(1-\zeta)}{2\frac{d}{c}} B_① \tag{3.17}$$

$$B_② = \frac{(1+\zeta)}{2\frac{d}{c}} B_① \tag{3.18}$$

$$A_③ = \frac{(1+\zeta) - e^{-2\varphi}(1-\zeta)}{2\frac{d}{c}e^{-\varphi}} B_① \tag{3.19}$$

The relationships presented in this section are generalised and applicable to any Fabry-Pérot resonator problem, resulting in a matrix system similar to (3.1).

3.3 Eigenvalue Solution of a Lossy Fabry-Pérot Resonator

A Fabry-Pérot resonator formed from layers of planar semi-finite media can be treated as a transmission-reflection problem. The solution assumes plane waves incident normal to the interface, as shown in Fig. 3.1. It is assumed that the resonator walls extend to infinity and there are no reflected waves in the wall medium. The simplest case of a plane wave normally incident at the interface is considered here, which is essentially a 1-D problem. The solutions for TE or TM incidence can be easily obtained from the field expressions for these respective cases. Writing the expressions for incident and reflected electric and magnetic fields,

$$E_{x①} = A_① e^{-\gamma_① z} + B_① e^{\gamma_① z} \tag{3.20}$$

$$H_{y①} = \frac{1}{\eta_①}\left(A_① e^{-\gamma_① z} - B_① e^{\gamma_① z}\right) \tag{3.21}$$

$$E_{x②} = A_② e^{-\gamma_② z} + B_② e^{\gamma_② z} \tag{3.22}$$

$$H_{y②} = \frac{1}{\eta_②}\left(A_② e^{-\gamma_② z} - B_② e^{\gamma_② z}\right) \tag{3.23}$$

$$E_{x③} = A_③ e^{-\gamma_③ (z-l)} \tag{3.24}$$

$$H_{y③} = \frac{1}{\eta_③} A_③ e^{-\gamma_③ (z-l)} \tag{3.25}$$

where the propagation constant is given by,

$$\gamma_i = j\omega\sqrt{\tilde{\mu}_{effi}\tilde{\varepsilon}_{effi}} \quad \text{with} \quad i = ①, ②, ③ \tag{3.26}$$

with, $\gamma_③ = \gamma_①$, ω is the angular frequency in radian/s, $\tilde{\mu}_{effi}$ is the effective complex permeability of medium i which is set as the permeability of free space (μ_0) here, $\tilde{\varepsilon}_{effi}$ is the effective complex permittivity of medium i given by,

$$\tilde{\varepsilon}_{effi} = \varepsilon_0 \tilde{\varepsilon}_{reffi} = \varepsilon_0(\varepsilon_{ri} - j\frac{\sigma_i}{\omega\varepsilon_0}) \tag{3.27}$$

where, ε_0 is the dielectric constant in free space, ε_{ri} is the dielectric constant of medium i, σ_i is the DC bulk conductivity in S/m of medium i, and η_i is the intrinsic impedance of medium i in Ω.

Boundary conditions require tangential components of electric and magnetic fields to be continuous across the interface at $z = 0$ and at $z = l$. Setting $E_{x①}(z = 0) = E_{x②}(z = 0)$, $H_{y①}(z = 0) = H_{y②}(z = 0)$, $E_{x②}(z = l) = E_{x③}(z = l)$ and $H_{y②}(z = l) = H_{y③}(z = l)$, the following

characteristic matrix system is obtained,

$$\begin{bmatrix} 1 & 1 & -1 & -1 & 0 \\ \eta_{②} & -\eta_{②} & -\eta_{①} & \eta_{①} & 0 \\ 0 & 0 & e^{-\gamma_{②}l} & e^{\gamma_{②}l} & -1 \\ 0 & 0 & \eta_{①}e^{-\gamma_{②}l} & -\eta_{①}e^{\gamma_{②}l} & -\eta_{②} \end{bmatrix} \begin{bmatrix} A_{①} \\ B_{①} \\ A_{②} \\ B_{②} \\ B_{③} \end{bmatrix} = \begin{bmatrix} 0 \\ 0 \\ 0 \\ 0 \end{bmatrix} \tag{3.28}$$

Making use of (3.1)-(3.2) and setting $A_{①}$ equal to unity, the S-parameters are obtained as,

$$S_{11} = \frac{\left(1 - e^{-2\gamma_{②}l}\right)\left(1 - \frac{\eta_{②}}{\eta_{②}}\right)\left(1 + \frac{\eta_{②}}{\eta_{②}}\right)}{\left(1 + \frac{\eta_{②}}{\eta_{②}}\right)^2 - e^{-2\gamma_{②}l}\left(1 - \frac{\eta_{②}}{\eta_{②}}\right)^2} \tag{3.29}$$

$$S_{21} = \frac{4\frac{\eta_{②}}{\eta_{②}}e^{-\gamma_{②}l}}{\left(1 + \frac{\eta_{②}}{\eta_{②}}\right)^2 - e^{-2\gamma_{②}l}\left(1 - \frac{\eta_{②}}{\eta_{②}}\right)^2} \tag{3.30}$$

The complex eigenfrequencies of the resonator can be obtained by setting the denominator of S_{11} equal to zero given by,

$$\left(1 + \frac{\eta_{①}}{\eta_{②}}\right)^2 - e^{-2\gamma_{②}l}\left(1 - \frac{\eta_{①}}{\eta_{②}}\right)^2 = 0 \tag{3.31}$$

From this, following equations can be obtained for even and odd modes,

$$\left(1 + \frac{\eta_{①}}{\eta_{②}}\right) + e^{-\gamma_{②}l}\left(1 - \frac{\eta_{①}}{\eta_{②}}\right) = 0 \quad \text{Even modes} \tag{3.32}$$

$$\left(1 + \frac{\eta_{①}}{\eta_{②}}\right) - e^{-\gamma_{②}l}\left(1 - \frac{\eta_{①}}{\eta_{②}}\right) = 0 \quad \text{Odd modes} \tag{3.33}$$

3.3.1 Example: Lossy Three-Media Fabry-Pérot Resonator

A lossy 1-D Fabry-Pérot resonator made of consecutive, semi-infinite layers of planar media is considered as shown in Fig. 3.1. Here, $l = 300$ μm, $\varepsilon_{r①} = \varepsilon_{r①} = \varepsilon_{r③} = 1$ and $\sigma_{②} = 0$. Losses were introduced by varying the value of bulk DC conductivity of the surrounding media ① and ③. Since, the resonator itself is lossless and there are no conductive or polarisation losses inside the resonator medium ②, the losses are entirely due to radiation or EM energy from the resonator boundaries after partial reflection. The eigenfrequencies of this 1-D Fabry-Pérot resonator were obtained by numerically solving (3.32) and (3.32), using the MATLAB function *'vpasolve'* [4]. As resonator-wall bulk DC conductivity $\sigma_{①}$ (with $\sigma_{③} = \sigma_{①}$) is varied over the range $0 < \sigma_{①} < \infty$, the resulting complex eigenfrequencies are plotted in Fig. 3.2. A very high value of bulk DC conductivity effectively mimics a PEC medium with the resonator, being able to retain all of the energy inside it, acting like an ideal resonator. It can be generally expected that as the conductivity of the surrounding media

is reduced, resonator losses will increase. An interesting result from the study of lossy spherical resonators by Papantonis and Lucyszyn [1] was that as the bulk DC conductivity (σ_c)of spherical resonator walls was reduced, the resulting value of f_0' generally decreased in a monotonic manner; but around a value of $\sigma_c = 80$ S/m, f_0' suddenly increased before again decreasing monotonically.

The resonant frequency of the m^{th} mode of an ideal resonator ($\sigma_① \to \infty$) is given by,

$$f_m = \frac{mv}{2l} \tag{3.34}$$

where, $f_I = c/2l = 0.4997$ THz is the fundamental resonant frequency of the ideal resonator with mode number $m = 1$ and speed of light in resonator $v = c/\sqrt{\varepsilon_{r②}} = c$; c being the speed of light in free space and $\varepsilon_{r②} = 1$.

The solution of the fundamental mode from (3.32) and *COMSOL Multiphysics*® eigenmode solver are shown in Fig.3.2(a). It can be observed from Fig.3.2(a) that *COMSOL Multiphysics*® eigenmode solver does not converge to the correct solution when $\sigma_① < 10$ S/m. An interesting observation is that close to 1 S/m, the real part of the complex eigenfrquency goes to zero, i.e., $f_0' \to 0$, which indicates transformation of the fundamental mode into, essentially, a static mode. Figure 3.2(b) shows the plot of the next higher order mode with $m = 2$, which tends to transform into the fundamental mode as $\sigma_① \to 0$. A plot of the first five modes in Fig. 3.2(c) shows the same trend with these modes. These results are consistent with the results obtained by Wolff for lossy spherical resonators [2]–[3].

Figure 3.3(a) shows a comparison of theoretical unloaded Q-factor and that obtained from the *COMSOL Multiphysics*® eigenmode solver. The disagreement between theoretical and numerical results at higher values of $\sigma_①$ is possibly due to the sensitive nature of (3.13) with $f_0'' \to 0$ in the denominator as $\sigma_① \to \infty$. Figure 3.4 shows a plot of S-parameters based on the conventional pseudo wave and power wave definitions, respectively, published in the open literature [5]–[6]. Here, the conductivity of the resonator walls was set to $\sigma_① = \sigma_③ = 100$ S/m. The reference impedance for S-parameters in this case was $\eta_①$ which is complex, therefore, energy conservation does not hold ($|S_{11}|^2 + |S_{21}|^2 \neq 1$). However, with the power scattering (Sp-) parameters, and 50 Ω referenced S-parameters, energy conservation is satisfied, (i.e., $|S_{p11}|^2 + |S_{p21}|^2 = 1$).

Figure 3.5 shows a plot of return loss ($20\log_{10}|S_{11}|$) in the complex frequency plane with $\sigma_① = 100$ S/m, representing a fairly lossy resonator, where the shift in peaks of S_{21} and dips of S_{11} can be clearly seen. The poles of return loss zero indicated by red dots are the complex eigenfrequencies, while zeros indicated by blue dots correspond to the ideal modes. Figure 3.6 shows the plot of insertion loss ($20\log_{10}|S_{21}|$) as a function of bulk DC conductivity of resonator walls $\sigma_①$. The peaks of transmission are indicated by the resonances of the cavity resonator, which become

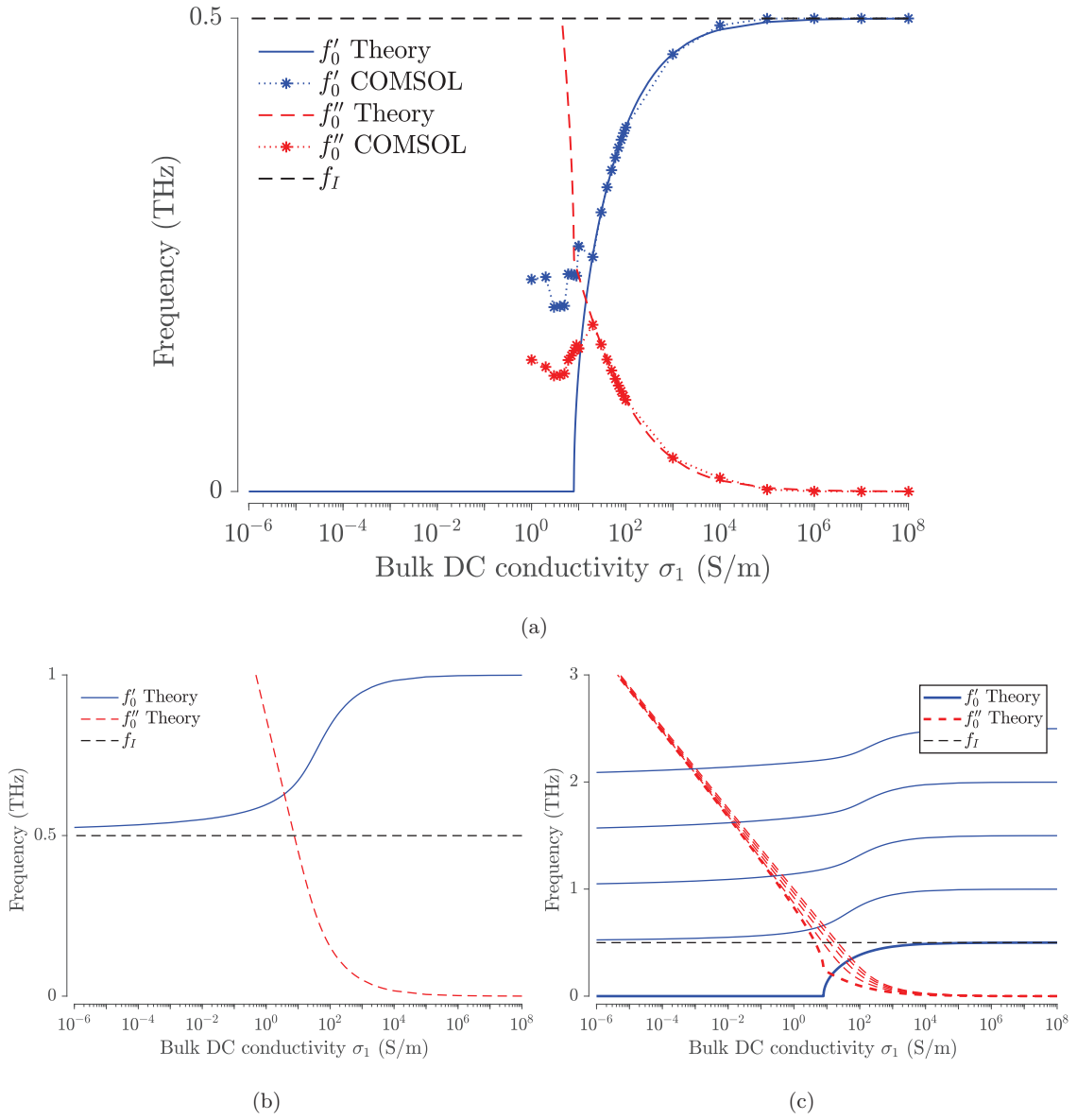


Figure 3.2: Plot of complex eigenfrequency components f_0' and f_0'' as a function of bulk DC conductivity of resonator walls $\sigma_①$: (a) comparison of the fundamental mode obtained from theory and *COMSOL Multiphysics*® eigenmode solver, which shows that the *COMSOL Multiphysics*® eigenmode solver does not converge to correct solution for $\sigma_① < 30$ S/m as the fundamental transforms into static mode; (b) transformation of next higher order mode with $m = 2$ into fundamental mode with $m = 1$ as the resonator becomes very lossy; and (c) first five modes with fundamental mode indicated by thick line plots. The higher order modes tend to transform into the next lower mode as the resonator becomes very lossy.

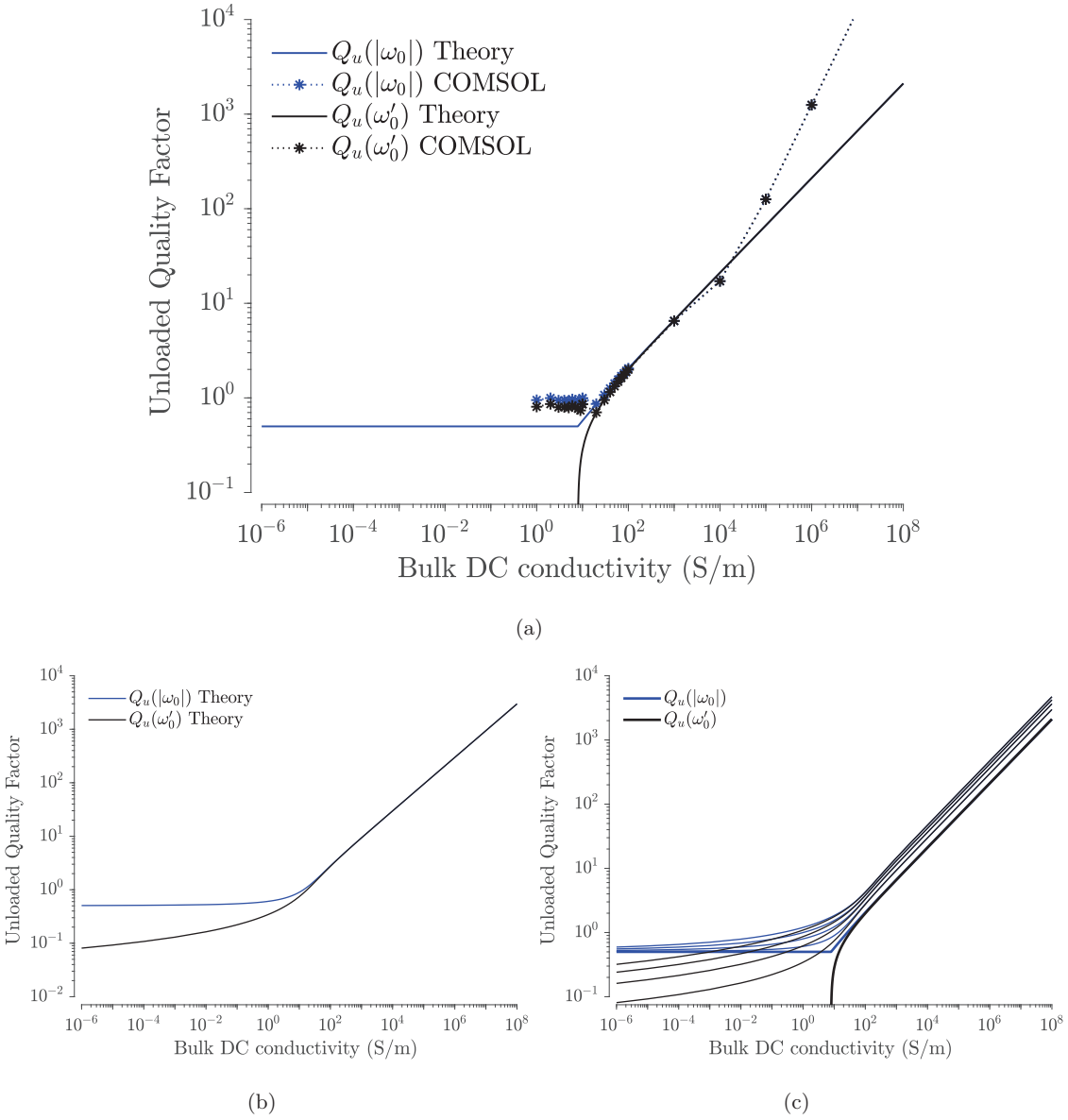


Figure 3.3: Plot of unloaded Q-factors $Q_u(|\omega_0|)$ and $Q_u(\omega_0')$ against bulk DC conductivity of resonator walls $\sigma_{①}$: (a) fundamental mode obtained from theory and *COMSOL Multiphysics*® eigenmode solver, which shows that the *COMSOL Multiphysics*® eigenmode solver does not converge to correct solution for $\sigma_{①} < 30$ S/m and also displays a disagreement with theory for $\sigma_{①} > 10^4$ S/m due to sensitive nature of quality factor relationship given by (3.12) and (3.13); (b) next higher order mode with $m = 2$ suggesting that (3.13) is more useful for computing quality factor; and (c) first five modes with fundamental mode indicated by thick line plots.

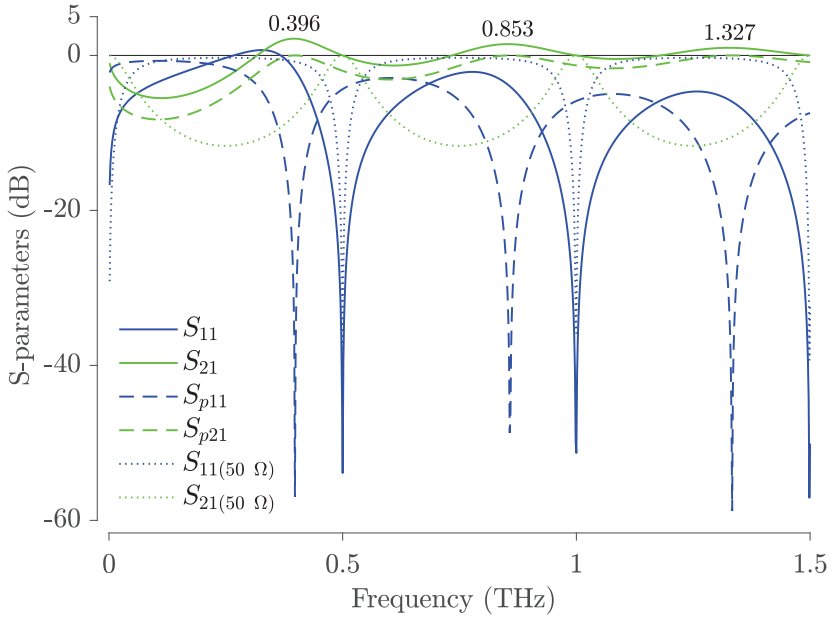


Figure 3.4: Plot of S-parameters of 1-D Fabry-Pérot resonator with $\sigma_{①} = \sigma_{③} = 100$ S/m based on the conventional and power wave definitions, respectively. With conventional complex-referenced S-parameters, the insertion and return loss exceed 0 dB, however, the S_p-parameter response shows that the total energy is conserved. Frequencies at S-parameter resonant peaks are also indicated.

sharper as radiative losses from walls are reduced. A line scatter plot of complex eigenfrequencies with varying DC bulk conductivity of walls $\sigma_{①}$ is shown in Fig. 3.7. The complex eigenfrequencies of the first three modes obtained from *COMSOL Multiphysics*® eigenmode solver are summarised in Table 3.1.

3.3.2 Example: The 'Inverse' Three-Media Fabry-Pérot Resonator

It is interesting to consider the case of 'inverse' Fabry-Pérot resonator by interchanging the material parameters of walls and Fabry-Pérot resonator medium. The length of resonator is kept $l = 300$ μm while $\sigma_{①} = \sigma_{③} = 0$ is kept constant and $\sigma_{②}$ is varied over the range $0 < \sigma_{②} < \infty$. Here, losses are not only due to radiation of EM energy from resonator walls but also due to the conduction losses inside the resonator. There is an optimal value of conductivity $\sigma_{②} = 30$ S/m at which the resonator Q-factor is highest. Figure 3.8 shows a comparison of complex eigenfrequencies obtained from theory by numerically solving (3.32) and (3.33); and those obtained from *COMSOL Multiphysics*® eigenmode solver. It can be seen in Fig. 3.8(a) that as the bulk DC conductivity $\sigma_{②} < 10$ *COMSOL Multiphysics*® eigenmode solver tends to converge to next higher order mode with $m = 2$ and is no longer able to solve for a stable solution for $m = 1$. The Q-factors of the inverse Fabry-Pérot

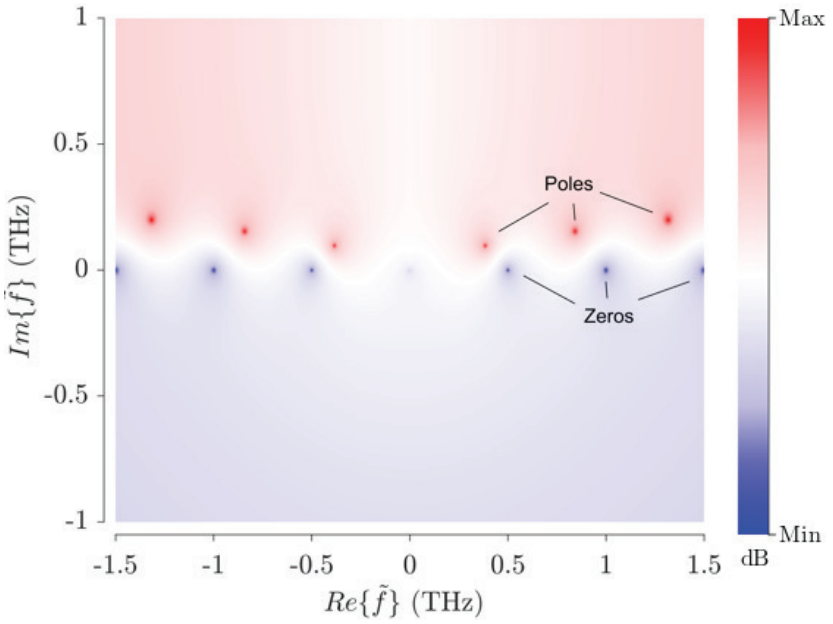


Figure 3.5: Plot of return loss ($20\log_{10}|S_{11}|$) in the complex frequency plane with $\sigma_{①} = 100$ S/m. The poles of return loss zero indicated by red dots are the complex eigenfrequencies, while zeros indicated by blue dots correspond to the spectral location of ideal modes on the $Im\{\tilde{f}\} = 0$ line. Notice, however, that the resonator medium itself is lossless; indicated by the close proximity of zeros to the $Im\{\tilde{f}\} = 0$ line.

Table 3.1: Comparison of numerically computed eigenfrequencies of the lossy 1-D resonator with ideal case. Resonator length is $l = 300$ μm with bulk DC conductivity of resonator wall being 100 S/m. The computed absolute value of complex eigenfrequency $|\tilde{f}_0|$ corresponds to the spectral location of peaks of S_{21} in Fig.3.4. The ideal response corresponds to the spectral location of dips of S_{11} in Fig.3.4.

m	Ideal [THz]	Eigenfrequency ($\tilde{f}_0$) [THz]	$\lvert\tilde{f}_0\rvert$ [THz]	$Q_u(\lvert\omega_0\rvert)$	$Q_u(\omega_0')$
1	0.4997	$0.3844 + j0.0966$	0.396	2.052	1.988
2	0.9995	$0.8407 + j0.1528$	0.855	2.796	2.751
3	1.5001	$1.311 + j0.1946$	1.325	3.405	3.369

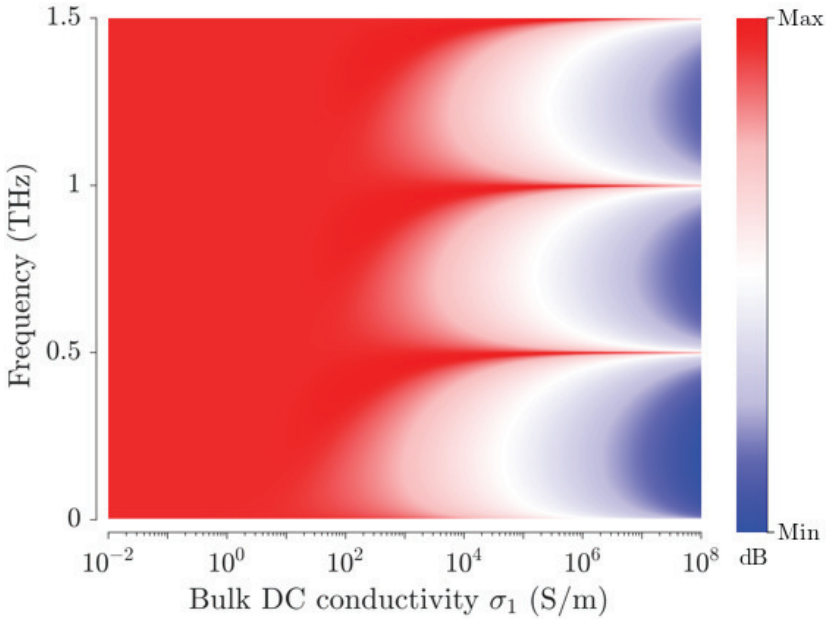


Figure 3.6: Plot of insertion loss ($20\log_{10}|S_{21}|$) as a function of bulk DC conductivity. A decrease in Q-factor can be observed from the broadening of resonances as $\sigma_① \to 0$; and convergence of resonances, at return loss zero frequencies, as $\sigma_① \to \infty$.

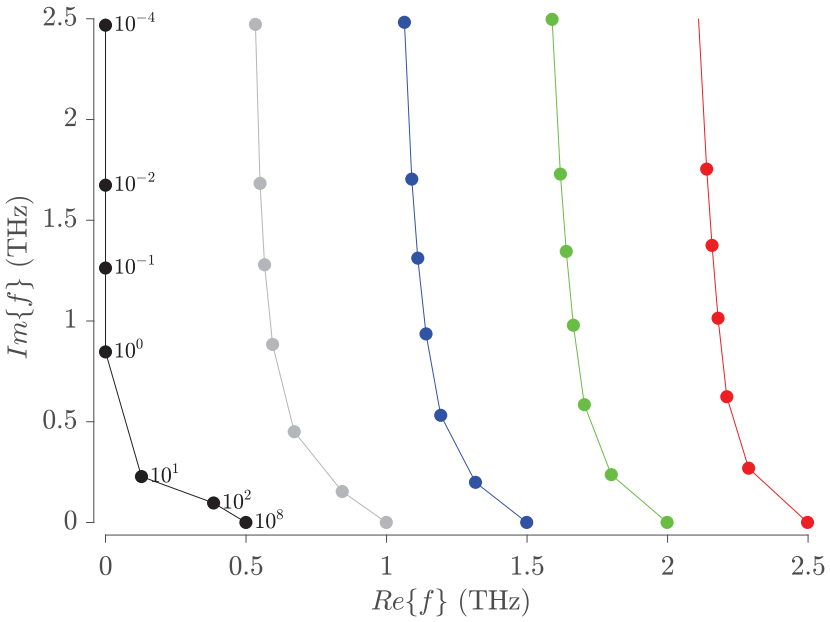


Figure 3.7: Visual summary of the response of the lossy Fabry-Pérot resonator with a line scatter plot of the complex eigenfrequencies in the complex frequency plane with selected spot values of bulk DC conductivity. The fundamental mode is indicated with spot values of bulk DC conductivity. The higher order modes tend to transform into the next lower mode as the resonator becomes lossy.

resonator are plotted in Fig. 3.9. The S- and S_p-parameters of the inverse Fabry-Pérot resonator are plotted in Fig. 3.10 at $\sigma_{②} = 20$ S/m with transmission being heavily damped. Figure 3.11 shows the plot of return loss ($20\log_{10}|S_{11}|$) of the inverse Fabry-Pérot resonator in the complex frequency plane with $\sigma_{②} = 20$ S/m. Poles indicated by red dots are the complex eigenfrequencies while zeros denoted by blue dots correspond to ideal modes.

3.4 Conclusion

Lossy 1-D cavity resonators have been studied by varying the DC bulk conductivity of wall media in the limit $0 < \sigma_0 < \infty$. In the limit $\sigma_0 \to 0$, modes degrade to the next lower order mode while the fundamental mode transforms into static mode. In the limit $\sigma_0 \to \infty$, modes tend to ideal resonant frequencies. The lossy inverse resonator was also analysed. The inverse lossy resonator not only included lossy from walls but the resonator medium itself was lossy, with the quality factor reaching a maximum for a certain value of bulk DC conductivity.

3.5 Acknowledgements

The work presented in this chapter was done under the supervision of Prof. Stepan Lucyszyn and is based on the original work by Papantonis and Lucyszyn [1] on lossy spherical resonators.

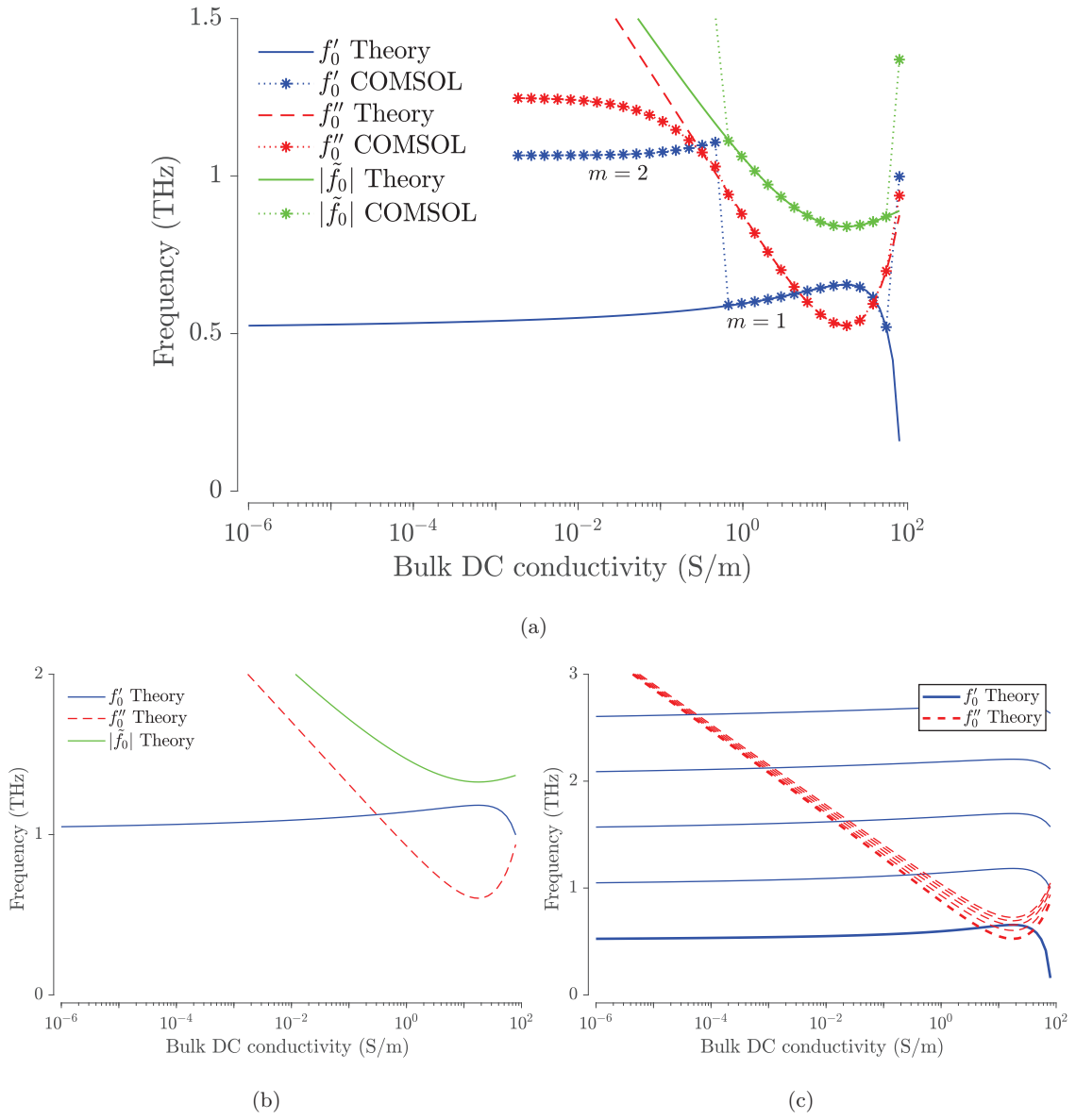


Figure 3.8: Plot of complex eigenfrequency components f_0' and f_0'' as a function of bulk DC conductivity of resonator $\sigma_{②}$: (a) comparison of fundamental mode obtained from theory and *COMSOL Multiphysics*® eigenmode solver showing the limitation of the *COMSOL Multiphysics*® eigenmode solver to give correct solution only for a certain range of values of $\sigma_{②}$. Furthermore, the solution for fundamental mode by the *COMSOL Multiphysics*® eigenmode solver incorrectly tries to converge to next higher mode with $m = 2$. (b) Next higher order mode with $m = 2$; and (c) first five modes with fundamental mode indicated by thick line plots.

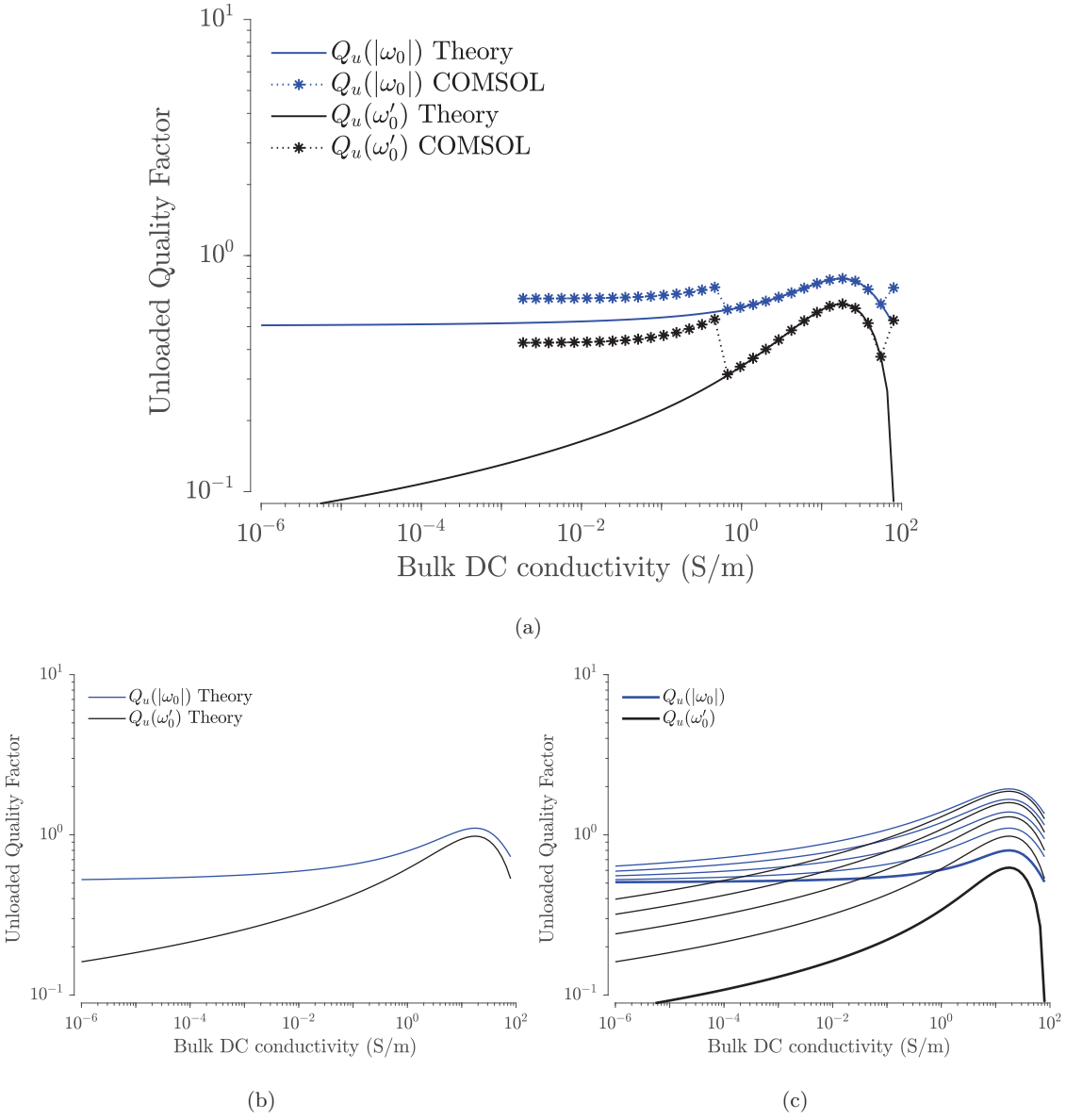


Figure 3.9: Plot of unloaded Q-factors $Q_u(|\omega_0|)$ and $Q_u(\omega_0')$ against bulk DC conductivity of resonator walls $\sigma_{①}$: (a) fundamental mode obtained from theory and *COMSOL Multiphysics*® eigenmode solver, which shows that the *COMSOL Multiphysics*® eigenmode solver does not converge to correct solution for $\sigma_{①} < 30$ S/m and also displays a disagreement with theory for $\sigma_{①} > 10^4$ S/m due to sensitive nature of quality factor relationship given by (3.12) and (3.13); (b) next higher order mode with $m = 2$ suggesting that (3.13) is more useful for computing quality factor; and (c) first five modes with fundamental mode indicated by thick line plots.

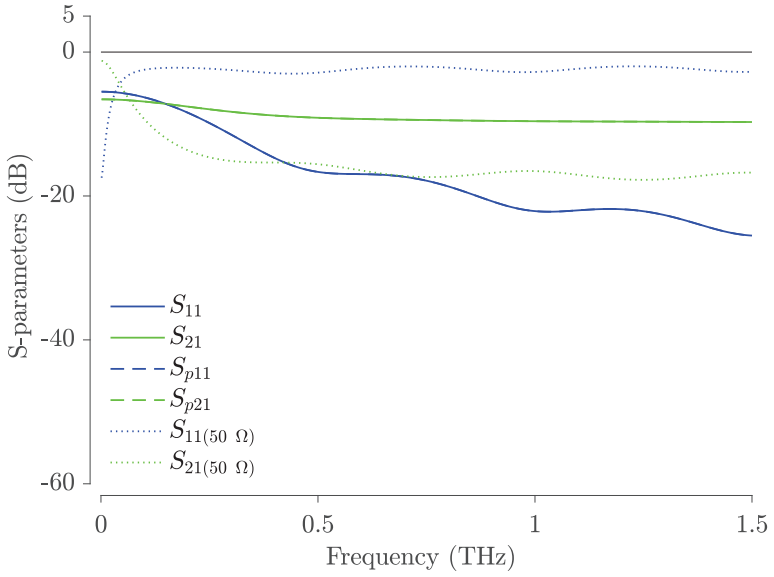


Figure 3.10: Plot of S-parameters of the inverse Fabry-Pérot resonator with $\sigma_{②} = 20$ S/m based on the conventional and power wave definitions, respectively. Due to the resonator medium itself being lossy and dominant, the S-parameter response shows a broadening of resonances. The resonator almost acts like an absorber at higher frequencies, with return loss less than -20 dB and insertion loss close to 10 dB at 1.5 THz.

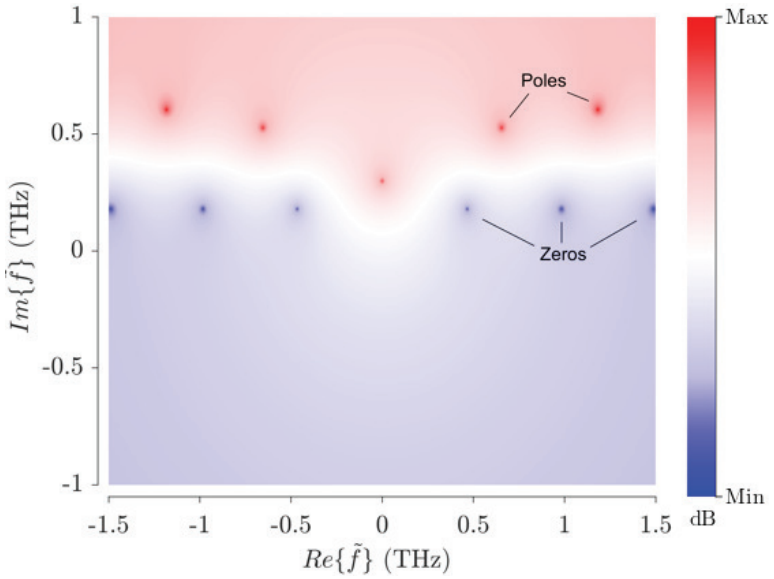


Figure 3.11: Plot of return loss ($20\log_{10}|S_{11}|$) in the complex frequency plane with $\sigma_{①} = 20$ S/m. The poles of return loss zero indicated by red dots are the complex eigenfrequencies, while zeros indicated by blue dots correspond to the spectral location of ideal modes on the $Im\{\tilde{f}\} = 0$ line. The shift of zeros well above the $Im\{\tilde{f}\} = 0$ line indicates the resonator medium is also lossy.

References

[1] S. Papantonis and S. Lucyszyn, "Lossy spherical cavity resonators for stress-testing arbitrary 3D eigenmode solvers," *PIER*, vol. 151, pp. 151–167, 2015.

[2] I. Wolff, "The influence of dielectric and conductor losses on the properties of spherical resonators," in *Proc. IEEE MTT-S Int. Microw. Symp. (IMS)*, pp. 1–4, May 2016.

[3] I. Wolff, "Mode conversion processes in multilayer spherical resonators," in *Proc. 48th Euro. Microw. Conf. (EuMC)*, pp. 1501–1504, Sept. 2018.

[4] MATLAB Functions. Accessed: ov. 13, 2019. [Online]. Available: `https://uk.mathworks.com/help/matlab/functions.html`.

[5] D. Youla, "On scattering matrices normalized to complex port numbers," *Proc. Inst. Radio Engineers*, vol. 49, no. 7, p. 1221, 1961.

[6] R. B. Marks and D. F. Williams, "A general waveguide circuit theory," *J. Res. Nat. Inst. Stand. Technol.*, vol. 97, no. 5, pp. 533–562, 1992.

Chapter 4

Excitation of 'Open-Box' Modes in FDM 3-D Printed Dielectric-Filled Metal-Pipe Rectangular Waveguides

4.1 Introduction

Microwave material characterisation techniques involve a dielectric sample of unknown material parameters and known dimensions, usually placed in an air-filled waveguide. The dielectric sample essentially acts like a Fabry-Pérot resonator. The S-parameters response of the dielectric sample are then compared with the theoretical ideal response of a known material of same dimensions to compute the material properties of the unknown sample.

In a recently published paper by Sun *et al.* [1], a new graphical technique, originally introduced by Sun and Lucyszyn [2], was used to extract the complex dielectric properties of an fused deposition modelling (FDM) 3-D printed acrylonitrile butadiene-styrene (ABS) sample, under noisy measurement conditions. The sample under test, of known dimensions, was placed in a WR-90 standard metal-pipe rectangular waveguide (MPRWG) operating at X-band, and S-parameters of the experimental set-up were measured using the thru-reflect-line (TRL) calibration technique. A dielectric sample placed in an air-filled MPRWG essentially behaves as a Fabry-Pérot resonator. The measured response included a Fabry-Pérot resonance at return loss zero at X-band [2].

Sun *et al.* [1] showed that the modelled S-parameters, of the dielectric-filled section of the MPRWG, can be fitted to the measured S-parameters at the Fabry-Pérot resonance frequency to predict the dielectric constant and loss tangent of the sample under test, at the Fabry-Pérot resonance frequency only. According to Sun *et al.* [1], the spectral location of the return loss zero is

very sensitive to the dielectric constant but not so to the loss tangent; on the other hand, the peak value of insertion loss is very sensitive to loss tangent but not so to the dielectric constant. Sun *et al.* [1] 'extracted' the values of dielectric constant and loss tangent by visually fitting the modelled return and insertion loss, to the measured return and insertion loss, respectively. The value of dielectric constant was varied so that the modelled return loss zero would occur at the location of measured return loss zero. Similarly, the value of loss tangent was varied so that the peak values of modelled and measured insertion loss would coincide. Sun *et al.* [1] called this "the Fabry-Pérot resonance modelling" technique for extraction of dielectric properties of a sample under test.

Sun *et al.* [1] used two similar FDM 3-D printed samples, which they called Sample #1 and #2. Several modelling approaches were used by Sun *et al.* [1] to extract the dielectric properties of their samples, using the Fabry-Pérot resonance modelling technique, at the Fabry-Pérot resonance frequency. These modelling techniques included: (i) accurate analytical variational modelling (designated M1); (ii) analytical text book modelling (M2); (iii) MPRWG and RLC equivalent-circuit modelling (M3 and M4); and (iv) numerical finite-element modelling (M5).

In addition to the expected driven Fabry-Pérot resonance, Sun *et al.* [1] also observed spurious resonances in the measured S-parameter response of their dielectric samples, when placed in MPRWG. They called these resonances, the 'open-box' modes of the dielectric sample under test [1].

In this chapter, analytical field-based and numerical finite-element approaches used by Sun *et al.* [1] for modelling S-parameters will be presented. Also, Q-factor calculations of dielectric-filled MPRWG from field-based integrals using analytical and numerical methods by Sun *et al.* [1] will also be presented. After that, numerical, as well as, rigorous analytical analysis of the open-box mode resonances will be presented with reference to the published work by Sun *et al.* [1]. Additionally, with numerical methods, a technique for exciting open-box modes by defining an in-homogeneous and anisotropic permittivity tensor will be presented.

4.2 Analytical Variational Modelling (M1)

In any medium (unbound, transmission line or waveguide), the generic complex propagation constant $\gamma = \alpha + j\beta$, where α is the attenuation constant and β is the phase constant. These constants can be accurately calculated for a dielectric-filled MPRWG using the *variational* method described in detail by Collin [3] for all transverse electric $\mathrm{TE_{mn}}$ modes; given here for just the $\mathrm{TE_{m0}}$ modes [1], [4],

$$\gamma_{m0}^2 = \gamma_g^2 + \frac{2}{\gamma_s b}\left[\gamma_{ud}^2 + \left(\frac{2b}{a}\right)\gamma_{cm0}^2\right] \tag{4.1}$$

With the internal waveguide walls made from a perfect electrical conductor (PEC), i.e. with

$\sigma \to \infty$, the waveguide propagation constant γ_g is related to the unbound dielectric γ_{ud} and cut-off γ_{cm0} propagation constants as [1],

$$\gamma_g^2 = \gamma_{ud}^2 - \gamma_{cm0}^2 \tag{4.2}$$

$$\gamma_{ud} = jk_{ud} \equiv j\beta_0\tilde{n} \quad \text{and} \quad \gamma_{cm0} = jk_{cm0} \equiv j\beta_{cm0} \tag{4.3}$$

All variables have their usual meanings: k_{ud} is the complex wavenumber within an unbound dielectric; $\beta_0 = \omega/c$ is the phase constant of free space; $\omega = 2\pi f$ is the angular frequency of excitation and f is the associated excitation frequency; $c = 1/\sqrt{\mu_0\varepsilon_0}$ is the speed of light in free space, μ_0 and ε_0 are the permeability and permittivity of free space, respectively; the complex refractive index $\tilde{n} = \sqrt{\tilde{\mu}_r\tilde{\varepsilon}_{reff}}$ and loss tangent $\tan\delta = Im\{\tilde{n}^2\}/Re\{\tilde{n}^2\}$; $\tilde{\mu}_r = \mu_r' - j\mu_r''$ is the complex relative permeability for the dielectric (it is assumed *a priori* that the ABS samples are non-magnetic and, thus, $\tilde{\mu}_r = 1$); $\tilde{\varepsilon}_{reff} = \varepsilon_{reff}' - j\varepsilon_{reff}''$ is the effective complex relative permittivity, ε_r' and $\tan\delta_e = \tan\delta|_{\mu_r''=0} = \varepsilon_{reff}''/\varepsilon_{reff}'$ are the dielectric constant and electric loss tangent, respectively; $k_{cm0} = m\pi/a$ is the waveguide cut-off wavenumber for $\mathrm{TE_{m0}}$ modes; $\beta_{cm0} = \omega_{cm0}/c$ is the bound phase constant associated with the angular cut-off frequency for the air-filled waveguide, $\omega_{cm0} = 2\pi f_{cm0}$ and $f_{cm0} = k_{cm0}c/2\pi \Rightarrow f_c\sqrt{\mu_r'\varepsilon_{reff}'}$ is the angular cut-off frequency for the air-filled waveguide ($f_{cm0} \cong 6.55714$ GHz for the $\mathrm{TE_{10}}$ mode with WR-90 waveguides), with f_c being that for the dielectric-filled waveguide; γ_s is the complex propagation constant for the transverse electromagnetic (TEM) wave within the MPRWG's internal conducting metal walls (assumed here to be non-magnetic and so its permeability $\mu = \mu_0$) and Z_s is the associated surface impedance having an intrinsic bulk conductivity σ (with $\sigma \cong \sigma_0$ at X-band) [1],

$$\gamma_s = \frac{j\omega\mu}{Z_s} \tag{4.4}$$

$$Z_s = \sqrt{\frac{j\omega\mu}{\sigma + j\omega\varepsilon_0}} \cong \sqrt{\frac{\omega\mu_0}{2\sigma_0}}\,(1+j) \quad \text{at X-band} \tag{4.5}$$

The wave impedance and propagation constant for the $\mathrm{TE_{m0}}$ modes and γ_{m0}, respectively, can be determined from [1],

$$Z_{TEm0} = \frac{j\omega\mu_0\tilde{\mu}_r}{\gamma_{m0}} \quad \text{with} \quad Z_{TEm0}^{air} = \frac{j\omega\mu_0}{\gamma_{m0}^{air}} \tag{4.6}$$

where, Z_{TEm0}^{air} and γ_{m0}^{air} represent the wave impedance and propagation constant for an air-filled waveguide (associated with the test ports). For the $\mathrm{TE_{10}}$ mode, the equivalent *power-voltage* definition for characteristic impedance Z_0 gives,

$$Z_0 = \left(\frac{2b}{a}\right) Z_{TE10} \quad \text{with} \quad Z_0^{air} = \left(\frac{2b}{a}\right) Z_{TE10}^{air} \quad \text{and} \quad \xi = \frac{Z_0}{Z_0^{air}} = \frac{Z_{TE10}}{Z_{TE10}^{air}} = \frac{\gamma_{10}^{air}}{\gamma_{10}}\tilde{\mu}_r \tag{4.7}$$

where, ξ is the normalised impedance for the medium.

Propagation constant γ, wavenumber k and wavelength $\tilde{\lambda}$ are all generic complex variables related to one another by,

$$\gamma = jk = j\frac{\pi}{\tilde{\lambda}} \tag{4.8}$$

With a dielectric-filled MPRWG, (4.1) can be greatly simplified with PEC internal waveguide walls. Thus, using simple trigonometry, the propagation constant for the unbound dielectric γ_{ud} can be expressed in terms of the longitudinal guided-wave propagation constant γ_g and transverse waveguide cut-off propagation constant γ_{cm0} as,

$$\gamma_{ud}^2 = \gamma_g^2 + \gamma_{cm0}^2 \tag{4.9}$$

giving the following wavenumber and wavelength relationships,

$$k_g^2 = k_{ud}^2 - k_{cm0}^2 \tag{4.10}$$

and,

$$\frac{1}{\tilde{\lambda}_g^2} = \frac{1}{\tilde{\lambda}_{ud}^2} - \frac{1}{\lambda_{cm0}^2} \tag{4.11}$$

where [1],

$$\tilde{\lambda}_{ud} = \frac{\lambda_0}{\tilde{n}} \quad \text{and} \quad \lambda_0 = \frac{c}{f} = \frac{2\pi}{\beta_0} \tag{4.12}$$

$$\lambda_{cm0} = \frac{c}{f_{cm0}} = \frac{2\pi}{k_{cm0}} \rightarrow \frac{2a}{m} \quad \text{for TE}_{\text{m0}} \text{ modes} \tag{4.13}$$

The complex guided-wavelength is [1],

$$\tilde{\lambda}_g = \frac{\tilde{\lambda}_{ud}}{\sqrt{1 - \left(\frac{\tilde{\lambda}_{ud}}{\lambda_{cm0}}\right)^2}} = \frac{\lambda_0}{\sqrt{\tilde{n}^2 - \left(\frac{\lambda_0}{\lambda_{cm0}}\right)^2}} \tag{4.14}$$

By setting $Z_s = 0$, $\gamma_s \rightarrow \infty$ and (4.1) reduces to,

$$\gamma_{m0} = \gamma_g \tag{4.15}$$

In general, with PEC walls, the waveguide propagation constant for TE_{mn} or TM_{mn} modes is given by [1],

$$\gamma_{mn}^2 = \gamma_{gmn}^2 = \gamma_{ud}^2 - \gamma_{cmn}^2 \tag{4.16}$$

The complex phase constant $\tilde{\beta} \equiv k_g = 2\pi/\tilde{\lambda}_g$ is given by [1],

$$\tilde{\beta} = k_{ud}\sqrt{1 - \left(\frac{\tilde{\lambda}_{ud}}{\lambda_{cm0}}\right)^2} = \beta_0\sqrt{\tilde{n}^2 - \left(\frac{\lambda_0}{\lambda_{cm0}}\right)^2} \tag{4.17}$$

For a lossless waveguide, the lowest-order Fabry-Pérot resonance frequency can be calculated with guided-wavelength $\lambda_g(f_{fp}) = 2\pi/\beta(f_{fp}) = 2l$. As a result, it can be shown for $\mathrm{TE_{m0}}$ modes that [1],

$$f_{fp} \Rightarrow \frac{c/\sqrt{\mu_r^{'}\varepsilon_{reff}^{'}}}{2l}\sqrt{1+(l/a)^2} \tag{4.18}$$

The textbook approximation for $\mathrm{TE_{m0}}$ mode wave impedance is [1],

$$Z_{TEm0} \Rightarrow \frac{\eta_0\mu_r^{'}}{\sqrt{\mu_r^{'}\varepsilon_{reff}^{'} - \left(\frac{f_{cm0}}{f}\right)^2}} = \frac{\eta_o\sqrt{\mu_r^{'}/\varepsilon_{reff}^{'}}}{\sqrt{1-\left(\frac{f_c}{f}\right)^2}} \tag{4.19}$$

The associated wave impedance for air-filled waveguide is given by [1],

$$Z_{TEm0}^{air} = \frac{\eta_0}{\sqrt{1-\left(\frac{f_{cm0}}{f}\right)^2}} \tag{4.20}$$

4.3 Field-Based Analytical Modelling of Dielectric-Filled MPRWG

Consider the waveguide structure shown in Fig. 4.1, where a TE wave is incident on a dielectric-filled section of MPRWG. For a WR-90 waveguide operating at X-band the, the cross-sectional dimensions are given by, $a = 22.860$ mm and $b = 10.160$ mm [1]. Under steady-state sinusoidal excitation, there will be forward and backward travelling waves, with As representing the complex amplitude coefficients for the forward travelling waves and Bs representing the backward travelling waves. There are no reflected waves within Section ③ of the waveguide structure. It is assumed that Sections ① and ③ have the same material parameters. For the $\mathrm{TE_{mn}}$ mode, the electric (E-)field and magnetic (H-)field components within the three waveguide sections are [5],

$$E_{y①} = \frac{\omega\tilde{\mu}_①\gamma_{cm0}}{\gamma_{cmn}^2}\left(A_{mn①}e^{-\gamma_{mn①}z} + B_{mn①}e^{\gamma_{mn①}z}\right)\sin(k_{cm0}x)\cos(k_{c0n}y) \tag{4.21}$$

$$H_{x①} = -j\frac{\gamma_{mn①}\gamma_{cm0}}{\gamma_{cmn}^2}\left(A_{mn①}e^{-\gamma_{mn①}z} - B_{mn①}e^{\gamma_{mn①}z}\right)\sin(k_{cm0}x)\cos(k_{c0n}y) \tag{4.22}$$

$$H_{z①} = \left(A_{mn①}e^{-\gamma_{mn①}z} - B_{mn①}e^{\gamma_{mn①}z}\right)\cos(k_{cm0}x)\cos(k_{c0n}y) \tag{4.23}$$

$$E_{y②} = \frac{\omega\tilde{\mu}_②\gamma_{cm0}}{\gamma_{cmn}^2}\left(A_{mn②}e^{-\gamma_{mn②}z} + B_{mn②}e^{\gamma_{mn}z}\right)\sin(k_{cm0}x)\cos(k_{c0n}y) \tag{4.24}$$

$$H_{x②} = -j\frac{\gamma_{mn②}\gamma_{cm0}}{\gamma_{cmn}^2}\left(A_{mn②}e^{-\gamma_{mn②}z} - B_{mn②}e^{\gamma_{mn②}z}\right)\sin(k_{cm0}x)\cos(k_{c0n}y) \tag{4.25}$$

$$H_{z②} = \left(A_{mn②}e^{-\gamma_{mn②}z} - B_{mn②}e^{\gamma_{mn②}z}\right)\cos(k_{cm0}x)\cos(k_{c0n}y) \tag{4.26}$$

$$E_{y③} = \frac{\omega\tilde{\mu}_③\gamma_{cm0}}{\gamma_{cmn}^2}A_{mn③}e^{-\gamma_{mn③}(z-l)}\sin(k_{cm0}x)\cos(k_{c0n}y) \tag{4.27}$$

$$H_{x③} = -j\frac{\gamma_{mn③}\gamma_{cm0}}{\gamma_{cmn}^2}A_{mn③}e^{-\gamma_{mn③s}(z-l)}\sin(k_{cm0}x)\cos(k_{c0n}y) \tag{4.28}$$

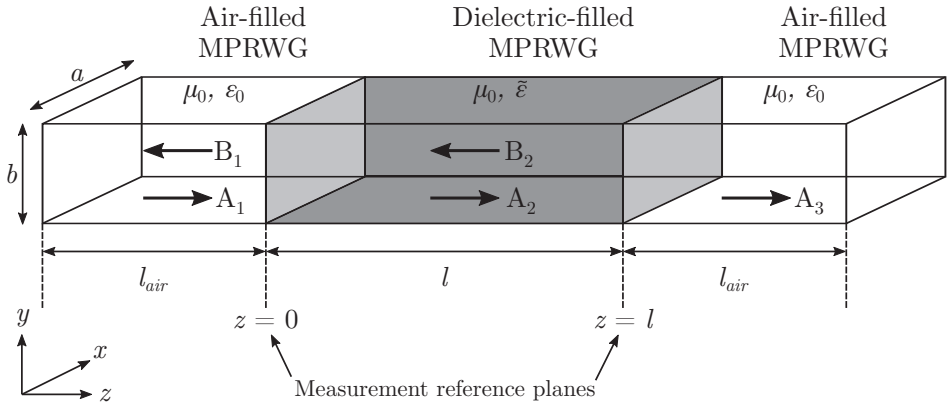


Figure 4.1: Illustration of an ideal dielectric-filled metal-pipe rectangular waveguide of dimensions $a \times b$. The length of the dielectric sample is l while the air-filled sections are of length l_{air}. In any section, As and Bs are the incident and reflected fields, respectively. Figure redrawn from Sun *et al.* [1].

$$H_{z③} = A_{mn③} e^{-\gamma_{mn③}(z-l)} \cos(k_{cm0}x) \cos(k_{c0n}y) \tag{4.29}$$

where,

$$\gamma_{cmn} = jk_{cmn} = j\sqrt{\left(\frac{m\pi}{a}\right)^2 + \left(\frac{n\pi}{b}\right)^2} \tag{4.30}$$

and,

$$k_{cm0} = \frac{m\pi}{a} \quad \text{and} \quad k_{c0n} = \frac{n\pi}{b} \tag{4.31}$$

Here, m and n correspond to the mode numbers in the horizontal x- and vertical y-directions in the transverse plane, respectively; $\gamma_{mn①}$ and $\gamma_{mn②}$ are the generalised propagation constants for the TE_{mn} modes within Sections ①, ③, and Section ②, respectively. With respect to Fig. 4.1, $\gamma_{mn①} \rightarrow \gamma_{10}^{air}$ and $\gamma_{mn②} \rightarrow \gamma_{10}$ are the propagation constants for the TE_{10} mode within the air-filled (Sections ①, ③) and dielectric-filled (Section ②) waveguide sections, respectively.

The reference plane for fields with coefficient $A_{mn③}$ is $z = l$ as indicated by the $z - l$ shift in the term $A_{mn③}e^{-\gamma_{mn①}(z-l)}$. The reference plane for all other fields is $z = 0$.

By applying boundary conditions: $E_{y①}(z = 0) = E_{y②}(z = 0)$, $E_{y②}(z = l) = E_{y③}(z = l)$, $H_{x①}(z = 0) = H_{x②}(z = 0)$, $H_{x②}(z = l) = H_{x③}(z = l)$, and after some algebraic manipulations, the

following is obtained [1],

$$\begin{bmatrix} \tilde{\mu}_{①} & \tilde{\mu}_{①} & -\tilde{\mu}_{②} & -\tilde{\mu}_{②} & 0 \\ \gamma_{mn①} & -\gamma_{mn①} & -\gamma_{mn②} & \gamma_{mn②} & 0 \\ 0 & 0 & \tilde{\mu}_{②}e^{-\gamma_{mn②}l} & \tilde{\mu}_{②}e^{\gamma_{mn②}l} & -\tilde{\mu}_{①} \\ 0 & 0 & \gamma_{mn②}e^{-\gamma_{mn②}l} & -\gamma_{mn②}e^{\gamma_{mn②}l} & -\gamma_{mn①} \end{bmatrix} \begin{bmatrix} A_{mn①} \\ B_{mn①} \\ A_{mn②} \\ B_{mn②} \\ A_{mn③} \end{bmatrix} = \begin{bmatrix} 0 \\ 0 \\ 0 \\ 0 \end{bmatrix} \tag{4.32}$$

For convenience, the waveguide structure in Fig. 4.1 is excited by setting $A_{mn①}$ to unity and the rest of the amplitude coefficients can then be obtained from (4.32) as [1],

$$B_{mn①} = \frac{\left(1 - e^{-2\gamma_{mn②}l}\right)(1-\zeta)(1+\zeta)}{(1+\zeta)^2 - e^{-2\gamma_{mn②}l}(1-\zeta)^2} \tag{4.33}$$

$$A_{mn②} = \frac{-2\varsigma(1+\zeta)}{(1+\zeta)^2 - e^{-2\gamma_{mn②}l}(1-\zeta)^2} \tag{4.34}$$

$$B_{mn②} = \frac{-2\varsigma e^{-2\gamma_{mn②}l}(1-\zeta)}{(1+\zeta)^2 - e^{-2\gamma_{mn②}l}(1-\zeta)^2} \tag{4.35}$$

$$A_{mn③} = \frac{4\zeta e^{-\gamma_{mn②}l}}{(1+\zeta)^2 - e^{-2\gamma_{mn②}l}(1-\zeta)^2} \tag{4.36}$$

with generalised coefficients,

$$\zeta = \begin{cases} \frac{\tilde{\varepsilon}_{②}\gamma_{mn①}}{\tilde{\varepsilon}_{①}\gamma_{mn②}} & \text{TM}_{\text{mn}} \text{ modes} \\ \frac{\tilde{\mu}_{①}\gamma_{mn②}}{\tilde{\mu}_{②}\gamma_{mn①}} & \text{TE}_{\text{mn}} \text{ modes} \end{cases} \tag{4.37}$$

and,

$$\varsigma = \begin{cases} \frac{\gamma_{mn①}}{\gamma_{mn②}} & \text{TM}_{\text{mn}} \text{ modes} \\ \frac{\tilde{\mu}_{①}}{\tilde{\mu}_{②}} & \text{TE}_{\text{mn}} \text{ modes} \end{cases} \tag{4.38}$$

where, scattering parameters are defined as,

$$S_{11} \equiv \left.\frac{B_{mn①}}{A_{mn①}}\right|_{B_{mn②}=0} \rightarrow B_{mn①} \quad \text{with} \quad A_{mn①} = 1 \tag{4.39}$$

$$S_{21} \equiv \left.\frac{A_{mn③}}{A_{mn①}}\right|_{B_{mn②}=0} \rightarrow A_{mn③} \quad \text{with} \quad A_{mn①} = 1 \tag{4.40}$$

Therefore, with no waveguide wall or dielectric losses, at the Fabry-Pérot resonance frequency, there is a return loss zero with $B_{mn①} = 0$ and $A_{mn③} = 1$.

With a PEC-walled waveguide, the propagation constant for an unbound dielectric is given by [1],

$$\gamma_{ud}^2 = \gamma_{mn}^2 + \gamma_{cmn}^2 = -\omega^2\tilde{\mu}\tilde{\varepsilon} \tag{4.41}$$

With the scenario depicted in Fig. 4.1, $\tilde{\mu}_{①,③} = \mu_0\tilde{\mu}_{r①,③} \rightarrow \mu_0$, $\tilde{\mu}_{②} = \mu_0\tilde{\mu}_{r②} \rightarrow \mu_0\mu_r^{'}$, $\tilde{\varepsilon}_{①,③} = \varepsilon_0\tilde{\varepsilon}_{reff①,③} \rightarrow \varepsilon_0$ and $\tilde{\varepsilon}_{②} = \varepsilon_0\tilde{\varepsilon}_{reff②} \rightarrow \varepsilon_0\tilde{\varepsilon}_{reff}$. Therefore, the respective waveguide propagation constants for Sections ①, ③ and Section ② are [1],

$$\gamma_{mn①,③} = \sqrt{k_{cmn}^2 - \omega^2\tilde{\mu}_{①,③}\tilde{\varepsilon}_{①,③}} \rightarrow \sqrt{k_{cmn}^2 - \omega^2\mu_0\varepsilon_0} \tag{4.42}$$

and,

$$\gamma_{mn②} = \sqrt{k_{cmn}^2 - \omega^2\tilde{\mu}_{②}\tilde{\varepsilon}_{②}} \rightarrow \sqrt{k_{cmn}^2 - \omega^2\mu_0\mu_r^{'}\varepsilon_0\tilde{\varepsilon}_{reff}} \tag{4.43}$$

4.4 Numerical Modelling of Dielectric-Filled MPRWG (M5)

Finite-element-based numerical solvers within *COMSOL Multiphysics*® [6] were used to perform numerical modelling of the waveguide structure [1], illustrated in Fig. 4.1, considering both the finite conductivity of the waveguide's internal walls and dielectric sample losses. The RF Module with *COMSOL Multiphysics*® provides a steady-state frequency-domain solver (which is a rigorous full-wave simulator that solvers Maxwell's equations with a solution that is the superposition of all possible modes; with a MPRWG: TE_{mn}, TE_{mnp}, TM_{mn}, TM_{mnp}) and an eigenmode solver (which is a rigorous simulator that solves Maxwell's equations for individual standing-wave modes; with a MPRWG: TE_{mnp} and TM_{mnp}). The frequency domain solver rigorously solves Maxwell's equations at each frequency, subject to an external steady-state sinusoidal excitation at the ports. With the eigenmode solver, the magnitude of the generated complex eigenfrequency $\tilde{f}_{fp} = f'_{fp} + jf''_{fp}$ gives the driven (undamped) resonance frequency $f_{fp} = |\tilde{f}_{fp}|$ corresponding to that seen with the former in the frequency domain [7].

Both propagating-wave Fabry-Pérot mode resonances and standing-wave *'open-box'* mode resonances, associated with the dielectric-filled waveguide section, were simulated using frequency-domain and eigenmode solvers, respectively.

The frequency-domain solver computes the steady-state response of the structure at a single excitation frequency. The simulations had a frequency resolution of 0.01 GHz with 421 frequency points equally spaced between 8.2 and 12.4 GHz [1]. Reflection-less waveguide ports are generally located at the ends of a structure (in this case a rectangular surface boundary is defined, which is excited by a single mode). S-parameters are computed from reflected and transmitted fields at these ports, with respect to a predefined incident field excitation at one of the ports. There are two approaches that can be adopted for the numerical modelling of the experimental setup using *COMSOL Multiphysics*®; both require post-processing of the S-parameters.

The first approach is to simulate the complete structure illustrated in Fig. 4.1 directly, by

defining ports at the ends of the air-filled waveguide sections and then de-embedding these sections to move the S-parameter reference planes from the ports to the dielectric sample under test. In this case, the reference port impedance is the wave impedance of the TE_{10} mode within a lossless air-filed waveguide (i.e., $Z_T = Z^{air}_{TE10}$ [1]). This approach has the advantage that de-embedding is simple for air-filled waveguide sections and only requires multiplication of simulated S-parameters by $e^{+2\gamma^{air}_{10} l_{air}}$, where l_{air} is the length of both air-filled sections (with $l_{air} = l$ in the simulations). The main disadvantage is that there is a computational overhead, as the air-filled sections must also be simulated. It should be noted that while it is possible to reduce l_{air}, a smaller distance between the waveguide port and air-dielectric boundary might be meshed densely by the automatic meshing utility in *COMSOL Multiphysics*® if $l_{air} \ll \lambda_g$ [1].

The second approach only simulates the dielectric-filled waveguide section. In this case the reference port impedance is the wave impedance of the TE_{10} mode within the dielectric-filled waveguide (i.e., $Z_T = Z_{TE10}$). The S-parameters obtained must then be renormalised to the impedance of the TE_{10} mode in lossless air-filled waveguide. This approach has the advantage that the simulated structure is just a rectangular block, thus, having simplified geometry and potentially resulting in reduced mesh size, simulation time and memory requirements. However, as was later found, this approach required a much finer mesh to achieve the same accuracy compared to the first approach. This could be due to a shorter wavelength near the ports, which is much less than the first approach, thus, requiring a denser mesh to achieve the same number of mesh elements per wavelength. Another disadvantage is that renormalisation of S-parameters is not straight-forward and requires matrix manipulation [8].

Numerical finite-element simulations were run on dual-core Intel Xeon E5-2665 CPU with 16 cores and 256 GB of RAM. Mesh densities were manually set to achieve similar accuracies within *COMSOL Multiphysics*® for both approaches. The meshed geometries had a total of 4,429 and 18,032 tetrahedral mesh elements (respectively, taking 24 and 54 minutes to simulate), for the first and second approaches, respectively. The results from both approaches are shown in Table 4.1 [1] (second approach values in brackets), giving very similar results.

When compared to the analytical modelling by Sun *et al.* [1], the return losses are slightly different; which can be attributed to a non-zero mesh resolution. As expected, the differential-phse group delay and associated Q-factors are the same as those found with analytical (*variational*) modelling M1 in [1].

4.5 Analytical Field-Based Q-Factor Modelling

The constituent Q-factor contributions associated with Fabry-Pérot resonance have been modelled analytically using an EM field-based approach, with its bespoke textbook derivation given here. EM field integrals are calculated either using purely analytical expressions for the electric and magnetic field components or computed directly within *COMSOL Multiphysics*® (by defining the surface and volume integrals of the individual field components) from numerical (finite-element) simulations. The results are shown in the lower-half of Table 4.1. As expected, Q-factors predicted using both analytical field-based modelling strategies give consistent results with the numerical modelling approach M3.

For a medium that is terminated at both ends by the same reference port impedance Z_T, quality (Q-)factor can be broken down in to constituent components; loaded Q_L and unloaded Q_U Q-factors are related by [1],

$$\frac{1}{Q_L} = \frac{1}{Q_U} + \frac{1}{Q_e} \quad \text{where} \quad \frac{1}{Q_U} = \frac{1}{Q_c} + \frac{1}{Q_d} + \frac{1}{Q_r} \tag{4.44}$$

where, Q_e, Q_c, Q_d and Q_r are the respective Q-factors associated with external (e) loading from the terminating impedances and contributions due to conductive (c), dielectric (d) and radiative (r) losses.

Now, the total energy stored inside the dielectric sample under test W_T can be computed from,

$$W = W_M + W_E \tag{4.45}$$

where, W_M and W_E are the time-averaged magnetic and electric energies, respectively, given by the volume integrals (where the total volume of the dielectric sample under test $V = a \times b \times l$) [5],

$$W_M = \frac{\mu_0 \mu_r^{'}}{4} \left\langle \int_v |H_{x②}|^2 + |H_{z②}|^2 \, dv \right\rangle \tag{4.46}$$

$$W_E = \frac{\varepsilon_0 \varepsilon_{reff}^{'}}{4} \left\langle \int_v |E_{y②}|^2 \, dv \right\rangle \tag{4.47}$$

At the Fabry-Pérot resonance frequency, the loaded Q-factor for the TE_{10} mode can be calculated by considering the loss contributions to the total dissipated power $P_T = P_c + P_d + P_e$, where P_c is due to the waveguide's conducting wall loses, P_d is due to the dielectric losses and P_e is due to the external impedance loading at both waveguide test ports. The corresponding constituent Q-factor components given in (4.44) are then [5],

$$Q_c = \omega_{fp} \, \frac{(W_M + W_E)}{P_c} \tag{4.48}$$

$$Q_d = \omega_{fp} \, \frac{(W_M + W_E)}{P_d} \tag{4.49}$$

$$Q_e = \omega_{fp} \, \frac{(W_M + W_E)}{P_e} \tag{4.50}$$

where, the corresponding time-average power dissipation contributions can be computed from [5],

$$P_c = R_s \left\langle \int_{x=0} |H_{x②}|^2 \, ds \right\rangle + R_s \left\langle \int_{y=0} (|H_{x②}|^2 + |H_{z②}|^2) ds \right\rangle \tag{4.51}$$

$$P_d = \frac{\sigma_d}{2} \, \left\langle \int_v |E_{y②}|^2 \, dv \right\rangle \tag{4.52}$$

$$P_e = \frac{1}{2} Re \left\{ \left\langle \int_{z=0} (E_{y①} \times H^*_{x①}) ds \right\rangle + \left\langle \int_{z=l} (E_{y③} \times H^*_{x③}) ds \right\rangle \right\} \tag{4.53}$$

The field integrals given in (4.46)–(4.47) and (4.51)–(4.53) (contained within the angle brackets $\langle \, \rangle$) are either calculated analytically, using (4.32)–(4.38) with the resulting fields defined by (4.21)–(4.29), or computed within *COMSOL Multiphysics*®; the results are shown in the bottom half of Table 4.1.

4.6 Open-Box Mode Resonance Modelling

The measured normalised power responses are shown in Fig. 4.2 for Samples #1 and #2 [1]. It can be seen that both samples give almost identical power responses across the whole X-band. Any dominant TE or TM travelling-waves propagate through the dielectric-filled MPRWG in the longitudinal direction and, obviously, do not require any form of imperfections/inhomogeneity to excite these modes. In contrast, however, the dielectric-filled MPRWG section also behaves as a parallel-plate dielectric waveguide with short circuits at both ends in the transverse direction; any imperfection/inhomogeneity in the sample excite standing-wave resonant modes, which are confined in the transverse direction. The presence of these *'open-box'* modes are evident by small notches centred at their resonance frequencies, seen in the transmittance and absorptance responses of Fig. 4.2 [1].

The dielectric constant and loss tangent values, extracted at the Fabry-Pérot resonance frequency, were adopted from numerical Fabry-Pérot modelling called M3 in [1]. With finite conductivity waveguide walls, the *COMSOL Multiphysics*® eigenmode solver predicts the complex eigenfrequencies directly. Then, by observing the resulting field patterns (given in this section for Sample #1), the open-box modes within X-band seen in Fig. 4.2 were identified as the TE_{201}, TE_{011} and TE_{111} modes. In addition, from first principles with a PEC-walled waveguide, this section gives a field-based analytical derivation for the open-box mode resonance frequencies as published in [1].

The numerically and analytically predicted open-box mode resonance frequencies for both Samples #1 and #2 are listed in Table 4.2 (giving less than 1% error, when compared to measurements) [1]. By inspection of Table 4.2, it can be seen that there is less than 0.02% discrepancy

Table 4.1: Fabry-Pérot resonance simulation results with numerical modelling M5. Table reproduced from Sun *et al.* [1].

Parameter at ω_{fp}		Sample #1	Sample #2
M5: Numerical (Finite-element) Modelling using *COMSOL Multiphysics*® (Using measured f_{fp}, $\lvert S_{21}\rvert$ from [1])	ε'_{reff}	2.3284 (2.3270)	2.3080 (2.3061)
	$\tan\delta_e \times 10^4$	19.148 (19.148)	14.798 (14.798)
	f_{fp} [GHz]	11.080	11.130
	$\lvert S_{11}\rvert$ [dB]	-53.2565 (-52.4620)	-55.4752 (-54.3515)
	$\lvert S_{21}\rvert$ [dB]	-0.03800 (-0.03811)	-0.02980 (-0.02990)
	τ_g [ps]	61.405 (61.514)	60.942 (61.045)
	Q_U	489.2 (489.1)	621.2 (621.1)
	Q_e	2.146 (2.150)	2.138 (2.142)
	Q_L	2.137 (2.141)	2.131 (2.135)
Analytical modelling with field integrals calculated from analytical expressions for the EM fields (Using f_{fp}, ε'_{reff} and $\tan\delta_e$ from M5 [1])	Q_c	8008.6 (8066.0)	8027.5 (8084.0)
	Q_d	521.4 (517.90)	674.65 (670.20)
	Q_U	489.53 (486.70)	622.35 (628.90)
	Q_e	2.1501 (2.1868)	2.1436 (2.1798)
	Q_L	2.1407 (2.1770)	2.1362 (2.1722)
Analytical modelling with field integrals computed within *COMSOL Multiphysics*® from finite-element simulations of EM fields (Using f_{fp}, ε'_{reff} and $\tan\delta_e$ from M5 [1])	Q_c	7494.6 (7515.0)	7511.9 (7532.0)
	Q_d	522.04 (522.22)	675.50 (675.70)
	Q_U	488.04 (488.30)	629.76 (620.10)
	Q_e	2.1171 (1.8425)	2.1105 (1.8250)
	Q_L	2.1079 (1.8356)	2.1034 (1.8370)

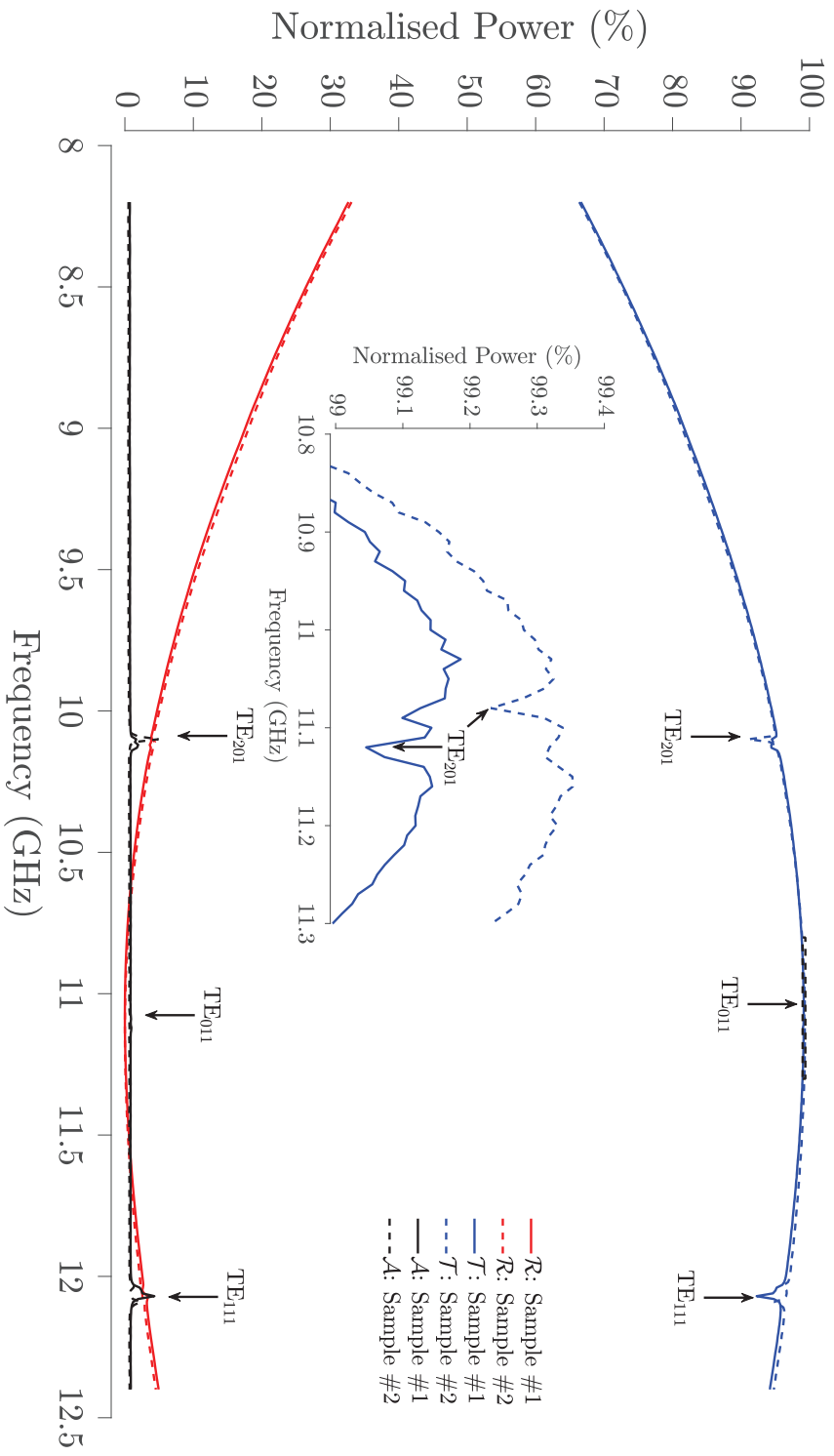


Figure 4.2: Normalised power responses for fused deposition modelling (FDM) 3-D printed acrylonitrile butadiene-styrene (ABS) Samples #1 and #2 filling the standard WR-90 quarter-wavelength thru line waveguide. The spectral location of open-box mode resonances are indicated and appear as sharp spikes in the measured response. Figure redrawn from Sun *et al.* [1].

between the results from the numerical (finite-element) eigenmode solver that considers both conductor and dielectric losses and analytical modelling that assumes a PEC-walled waveguide.

4.6.1 Qualitative Excitation of Open-Box Mode Resonances With a Frequency-Domain Solver

Open-box modes can be excited by in-homogeneities. With the FDM 3-D printed samples, open-box modes reveal themselves as notches in the frequency-domain S-parameter measurements as shown in Fig. 4.2. From the SEM microphotographs of the 3-D printed ABS sample reproduced from Sun *et al.* [1] and shown in Fig. 4.3, the sample is composed of layers of ABS deposited layer-by-layer like a woodpile structure. Numerical modelling of a to-scale 3-D woodpile metamaterial structure is not possible, due to the extremely fine meshing required to model the very small spatial features [1]. However, three approaches can be adopted to qualitatively model the open-box mode resonances. The first approach, adopted by Sun *et al.* [1], is to introduce an artificial in-homogeneity by using a coarse meshing scheme with a homogeneous structure. The second approach, presented here, is to model an ABS sample with up-scaled spatial features, that can be meshed and simulated in a realistic amount of time. With this approach, the size of layer height and width of woodpile was increased while keeping the overall dimensions of the sample fixed. The third approach is the most robust and can accurately predict the excitation of box-mode resonances to within 0.2 GHz. With this approach, the modelled permittivity of the dielectric sample is defined as an inhomogeneous and anisotropic, but symmetric, tensor. This approach also has the advantage that it is independent of mesh size. Figure 4.6 is an illustration of layer-by-layer printing of an ABS sample which shows that each alternate layer is printed with a 180° shift in angle of straight paths.

With the first approach, the sample was simulated by Sun *et al.* [1] using a mesh having only 84 tetrahedral elements, as shown in Fig. 4.5(a). The corresponding frequency-domain simulated S-parameters in Fig. 4.5(b) clearly show excitation of the expected open-box mode resonances at their predicted frequencies.

With the second approach, a periodic woodpile structure was mathematically defined in *COMSOL Multiphysics*® by varying the dielectric constant of the sample under test. The periodicity of the woodpile structure in the xz-plane was varied as a function of y to simulate a change in dielectric *constant* with a change in ambient temperature, as the printing head moves away from the heated build-plate. The dielectric constant of the dielectric-filled section of MPRWG in *COMSOL Multiphysics*® was defined as,

$$\varepsilon_r(x,y,z) = (\varepsilon_{rbulk} - 1)Pulse_1(k_a(1+\frac{y}{l})(Pulse_2(4k_a y)x + z)) + 1 \tag{4.54}$$

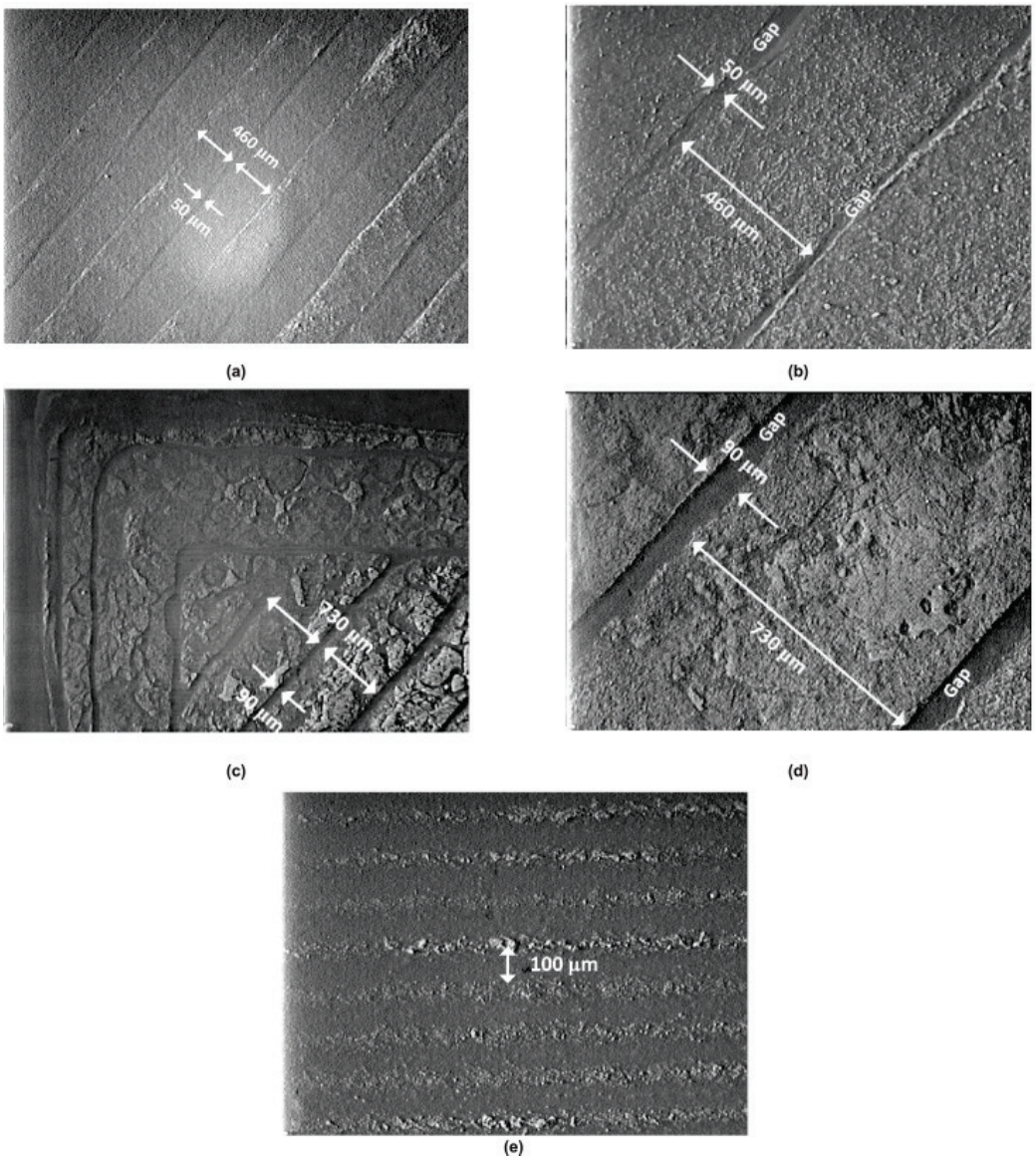


Figure 4.3: Photomicrographs of an FDM 3-D printed ABS sample under test with nominal 100 μm layer height and 100% infill printer settings: (a) top layer x-y plane view; (b) top layer x-y plane close-in view; (c) bottom layer x-y plane view of a corner; (d) bottom layer x-y plane close-in view; and (e) vertical build x-z plane view. Figure reproduced from Sun *et al.* [1].

where $l = 9.626$ mm is the length of dielectric-filled section of MPRWG (chosen from average measurements of the printed ABS samples) [1], $\varepsilon_{rbulk} = 2.541$ is the bulk dielectric constant of sample under test, $k_a = 2\pi/l_p$ is the spatial frequency where $l_p = 6.400$ mm was set as spatial length of one period. $Pulse_1$ and $Pulse_2$ are two periodic square pulse functions, which define the spatial fill-factor in xz-plane and spatial periodicity along y-axis, respectively.

$$Pulse_1(x) = \begin{cases} 1 & \text{for} \quad 0 < x < 2\pi\check{\Delta} \\ 0 & \text{for} \quad 2\pi\check{\Delta} < x < 2\pi \\ Pulse_1(x + 2\pi) & \text{in general} \end{cases} \tag{4.55}$$

where, $\check{\Delta}$ is the duty cycle or fill factor set as 88.5%.

$$Pulse_2(x) = \begin{cases} 1 & \text{for} \quad 0 < x < 2\pi \\ -1 & \text{for} \quad 2\pi < x < 4\pi \\ Pulse_2(x + 4\pi) & \text{in general} \end{cases} \tag{4.56}$$

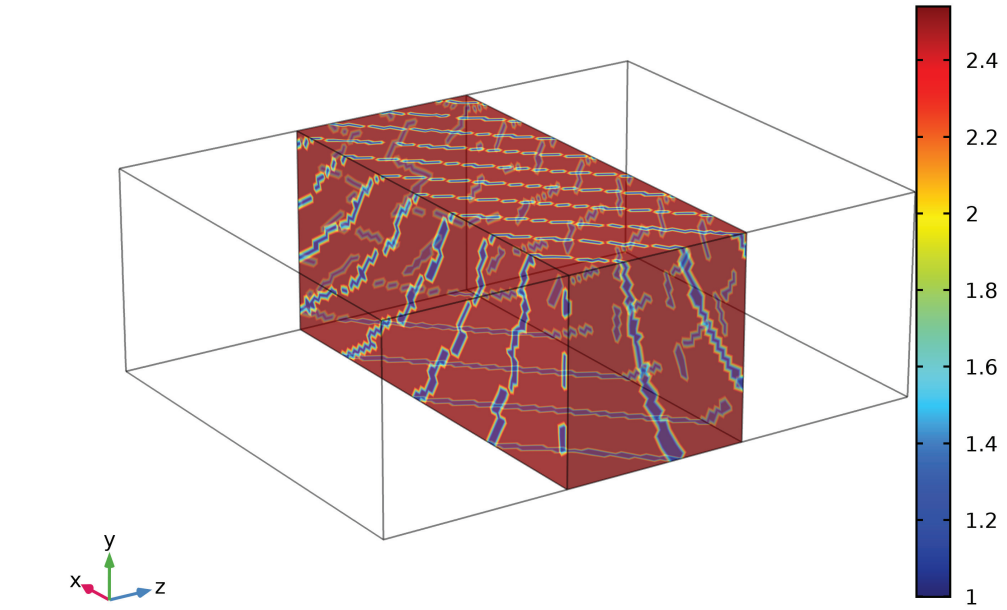
Figure 4.4(a) shows 3-D contour plot of dielectric constant in *COMSOL Multiphysics*® while the corresponding frequency-domain simulated S-parameters in Fig. 4.4(b) show the excitation of open-box modes at their predicted frequencies.

With the third approach, an in-homogeneous and anisotropic permittivity tensor was defined for the dielectric sample within *COMSOL Multiphysics*®. The permittivity tensor was kept symmetric to ensure that scattering parameters are independent of the propagation direction of electromagnetic wave in the waveguide. The permittivity tensor can be expressed as,

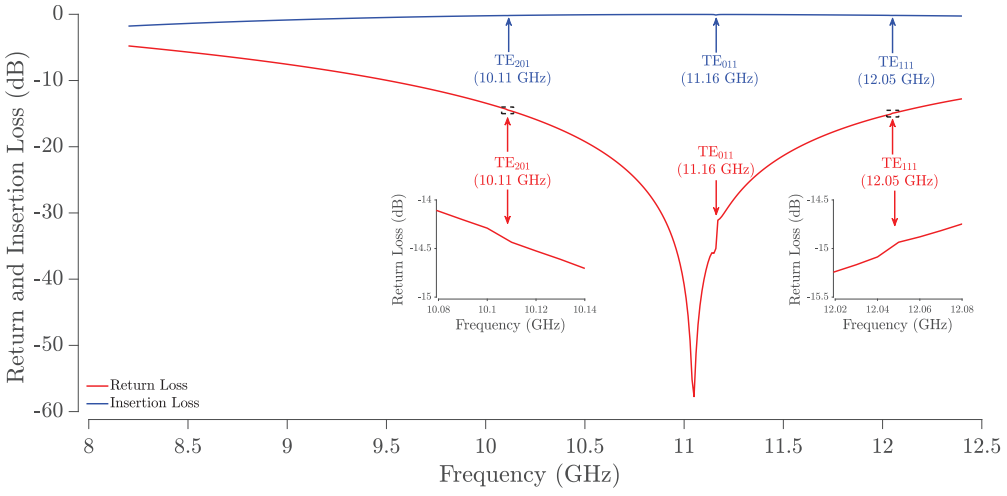
$$\dot{\varepsilon}'_{reff} = \begin{bmatrix} \varepsilon'_{reff}(1 + f_{xx}(x,y,z)) & c_{xy}f_{xy}(x,y,z) & c_{xz}f_{xz}(x,y,z) \\ c_{yx}f_{yx}(x,y,z) & \varepsilon'_{reff}(1 + f_{yy}(x,y,z)) & c_{yz}f_{yz}(x,y,z) \\ c_{zx}f_{zx}(x,y,z) & c_{zy}f_{zy}(x,y,z) & \varepsilon'_{reff}(1 + f_{zz}(x,y,z)) \end{bmatrix} \tag{4.57}$$

where, c_{uv} $(u, v \in \{x, y, z\})$ are scalars which control the amount of coupling between different field components due to anisotropy; and $f_{uv}(x, y, z)$ are spatially dependent scalar functions which control the amount of spatial variation in the permittivity. In order to ensure that the effective value of permittivity does not change over the bulk of the dielectric, f_{uv} should be chosen with a zero spatial mean over the volume of dielectric sample; otherwise the spectral location of resonances will shift unpredictably. A simple choice of f_{uv} with linear variation is,

$$f_{uv} = \pm\Delta^{\%x}_{\varepsilon'_{reff}} \frac{(x - a/2)}{a} \pm \Delta^{\%y}_{\varepsilon'_{reff}} \frac{(y - b/2)}{b} \pm \Delta^{\%z}_{\varepsilon'_{reff}} \frac{(z - l/2)}{l} \tag{4.58}$$

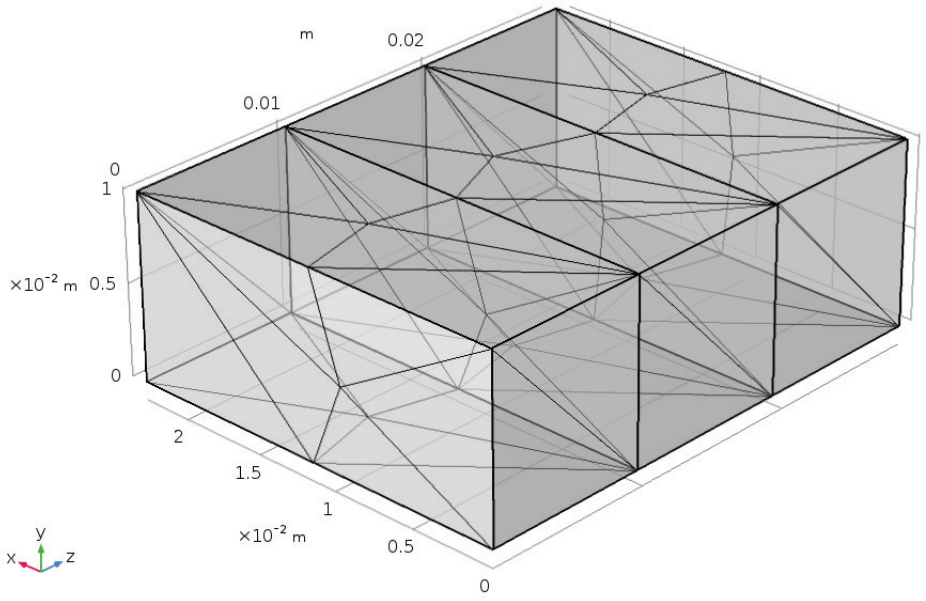


(a)

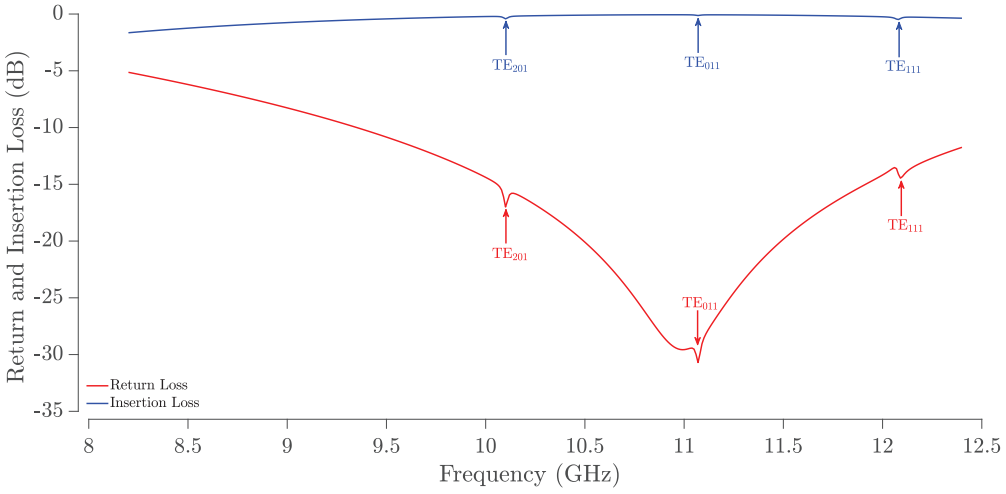


(b)

Figure 4.4: Numerical modelling of open-box mode excitation for Sample #1 with bulk dielectric constant and loss tangent of 2.541 and 8.188×10^{-4}, respectively, from M3 [1] using up-scaled geometry corresponding to the FDM 3-D-printed ABS sample: (a) 3-D contour plot of dielectric constant $\varepsilon_r(x, y, x)$ on the surface of simulated dielectric sample in *COMSOL Multiphysics*®, with $l_{air} = l$; and (b) resulting S-parameters showing open-box mode resonances at 10.11, 11.16 and 12.05 GHz.



(a)



(b)

Figure 4.5: Numerical modelling of open-box mode excitation for Sample #1 with dielectric constant and loss tangent of 2.3284 and 19.148×10^{-4}, respectively, from M3 using coarse meshing: (a) 3-D coarse meshing of the complete structure illustrated in Fig. 4.1, with $l_{air} = l$; and (b) resulting S-parameters showing open-box mode resonances at 10.17, 11.15 and 12.18 GHz. Figure reproduced from Sun *et al.* [1].

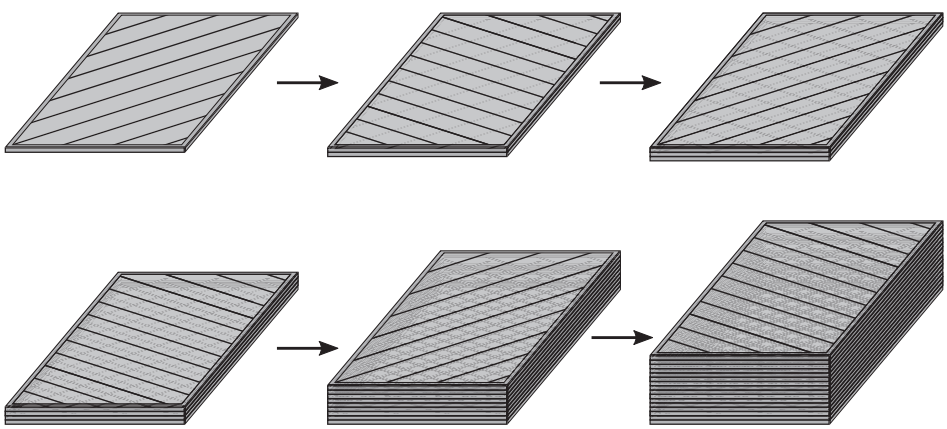


Figure 4.6: Illustration of layer-by-layer fused deposition modelling (FDM) 3-D printing of acrylonitrile butadiene-styrene (ABS) sample showing a 90° shift in angle for alternating layers. The ABS is deposited as molten filaments oriented at 45° relative to the sides of the sample and compressed to form several layers of a structure resembling a woodpile.

where, $\Delta^{\%x}_{\varepsilon'_{reff}}$, $\Delta^{\%y}_{\varepsilon'_{reff}}$ and $\Delta^{\%z}_{\varepsilon'_{reff}}$ are the percentage change in ε'_{reff} along x-, y- or z-direction, respectively. For example, a 5% change in permittivity along x-direction gives,

$$\Delta^{\%x}_{\varepsilon'_{reff}} = \frac{5}{100} \tag{4.59}$$

It is convenient to choose $\Delta^{\%}_{\varepsilon'_{reff}} = \Delta^{\%x}_{\varepsilon'_{reff}} = \Delta^{\%y}_{\varepsilon'_{reff}} = \Delta^{\%z}_{\varepsilon'_{reff}}$ as a single parameter for percentage change in $\varepsilon reff'$ along any direction. With a symmetric network, $c_{uv} = c_{vu}$ and $f_{uv} = fvu$. Within *COMSOL Multiphysics*®, the permittivity tensor for the dielectric medium was defined using (4.57), where,

$$f_{xx} = f_{xy} = f_{yx} = \Delta^{\%}_{\varepsilon'_{reff}} \left(-\frac{(x - a/2)}{a} + \frac{(y - b/2)}{b} + \frac{(z - l/2)}{l} \right) \tag{4.60}$$

$$f_{yy} = f_{yz} = f_{zy} = \Delta^{\%}_{\varepsilon'_{reff}} \left(\frac{(x - a/2)}{a} - \frac{(y - b/2)}{b} + \frac{(z - l/2)}{l} \right) \tag{4.61}$$

$$f_{zz} = f_{zx} = f_{xz} = \Delta^{\%}_{\varepsilon'_{reff}} \left(\frac{(x - a/2)}{a} + \frac{(y - b/2)}{b} - \frac{(z - l/2)}{l} \right) \tag{4.62}$$

with all the scalars c_{uv} set as unity and,

$$\Delta^{\%}_{\varepsilon'_{reff}} = \frac{2}{100} \tag{4.63}$$

The waveguide mode (TE_{10} in this case) must be specified with the *COMSOL Multiphysics*® frequency domain solver, as the solver computes S-parameters from the transverse field profile of the specified mode at a particular port. With *COMSOL Multiphysics*®, the simulation domain is normally terminated in a port, which absorbs the specified mode defined at that port for single mode operation. However, when multiple modes are being excited, any unmatched modes at a port will be

reflected back into the simulation domain. It was found that, with the specified inhomogeneous and anisotropic tensor within *COMSOL Multiphysics*®, the ports acted as PEC for non-TE_{10} modes; and the air-filled waveguide acted as a closed resonator for these modes. In order to let these modes escape the simulation space, PML-backed rectangular slit ports were defined within *COMSOL Multiphysics*® as shown in Fig. 4.7. It should be noted, that with *COMSOL Multiphysics*®, the ports are not located at the measurement reference planes. The obtained S-parameters, in this case, must be de-embedded (or shifted) so they coincide with the location of measurement planes. This can be achieved by simply multiplying S_{11} and S_{21} with $e^{+2j\gamma_{cmn}l}$. The ports were set to the dominant TE_{10} mode, with Port 1 acting as the source. The length of the air-filled and PML sections were set as $2l$, where $\varepsilon'_{reff} = 2.3284$ and $\tan\delta_e = 19.1480 \times 10^{-4}$ corresponding to values for Sample #1 from Table 4.2. The computed insertion loss and return loss from theory and those computed from *COMSOL Multiphysics*® frequency domain solver are plotted in Fig. 4.8(a). The box-mode resonances can be clearly seen in the absorptance plot shown in Fig. 4.8(b).

4.6.2 Open-Box Mode Resonance Field Plots From Eigenmode Solver

Numerical simulations using the eigenmode solver with fine meshing can be used to study the open-box mode resonances. Here, the two air-filled waveguide sections were increased in length to $l_{air} = 11.5l$, allowing the evanescent fields of the open-box modes to sufficiently decay outside of the sample. Also, the extreme ends of the air-filled sections are terminated with *second-order scattering* boundary conditions [6], which help to absorb incident waves. Figures 4.9–4.11 show field plots of open-box mode resonances from the eigenmode solver for Sample #1 [1].

It can be clearly seen in Fig. 4.5(b) that the open-box mode resonances observed with coarse meshing are only slightly higher (with less than ∼1% error) in frequency than those predicted with fine meshing, for the same dielectric constant and loss tangent values; making the former a useful technique with limited computational resources [1].

4.6.3 Analytical Modelling of Open-Box Mode Resonances

The TE_{mnp} open-box mode resonances observed with a dielectric-filled waveguide section can be modelled by extending the analysis given in Section 4.3. The associated complex eigenfrequencies are defined by the poles of $B_{mn①}$ in (4.33), by setting its denominator to zero (i.e., to extract its natural modes, without any external steady-state sinusoidal excitation so that $A_{mn①} = 0$) [1],

$$(1+\zeta)^2 - e^{-2\gamma_{mn②}l}(1-\zeta)^2 = 0 \tag{4.64}$$

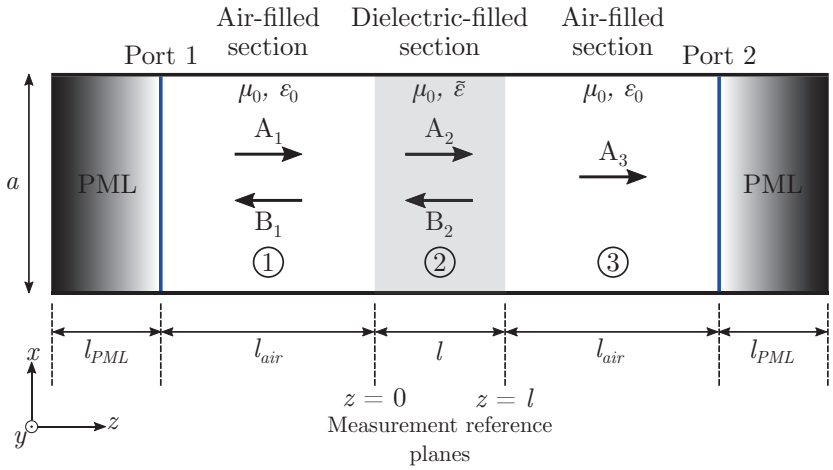


Figure 4.7: Longitudinal top-down cross-sectional view of the rectangular metal-pipe rectangular waveguide showing the dielectric-filled, air-filled and perfectly matched layer (PML) sections in the waveguide. Two slit ports were defined at the ends of the air-filled sections with excitation at Port 1. The ports were specified to compute scattering parameters for the dominant TE_{10} mode. Since the ports defined in *COMSOL Multiphysics*® do not coincide with the actual measurement reference planes, S-parameters obtained from *COMSOL Multiphysics*® must be de-embedded to give the correct S-parameters at the specified measurements reference planes.

An infinite number of solutions emerge from (4.64), which are either designated as even or odd modes depending on the corresponding symmetry of the electric fields. These even and odd modes can be obtained by solving the following equations for complex eigenfrequencies [1],

$$(1+\zeta) + e^{-\gamma_{mn②}l}(1-\zeta) = 0 \quad \text{Even modes} \tag{4.65}$$

$$(1+\zeta) - e^{-\gamma_{mn②}l}(1-\zeta) = 0 \quad \text{Odd modes} \tag{4.66}$$

After some algebraic manipulations, the following transcendental equations are obtained for TE modes [1],

$$\tilde{\mu}_{①}\gamma_{mn②} - \tilde{\mu}_{②}\gamma_{mn①}\coth\left(\frac{\gamma_{mn②}l}{2}\right) = 0 \quad \text{Even modes} \tag{4.67}$$

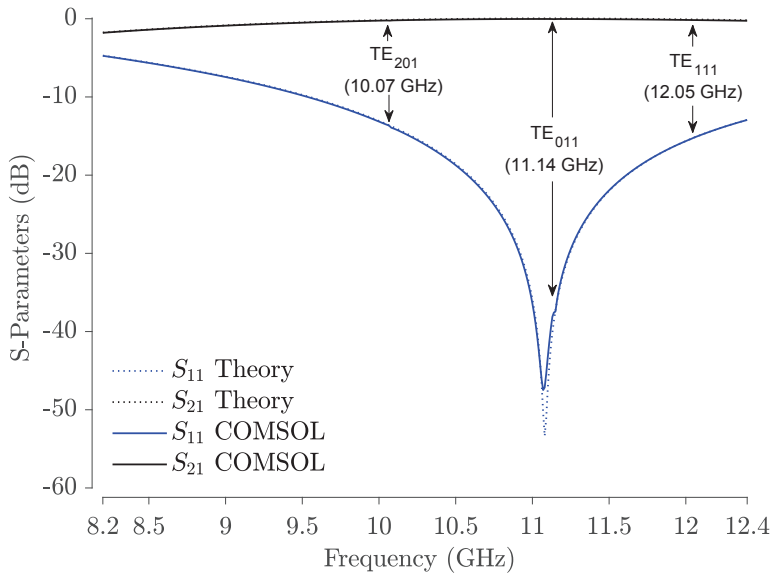
$$\tilde{\mu}_{①}\gamma_{mn②} - \tilde{\mu}_{②}\gamma_{mn①}\tanh\left(\frac{\gamma_{mn②}l}{2}\right) = 0 \quad \text{Odd modes} \tag{4.68}$$

These generalised expressions can be simplified by setting $\tilde{\mu}_{①} = \tilde{\mu}_{②}/\mu_r^{'} = \mu_0$ to obtain [1],

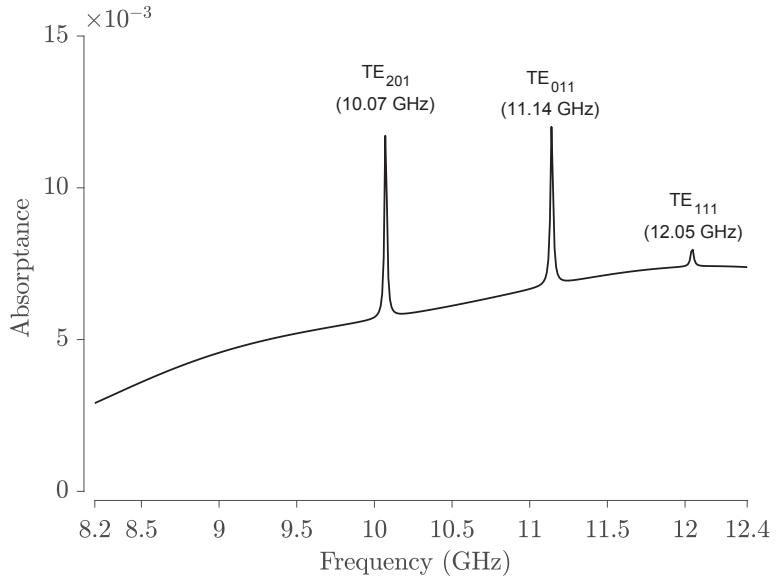
$$\mu_r^{'}\gamma_{mn①} - \gamma_{mn②}\tanh\left(\frac{\gamma_{mn②}l}{2}\right) = 0 \quad \text{Even modes} \tag{4.69}$$

$$\gamma_{mn②} - \mu_r^{'}\gamma_{mn①}\tanh\left(\frac{\gamma_{mn②}l}{2}\right) = 0 \quad \text{Odd modes} \tag{4.70}$$

The roots of (4.69) and (4.70) can be numerically solved to obtain the complex angular eigenfre-



(a)



(b)

Figure 4.8: Plot of (a) return loss and insertion loss; and (b) absorptance of the dielectric-filled metal-pipe rectangular waveguide operating in the dominant TE_{10} mode having dimensions $a = 22.86$ mm, $b = 10.16$ mm and dielectric section of length $l = 9.626$ mm; with dielectric constant $\varepsilon'_{reff②} = 2.3284$ and loss tangent $\tan\delta_{e②} = 19.1480 \times 10^{-4}$ of the filled in-homogeneous and anisotropic dielectric medium. Dotted lines in (a) show the ideal response computed from theory, while the solid lines show the simulated response from the *COMSOL Multiphysics*® frequency domain solver. The spectral location of box-mode resonances can be clearly seen in (b), with the predicted open-box mode resonance frequencies within 0.01 GHz compared to those computed from theory and eigenmode solver for Sample #1, given in Table 4.2.

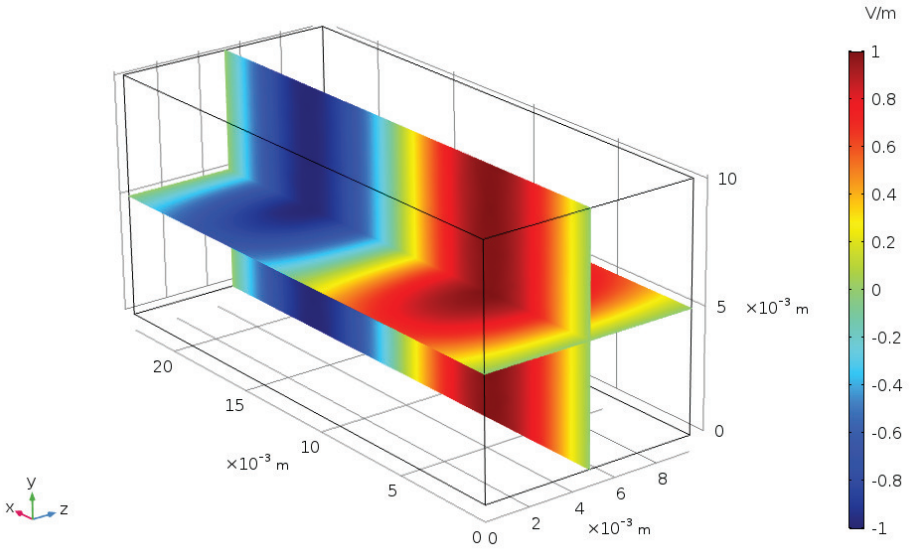


Figure 4.9: Numerically simulated E_y-field plot for TE_{201} open-box mode at $f_{201} = 10.074$ GHz for Sample #1 with dielectric constant loss tangent of 2.3284 and 19.148×10^{-4}, respectively, from M3. Figure reproduced from Sun *et al.* [1].

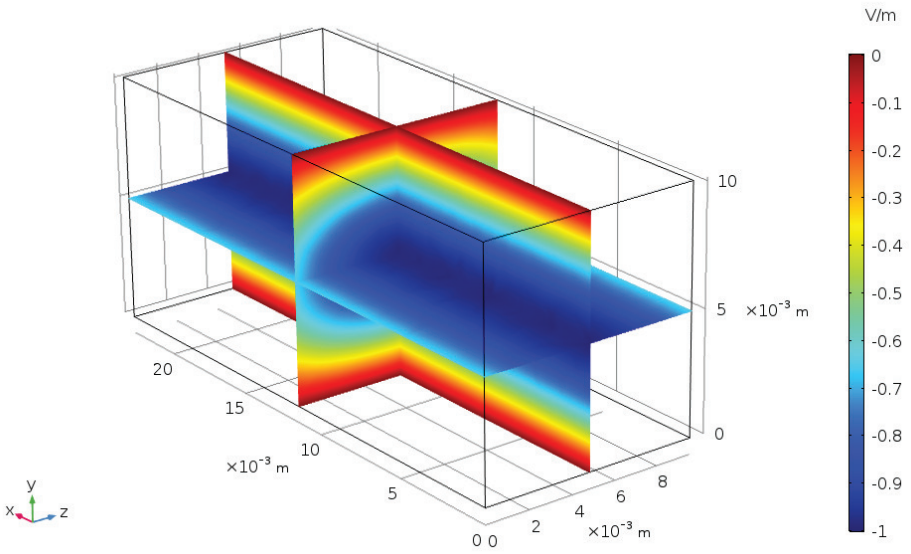
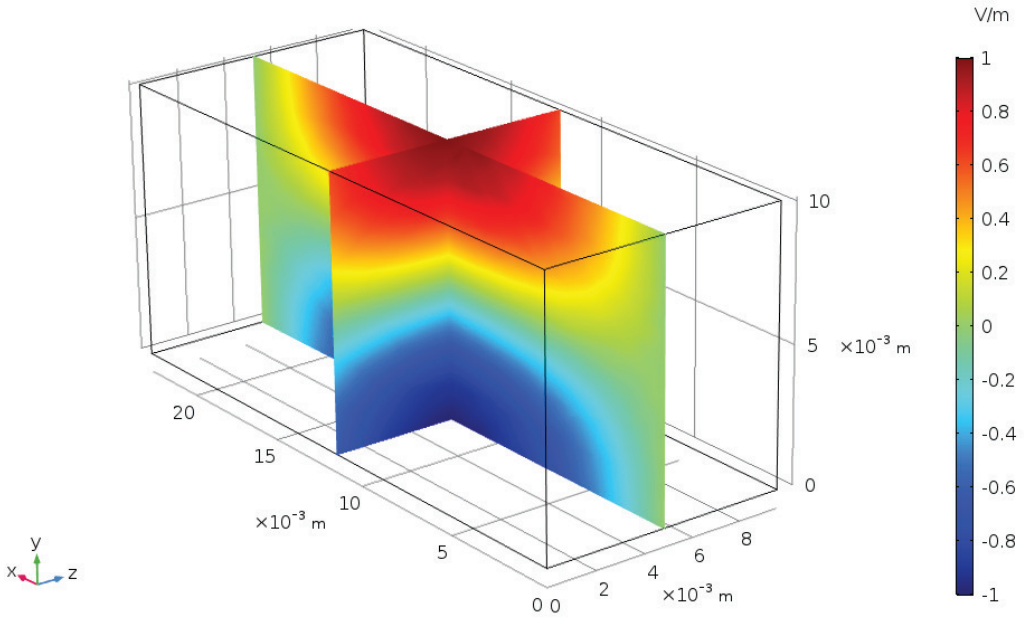
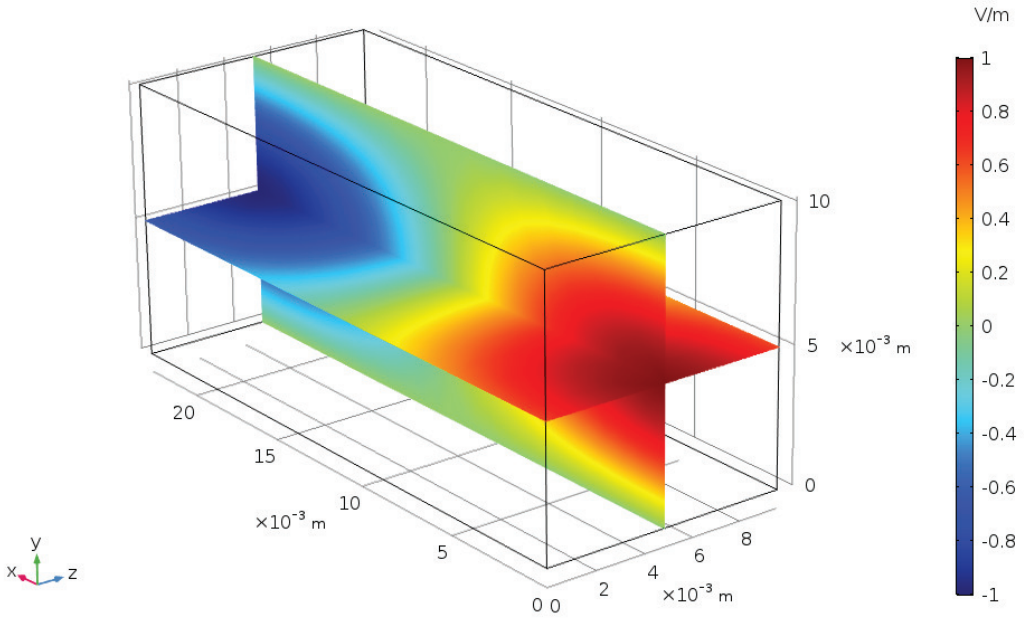


Figure 4.10: Numerically simulated E_x-field plot for TE_{011} open-box mode at $f_{011} = 11.144$ GHz for Sample #1 with dielectric constant loss tangent of 2.3284 and 19.148×10^{-4}, respectively, from M3. Figure reproduced from Sun *et al.* [1].



(a)



(b)

Figure 4.11: Numerically simulated field plots for TE_{111} open-box mode at $f_{111} = 12.046$ GHz for Sample #1 with dielectric constant loss tangent of 2.3284 and 19.148×10^{-4}, respectively, from M3: (a) E_y-field; and (b) E_x-field. Figure reproduced from Sun *et al.* [1].

Table 4.2: Open-box mode resonance frequencies (and associated mode Q-factors) spectroscopically measured and predicted using numerical eigenmode solver and field-based analytical solutions. Table reproduced from Sun *et al.* [1].

Open-box Mode		TE_{101}	TE_{201}	TE_{011}	TE_{111}
Sample #1					
$(e'_{reff} = 2.3284,\ tan\delta = 19.1480 \times 10^{-4})$					
$\lvert\tilde{f}_{mnp}\rvert$ [GHz]	Measured	-	10.115	11.115	12.065
$\tilde{f}_{mnp}$ $(\lvert\tilde{f}_{mnp}\rvert)$ $[Q_u(\lvert\tilde{f}_{mnp}\rvert)]$	Analytical Solution $\rho_0 = 0$	5.6065+ j0.0036 (5.607) [778.7]	10.0732+ j0.0084 (10.073) [599.6]	11.1431+ j0.0095 (11.143) [586.5]	12.0450+ j0.0105 (12.045) [573.6]
	Eigenmode Solver $\rho_0 = \rho_0\lvert_{brass}$	5.6035+ j0.0078 (5.604) [359.2]	10.074+ j0.005 (10.074) [1007.4]	11.144+ j0.0059 (11.144) [944.4]	12.046+ j0.006 (12.046) [1003.8]
Sample #2					
$(e'_{reff} = 2.3080,\ tan\delta = 14.7975 \times 10^{-4})$					
$\lvert\tilde{f}_{mnp}\rvert$ [GHz]	Measured	-	10.100	11.080	12.090
$\tilde{f}_{mnp}$ $(\lvert\tilde{f}_{mnp}\rvert)$ $[Q_u(\lvert\tilde{f}_{mnp}\rvert)]$	Analytical Solution $\rho_0 = 0$	5.6229+ j0.0028 (5.623) [1004.1]	10.1118+ j0.0065 (10.112) [777.8]	11.186+ j0.0074 (11.187) [755.9]	12.0931+ j0.0081 (12.093) [746.5]
	Eigenmode Solver $\rho_0 = \rho_0\lvert_{brass}$	5.6199+ j0.0068 (5.620) [413.2]	10.113+ j0.0043 (10.113) [1175.9]	11.118+ j0.0044 (11.188) [1271.4]	12.095+ j0.0045 (12.095) [1343.8]

quencies $\tilde{\omega}_{mnp} = \omega'_{mnp} + j\omega''_{mnp}$ for the even and odd TE_{mnp} open-box modes, respectively; the undamped (or driven) resonance frequencies, normally associated with frequency-domain simulations, is $f_{mnp} = |\tilde{\omega}_{mnp}|/2\pi$. Here, the multiple solutions from (4.69) and (4.70) correspond to different values of p. It is found, in our case, that the TE_{101}, TE_{201}, TE_{011} and TE_{111} modes all have even longitudinal symmetry about the centre of the sample [1].

It should be noted that the dominant TE_{101} open-box mode, which is loosely related to the Fabry-Pérot resonance (in terms of field patterns) is predicted to exist at 5.6056 GHz and 5.6229 GHz for Samples #1 and #2, respectively. These are above our dielectric-filled waveguide cut-off frequencies f_c of 4.30 GHz and 4.32 GHz, respectively, but below the recommended operational frequency range of WR-90 waveguide. It has been confirmed that f_{101} is relatively low because the evanescent fields outside of the dielectric sample decay exponentially over a relatively long distance [1].

For completeness, a similar approach can be used to derive the following generalised equations for the TM_{mnp} open-box modes (with the lowest-order TM_{111} mode having an eigenfrequency of $f_{111} = 12.8765$ GHz, which is just above the X-band frequency range of interest), with $\tilde{\varepsilon}_{①} = \tilde{\varepsilon}_{②}/\tilde{\varepsilon}_{reff} = \varepsilon_0$ [1],

$$\tilde{\varepsilon}_{reff}\gamma_{mn①} - \gamma_{mn②}\tanh\left(\frac{\gamma_{mn②}l}{2}\right) = 0 \quad \text{Odd modes} \tag{4.71}$$

$$\gamma_{mn②} - \tilde{\varepsilon}_{reff}\gamma_{mn①}\tanh\left(\frac{\gamma_{mn②}l}{2}\right) = 0 \quad \text{Even modes} \tag{4.72}$$

4.7 Conclusion

In this chapter, analytical field-based analysis of dielectric-filled metal-pipe rectangular waveguide (MPRWG) has been presented. In addition, the Q-factor of dielectric-filled MPRWG, acting as a Fabry-Pérot resonator, was also calculated using field-based integrals from analytical and numerical finte-element modelling. Finally, excitation of Fabry-Pérot 'open-box' modes in 3-D printed dielectric samples was investigated using analytical and numerical finite-element eigenmode solver. Three different techniques for modelling open-box mode resonances using the *COMSOL Multiphysics*® frequency domain solver were presented, which could closely model the actual MPRWG experimental setup operating in the dominant TE_{10} mode. The most accurate and reliable modelling technique was to define the dielectric section in the MPRWG as an in-homogeneous and anisotropic medium. The spectral location of the predicted box-mode resonances from this technique were within 0.01 GHz of those computed from the analytical method and the ones obtained from the *COMSOL Multiphysics*® eigenmode solver. Moreover, the predicted box-mode resonances were found to be within 0.05 GHz of those observed in measurements.

4.8 Acknowledgements

Work presented in this chapter was done under the supervision of Prof. Stepan Lucyszyn and was published in Sun *et al.* [1]. In addition, Prof. Lucyszyn went over each and every word of the original draft, provided helpful feedback and suggested improvements which were invaluable to the work presented in this chapter

References

[1] J. Sun, A. Dawood, W. J. Otter, N. M. Ridler, and S. Lucyszyn, "Microwave characterization of low-loss FDM 3-D printed ABS with dielectric-filled metal-pipe rectangular waveguide spectroscopy," *IEEE Access*, vol. 7, pp. 95455–95486, July 2019.

[2] J. Sun and S. Lucyszyn, "Extracting complex dielectric properties from reflection-transmission mode spectroscopy," *IEEE Access*, vol. 6, pp. 8302–8321, Mar. 2018.

[3] R. E. Collin, *Field theory of guided waves*, pp. 182–195. New York, NY: McGraw-Hill, 1960.

[4] S. Lucyszyn, D. Budimir, Q. H. Wang, and I. D. Robertson, "Design of compact monolithic dielectric-filled metal-pipe rectangular waveguides for millimetre-wave applications," *IEE Proc. Microw. Antennas and Prop.*, vol. 143, pp. 451–453, Oct. 1996.

[5] D. M. Pozar, *Microwave Engineering*, ch. Transmission lines and waveguides, pp. 111–119. John Wiley and Sons Inc., 4$^{\text{th}}$ ed., 2012.

[6] COMSOL RF Module. Accessed: 7 Mar. 2019. [Online]. Available: `https://uk.comsol.com/rf-module`.

[7] S. Papantonis and S. Lucyszyn, "Lossy spherical cavity resonators for stress-testing arbitrary 3D eigenmode solvers," *PIER*, vol. 151, pp. 151–167, 2015.

[8] R. B. Marks and D. F. Williams, "A general waveguide circuit theory," *J. Res. Nat. Inst. Stand. Technol.*, vol. 97, no. 5, pp. 533–562, 1992.

Chapter 5

Excitation of Fabry-Pérot Eigenmodes in Dielectric-Filled Waveguides

5.1 Introduction

3-D printing of microwave components has gained popularity in the last 5–10 years due to availability of affordable 3-D printers, which provides a cost-effective solution to testing and prototyping of 3-D printed microwave components [1]. With entry-level 3-D printers, 3-D printed metal-pipe rectangular waveguides (MPRWGs) have been demonstrated by D'Auria *et al.* [2], while, a 3-D printed MPRWG phase shifter was reported by Gillat *et al.* [3]. The terahertz (THz) spectral domain of the electromagnetic spectrum operating from 300 GHz up to 10 THz has recently attracted a lot of attention from researchers due to the potential for high-speed communication. Availability of better 3-D printers can enable 3-D printing for future applications [4] and waveguides operating up to 1.1 THz have been demonstrated [5].

Excitation of so-called Fabry-Pérot 'open-box' modes in MPRWG, with a 3-D printed dielectric-filled section, operating at X-band was recently reported by Sun *et al.* [6]. The reported WR-90 standard MPRWG with dimensions $a = 22.86$ mm and $b = 10.16$ mm was filled with an FDM 3-D printed ABS sample of target dimensions $22.860 \times 10.160 \times 9.626$ mm^3 [6]. For measurement purposes, the ends of the waveguide were terminated in air-filled sections coupling to a vector network analyser (VNA). In this set-up, the dominant TE_{10} mode was excited with the measured Scattering (S-) parameters showing dips in S_{11} and S_{21} at certain frequencies. These dips were observed for two different 3-D printed ABS samples. The dips or notches in measured response were identified as natural or damped/undriven resonances (or eigenmodes) of the dielectric sample under test in the open-ended waveguide. The authors called these resonances 'open-box' modes [6].

Excitation of these open-box modes were attributed to in-homogeneities and anisotropic behaviour of the 3-D printed ABS samples. Sun *et al.* [6] analysed these open-box modes using analytical and numerical methods but their analyses were restricted to MPRWG only. Here, the open-box modes in dielectric-filled parallel-plate (PPWG) and circular waveguides (CWG) is analysed using the commercial numerical package *COMSOL Multiphysics*® eigenmode solver. In addition, analytical expressions for these open-box modes have been derived for the PPWG and the CWG, from first principles using Maxwell's equations, which are then used to verity the numerical results. The results for the PPWG and the CWG are also compared against those for the MPRWG using the analytical and numerical methods presented in Chapter 4. Finally, a method to accurately predict the spectral location of these open-box modes in the driven S-parameter response, using the *COMSOL Multiphysics*® frequency domain solver, has been presented. Since these open-box modes can be excited in waveguide of any cross-sectional shape where the dielectric may not be in the form of a box as in MPRWG, in this study, these modes may be referred to as simply 'Fabry-Pérot eigenmodes' for generality.

5.2 Fabry-Pérot Eigenmodes in Parallel-Plate Waveguide

5.2.1 Theory

In any medium (unbound or guided), the generic complex propagation constant is given by,

$$\gamma_{ud} = \alpha + j\beta \equiv jk_{ud} \tag{5.1}$$

where, α is the attenuation constant, β is the phase constant and k_{ud} is the complex wavenumber within the unbound dielectric. In guided-wave media, the guided-wave propagation constant γ_g is defined as the propagation constant along the longitudinal direction of the waveguide. For the PPWG shown in Fig. 5.1 having perfect electric conductor (PEC) walls, operating in the $\mathrm{TE_m}$ or $\mathrm{TM_m}$ mode; the general text-book expression for guided wave propagation constant is,

$$\gamma_{gm}^2 = \gamma_{ud}^2 - \gamma_{cm}^2 \equiv \gamma_m^2 \tag{5.2}$$

All variables have their usual meaning, where subscript m denotes variations of mode field along the x-direction; γ_{ud} is the propagation constant in unbound dielectric medium; γ_{cm} is the cut-off propagation in guided media corresponding to mode number m; $\gamma_{ud} = jk_{ud} = j\omega\sqrt{\tilde{\mu}_{eff}\tilde{\varepsilon}_{eff}} = \omega\sqrt{\tilde{\mu}_{reff}\tilde{\varepsilon}_{reff}}/c$ where, $\omega = 2\pi f$ is the angular frequency in radians per second, f the frequency in Hertz; μ_0 and ε_0 being the permeability and permittivity of free space, respectively; and $c = 1/\sqrt{\mu_0\varepsilon_0}$ is the speed of light in free space; $\tilde{\mu}_{reff} = \tilde{\mu}_r = \mu_r' - j\mu_r''$ (the dielectric is assumed non-magnetic) and

$\tilde{\varepsilon}_{reff} = \tilde{\varepsilon}_r = \varepsilon_r' - j\varepsilon_r''$ are the effective complex relative permeability and permittivity, respectively; loss tangent is $\tan\delta = Im\{\tilde{n}^2\}/Re\{\tilde{n}^2\}$ and $\tilde{n} = \sqrt{\tilde{\mu}_{reff}\tilde{\varepsilon}_{reff}}$ is the complex refractive index of unbounded dielectric; ε_r' and $\tan\delta_e = \varepsilon_r''/\varepsilon_r'|_{\mu_r''=0}$ are the dielectric constant and loss tangent of the unbound dielectric, respectively; $k_{cm} = m\pi/a$ is the cut-off wavenumber of $\mathrm{TE_m}$ or $\mathrm{TM_m}$ modes; $\beta_{cm} = \omega_{cm}/c$ is the phase constant associated with angular cut-off frequency for the air-filled waveguide; $\omega_{cm} = 2\pi f_{cm}$ and $f_{cm} = k_{cm}c/2\pi$ are angular cut-off frequency and cut-off frequency, respectively, for the air-filled waveguide with mode number m.

Consider the PPWG structure shown in Fig. 5.1 where the structure is assumed to be infinite in y-direction, with PEC wall. Assume a TM wave is incident on the dielectric-filled section of the waveguide. Under steady-state conditions, there will be forward and backward waves, with As representing the complex amplitude coefficients associated with the forward travelling waves and Bs representing the complex amplitudes associated with the backward travelling waves. There are will be no reflected waves in Section ③ of the waveguide. Here, it is assumed for the sake of symmetry that Sections ① and ③ have the same material parameters. For the $\mathrm{TM_m}$ mode, the electric (E-)field and magnetic (H-)field components within the three waveguide sections are [7],

$$E_{x①} = -j\frac{\gamma_{m①}}{k_{cm}}\left(A_{m①}e^{-\gamma_{m①}z} + B_{m①}e^{-\gamma_{m①}z}\right)\cos\left(\frac{m\pi}{a}\right) \tag{5.3}$$

$$H_{y①} = -j\frac{\omega\tilde{\varepsilon}_{①}}{k_{cm}}\left(A_{m①}e^{-\gamma_{m①}z} - B_{m①}e^{-\gamma_{m①}z}\right)\cos\left(\frac{m\pi}{a}\right) \tag{5.4}$$

$$E_{z①} = \left(A_{m①}e^{-\gamma_{m①}z} + B_{m①}e^{-\gamma_{m①}z}\right)\sin\left(\frac{m\pi}{a}\right) \tag{5.5}$$

$$E_{x②} = -j\frac{\gamma_{m②}}{k_{cm}}\left(A_{m②}e^{-\gamma_{m②}z} + B_{m②}e^{-\gamma_{m②}z}\right)\cos\left(\frac{m\pi}{a}\right) \tag{5.6}$$

$$H_{y②} = -j\frac{\omega\tilde{\varepsilon}_{②}}{k_{cm}}\left(A_{m②}e^{-\gamma_{m②}z} - B_{m②}e^{-\gamma_{m②}z}\right)\cos\left(\frac{m\pi}{a}\right) \tag{5.7}$$

$$E_{z②} = \left(A_{m②}e^{-\gamma_{m②}z} + B_{m②}e^{-\gamma_{m②}z}\right)\sin\left(\frac{m\pi}{a}\right) \tag{5.8}$$

$$E_{x③} = -j\frac{\gamma_{m①}}{k_{cm}}A_{m①}e^{-\gamma_{m①}(z-l)}\cos\left(\frac{m\pi}{a}\right) \tag{5.9}$$

$$H_{y③} = -j\frac{\omega\tilde{\varepsilon}_{①}}{k_{cm}}A_{m③}e^{-\gamma_{①}(z-l)}\cos\left(\frac{m\pi}{a}\right) \tag{5.10}$$

$$E_{z③} = A_{m③}e^{-\gamma_{m①}(z-l)}\sin\left(\frac{m\pi}{a}\right) \tag{5.11}$$

The cut-off propagation constant is $\gamma_{cm} = jk_{cm} = m\pi/a$. For the air-filled Sections ① and ③, $\gamma_{①} = \gamma_{③}$. As shown in Fig. 5.1, the reference plane for fields with coefficient $A_{m③}$ is $z = l$ while the reference plane for rest of the fields is at $z = 0$. After applying boundary conditions $E_{x①}(z = 0) =$

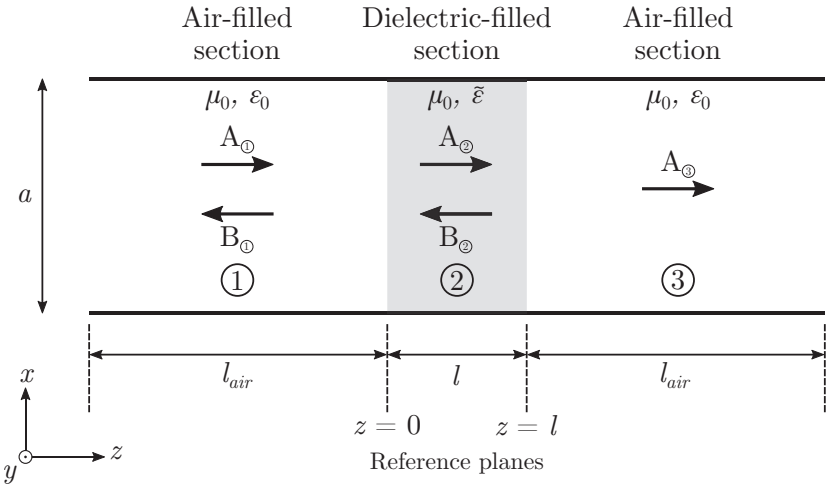


Figure 5.1: Illustration of an ideal dielectric-filled parallel-plate waveguide of width a. The length of the dielectric-filled section is l while the air-filled sections are of length l_{air}. In any section, As and Bs are the complex coefficients associated with the incident and reflected fields, respectively.

$E_{x②}(z=0)$, $H_{y①}(z=0) = H_{y②}(z=0)$, $E_{x②}(z=l) = E_{x③}(z=l)$ and $H_{y②}(z=l) = H_{y③}(z=l)$, the following characteristic matrix system is obtained,

$$\begin{bmatrix} \gamma_{m①} & \gamma_{m①} & -\gamma_{m②} & -\gamma_{m②} & 0 \\ \tilde{\varepsilon}_① & -\tilde{\varepsilon}_① & -\tilde{\varepsilon}_② & \tilde{\varepsilon}_② & 0 \\ 0 & 0 & \gamma_{m②}e^{-\gamma_{m②}l} & \gamma_{m②}e^{\gamma_{m②}l} & -\gamma_{m①} \\ 0 & 0 & \tilde{\varepsilon}_②e^{-\gamma_{m②}l} & -\tilde{\varepsilon}_②e^{\gamma_{m②}l} & -\tilde{\varepsilon}_① \end{bmatrix} \begin{bmatrix} A_{m①} \\ B_{m①} \\ A_{m②} \\ B_{m②} \\ A_{m③} \end{bmatrix} = \begin{bmatrix} 0 \\ 0 \\ 0 \\ 0 \end{bmatrix} \tag{5.12}$$

Using (5.12),

$$\frac{B_{m①}}{A_{m①}} = \frac{\left(1 - e^{-2\gamma_{m②}l}\right)(1-\zeta)(1+\zeta)}{(1+\zeta)^2 - e^{-2\gamma_{m②}l}(1-\zeta)^2} \tag{5.13}$$

$$\frac{A_{m②}}{A_{m①}} = \frac{-2\varsigma(1+\zeta)}{(1+\zeta)^2 - e^{-2\gamma_{m②}l}(1-\zeta)^2} \tag{5.14}$$

$$\frac{B_{m②}}{A_{m①}} = \frac{-2\varsigma e^{-2\gamma_{m②}l}(1-\zeta)}{(1+\zeta)^2 - e^{-2\gamma_{m②}l}(1-\zeta)^2} \tag{5.15}$$

$$\frac{A_{m③}}{A_{m①}} = \frac{4\zeta e^{-\gamma_{m②}l}}{(1+\zeta)^2 - e^{-2\gamma_{m②}l}(1-\zeta)^2} \tag{5.16}$$

with generalised coefficients,

$$\zeta = \begin{cases} \dfrac{\tilde{\varepsilon}_②\gamma_{m①}}{\tilde{\varepsilon}_①\gamma_{m②}} & \text{TM}_\text{m} \text{ modes} \\ \dfrac{\tilde{\mu}_①\gamma_{m②}}{\tilde{\mu}_②\gamma_{m①}} & \text{TE}_\text{m} \text{ modes} \end{cases} \tag{5.17}$$

and,

$$\varsigma = \begin{cases} \dfrac{\gamma_{m①}}{\gamma_{m②}} & \text{TM}_\text{m} \text{ modes} \\ \dfrac{\tilde{\mu}_①}{\tilde{\mu}_②} & \text{TE}_\text{m} \text{ modes} \end{cases} \tag{5.18}$$

where,

$$S_{11} \equiv \left.\frac{B_{m①}}{A_{m①}}\right|_{B_{m②}=0} \rightarrow B_{m①} \quad \text{with} \quad A_{m①} = 1 \tag{5.19}$$

and,

$$S_{21} \equiv \left.\frac{A_{m③}}{A_{m①}}\right|_{B_{m②}=0} \rightarrow A_{m③} \quad \text{with} \quad A_{m①} = 1 \tag{5.20}$$

Lossy resonators are characterised by their complex natural frequency [8],

$$\tilde{f}_0 = f_0^{'} + j f_0'' \tag{5.21}$$

where, f_0' is the damped or undriven resonant frequency and f_0'' denotes loss. For an ideal resonator without any losses, $f_0'' = 0$ and $\tilde{f}_0 = f_0'$. The unloaded Q-factor can be obtained from Papantonis and Lucyszyn [8] as,

$$Q_u(f_0') = \frac{f_0'}{2f_0''} \tag{5.22}$$

or [8],

$$Q_u(|\tilde{f}_0|) = \frac{|\tilde{f}_0|}{2f_0''} \tag{5.23}$$

The complex natural frequency, or eigenfrequency, response can be obtained by setting $A_{m①} = 0$ in (5.13), provided $B_{m①} \neq 0$, to obtain,

$$(1+\zeta)^2 - e^{-2\gamma_{m②}l}(1-\zeta)^2 = 0 \tag{5.24}$$

The solution of (5.24) results in an infinite number of solutions which are either designated as even or odd modes depending on the corresponding symmetry of electric field. The respective even and odd modes can be obtained by solving the following equations for complex eigenfrequencies,

$$(1+\zeta) + e^{-\gamma_{m②}l}(1-\zeta) = 0 \quad \text{Even modes} \tag{5.25}$$

$$(1+\zeta) - e^{-\gamma_{m②}l}(1-\zeta) = 0 \quad \text{Odd modes} \tag{5.26}$$

5.2.2 Results

A dielectric-filled PPWG was simulated using analytical results derived in Section 5.2 and using numerical finite element *COMSOL Multiphysics*® eigenmode solver. The dimensions of the PPWG were chosen as width $a = 22.86$ mm and the of length dielectric-filled section as $l = 9.626$ mm to correspond to the MPRWG dimensions from Sun *et al.* [6]. The dielectric constant chosen

as $\varepsilon'_{r②} = 2.325$ and loss tangent as $\tan\delta_{e②} = 19.73 \times 10^{-4}$ of the filled dielectric medium which corresponds to the extracted material parameters of the 3-D printed Sample #1 in Sun *et al.* [6]. The cut-off frequency of the air-filled PPWG was $f_c = 6.557$ GHz. It was assumed that the walls of the waveguide were made of PEC. The lowest order four Fabry-Pérot eigenmodes of the structure alongwith the associated unloaded Q-factors were computed using analytical and numerical eigenmode solver and the results are summarised in Table 5.1. The subscripts m and p in $\tilde{f}_{mp}$ refer to the number of variations along the x- and z-directions, respectively, of the electric or magnetic fields. From Table 5.1 it is clear that the first two resonant Fabry-Pérot eigenmodes, TE_{11} at 5.6092 GHz and TM_{11} at 6.1414 GHz, respectively; are well below the cut-off frequency (f_c) of the air-filled PPWG. The analytical and numerical results show excellent match with less than 0.13% discrepancy between the two sets of eigenfrequencies.

Following the approach outlined in Chapter 4 for excitation of open-box modes, using an anisotropic and in-homogeneous permittivity tensor, a 2-D PPWG structure was simulated using *COMSOL Multiphysics*® frequency domain solver. Within *COMSOL Multiphysics*®, the permittivity tensor for the dielectric-filled section of the PPWG was defined using (4.57), where,

$$f_{xx} = \Delta^{\%}_{\varepsilon'_{reff}} \left(-\frac{(x - a/2)}{a} + \frac{(z - l/2)}{l} \right) \tag{5.27}$$

$$f_{yy} = \Delta^{\%}_{\varepsilon'_{reff}} \left(\frac{(x - a/2)}{a} - \frac{(z - l/2)}{l} \right) \tag{5.28}$$

$$f_{zz} = \Delta^{\%}_{\varepsilon'_{reff}} \left(\frac{(x - a/2)}{a} + \frac{(z - l/2)}{l} \right) \tag{5.29}$$

$$f_{xy} = f_{yx} = f_{xz} = f_{zx} = f_{yz} = f_{zy} = \Delta^{\%}_{\varepsilon'_{reff}} \left(-\frac{(x - a/2)}{a} - \frac{(z - l/2)}{l} \right) \tag{5.30}$$

with all the scalars $c_{uv} = 5$ and,

$$\Delta^{\%}_{\varepsilon'_{reff}} = \frac{2}{100} \tag{5.31}$$

For a waveguide operating in the TE_1 mode at X-band (8.2–12.4 GHz), the return loss and insertion loss; using (5.19) and (5.20), respectively; are plotted in Fig. 5.2(a) (dotted lines) indicating a driven/undamped Fabry-Pérot resonance frequency close to 11 GHz. The solid lines in Fig. 5.2(a) correspond to simulated S-parameters from *COMSOL Multiphysics*®. Figure 5.2(b) is a plot of absorptance computed using,

$$\mathcal{A} = 1 - \mathcal{R} - \mathcal{T} = 1 - |S_{11}|^2 - |S_{21}|^2 \tag{5.32}$$

The absorptance plot clearly shows excitation of TE_{21} and TM_{21} open-box modes at 10.08 and 10.90 GHz, respectively, which is within 0.02 GHz of the predicted box-mode resonances obtained from the analytical method and the *COMSOL Multiphysics*® eigenmode solver, from Table 5.1.

Table 5.1: Fabry-Pérot eigenmodes (and associated mode Q-factors) computed using analytical field-based solutions and numerical eigenmode solver for the parallel-plate waveguide shown in Fig. 5.1.

Fabry-Pérot Eigenmode		TE_{11}	TM_{11}	TE_{21}	TM_{21}
$\tilde{f}_{mp}$ [GHz] (f'_{mp}) [$Q_u(f'_{mp})$]	Analytical	5.6092+ j0.003683 (5.6092) [761.5]	6.1414+ j0.001372 (6.1414) [2238.1]	10.0796+ j0.008648 (10.0796) [582.8]	10.8976+ j0.006639 (10.8976) [820.7]
	Numerical	5.6096+ j0.003593 (5.6096) [780.6]	6.1412+ j0.001364 (6.1412) [2251.2]	10.0920+ j0.008436 (10.0920) [598.2]	10.8990+ j0.006477 (10.8990) [841.4]

Electric field plots from numerically simulated *COMSOL Multiphysics*® eigenmode solver are shown in Figs. 5.3–5.6. MATLAB code for numerically solving the analytical equations (5.25) and (5.26) is given in Appendix I.

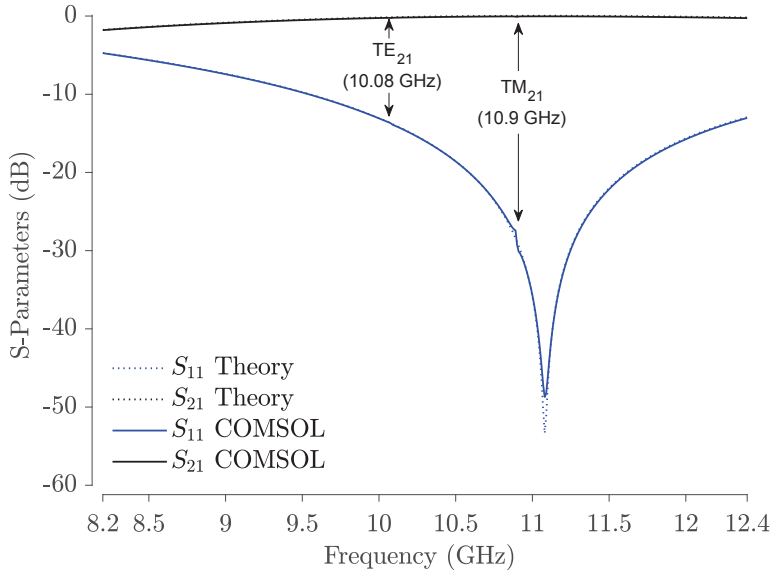
5.3 Fabry-Pérot Eigenmodes in Circular Waveguide

5.3.1 Theory

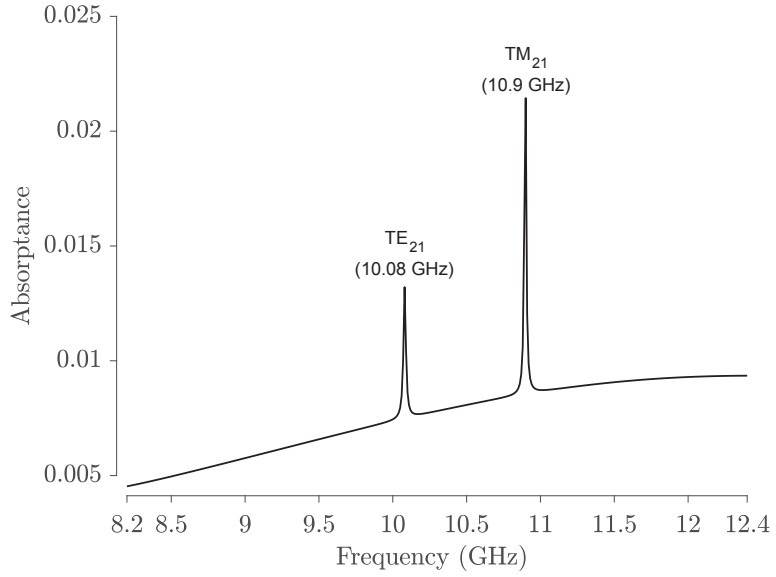
Consider the CWG structure shown in Fig. 5.7 where the structure is assumed to be infinite in either z-direction with PEC walls. Following the approach for PPWG using expressions for electric and magnetic field components [7], following characteristic matrix systems are obtained for the respective TM_{mn} and TE_{mn} mode operation of the waveguide,

$$\begin{bmatrix} \gamma_{mn①} & \gamma_{mn①} & -\gamma_{mn②} & -\gamma_{mn②} & 0 \\ \tilde{\varepsilon}_{①} & -\tilde{\varepsilon}_{①} & -\tilde{\varepsilon}_{②} & \tilde{\varepsilon}_{②} & 0 \\ 0 & 0 & \gamma_{mn②}e^{-\gamma_{mn②}l} & \gamma_{mn②}e^{\gamma_{mn②}l} & -\gamma_{mn①} \\ 0 & 0 & \tilde{\varepsilon}_{②}e^{-\gamma_{mn②}l} & -\tilde{\varepsilon}_{②}e^{\gamma_{mn②}l} & -\tilde{\varepsilon}_{①} \end{bmatrix} \begin{bmatrix} A_{mn①} \\ B_{mn①} \\ A_{mn②} \\ B_{mn②} \\ A_{mn③} \end{bmatrix} = \begin{bmatrix} 0 \\ 0 \\ 0 \\ 0 \end{bmatrix} \tag{5.33}$$

and,



(a)



(b)

Figure 5.2: Plot of (a) return loss and insertion loss; and (b) absorptance of the dielectric-filled parallel-plate waveguide, operating in the dominant TE_1 mode, with width $a = 22.86$ mm and dielectric section of length $l = 9.626$ mm; with dielectric constant $\varepsilon'_{reff②} = 2.325$ and loss tangent $\tan\delta_{e②} = 19.73 \times 10^{-4}$ of the filled in-homogeneous and anisotropic dielectric medium. Dotted lines in (a) show the ideal response computed from theory, while the solid lines show the simulated response from the *COMSOL Multiphysics*® frequency domain solver. The spectral location of box-mode resonances can be clearly seen in (b), with the predicted box-mode resonance frequencies within 0.02 GHz compared to those computed from theory and eigenmode solver, given in Table 5.1.

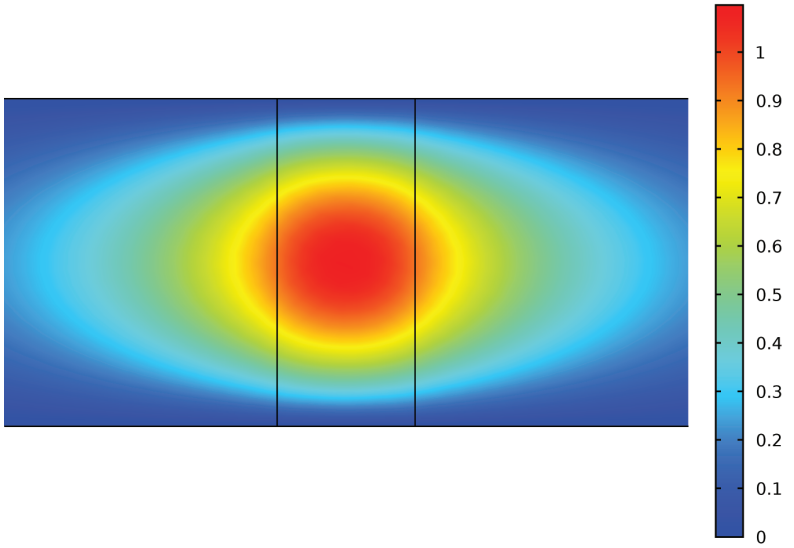


Figure 5.3: Numerically simulated E_y-field plot for the even TE_{11} Fabry-Pérot eigenmode at $f_{11} = 5.6096$ GHz for the parallel-plate waveguide. The field lines extend well outside the boundaries of the dielectric, while the mode exists well below the cut-off frequency of air-filled waveguide.

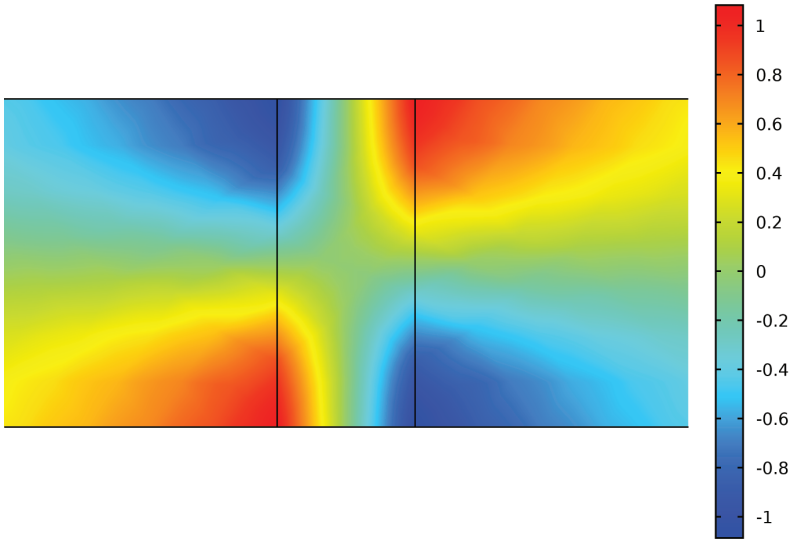


Figure 5.4: Numerically simulated E_x-field plot for the odd TM_{11} Fabry-Pérot eigenmode at $f_{11} = 6.1412$ GHz for the parallel-plate waveguide. The field lines extend well outside the boundaries of the dielectric, while the mode exists well below the cut-off frequency of air-filled waveguide.

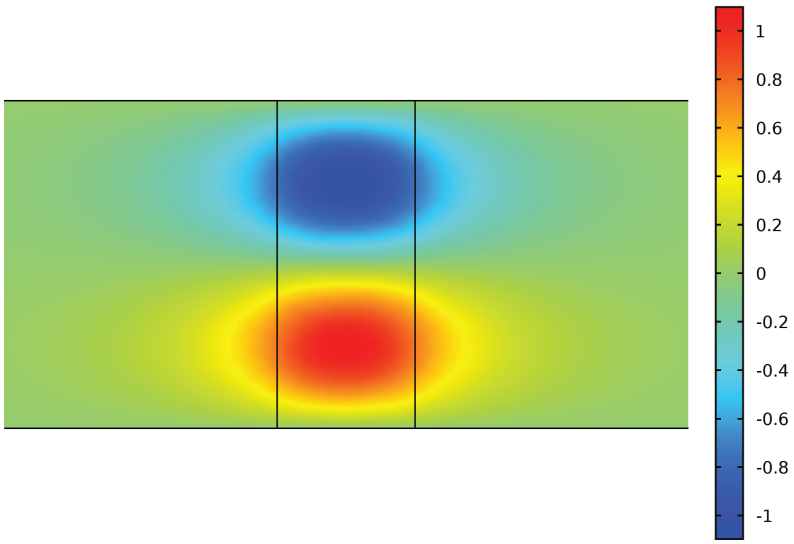


Figure 5.5: Numerically simulated E_y-field plot for the even TE_{21} Fabry-Pérot eigenmode at $f_{21} = 10.092$ GHz in the X-band for the parallel-plate waveguide.

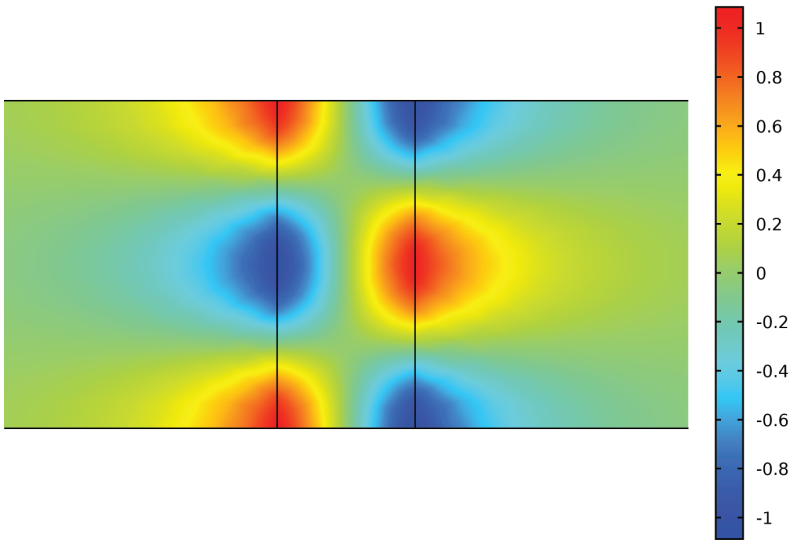


Figure 5.6: Numerically simulated E_x-field plot for the odd TM_{21} Fabry-Pérot eigenmode at $f_{21} = 10.899$ GHz in the X-band for the parallel-plate waveguide.

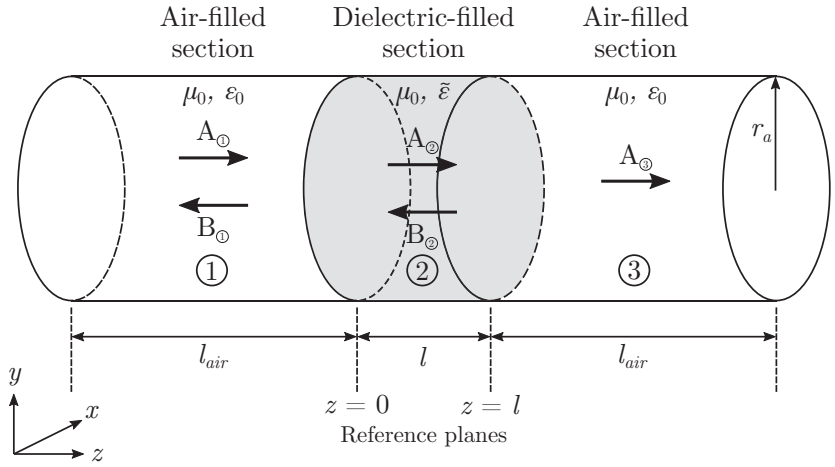


Figure 5.7: Illustration of an ideal dielectric-filled circular waveguide of radius r_a. The length of the dielectric-filled section is l while the air-filled sections are of length l_{air}. In any section, As and Bs are the complex coefficients associated with the incident and reflected fields, respectively.

$$\begin{bmatrix} \tilde{\mu}_① & \tilde{\mu}_① & -\tilde{\mu}_② & -\tilde{\mu}_② & 0 \\ \gamma_{mn①} & -\gamma_{mn①} & -\gamma_{mn②} & \gamma_{mn②} & 0 \\ 0 & 0 & \tilde{\mu}_② e^{-\gamma_{mn②} l} & \tilde{\mu}_② e^{\gamma_{mn②} l} & -\tilde{\mu}_① \\ 0 & 0 & \gamma_{mn②} e^{-\gamma_{mn②} l} & -\gamma_{mn②} e^{\gamma_{mn②} l} & -\gamma_{mn①} \end{bmatrix} \begin{bmatrix} A_{mn①} \\ B_{mn①} \\ A_{mn②} \\ B_{mn②} \\ A_{mn③} \end{bmatrix} = \begin{bmatrix} 0 \\ 0 \\ 0 \\ 0 \end{bmatrix} \tag{5.34}$$

where, the S-parameters are given by,

$$S_{11} = \frac{\left(1 - e^{-2\gamma_{mn②} l}\right)(1-\zeta)(1+\zeta)}{(1+\zeta)^2 - e^{-2\gamma_{mn②} l}(1-\zeta)^2} \tag{5.35}$$

and,

$$S_{21} = \frac{4\zeta e^{-\gamma_{mn②} l}}{(1+\zeta)^2 - e^{-2\gamma_{mn②} l}(1-\zeta)^2} \tag{5.36}$$

where,

$$\zeta = \begin{cases} \frac{\tilde{\varepsilon}_② \gamma_{mn①}}{\tilde{\varepsilon}_① \gamma_{mn②}} & \text{TM}_{\text{mn}} \text{ modes} \\ \frac{\tilde{\mu}_① \gamma_{mn②}}{\tilde{\mu}_② \gamma_{mn①}} & \text{TE}_{\text{mn}} \text{ modes} \end{cases} \tag{5.37}$$

with the guided wave propagation constant,

$$\gamma_{mn①,②} = \sqrt{k_{cmn}^2 - \omega^2 \tilde{\mu}_{①,②} \tilde{\varepsilon}_{①,②}} \tag{5.38}$$

where,

$$\gamma_{cmn} = j k_{cmn} = \begin{cases} j \frac{p_{mn}}{r_a} & \text{TM}_{\text{mn}} \text{ modes} \\ j \frac{p'_{mn}}{r_a} & \text{TE}_{\text{mn}} \text{ modes} \end{cases} \tag{5.39}$$

Here, r is the radial distance from the axis of the cylindrical waveguide, p_{mn} is the m$^{\text{th}}$ root of $J_n(x)$ such that $J_n(p_{mn}) = 0$, where $J_n(x)$ are the Bessel functions of the first kind. Similarly, p'_{mn} is the m$^{\text{th}}$ root of $J'_n(x)$ such that $J'_n(p'_{mn}) = 0$, where the operator $J'_n(x)$ is the derivative of $J_n(x)$. For the TM_{mn} and TE_{mn} propagating modes, the cut-off wavenumbers are $k_{cmn} = p_{mn}/r_a$ and $k_{cmn} = p'_{mn}/r_a$, respectively. The cut-off frequencies for the TM_{mn} and TE_{mn} propagating modes are then $f_{cmn} = k_c/2\pi\sqrt{\tilde{\mu}\tilde{\varepsilon}} = p_{mn}/2\pi r_a\sqrt{\tilde{\mu}\tilde{\varepsilon}}$ and $f_{cmn} = k_c/2\pi\sqrt{\tilde{\mu}\tilde{\varepsilon}} = p'_{mn}/2\pi r_a\sqrt{\tilde{\mu}\tilde{\varepsilon}}$, respectively. The subscripts m and n refer to the number of radial (r) and circumferential (ϕ) variations, respectively, of the electric or magnetic fields. Some of the values of p_{mn} and p'_{mn} for TM_{mn} and TE_{mn} propagating modes of the CWG are given in Table 5.2.

5.3.2 Results

The standard CWG operating at mid X-band (8.5–11.5 GHz) is specified to have a diameter $d_a = 23.83 = 2r_a$ mm [9]. Again, it was assumed that the wall of the waveguide is made of PEC with the dielectric constant and loss tangent of the filled section of the waveguide being $\varepsilon'_{r②} = 2.325$ and $\tan\delta_{e②} = 19.73 \times 10^{-4}$, respectively. The length of the dielectric-filled section was $l = 9.626$ mm. From Table 5.2, the smallest value of p'_{mn} (or p_{mn}) corresponds to the dominant TE_{11} propagating mode with a cut-off frequency of $f_{c11} = p_{11}c/2\pi r_a = 7.372$ GHz in air-filled CWG operating at X-band. The Fabry-Pérot eigenmodes of the resonant dielectric-filled waveguide are computed analytically and using the *COMSOL Multiphysics*® eigenmode solver with the obtained eigenfrequencies ($\tilde{f}_{mnp}$) listed in Table 5.3. Here, the subscripts m, n and p refer to the variation of fields along the radial r-, circumferential ϕ- and z-direction, respectively. The results obtained from analytical and numerical methods show excellent agreement with less than 0.02% discrepancy between the two sets of eigenfrequencies.

Following the approach outlined in Chapter 4 for excitation of open-box modes, using an anisotropic and in-homogeneous permittivity tensor, a 3-D CWG structure was simulated using *COMSOL Multiphysics*® frequency domain solver. Within *COMSOL Multiphysics*®, the permittivity tensor for the dielectric medium was defined using (4.57), where,

$$f_{xx} = \Delta^{\%}_{\varepsilon'_{reff}}\left(-\frac{x}{r_a} - \frac{y}{r_b} - \frac{(z-l/2)}{l}\right) \tag{5.40}$$

$$f_{yy} = \Delta^{\%}_{\varepsilon'_{reff}}\left(-\frac{x}{r_a} + \frac{y}{r_b} + \frac{(z-l/2)}{l}\right) \tag{5.41}$$

$$f_{zz} = \Delta^{\%}_{\varepsilon'_{reff}}\left(\frac{x}{r_a} + \frac{y}{r_b} - \frac{(z-l/2)}{l}\right) \tag{5.42}$$

$$f_{xy} = f_{yx} = f_{xz} = f_{zx} = f_{yz} = f_{zy} = \Delta^{\%}_{\varepsilon'_{reff}}\left(-\frac{x}{r_a} - \frac{y}{r_b} - \frac{(z-l/2)}{l}\right) \tag{5.43}$$

with all the scalars $c_{uv} = 5$ and,

$$\Delta^{\%}_{\varepsilon'_{reff}} = \frac{2}{100} \tag{5.44}$$

For a CWG operating in the TE_{11} mode at mid X-band (8.2–12.4 GHz), the return loss and insertion loss; using (5.19) and (5.20), respectively; are plotted in Fig. 5.8(a) (dotted lines) indicating a driven/undamped Fabry-Pérot resonance frequency close to 11.5 GHz. The solid lines in Fig. 5.8(a) correspond to simulated S-parameters from *COMSOL Multiphysics*® frequency domain solver. Figure 5.8(b) is a plot of absorptance; which clearly shows excitation of TM_{101}, TE_{121} and TE_{101} open-box modes at 8.81, 9.86 and 11.97 GHz, respectively; which is within 0.01 GHz of the predicted box-mode resonances obtained from the analytical method and the *COMSOL Multiphysics*® eigenmode solver, from Table 5.3.

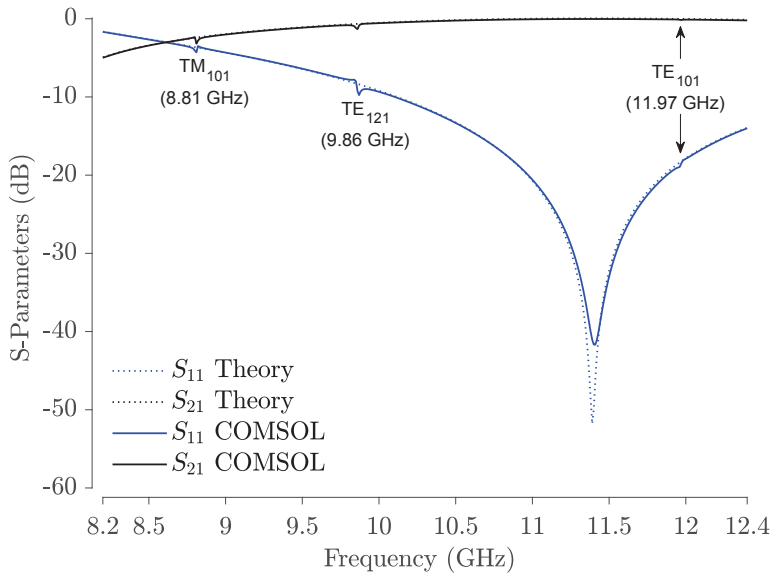
The 3-D surface field plots of respective Fabry-Pérot eigenmodes obtained from *COMSOL Multiphysics*® eigenmode solver are plotted in Figs. 5.9–5.12.

5.4 Conclusion

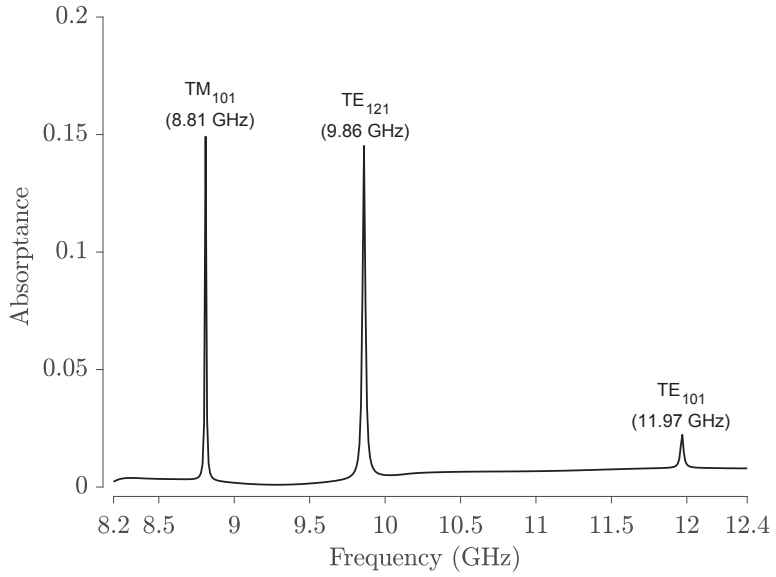
A rigorous analysis of Fabry-Pérot eigenmodes in dielectric-filled parallel-plate (PPWG) and circular waveguides (CWG) is presented using analytical methods from first principles. Eigenfrequencies of the resonant waveguide structures were obtained by numerically solving the analytical expressions for even and odd eigenmodes. The eigenfrequencies obtained from analytical method were compared against those obtained from numerical *COMSOL Multiphysics*® eigenmode solver showing less than 0.02% discrepancy agreement between the two approaches. Furthermore, based on the approach outlined in Chapter 4; for excitation of open-box modes in a waveguide, using in-homogeneous and anisotropic permittivity tensor; box-modes were modelled using *COMSOL Multiphysics*® frequency

Table 5.2: Numerical values of p_{mn} and p'_{mn} for selected mn mode numbers for the respective TM and TE modes in a circular waveguide. Table reproduced from Pozar [7].

n	TM			TE		
	p_{1n}	p_{2n}	p_{3n}	p'_{1n}	p'_{2n}	p'_{3n}
0	2.405	5.520	8.654	3.832	7.016	10.174
1	3.832	7.016	10.174	1.841	5.331	8.536
2	5.135	8.417	11.620	3.054	6.706	9.970

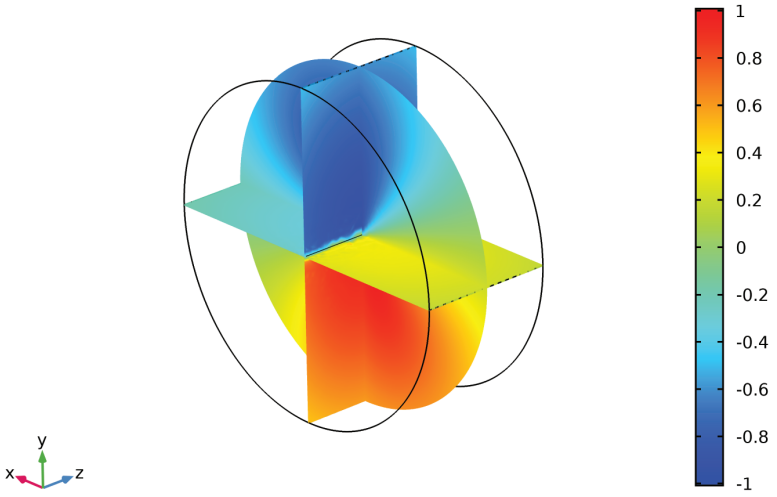


(a)

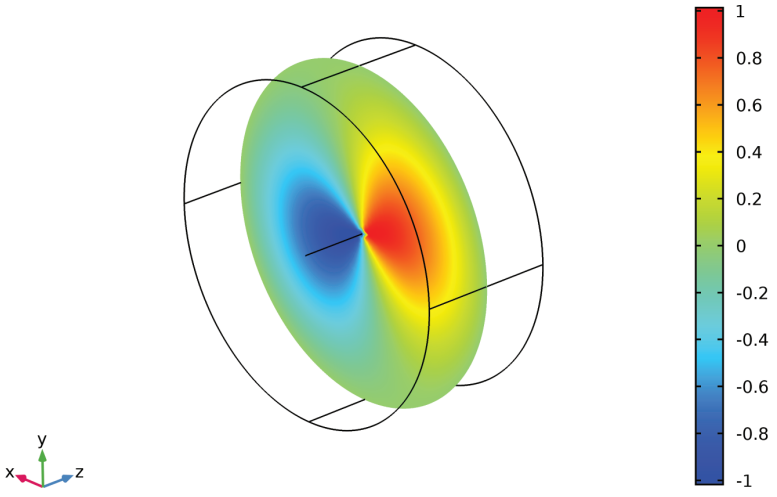


(b)

Figure 5.8: Plot of (a) return loss and insertion loss; and (b) absorptance of the dielectric-filled circular waveguide, operating in the dominant TE_{11} mode, with waveguide radius $r_a = 11.415$ mm and dielectric section of length $l = 9.626$ mm; with dielectric constant $\varepsilon'_{reff②} = 2.325$ and loss tangent $\tan\delta_{e②} = 19.73 \times 10^{-4}$ of the filled in-homogeneous and anisotropic dielectric medium. Dotted lines in (a) show the ideal response computed from theory, while the solid lines show the simulated response from the *COMSOL Multiphysics*® frequency domain solver. The spectral location of box-mode resonances can be clearly seen in (b), with the predicted box-mode resonance frequencies within 0.01 GHz compared to those computed from theory and eigenmode solver, given in Table 5.3.



(a)



(b)

Figure 5.9: Numerically simulated field plots for TE_{111} Fabry-Pérot eigenmode at $f_{111} = 6.4224$ GHz, obtained from *COMSOL Multiphysics*® for a dielectric-filled circular waveguide: (a) E_r-field; (b) E_ϕ-field. The mode exists well below the cut-off frequency of the waveguide.

Table 5.3: Fabry-Pérot eigenmodes (and associated mode Q-factors) in a circular waveguide computed using analytical field-based solutions and numerical eigenmode solver for the CWG (Fig. 5.7).

Fabry-Pérot Eigenmode		TE_{111}	TM_{101}	TE_{121}	TE_{101}
$\tilde{f}_{mp}$ [GHz] ($\lvert\tilde{f}_{mp}\rvert$) [$Q_u(f'_{mp})$]	Analytical	6.4221+ j0.004586 (6.4221) [700.2]	8.8146+ j0.003965 (8.8146) [1111.6]	9.8503+ j0.008397 (9.8503) [586.5]	11.9703+ j0.010698 (11.9703) [559.5]
	Numerical	6.4224+ j0.004791 (6.4224) [670.3]	8.8134+ j0.004054 (8.8134) [1087.0]	9.8512+ j0.008398 (9.8512) [586.5]	11.97+ j0.010698 (11.9700) [595.5]

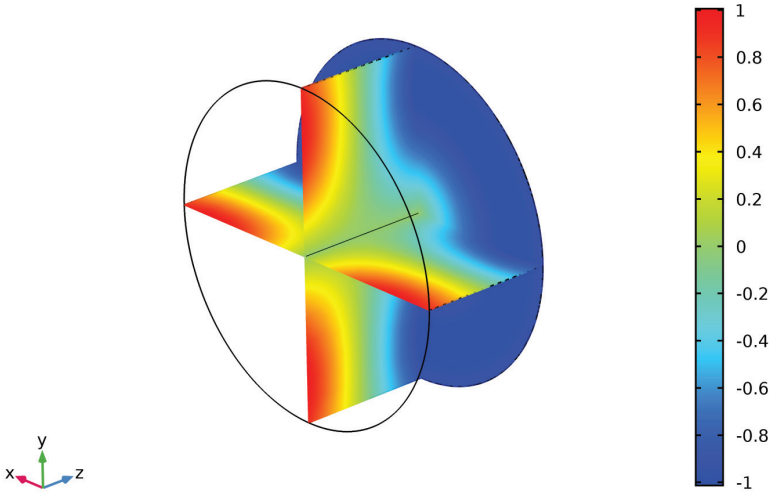


Figure 5.10: Numerically simulated E_r-field plot for the odd TM_{101} Fabry-Pérot eigenmode at $f_{101} = 8.8134$ GHz, obtained from *COMSOL Multiphysics*® eigenmode solver for a dielectric-filled circular waveguide.

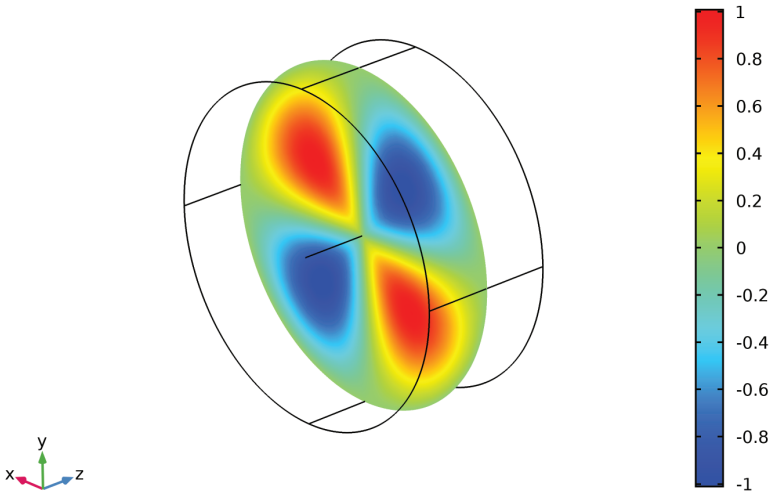


Figure 5.11: Numerically simulated E_ϕ-field plot for TE_{121} Fabry-Pérot eigenmode at $f_{121} = 9.8512$ GHz, obtained from *COMSOL Multiphysics*® eigenmode solver for a dielectric-filled circular waveguide.

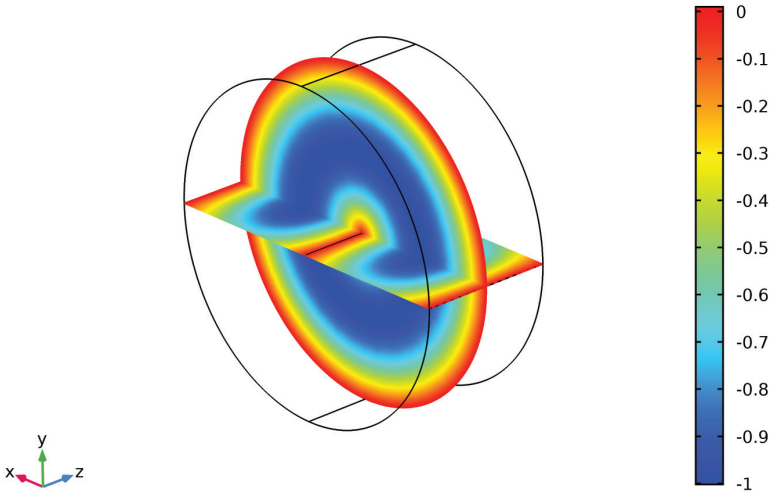


Figure 5.12: Numerically simulated E_ϕ-field plot for TE_{101} Fabry-Pérot eigenmode at $f_{101} = 11.97$ GHz, obtained from *COMSOL Multiphysics*® eigenmode solver for a dielectric-filled circular waveguide.

domain solver for the PPWG and the CWG. The predicted spectral location of box modes using this approach were found to be within 0.02 GHz of those obtained from the analytical method and those from the *COMSOL Multiphysics*® eigenmode solver. Thus, it has been demonstrated that *COMSOL Multiphysics*® frequency domain solver is a useful tool for modelling open-box modes in a driven dielectric-filled waveguide structure.

5.5 Acknowledgements

The work presented in this chapter was done under the supervision of Prof. Stepan Lucyszyn.

References

[1] W. J. Otter and S. Lucyszyn, "3-D printing of microwave components for 21st century applications," in *IEEE MTT-S International Microwave Workshop Series on Advanced Materials and Processes for RF and THz Applications (IMWS-AMP)*, Chengdu, China, pp. 1–3, IEEE, July 2016.

[2] M. D'Auria, W. J. Otter, J. Hazell, B. T. Gillatt, C. Long-Collins, N. M. Ridler, and S. Lucyszyn, "3-D printed metal-pipe rectangular waveguides," *IEEE Trans. Compon. Packag. Manuf. Technol.*, vol. 5, pp. 1339–1349, Sept. 2015.

[3] B. T. Gillatt, M. D'Auria, W. J. Otter, N. M. Ridler, and S. Lucyszyn, "3-D printed variable phase shifter," *IEEE Microw. Wireless Compon. Lett.*, vol. 26, pp. 822–824, Oct. 2016.

[4] W. J. Otter and S. Lucyszyn, "Hybrid 3-D-printing technology for tunable THz applications," *Proc. IEEE*, vol. 105, pp. 756–767, Apr. 2016.

[5] W. J. Otter, N. M. Ridler, H. Yasukochi, K. Soeda, K. Konishi, J. Yumoto, M. Kuwata-Gonokami, and S. Lucyszyn, "3D printed 1.1 THz waveguides," *Electron. Lett.*, vol. 53, pp. 471–473, Mar. 2017.

[6] J. Sun, A. Dawood, W. J. Otter, N. M. Ridler, and S. Lucyszyn, "Microwave characterization of low-loss FDM 3-D printed ABS with dielectric-filled metal-pipe rectangular waveguide spectroscopy," *IEEE Access*, vol. 7, pp. 95455–95486, July 2019.

[7] D. M. Pozar, *Microwave Engineering*, ch. Transmission lines and waveguides, pp. 102–110. John Wiley and Sons Inc., 4$^{\text{th}}$ ed., 2012.

[8] S. Papantonis and S. Lucyszyn, "Lossy spherical cavity resonators for stress-testing arbitrary 3D eigenmode solvers," *PIER*, vol. 151, pp. 151–167, 2015.

[9] Everyting RF: Waveguide sizes. Accessed: Nov. 27 2019. [Online]. Available: `https://www.everythingrf.com/tech-resources/waveguides-sizes`.

Chapter 6

An S-Parameter Renormalisation Technique for Resolving Ambiguities Under Noisy Measurement Conditions

6.1 Introduction

A manual graphical technique was introduced by Sun and Lucyszyn [1] for extraction of complex dielectric properties using reflection-transmission mode spectroscopy. The strength of this particular graphical technique was that it could recover the dielectric properties of a sample under test under noiseless conditions from only the power responses and was intended as a low-cost spectroscopy technique. Only three power response measurements were sufficient, namely reflectance, transmittance and reflectance with a PEC termination. The graphical technique was further improved by Sun *et al.* [2] who used the graphical technique, for the first time, to extract complex dielectric properties of an FDM 3-D printed ABS sample, under noisy measurement conditions. The sample under test, of known dimensions, was placed in an MPRWG and S-parameters of the experimental set-up were measured using the TRL calibration technique.

Sun *et al.* [2] proposed that, by introducing mathematically computed S-parameters of a half-stage and a cascaded stage, ambiguities resulting from noisy measurements could be resolved. One drawback of the graphical technique was that, at each frequency point, the complex dielectric properties must be manually extracted using visual inspection from plots of constraint equations. For this reason, Sun *et al.* have proposed a technique based on S-parameter renormalisation for resolving ambiguities, which are due to inherent noise in measurements. Sun *et al.* have also estimated the signal-to-noise ratio of the vector network analyser (VNA) from measurements of a

thru section of MPRWG operating at X-band [2].

In this chapter, the automated S-parameter renormalisation technique by Sun *et al.* [2] will be presented with reference to their published results. In addition, the results from VNA noise analysis done by Sun *et al.* [2] will also be presented.

6.2 Spectroscopic Extraction of Complex Dielectric Properties Using the Graphical Method

The *graphical*-based technique proposed by Sun *et al.* [1] for extracting complex dielectric properties was originally intended for low-cost, scalar, reflection-transmission mode spectroscopy [2]. In theory, a scalar network analyser only requires three physical measurements to resolve the ambiguity with multiple solutions possible in $n - \kappa$ space: (i) reflectance, (ii) transmittance; and (iii) reflectance with a PEC backshort (i.e., with $Z_T = 0$ at port-2) [2]. However, the third measurement is not physically necessary if a VNA is employed, as it provides both the magnitude and phase information needed to mathematically emulate it; avoiding the introduction of any additional measurement uncertainty [2].

By mathematically short circuiting the output port of an original two-port S-parameter network, having matrix $[S]$, the S_{11}^{PEC} and resulting PEC reflectance $\mathcal{R}^{PEC}$ from the resulting one-port network (i.e., shorted l-stage, where l represents the thickness of the dielectric-filled material) can be mathematically emulated using the following [1],

$$S_{11}^{PEC} = S_{11} - \frac{S_{12}S_{21}}{1 + S_{22}} \tag{6.1}$$

$$\mathcal{R}^{PEC} \equiv \left| S_{11}^{PEC} \right|^2 \tag{6.2}$$

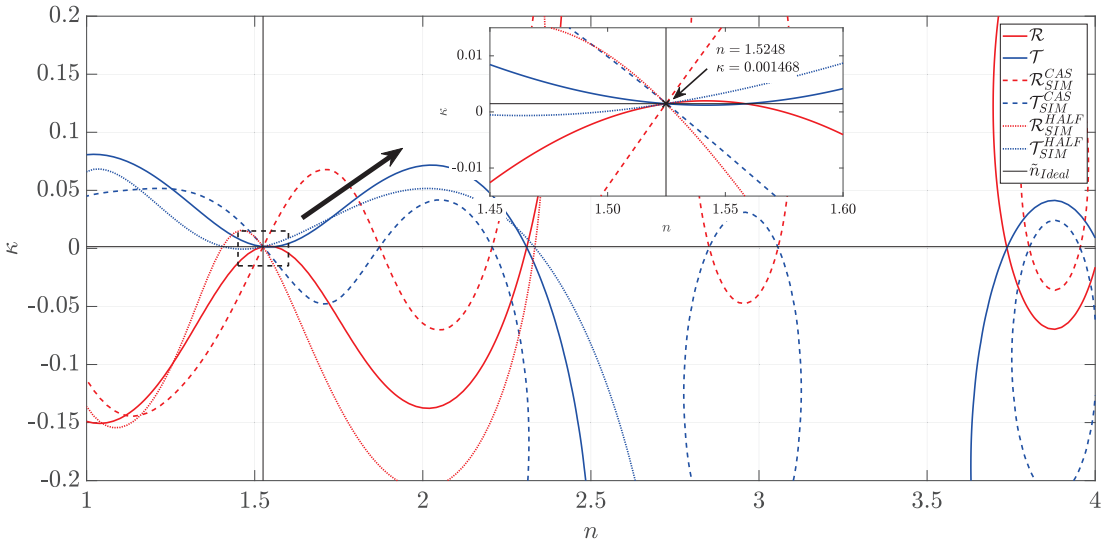
The exact complex dielectric properties can then be theoretically extracted by finding the simultaneous solution for the following three equations using the Graphical technique with ideal measured values [1],

$$\left| S_{11SIM}\left(\tilde{n}\right) \right|^2 - \mathcal{R}_{MEAS} = 0 \tag{6.3}$$

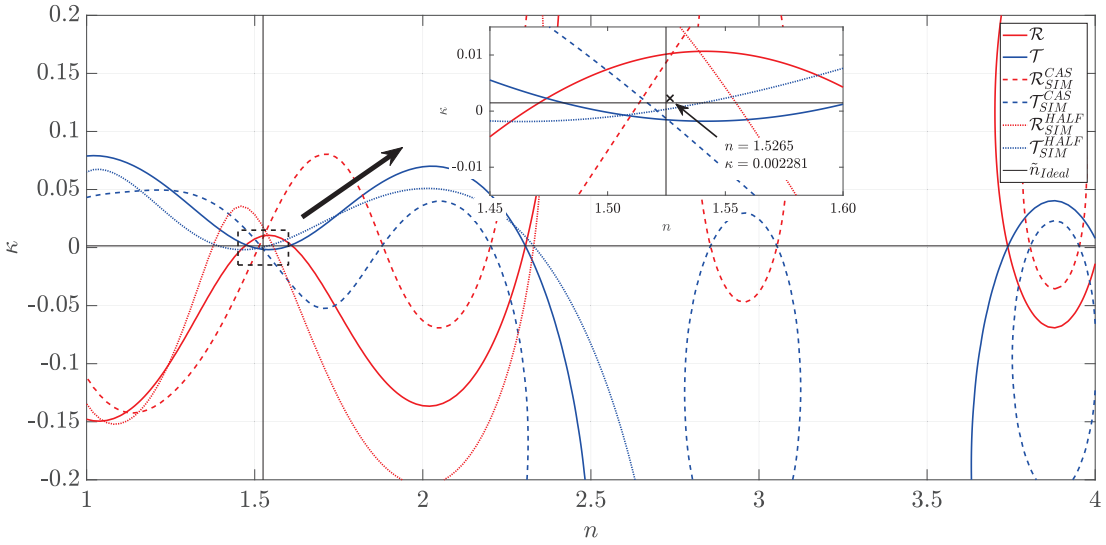
$$\left| S_{21SIM}\left(\tilde{n}\right) \right|^2 - \mathcal{T}_{MEAS} = 0 \tag{6.4}$$

$$\left| S_{11SIM}^{PEC}\left(\tilde{n}\right) \right|^2 - \mathcal{R}_{MEAS}^{PEC} = 0 \tag{6.5}$$

where, $S_{11SIM}(\tilde{n})$, $S_{21SIM}(\tilde{n})$ and $S_{11SIM}^{PEC}(\tilde{n})$ are analytically simulated variables, all being a function of the extractable complex refractive index $\tilde{n} = n - j\kappa = \sqrt{\tilde{\mu}_r \tilde{\varepsilon}_{reff}}$; optical constants n and κ are the associated index of refraction (or refractive index) and extinction coefficient (or absorption



(a)



(b)

Figure 6.1: Individual solutions in $n - \kappa$ space at 8.2 GHz from (a) ideal noiseless measurements emulated with $\tilde{n}_{ideal} = 1.5248 - j0.001468$ (set equal to $\tilde{n}(11.08\text{ GHz})$ from Sample #1 associated with Fabry-Pérot resonance modelling with the *variational* method); and (b) real noisy measurements for Sample #1, having $\tilde{n}_{extracted} = 1.5265 - j0.002281$ (corresponding to a dielectric constant and loss tangent of 2.330 and 29.89×10^{-4}, respectively). Figure redrawn from Sun *et al.* [2].

index), respectively [1]; $\mathcal{R}_{MEAS}$ and $\mathcal{T}_{MEAS}$ are the measured reflectance and transmittance for the l-stage network, respectively.

With ideal measured values [1], all responses from the l-stage reflectance, transmittance and port-1 reflectance with port-2 short-circuited simultaneously coincide at the true values for n and κ in $n-\kappa$ space. It was found by Sun *et al.* [2] that (6.5) is sensitive to measurement noise and a more resilient Graphical approach proposed by them replaced (6.5) with alternative constraints. For example, $2l$-stage responses, where two identical S-parameters for the l-stage matrix $[S]$ are cascaded together to create matrix $[S^{CAS}]$, which emulates a double-length section having S-parameters [2]:

$$S_{11}^{CAS} = S_{11}\left(1 + S_{21}^{CAS}\right) \quad \text{and} \quad S_{21}^{CAS} = \frac{{S_{21}}^2}{1 - {S_{11}}^2} \tag{6.6}$$

$$\mathcal{R}^{CAS} \equiv \left|S_{11}^{CAS}\right|^2 \quad \text{and} \quad \mathcal{T}^{CAS} \equiv \left|S_{21}^{CAS}\right|^2 \tag{6.7}$$

where, $\mathcal{R}^{CAS}$ and $\mathcal{T}^{CAS}$ are the reflectance and transmittance for the $2l$-stage cascaded network, respectively.

Therefore, the complex refractive index can be extracted by simultaneously solving the following equations for the $2l$-stage responses in addition to (6.3)–(6.4) for the l-stage [2],

$$\left|S_{11SIM}^{CAS}\left(\tilde{n}\right)\right|^2 - \mathcal{R}_{MEAS}^{CAS} = 0 \tag{6.8}$$

$$\left|S_{21SIM}^{CAS}\left(\tilde{n}\right)\right|^2 - \mathcal{T}_{MEAS}^{CAS} = 0 \tag{6.9}$$

Similarly, it is also possible to emulate the half-length section (i.e., $l/2$-stage) S-parameters from the following [2]:

$$S_{11}^{HALF} = \frac{S_{11}}{1 + S_{21}} \quad \text{and} \quad S_{21}^{HALF} = \sqrt{S_{21}\left[1 - \left(\frac{S_{11}}{1 + S_{21}}\right)^2\right]} \tag{6.10}$$

It can be shown that the $l/2$- and l-stage S-parameters from (6.10) are, respectively, equal to the l- and $2l$-stage S-parameters from (6.6). The $l/2$-stage reflectance and transmittance are [2],

$$\mathcal{R}^{HALF} \equiv \left|S_{11}^{HALF}\right|^2 \quad \text{and} \quad \mathcal{T}^{HALF} \equiv \left|S_{21}^{HALF}\right|^2 \tag{6.11}$$

where, $\mathcal{R}^{HALF}$ and $\mathcal{T}^{HALF}$ are the respective reflectance and transmittance for the $l/2$-stage cascaded network.

Therefore, in principle, the complex refractive index can be extracted by simultaneously solving the following equations for the $l/2$-stage responses in addition to (6.3)–(6.4) for the l-stage and (6.8)–(6.9) for the $2l$-stage [2],

$$\left|S_{11SIM}^{HALF}\left(\tilde{n}\right)\right|^2 - \mathcal{R}_{MEAS}^{HALF} = 0 \tag{6.12}$$

$$\left|S_{21SIM}^{HALF}\left(\tilde{n}\right)\right|^2 - \mathcal{T}_{MEAS}^{HALF} = 0 \tag{6.13}$$

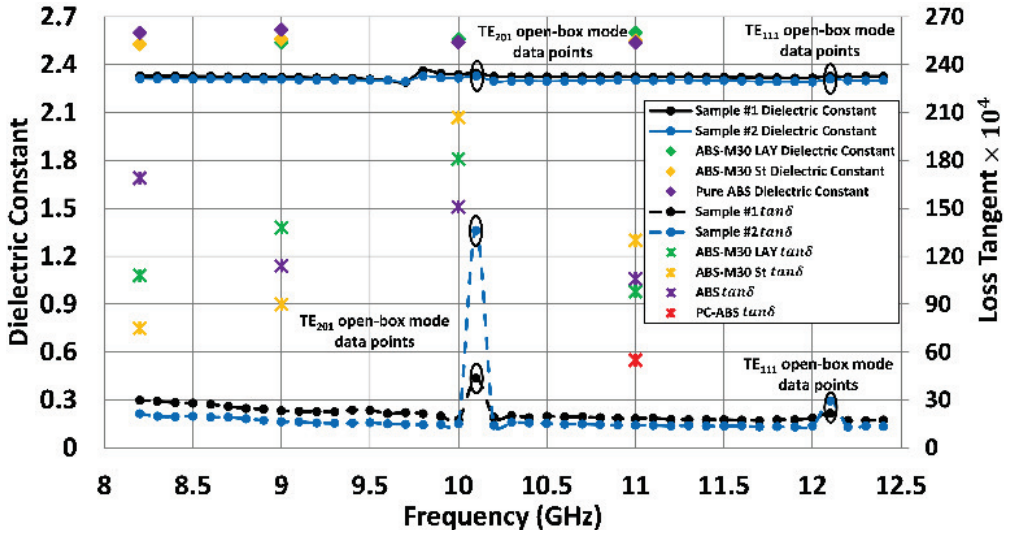


Figure 6.2: Extracted values for dielectric constant and loss tangent (in 0.1 GHz steps) using the manual Graphical approach with l- and $2l$-stages for Samples #1 and #2. Figure reproduced from Sun *et al.* [2].

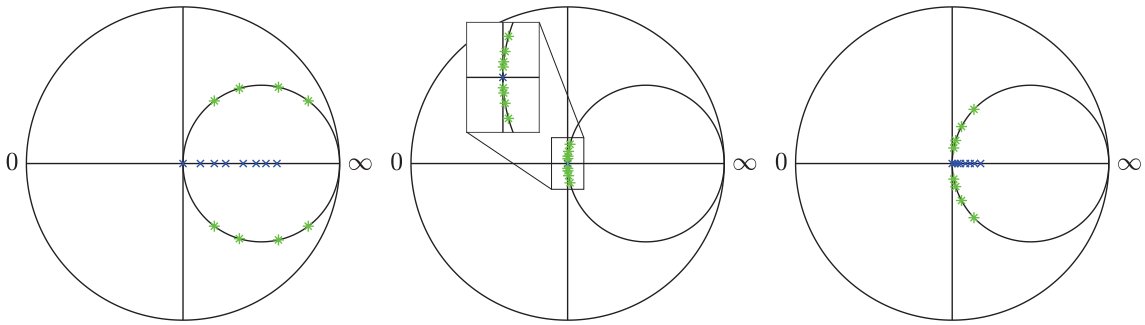
6.3 Spectroscopic Extraction of Complex Dielectric Properties Using The S-Parameter 'Renormalisation' Method

With ideal measured values, at each individual frequency, the simultaneous complex root solutions to (6.3)–(6.5) give the ideal complex refractive index $\tilde{n}_{ideal}$, seen as a single intersection point in $n - \kappa$ space. However, as previously seen, with real, noisy, measurements there is no longer a single intersection point [2]. By scanning $n - \kappa$ space, the magnitudes of the right-hand sides of (6.3)–(6.5) can be summed and projected onto a contour plot. As a result, with ideal measured values there will be a single one-dimensional spike in $n - \kappa$ space, touching zero at the simultaneous solution; while with real-noise-affected, measurements a three-dimensional spike will approach zero [2]. The problem is that of essentially searching for the minimum value as outlined by Challa *et al.* [3]. However, the approach by Challa *et al.* [3] does not consider singularities resulting from Fabry-Pérot resonances. The Renormalisation approach adds more constraints to the original l-stage and $2l$-stage equations by considering renormalised sets of S-parameters to eliminate ambiguities due to Fabry-Pérot resonance as demonstrated [2] and discussed here. In practice, the contour plot can be best observed on a logarithmic scale, by first subtracting the minimum value and then dividing throughout by the maximum value (giving normalised values between 0 and 1). At some frequencies there may be multiple intersection points in $n - \kappa$ space that result in multiple minima.

The dominant minimum in this case might correspond to incorrect values for n and κ [2].

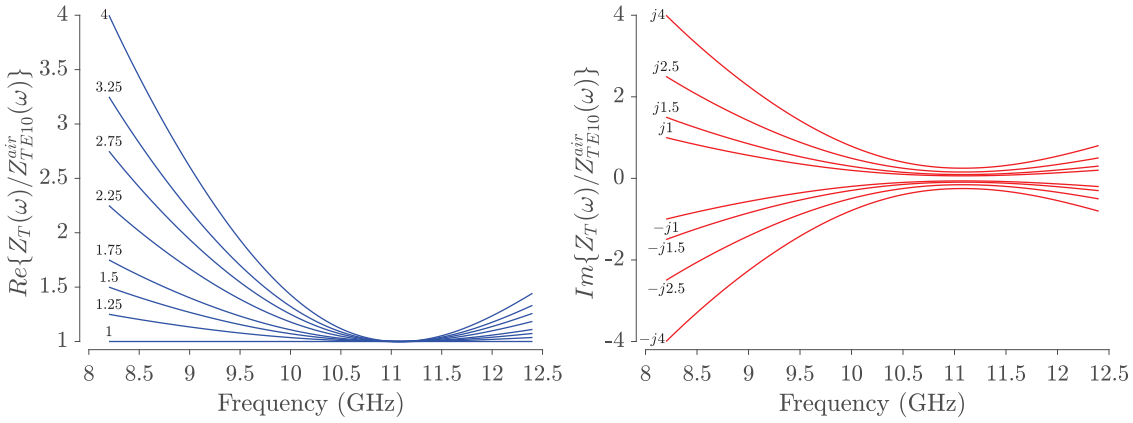
Adding more equations (increasing sensitivity) and including more constraints to the existing equations (increasing robustness) lead to a sharper spike at the correct simultaneous solution in $n-\kappa$ space. The former can be implemented by mathematically introducing additional sub- and multiple-stages (e.g., $l/2$-stage and $2l$-stage) to the original l-stage and shorted l-stage. The latter can employ port reference impedance renormalisation [2]. While spurious minima are generated, the correct solution will have the dominant (deepest) spike. This is because, with impedance renormalisation, the correct intersections will remain fixed in $n-\kappa$ space, while spurious intersections move around and are subsequently averaged-out on aggregate [2]. Spurious spikes can be removed by [2]: (i) increasing grid resolution (thereby reducing discretisation error); (ii) introducing more sub- or multiple-stages; (iii) choosing a different port reference impedance renormalisation set. As a general rule-of-thumb, in addition to the original S-parameters (i.e., l-stage having $Z_T(\omega) = Z^{air}_{TE10}(\omega)$, calculated using (4.20)) it was found by Sun *et al.* [2] that the best selection of renormalisation impedances includes several purely resistive impedances above $Z^{air}_{TE10}(\omega)$ (sharpening the spike in the κ-direction) and introducing an equal number of positive and negative reactances (sharpening the spike in the n-direction). It was found that at the Fabry-Pérot resonance frequency, the method is very sensitive [2]. As a result, the port reference impedances should be close to $Z^{air}_{TE10}(\omega)$ at the Fabry-Pérot resonance frequency, while spreading out more from $Z^{air}_{TE10}(\omega)$ when moving further away from the Fabry-Pérot resonance frequency. A good implementation has a spread of port reference impedances with $r = Re\{Z_T(\omega)/Z^{air}_{TE10}(\omega)\} \in [1, 4]$ and $x = Im\{Z_T(\omega)/Z^{air}_{TE10}(\omega)\} \in [-4, 4]$. As a good example, when normalised to $Z^{air}_{TE10}(\omega)$, one can adopt the following recommended port reference impedance set [2]: $Z_T(\omega)/Z^{air}_{TE10}(\omega) \in [1, 1.25, 1.5, 1.75, 2.25, 2.75, 3.25, 4, 1 \pm j1, 1 \pm j1.5, 1 \pm j2.5, 1 \pm j4]$ used at all frequencies; purely real port reference impedances lie on the $r \pm j0$ line above unity, while complex impedances lie on the $1 \pm jx$ circle. This dynamic spread is shown in the Smith chart illustrations of Fig. 6.3(a) at 8.2 Ghz, with Fig. 6.3(b) at the Fabry-Pérot resonance frequency and Fig. 6.3(c) at 12.5 GHz. Figure 6.4 shows port reference impedances as a function of frequency with $|S_{11SIM}|^2$ used as a scaling function. The choice of port reference impedances renormalisation set is flexible (in terms of size and values), which can change with frequency and/or measurement conditions.

This measurement post-processing technique can be fully automated, as demonstrated in this section for all the frequency points generated by the VNA. As an implementation consideration, there may be a practical limit on the discretisation of $n-\kappa$ space, in terms of computational time and memory storage. The optimal approach is to first run coarse discretisation over a wide $n-\kappa$



(a) (b) (c)

Figure 6.3: Port reference impedances plotted on impedance Smith chart normalised to $Z^{air}_{TE10}(\omega)$ for the 3-D printed Sample #1 [2]. Blue crosses represent purely real impedances, while green asterisks represent complex impedances on the $1 \pm jx$ circle: (a) 8.2 GHz; (b) 11.08 GHz; (c) 12.4 GHz. Figure redrawn from Sun *et al.* [2].



(a) (b)

Figure 6.4: Port reference impedance plotted against frequency normalised to $Z^{air}_{TE10}(\omega)$ for the 3-D printed Sample #1 [2], corresponding to recommended data set: (a) $Re\{Z_T(\omega)/Z^{air}_{TE10}(\omega)\}$ corresponding to the $r \pm j0$ line; (b) $Im\{Z_T(\omega)/Z^{air}_{TE10}(\omega)\}$ corresponding to the $1 \pm jx$ circle. Figure redrawn from Sun *et al.* [2].

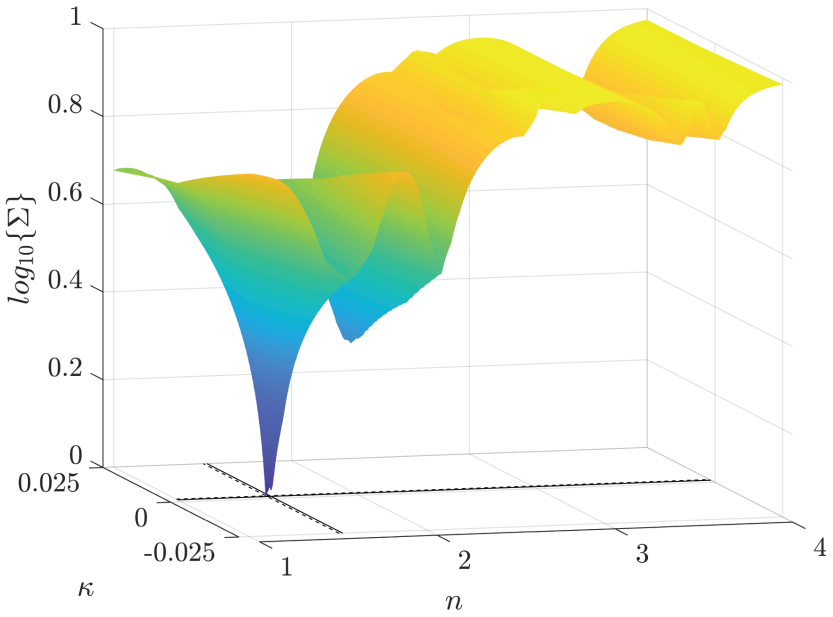
space, followed by finer discretisation over a reduced $n - \kappa$ space centred on the expected value.

With the previously recommended port reference impedance renormalisation set, dielectric properties were automatically extracted. Coarse discretisation had $n \in [1, 4]$ and $\kappa \in [-0.025, 0.025]$ and the finer discretisation had $n \in [1.5, 1.55]$ and $\kappa \in [0, 0.009]$, while grid size was kept at 1000^2 for both runs. With the latter, contour plots have less spikes that allow for easy identification of $\tilde{n}_{extracted}$. The former gives the worst-case condition. For example, contour plots with coarse discretisation are shown for Sample #1 at 9 GHz, without impedance renormalisation in Fig. 6.5 and with impedance renormalisation in Fig. 6.6, where both figures represent the common log of the summation Σ of (6.3)–(6.5), (6.8)–(6.9) and (6.12)–(6.13). The solid black lines in Fig. 6.5(b) and Fig. 6.6(b) correspond to $\tilde{n}$(11.08 GHz) for Sample #1 associated with Fabry-Pérot resonance modelling with the *variational* method M1., while the dashed black liens show the location of absolute minimum (extracted value). As expected, without impedance renormalisation there are multiple minima; while the contour plot with impedance renormalisation shows that the deepest spike corresponds to the absolute minimum close to $\tilde{n}$(11.08 Ghz) and other spikes are suppressed.

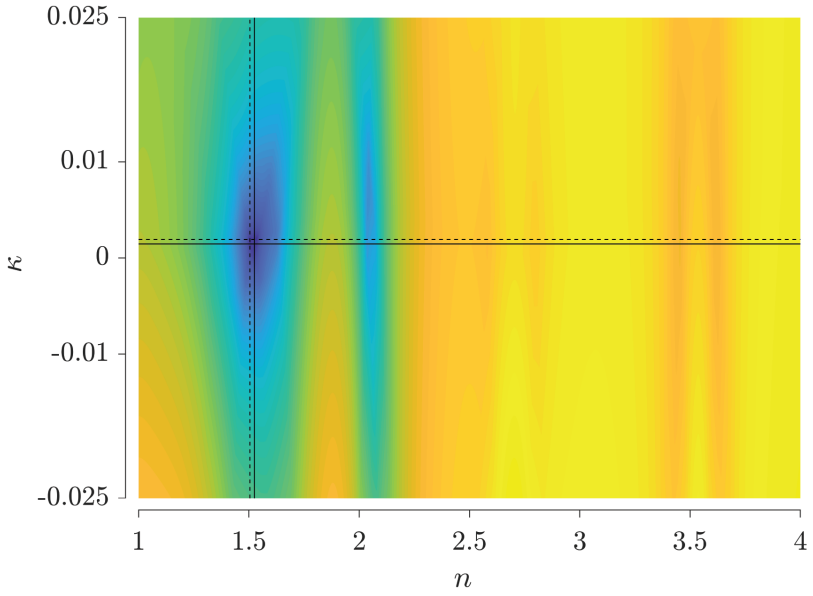
The spectroscopic results from all frequency points generated by VNA (in 0.01 GHz steps) are shown in Fig. 6.7(a) without impedance renormalisation and in Fig. 6.7(b) with impedance renormalisation. The effect of absorption due to box modes can be seen as sharp spikes in the extracted values of loss tangent. Clearly, impedance renormalisation gives the expected dielectric properties.

6.4 Modelling Comparison With Nicolson-Ross-Weir (NRW) Approach

Values of dielectric constant and loss tangent for ABS (pure ABS and two FDM 3-D printed Stratasys ABS-M30 samples in 'laying down' (LD) and 'standing up' (SU) orientations), extracted using the Nicolson-Ross-Weir (NRW) approach, have been published in the open literature by Deffenbaugh *et al.* [4], having a sample size of $22.60 \times 10.06 \times 7.63$ mm^3; all the available X-band data is included in Fig. 6.2 and Table 6.1. TRL calibration was also employed before measurements and their samples were similarly made to fit a shorter 7.63 mm long air-filled quarter-wavelength thru line section of WR-90 waveguide [4]. Their sample length resulted in Fabry-Pérot resonances above *ca.* 11 GHz [4]; with $f_{fp} \sim$13 GHz, predicted using (4.18), having broader spectral features (due to their much greater loss tangents). It can be seen from the published data (recorded at only 8.2, 9.0, 10.0 and 11.0 GHz), that their ABS samples have an extracted dielectric constant of

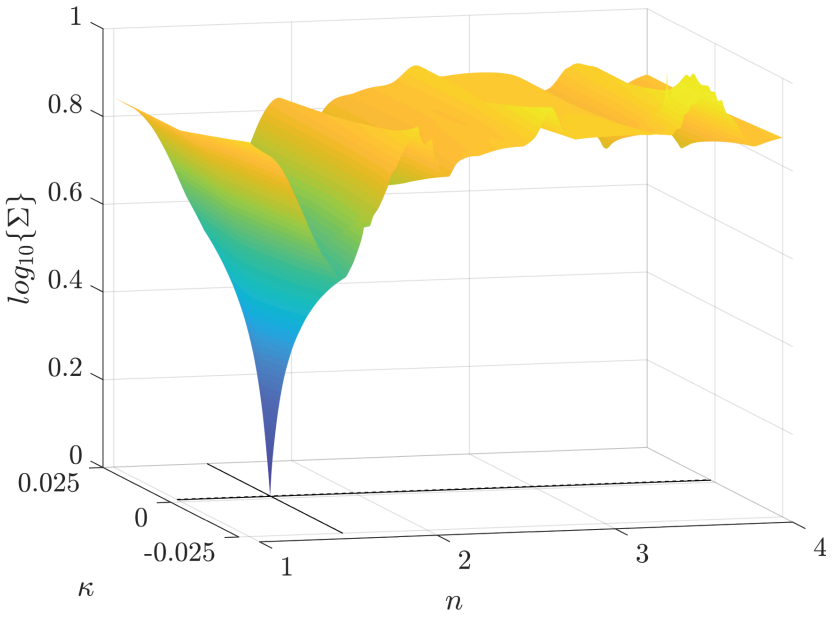


(a)

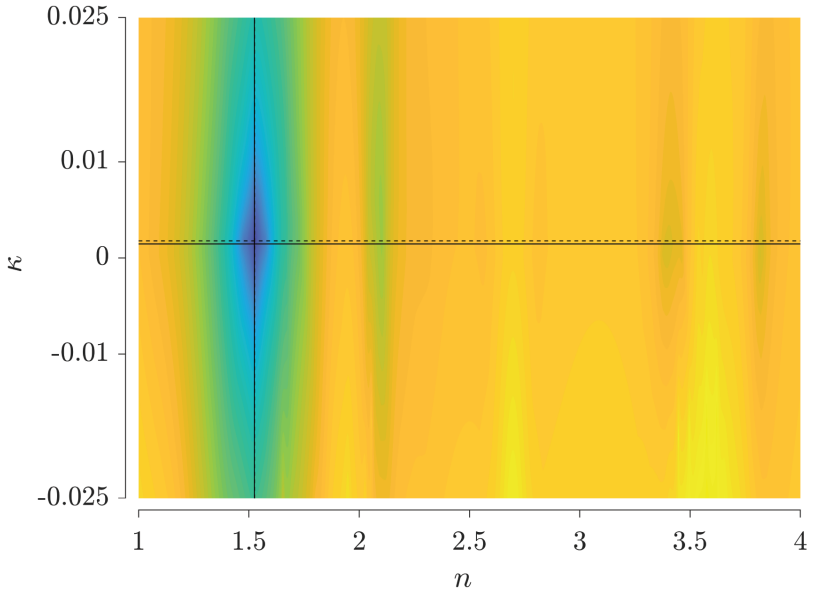


(b)

Figure 6.5: Contour plots for common log of summations of the right-hand sides for (6.3)–(6.5), (6.8)–(6.9) and (6.12)–(6.13) for 3-D printed Sample #1 [2] at 9 GHz without renormalisation: (a) side view; (b) top view with solid black lines showing the target value $\tilde{n}$(11.08 GHz) and dotted black lines showing the extracted value. Figure reproduced from Sun *et al.* [2].

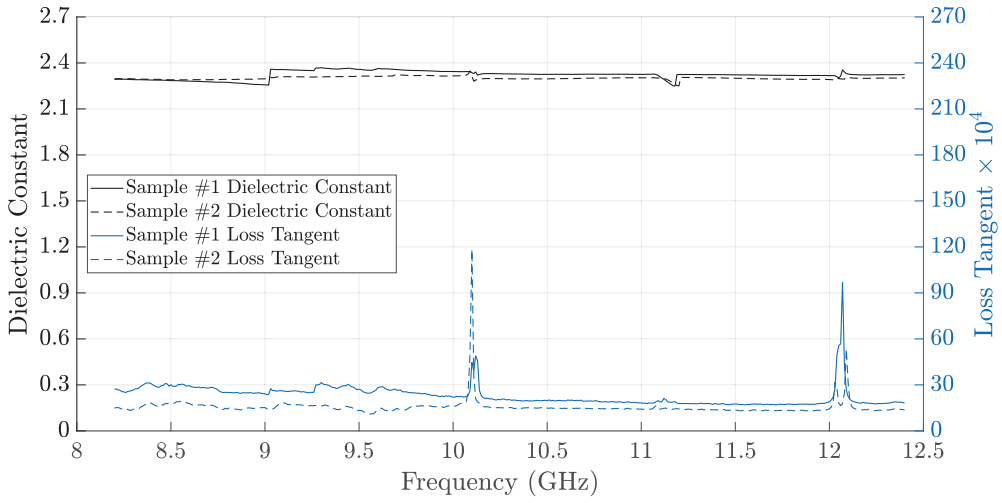


(a)

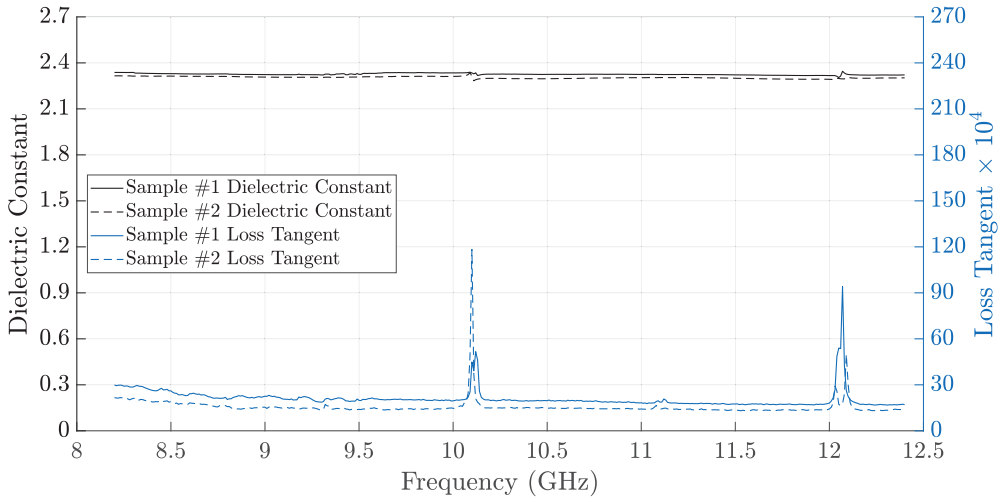


(b)

Figure 6.6: Contour plots for common log of summations of the right-hand sides for (6.3)–(6.5), (6.8)–(6.9) and (6.12)–(6.13) for the 3-D printed Sample #1 [2] at 9 GHz with renormalisation: (a) side view; (b) top view with solid black lines showing the target value $\tilde{n}$(11.08 GHz) and dotted black lines showing the extracted value. Figure reproduced from *Sun et al.* [2].



(a)



(b)

Figure 6.7: Extracted values for dielectric constant and loss tangent (in 0.01 GHz steps) using automated Renormalisation technique with $l/2$-, l-, $2l$-stages and shorted l-stage: (a) without impedance renormalisation; and (b) with impedance renormalisation. The spectral location of sharp spikes correspond to the 'open-box' mode resonances which affect the extracted values of dielectric constant and loss tangent. Without impedance renormalisation (a), abrupt changes in dielectric constant can be observed, most notably at the Fabry-Pérot resonance frequency, due to ambiguities. With renormalisation (b), however, the extracted responses are much smoother and not affected by the Fabry-Pérot resonance. Figure reproduced from *Sun et al.* [2].

Table 6.1: NRW extracted X-band dielectric properties for all ABS samples reported by Deffenbaugh *et al.* [4]. Table reproduced from *Sun et al.* [2].

Dielectric Property	Spot Frequencies [GHz]				
	8.20	9.00	10.00	11.00	12.40
Pure ABS					
Dielectric Constant	2.6	2.62	2.54	2.54	-
Loss Tangent $\times 10^4$	169	114	151	106	-
ABS-M30(LD)					
Dielectric Constant	2.53	2.54	2.56	2.6	-
Loss Tangent $\times 10^4$	108	138	181	98	-
ABS-M30(SU)					
Dielectric Constant	2.53	2.56	2.54	2.55	-
Loss Tangent $\times 10^4$	75	90	207	130	-

between 2.53 and 2.62; higher than the extracted values in this work [2]. Moreover, the associated loss tangents vary from 75×10^{-4} to 207×10^{-4} (extreme case for ABS-M30(SU)); considerably more lossy than the FDM 3-D printed ABS Samples #1 and #2 from this work [2].

It is worth noting that Deffenbaugh *et al.* also present extracted dielectric constant data, using non-waveguide techniques, for ABS at 1, 2, 100, 500 and 1,000 MHz; giving values ranging from 2.59 to 2.83, which correspond more closely to their fixed data sheet value of 2.8 for all ABS samples [4].

The well-established NRW approach [5], [6] represents a closed-form analytical method for characterising dielectric and magnetic materials, without using iterations and an initial guess. The original, highly cited, paper by Nicolson and Ross was developed for TEM waves, normally associated with coaxial cables [5] (it is not possible to 3-D print truly cylindrical samples with FDM for this application). However, it has also been used with TE and TM modes normally associated with waveguides [4], [6]–[7]. For the purposes of clarity, this approach is referred to here as the Original NRW approach.

Given the dielectric properties, *a priori*, the S-parameters for any medium can be calculated using [1],

$$S_{11} = \left[\frac{1 \; - \; P^2}{1 \; - \; (\rho_0 P)^2} \right] \rho_0 \equiv S_{22} \tag{6.14}$$

$$S_{21} = \left[\frac{1 \; - \; {\rho_0}^2}{1 \; - \; (\rho_0 P)^2}\right] P \equiv S_{12} \tag{6.15}$$

where, using (4.6) for Z_{TEm0} and Z^{air}_{TEm0}, the zero-order electric-field wave (or complex Fresnel) reflection coefficient ρ_0 at the interface between the reference air-filled and sample dielectric-filled sections of a MPRWG is,

$$\rho_0 = \frac{Z_{TEm0} \; - \; Z^{air}_{TEm0}}{Z_{TEm0} \; + \; Z^{air}_{TEm0}} \tag{6.16}$$

and, using (4.1) for γ_{m0}, the propagation factor $P = e^{-\gamma_{m0} l}$. Here, the propagation constant $\gamma_{m0} \rightarrow \gamma_g = j\tilde{\beta}$, using (4.17) for $\tilde{\beta}$; this implicitly assumes a PEC-walled MPRWG.

Now, the reverse process of extracting the dielectric properties from any medium can be performed. For example, using a dielectric slab in free space [1], coaxial cable [5] and rectangular waveguide [4], [6]–[7], by solving the following quadratic function,

$$\rho_o^2 - 2\chi\rho_o + 1 = 0 \tag{6.17}$$

giving,

$$\rho_o = \frac{\xi - 1}{\xi + 1} \equiv \chi \pm \sqrt{\chi^2 - 1} \tag{6.18}$$

where,

$$\chi = \frac{1 - S_{21}^2 + S_{11}^2}{2S_{11}} \tag{6.19}$$

The complex propagation factor $P = e^{-j2\pi l/\tilde{\lambda}_g}$ can now be found directly from measurements with (6.19) using,

$$P = \frac{S_{11} + S_{21} - \rho_0}{1 - (S_{11} + S_{21})\rho_0} \tag{6.20}$$

In principle, the complex relative effective permittivity $\tilde{\varepsilon}_{reff}$ and permeability $\tilde{\mu}_r$ can be extracted using (4.11)–(4.14) [2],

$$\frac{1}{\tilde{\lambda}_g^2} = -\left[\frac{ln\{P\}}{2\pi l}\right]^2 = \left(\frac{\tilde{\mu}_r\tilde{\varepsilon}_{reff}}{\lambda_0^2} - \frac{1}{\lambda_{cm0}^2}\right) \tag{6.21}$$

Rearranging (6.21) gives,

$$\tilde{\varepsilon}_{reff} = \frac{\lambda_0^2}{\tilde{\mu}_r}\left(\frac{1}{\tilde{\lambda}_g^2} + \frac{1}{\lambda_{cm0}^2}\right) \tag{6.22}$$

where, with (4.7) and the general identities in (4.8),

$$\tilde{\mu}_r = \xi \cdot \frac{\lambda_g^{air}}{\tilde{\lambda}_g} \tag{6.23}$$

and,

$$\xi = \frac{1 + \rho_0}{1 - \rho_0} \quad \text{and} \quad \lambda_g^{air} = \lambda_0 \frac{Z_{TE}^{air}}{\eta_0} \tag{6.24}$$

In practice, the VNA measures S-parameters with wrapped phase angles (i.e., with values limited between $-\pi$ and $+\pi$); the resulting phase ambiguities in P lead to an infinite number of roots

when evaluating $ln\{P\}$ in (6.21) [6]. In practice (with finite $Q_0(f_{fp})$), the effects of the Fabry-Pérot resonances excludes practical extraction of the dielectric properties above *ca.* 10.5 GHz for Sample #1 and above *ca.* 10.75 GHz for Sample #2; the latter exhibiting a higher $Q_0(f_{fp})$ [2]. Fortunately, phase correction can be applied to the propagation factor (i.e., adding integer multiples n_φ of 2π to $-\beta l$ by multiplying P in (6.20) by $e^{+jn_\varphi 2\pi}$) between the n_φ and $n_\varphi + 1$ Fabry-Pérot resonance frequencies [7], [8].

In this study, the measured S-parameters were applied to these NRW equations, using (6.19)–(6.24), with phase correction applied, and the extracted relative (effective permittivity and permeability) values are shown in Fig. 6.8. This methodology is referred to here as the Original NRW approach [2].

In addition to the problem of phase ambiguity, there is also an issue with mathematical instability. With ideal measurements, at the Fabry-Pérot resonance frequency (with $S_{11}(\omega_{fp}) \cong 0$ and $S_{21}(\omega_{fp}) \cong -1$ for low loss samples), singularities are not seen in (6.19), as $\chi = \lim_{a\to 0}\{a\}/\lim_{b\to 0}\{b\}$. However, with real measured values, a singularity propagates from (6.19) to the propagation factor, resulting in the mathematical instability in both $\tilde{\mu}_r$ and ε_{reff} [2]. In 2012, Barroso and de Paula reported a way to minimise the instability and relative permittivity [7]; $Re\{\tilde{\mu}_r\tilde{\varepsilon}_{reff}\} = \mu'_r\varepsilon'_{reff} - \mu''_r\varepsilon''_{reff}$ and $Im\{\tilde{\mu}_r\tilde{\varepsilon}_{reff}\} = \mu'_r\varepsilon''_{reff} + \mu''_r\varepsilon'_{reff}$ and $\tilde{\mu}_r$ constrained to a value of unity (restricting this technique to purely non-magnetic materials). This methodology is referred to in this paper as the Modified NRW approach. Here, it is implicitly assumed throughout that phase correction has been applied. Extracted values of $\tilde{\mu}_r\tilde{\varepsilon}_{reff}$, for both samples, are also shown in Fig. 6.8, where dielectric constant $\varepsilon_{reff} = Re\{\tilde{\mu}_r\tilde{\varepsilon}_{reff}\}|_{\tilde{\mu}_r=1}$ is replaced with $Re\{\tilde{\mu}_r\tilde{\varepsilon}_{reff}\}$ and loss tangent $\tan\delta_e = \tan\delta|_{\mu''_r=0} = \varepsilon''_{reff}/\varepsilon'_{reff}$ replaced with $\tan\delta = Im\{\tilde{\mu}_r\tilde{\varepsilon}_{reff}\}/Re\{\tilde{\mu}_r\tilde{\varepsilon}_{reff}\}$ [2].

It is important to note that the extraction of dielectric property for rectangular waveguides using (6.19)–(6.24), as originally proposed by Weir [6] and later adopted by others [4], [9]–[7], implicitly assumes PEC-walled MPRWGs. Therefore, with the practical measurements in this study having waveguides with finite conductivity metal walls ($\sigma_0 \approx 1.6 \times 10^7$ S/m), extraction using the NRW equations must exhibit errors (a detailed analysis of the impact of finite σ_0 on $\tilde{\varepsilon}_{reff}$ and $\tilde{\mu}_r$ is the beyond the scope of this study). It can be seen from Fig. 6.8 that, with the Original NRW approach, the extracted relative values and loss tangent exhibit mathematical instabilities at the Fabry-Pérot resonance frequencies ($f_{fp} = 11.08$ GHz for Sample #1 and $f_{fp} = 11.13$ GHz for Sample #2) with $\tilde{\varepsilon}_{reff} \not\equiv \tilde{\mu}_r\tilde{\varepsilon}_{reff}|_{\tilde{\mu}_r=1}$ [2].

For this reason, with the Original NRW approach, sample length must be constrained to $l < \lambda_g(f_{fp})/2$ (i.e., so that $\beta(\omega)l < \pi$) increasing measurement uncertainty due to low opacity [1], [6]. For

example, with the Graphical approach in this study, the extracted value of $\varepsilon'_{reff}(11\text{ GHz}) = 2.3256$ for Sample #1, and so the maximum length $l_{max}(11\text{ GHz}) = 9.708$ mm. As expected, this just exceeds $l = 9.627$ mm, in theory (for $Q_0(f_{fp}) \to \infty$), allowing extraction of dielectric properties below *ca.* 11 GHz only [2]. For arbitrary lengths, one way to resolve the phase ambiguities in P is to test for spectral continuity in the differential-phase group delay [5].

In general, mathematical instabilities are not observed with the Modified NRW method. However, it was found that with Sample #2 an instability was evident just above f_{fp}, where loss tangent spiked to a small negative value [2].

As seen in Fig. 6.8 (ignoring box-mode resonances), the Modified NRW approach gives $Re\{\tilde{\mu}_r\tilde{\varepsilon}_{reff}\} = 2.3080 \pm 0.0019$ ($\pm 0.1\%$ variation), while the respective Graphical and Renormalisation approaches give $\varepsilon'_{reff} = 2.3273 \pm 0.0366$ ($\pm 1.6\%$ variation [2]; this relatively large value may be due to systematic errors and noise in the measurements) and 2.3281 ± 0.0105 ($\pm 0.4\%$ variation) across X-band for Sample #1; for Sample #2, the Modified NRW approach gives $Re\{\tilde{\mu}_r\tilde{\varepsilon}_{reff}\} = 2.3030 \pm 0.0035$ ($\pm 0.2\%$ variation), while the respective Graphical and Renormalisation approaches give $\varepsilon'_{reff} = 2.3105 \pm 0.0183$ ($\pm 0.8\%$ variation and 2.3047 ± 0.0119 ($\pm 0.5\%$ variation) across X-band [2].

Similarly, with loss tangent across X-band, the Modified NRW approach gives $Im\{\tilde{\mu}_r\tilde{\varepsilon}_{reff}\}/Re\{\tilde{\mu}_r\tilde{\varepsilon}_{reff}\}$ between 18.861×10^{-4} and 31.58×10^{-4}, while the respective Graphical and Renormalisation approaches give $\varepsilon''_{reff}/\varepsilon'_{reff}$ from 17.227×10^{-4} to 29.885×10^{-4} and 16.675×10^{-4} to 29.693×10^{-4} for Sample #1. For Sample #2, the Modified NRW approach gives $Im\{\tilde{\mu}_r\tilde{\varepsilon}_{reff}\}/Re\{\tilde{\mu}_r\tilde{\varepsilon}_{reff}\}$ between 13.514×10^{-4} and 48.97×10^{-4}, while the respective Graphical and Renormalisation approaches give $\varepsilon''_{reff}/\varepsilon'_{reff}$ from 13.195×10^{-4} to 21.473×10^{-4} and 12.948×10^{-4} to 21.429×10^{-4} [2].

A summary of the dielectric properties for ABS extracted using various strategies is shown in Table 6.2, for both Samples #1 and #2. It can be seen that at the Fabry-Pérot resonance frequencies the extracted dielectric constants are consistent amongst the various extraction strategies, with the exception of the two NRW methods. The Original NRW method is not stable at this frequency and so generates wildly unpredictable values; while the Modified NRW method delivers a lower value from the average (within 0.7% of the other methods) [2]. If it is initially assumed that the dielectric constant is non-dispersive across X-band, it is possible to compare extraction strategies (given their resulting standard deviation) for the five spot frequency values given in Table 6.2 [2].

Table 6.3 [2] shows the resulting averages for the spot frequency values and their standard deviations. It can be seen that, with both Samples #1 and #2, the Graphical and Renormalisation approaches agree with one another and exhibit a very low standard deviation across X-band;

effectively extracting non-dispersive values for dielectric constant of 2.329 and 2.309 for Sample #1 and Sample #2, respectively, with discrepancies being attributed to arbitrary defects in the two 3-D printed samples and only having one frequency-swept measurement for each sample. The two NRW methods also agree with one another; with the Original method having a higher standard deviation and Modified method having a lower standard deviation, when both are compared to the Graphical and Renormalisation approaches. However, the NRW methods give slightly lower values of dielectric constant (within 1.6% of the other methods). Nevertheless, this simple analysis confirms the initial assumption that the dielectric constant of ABS is non-dispersive across X-band. It can be seen from Table 6.2, with the Graphical and Renormalisation approaches that, when ignoring the Fabry-Pérot resonance frequency, loss tangent for ABS decrease with increasing frequency across X-band. As a result, a non-dispersive analysis is not possible with loss tangent [2].

In contrast, from Table 6.1, while the average dielectric constants for all three ABS samples reported by Deffenbaugh *et al.* [4] are within 1.2% of each other, they are inflated by approximately 10% and have an order of magnitude increase in standard deviation, when compare to the results in this study. Moreover, from Table 6.1, it can be seen that there is no consistent spectral trend in loss tangent [2].

Clearly, the dielectric properties for the FDM 3-D printed ABS in this work do not correspond to those for pure ABS or FDM 3-D printed ABS-M30 reported by Deffenbaugh *et al.* [4]. For example, with pure ABS between 8.2 GHz and 11 GHz, the reported extracted dielectric constant was 2.58 ± 0.04 ($\pm 1.6\%$ variation) with loss tangent fluctuating between 106×10^{-4} and 169×10^{-4} [4]; with very similar results for the FDM 3-D printed Stratsys ABS-M30 samples [2].

Since the results for ABS reported by Deffenbaugh *et al.* [4] do not include extracted data above 11 GHz, it can be inferred that they are likely to have adopted the Original NRW approach; with such a high recorded loss tangent, the effects of having $f_{fp} \sim$13 GHz is likely to have restricted the upper frequency limit to *ca.* 11 GHz [2].

In summary, the Graphical and Renormalisation approaches are in agreement with all the various Fabry-Pérot resonance modelling strategies, at the Fabry-Pérot resonance frequency; it does not assume a PEC-walled MPRWG or exhibit the mathematical instabilities or $\tilde{\mu}_r\tilde{\varepsilon}_{reff}$ ambiguity associated with the NRW methods. From all the various modelling strategies, there is general agreement in the dielectric properties extracted. Sample #1 has a frequency independent dielectric constant of 2.33 across X-band, while its loss tangent tends to decrease from 30×10^{-4} down to 17×10^{-4} as frequency increases across X-band [2]. Sample #2 hs a frequency independent dielectric constant of 2.31 across X-band, while its loss tangent tends to decrease from 21×10^{-4} to 14×10^{-4}

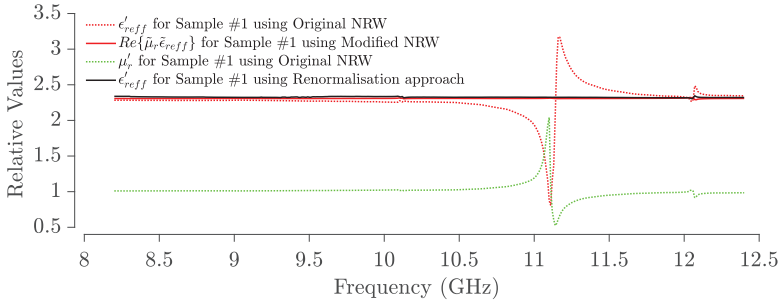
as frequency increases across X-band. These results are clearly less than those previously published in the open literature for pure ABS, shown in Table 6.1 [2], [4].

6.5 Measurement Noise Resilience Analysis

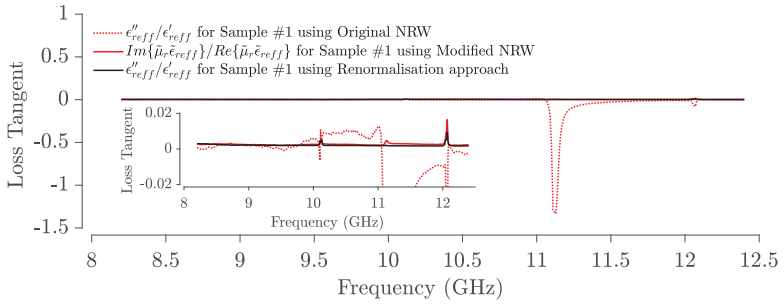
With a modern space-domain Fourier-transform infrared (FTIR) spectrometer, the upper-bound *measurement* signal-to-noise power ratio (SNR or S/N) has a specific definition. With power transmission(reflection)-mode spectroscopy, without any sample under test, *signal* power $P_{reference}$ is represented by a 100% transmittance(reflectance) reference level (assuming no systematic errors within a calibrated system) and neither the peak-to-peak or root-mean square (RMS) deviation from this reference level represents the generalised *noise* power P_{noise}, across the spectrum of interest [10]. With sub-millisecond integration times, FTIR systems have very low values of S/N [1]. Alternatively, the IRisF1 instrument (from IRsweep AG, Switzerland) is a quantum cascade laser frequency comb spectrometer that has $S/N|_{\mathrm{dB}} = 20$ dB with a 1 μs integration time (without any sample under test), which improves with integration time [11]. In contrast, modern frequency-domain VNAs can have a relatively high S/N, while terahertz time-domain spectroscopy (THz TDS) offers an extremely high S/N [1], [2].

In practical metrology there may be numerous sources of measurement noise, having a variety of possible probability density function distributions. Within the limited scope of the analysis presented here, it is not feasible to investigate all possible sources of noise and their interactions within a modern commercial VNA. Nevertheless, it is assumed here that the overall noise from the various contributions exhibit an additive white Gaussian noise (AWGN) type of distribution. In addition, local oscillator phase noise can also be significant at higher frequencies; both assumed to be independent and uncorrelated. Investigating the impact of just AWGN can still reveal potential weaknesses with dielectric property extraction. For this reason, a simple AWGN-only analysis is undertaken [2].

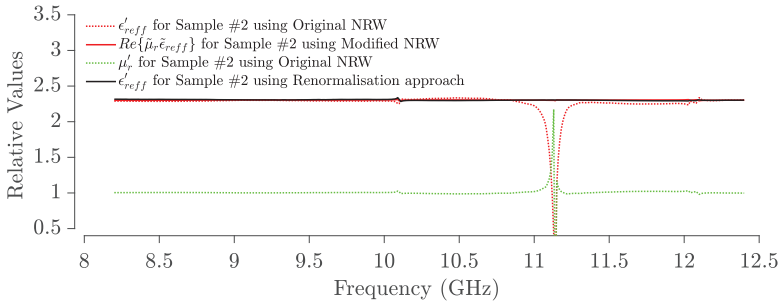
First, the real and imaginary parts of noiseless S-parameters for S_{11} and S_{21} are mathematically emulated; this assumes a symmetrical and reciprocal scenario for a hypothetical non-magnetic dielectric sample under test. Based on the sample average extracted values from Table 6.2, at 9 GHz, this sample has a dielectric constant $\varepsilon_{reff} = 2.31$ and loss tangent $\varepsilon''_{reff}/\varepsilon'_{reff} = 20 \times 10^{-4}$, as fixed target values for subsequent $\tilde{n}_{Target}$ extraction (with $n_{Target} = 1.51987$ and $\kappa_{Target} = 1.52 \times 10^{-3}$ at 9 GHz) [2]. This sample is then inserted into the simulated thru section of waveguide, modelled at 9 GHz using the *variational* method. These for noiseless S-parameter values effectively represent the simulation of four independent noiseless *'signal voltage measurements'* $\nu_{noiseless}$ to which



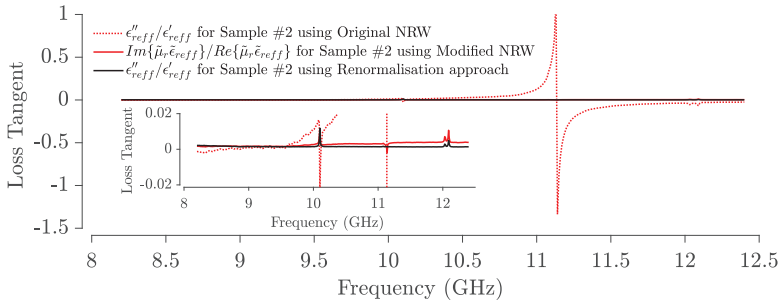
(a)



(b)



(c)



(d)

Figure 6.8: Extracted relative (effective permittivity and permeability) values using the Nicolson-Ross-Weir (in 0.01 GHz steps) and automated Renormalisation approaches: (a) real part of relative values for Sample #1; (b) loss tangent for Sample #1; (c) real part of relative values for Sample #2; and (d) loss tangent for Sample #2. Figure reproduced from Sun *et al.* [2].

Table 6.2: Summary of dielectric properties for ABS extracted using various strategies. Table reproduced from Sun *et al.* [2].

Dielectric Property	Extraction Strategy		Frequencies [GHz]				
			8.20	9.00	10.00	11.1	12.40
Sample #1							
ε'_{reff} $(\tilde{\mu}_r = 1)$	Fabry-Pérot	M1	-	-	-	2.325	-
	Resonance	M3	-	-	-	2.3284	-
	Graphical		2.3303	2.3210	2.3394	2.3250	2.3271
	Renrormalisation		2.3384	2.3240	2.3352	2.3254	2.3216
	Original NRW		2.2830	2.2831	2.2576	-	2.3450
$Re\{\tilde{\mu}_r\tilde{\varepsilon}_{reff}\}$	Modified NRW		2.3066	2.3085	2.3086	2.3103	2.3083
$\varepsilon''_{reff}/\varepsilon'_{reff} \times 10^4$ $(\tilde{\mu}_r = 1)$	Fabry-Pérot	M1	-	-	-	19.25	-
	Resonance	M3	-	-	-	19.148	-
	Graphical		29.885	23.328	17.561	19.250	17.450
	Renormalisation		29.693	22.220	19.455	19.023	16.910
	Original NRW		6.6063	19.259	56.025	-	-23.776
$Im\{\tilde{\mu}_r\tilde{\varepsilon}_{reff}\}/Re\{\tilde{\mu}_r\tilde{\varepsilon}_{reff}\} \times 10^4$	Modified NRW		27.796	24.510	25.464	23.888	22.393
Sample #2							
ε'_{reff} $(\tilde{\mu}_r = 1)$	Fabry-Pérot	M1	-	-	-	2.3045	-
	Resonance	M3	-	-	-	2.3080	-
	Graphical		2.3134	2.3089	2.3165	2.3043	2.3028
	Renormalisation		2.3161	2.3077	2.3124	2.3045	2.3027
	Original NRW		2.2896	2.2988	2.2899	-	2.3044
$Re\{\tilde{\mu}_r\tilde{\varepsilon}_{reff}\}$	Modified NRW		2.3003	2.3046	2.3050	2.2999	2.3008
$\varepsilon''_{reff}/\varepsilon'_{reff} \times 10^4$ $(\tilde{\mu}_r = 1)$	Fabry-Pérot	M1	-	-	-	14.720	-
	Resonance	M3	-	-	-	14.798	-
	Graphical		21.473	16.519	15.164	14.875	13.522
	Renormalisation		21.311	14.945	14.455	14.718	13.417
	Original NRW		-12.914	9.9508	109.78	-	-242.8
$Im\{\tilde{\mu}_r\tilde{\varepsilon}_{reff}\}/Re\{\tilde{\mu}_r\tilde{\varepsilon}_{reff}\} \times 10^4$	Modified NRW		17.130	17.081	26.651	9.046	38.295

Table 6.3: X-band averages of dielectric constant extracted using various strategies. Table reproduced from Sun *et al.* [2].

	Dielectric Property	Extraction Strategy		Average	Standard Deviation
Sample #1	ε'_{reff} ($\tilde{\mu}_r = 1$)	Fabry-Pérot Resonance	M1	2.325	-
			M3	2.3284	-
		Graphical		2.3285	0.0069
		Renormalisation		2.3289	0.0074
		Original NRW *		2.2922	0.0372
	$Re\{\tilde{\mu}_r\tilde{\varepsilon}_{reff}\}$	Modified NRW		2.3085	0.0013
Sample #2	ε'_{reff} ($\tilde{\mu}_r = 1$)	Fabry-Pérot Resonance	M1	2.3045	-
			M3	2.3080	-
		Graphical		2.3092	0.0058
		Renormalisation		2.3087	0.0055
		Original NRW *		2.2957	0.0072
	$Re\{\tilde{\mu}_r\tilde{\varepsilon}_{reff}\}$	Modified NRW		2.3021	0.0025
Pure ABS Sample **	Dielectric Constant	NRW		2.575	0.0412
ABS-M30(LD) Sample **	Dielectric Constant	NRW		2.5575	0.0310
ABS-M30(SU) Sample **	Dielectric Constant	NRW		2.5450	0.0129

* excluding Fabry-Pérot resonance frequency value.

** using the quoted values taken from Deffenbaugh *et al.* [4].

independent and uncorrelated random noise voltages will be added (having AWGN distributions); effectively representing the emulation of 40 *'RMS noise voltage measurements'* ν_{AWGN}. Within this limited study, only 10 noisy *'S-parameter measurements'* for both S_{11} and S_{21} were emulated at 9 GHZ, represented by 40 noisy *'signal voltage measurements'* $\nu_{noisy} = \nu_{noiseless} + \nu_{noise}$, where $\nu_{noise} \rightarrow \nu_{AWGN}$. The 9 GHz spot frequency was chosen as it represents a featureless part of X-band (i.e., well away from any band-edges or resonance frequencies) [2].

At this point, it is necessary to define the upper-bound *measurement* signal-to-noise power ratio in terms of effective *'RMS noise voltage measurements'* $\nu_{noise}|_{RMS}$. Here, the RMS FTIR spectrometer definition for the upper-bound *measurement* S/N is adopted, because it is independent of any arbitrary S-parameter measurements [2]:

$$S/N|_{\text{dB}} = 10\log_{10}\{S/N\} \tag{6.25}$$

with,

$$S/N = \frac{P_{reference}}{P_{noise}} = \frac{\nu_{noiseless}|^2_{RMS}}{\nu_{noise}|^2_{RMS}} \rightarrow S/N_{AWGN} = \frac{1}{\nu_{AWGN}|^2_{RMS}} \tag{6.26}$$

With (6.26), the specific level of $S/N|_{\text{dB}}$, sets the upper RMS limit for $\nu_{noise} \rightarrow \nu_{AWGN}$. In practice, (6.26) is implemented with the built-in MATLAB function *'awgn'* [12] to produce 40 random sample values of ν_{AWGN} within this RMS limit [2],

$$\nu_{AWGN} = awgn(\nu_{noiseless},\ S/N_{AWGN}|_{\text{dB}}) \tag{6.27}$$

It should be noted that while the real and imaginary parts of both S_{11} and S_{21} are assigned the same level of $S/N|_{\text{dB}}$, using (6.27), this same level also independently applies exactly to both $|S_{11}|$ and $|S_{21}|$. Within this limited study, a broad range of $S/N|_{\text{dB}}$ levels were investigated for extracting $\tilde{n}$, from 10 dB (representing poor sensitivity instruments) to 100 dB (representing high sensitivity instruments), in steps of 10 dB. In addition, noiseless values $\tilde{n}_{noiseless}$ were extracted as a benchmark for the various methodologies used in this study [2].

The results using the various extraction strategies are shown in 6.9. With all methodologies, there is a greater spread on refractive index, when compared to the extinction coefficient, but in terms of percentage change the reverse is true. For all levels of $S/N|_{\text{dB}}$, it can be seen that the scatter of extracted values for $\tilde{n}$ is less confined with the Original NRW method, when compared to the Modified NRW method. However, with the Original method the extracted values for $\tilde{n}$ cluster at a noiseless point $\tilde{n}_{noiseless}$ that is closer to the target value $\tilde{n}_{Target}$. This highlights a fundamental weakness with both NRW methodologies, in that $\tilde{n}_{noiseless} \neq \tilde{n}_{Target}$, since the ohmic losses associated with the conducting metal walls of the MPRWG are not considered. In contrast, with both Graphical and Renormalisation methods, $\tilde{n}_{noiseless} = \tilde{n}_{Target}$ [2].

The data spread in 6.9 has been summarised in Table 6.4 with the use of a worst-case normalised *measurement* peak error vector magnitude $EVM\% = (EVM_{PEAK}/|\tilde{n}_{Target}|) \times 100\%$, where EVM_{PEAK} is the minimum radius for the circle that encompasses all 10 extracted $\tilde{n}$ points (from the 10 emulated noisy *'S-parameter measurements'* for S_{11} and S_{21}) with its centre at $\tilde{n}_{Target}$ [2]. It is expected that EVM_{PEAK} dramatically increases as S/N degrades; this is seen Table 6.4.

Alternatively, EVM_{RMS} can be defined as the RMS radius for the circles that correspond to the 10 extracted $\tilde{n}$ points with their centre at $\tilde{n}_{Target}$. Within a linear system, given $\tilde{n}_{Target}$ and EVM_{RMS}, the corresponding S/N_{AWGN} can be estimated using an equation of the form (4.19) [2],

$$\frac{EVM_{RMS}}{|\tilde{n}_{Target}|} \approx \begin{cases} \sqrt{\frac{1}{S/N_{AWGN}} + \sigma_{error}^2} \\ (S/N_{AWGN})^{-1/2} \quad \text{for} \quad S/N_{AWGN}|_{\text{dB}} \gtrsim 20 \text{ dB} \end{cases} \tag{6.28}$$

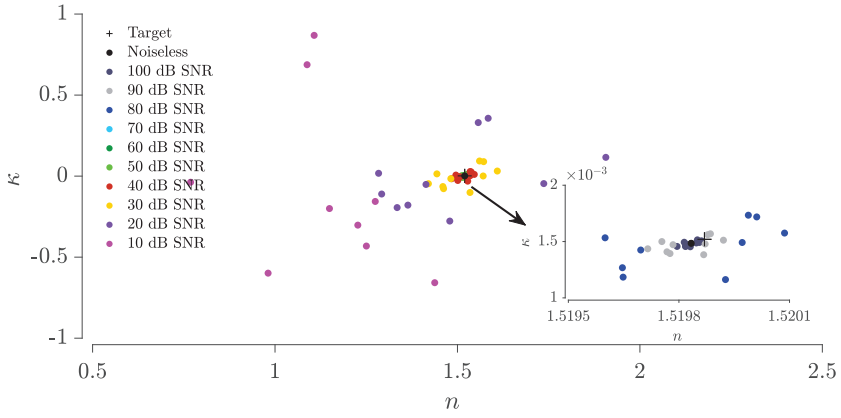
where σ_{error} is an RMS error in the extraction process (effectively representing additional uncorrelated noise). EVM_{RMS} is plotted in Fig. 6.10 for different methodologies. It can be seen that all approaches generally follow the approximation given (6.28). As S/N_{AWGN} increases, with both NRW approaches, EVM_{RMS} approaches their residual value $|\tilde{a}_{noiseless} - \tilde{n}_{Target}|$ [2].

In summary, errors in the extracted value of $\tilde{n}$ are negligibly small with the Graphical and Renormalisation methods, while both NRW methodologies have significant errors are inhered – due to the PEC-walled MPRWG assumption. As $S/N|_{\text{dB}}$ degrades, both Graphical and Renormalisation methods maintain their resilience as long as the minimum grid resolution can increase. Further improvements with the Renormalisation method can be made by having a more aggressive port reference impedance optimisation strategy [2].

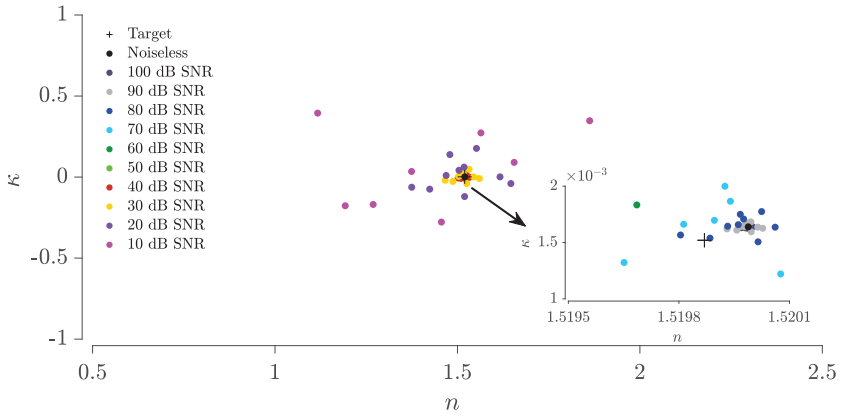
Next section gives an analysis of the *measurement* $S/N|_{\text{dB}}$ for the calibrated VNA system used to generate the S-parameters. A *measurement* $S/N|_{\text{dB}}$ of 88.5 dB can be inferred, when based on the RMS approach. Therefore, it can be seen from Table 6.4 that in this particular example, the Graphical method has the lowest *measurement* $EVM\%$ [2].

6.6 Estimation of VNA S/N

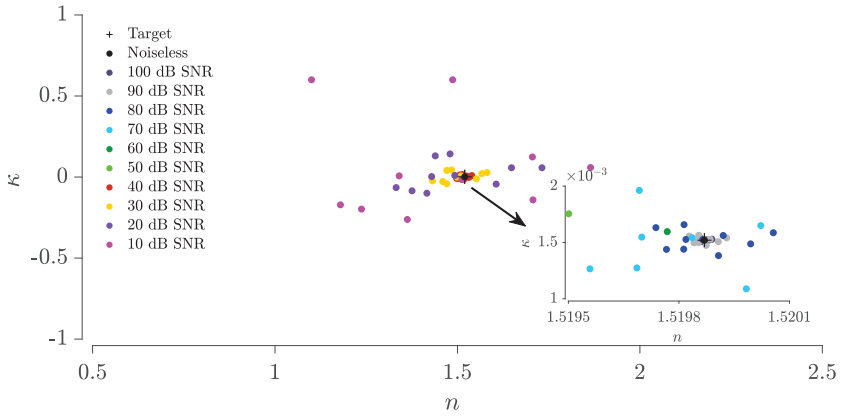
It is interesting to estimate the upper-bound *measurement* $S/N|_{\text{dB}}$ for the calibrated VNA system (Agilent E8364C PNA Network Analyzer [13]) used to generate the S-parameters in this study. It is assumed here that the signal-to-noise power ratio is frequency independent across X-band. Noise presents a random deviation from the noiseless measurements, plotted against frequency, but considered as a sequence of sample points. First, the adopted RMS definition for a transmission mode FTIR spectrometer is used, with 421 spectral measurements from 8.2 to 12.4 GHz (in 0.01 GHz



(a)



(b)



(c)

Figure 6.9: Noise sensitivity for a hypothetical dielectric sample having a fixed dielectric constant $\varepsilon'_{reff} = 2.31$ and loss tangent $\varepsilon''_{reff}/\varepsilon'_{reff} = 20 \times 10^{-4}$ (with $n_{Target} = 1.51987$ and $\kappa_{Target} = 1.52 \times 10^{-3}$ at 9 GHz) inserted into the simulated thru section of waveguide modelled at 9 GHz using the *variational* method: (a) Original NRW; (b) Modified NRW; and (c) Renormalisation method. Figure reproduced from Sun *et al.* [2].

Table 6.4: Worst-case normalised *measurement* peak error vector magnitudes from Fig. 6.9 for different methodologies. Table reproduced from Sun *et al.* [2].

$S/N\|_{\text{dB}}$	*Measurement Peak EVM%*			
	Original NRW	Modified NRW	Graphical *	Renormalisation
10	67.4308	67.3107	47.4651	71.2671
20	26.5339	11.7441	23.8831	14.4112
30	7.2725	3.7859	16.2645	4.9536
40	2.6203	1.2554	1.2817	1.5948
50	0.8692	0.3974	0.3755	0.4360
60	0.2811	0.1196	0.1181	0.1373
70	0.0915	0.0392	0.0417	0.0415
80	0.0312	0.0196	0.0122	0.0131
90	0.0121	0.0137	0.0039	0.0042
100	0.0061	0.0119	0.0011	0.0013
Noiseless	0.0033	0.0111	55×10^{-6}	4×10^{-6}

* Graphical method analysis done by Dr. Sun using the maximum obtainable zoomed-in level to observe the graphs [2].

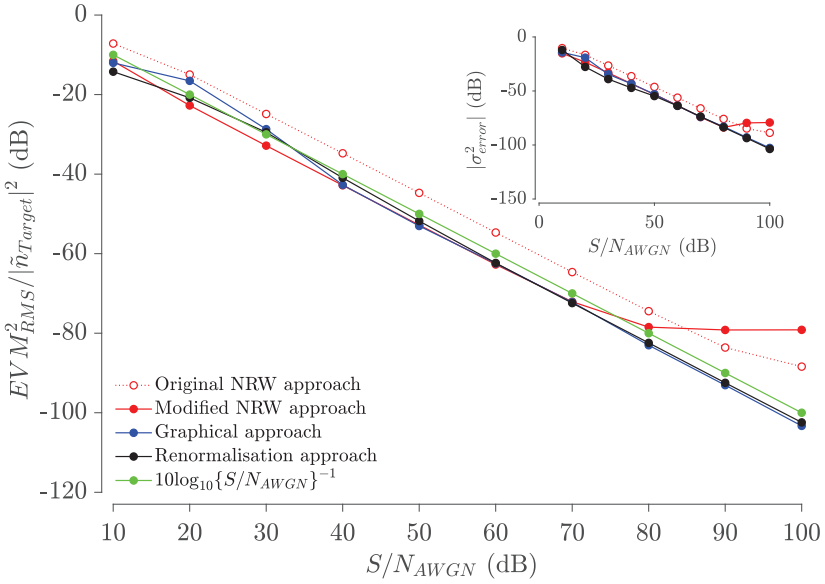


Figure 6.10: Normalised *measurement* RMS error vector magnitudes from Fig. 6.9 for different methodologies. Figure reproduced from Sun *et al.* [2].

steps). The S_{21} and S_{12} for the air-filled 9.626 mm long thru line section of MPRWG were measured, with the results for $|S_{21}| = |S_{21noisy}| \rightarrow \nu_{noisy}$ shown by the thin black curve in Fig. 6.11. The 10-point running average is estimated using the built-in MATLAB *'polyfit'* function [12], to give $|S_{21noiseless}| \rightarrow \nu_{noiseless} \neq 1$ illustrating the effects of systematic errors within the calibrated instrument, shown by the bold black cure in Fig.6.11. The running average is then subtracted from the measured response, to give the random noise spectral response ν_{noise} centred around zero, shown in Fig. 6.11. By taking the Fourier transform of ν_{noise} extracted from measurements and comparing this with ν_{AWGN} generated previously, it is found that they have almost identical probability density functions; confirming the initial assumption made that AWGN dominates.

It is then possible to estimate the *measurement* $S/N|_{\mathrm{dB}}$,

$$S/N|_{\mathrm{dB}} = 10\log_{10}\left\{\frac{\nu_{noiseless}|_{RMS}}{\nu_{noise}|_{RMS}}\right\}^2 \tag{6.29}$$

Given $\nu_{noiseless}$ and ν_{noise}, (6.29) is implemented using the inverse of (6.27) with the built-in MATLAB function *'snr'* [12],

$$S/N|_{\mathrm{dB}} = snr(\nu_{noiseless},\ \nu_{noise}) \tag{6.30}$$

The peak-to-peak representation of the signal-to-noise power ratio $S/N|_{\mathrm{dB,p-p}}$ can be defined as,

$$S/N|_{\mathrm{dB,p-p}} = 10\log_{10}\left\{\frac{1}{\nu_{noise}|_{p-p}}\right\}^2 \tag{6.31}$$

with

$$\nu_{noise}|_{p-p} = 2|\nu_{noise}|_{MAX} \tag{6.32}$$

Given ν_{noise}, (6.32) is implemented with the built-in MATLAB function *'max'* [12],

$$|\nu_{noise}|_{MAX} = max(abs(\nu_{noise})) \tag{6.33}$$

Using this simplified approach, it has been found that *measurement* $S/N|_{\mathrm{db}}$ is approximately 88.5 dB and 72.0 dB when based on RMS and peak-to-peak approaches, respectively from our VNA measurements. A more detailed sub-band breakdown is shown in Table 6.5. It is seen in Table 6.5 that all four sub-bands have a *measurement* $S/N|_{\mathrm{db}}$ within a very narrow range, between 88 dB and 89 dB, with the RMS approach, which justifies our initial assumption that *measurement* $S/N|_{\mathrm{db}}$ is independent of frequency across X-band. The peak-to-peak approach exhibits a wider range, between 71 dB and 75 dB, due to the single point outliers that are observed in Fig. 6.11.

It is interesting to note that for the Agilent E8364C PNA, the specification standard test port input noise floor is less than approximately -117.0 dBm (at X-band within and IF bandwidth of

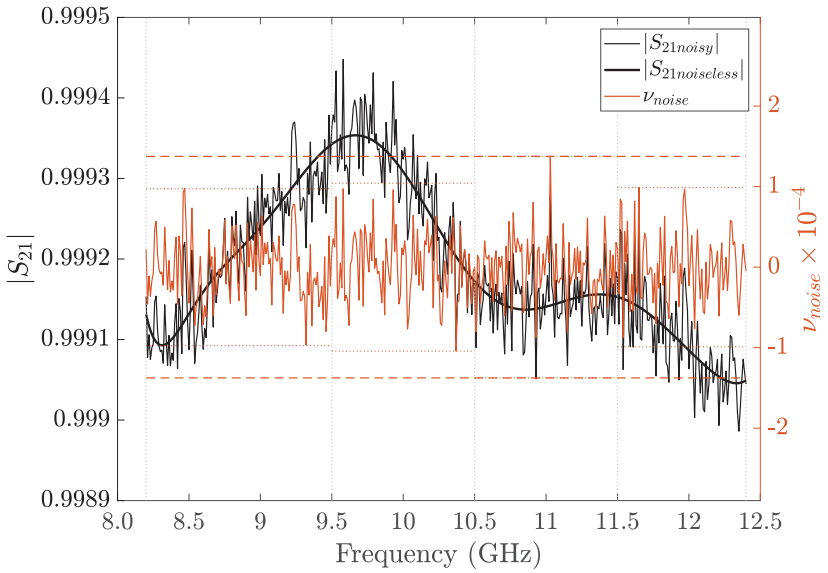


Figure 6.11: Measured $|S_{21}|$ for the air-filled 9.626 mm long thru line section of MPRWG, with its running average and extracted random noise components. Figure reproduced from Sun *et al.* [2].

Table 6.5: Upper-bound *Measurement* $S/N|_{\text{db}}$ summary for the calibrated Agilent E8364 PNA Network Analyzer calibrated in waveguide at X-band. Table reproduced from Sun *et al.* [2].

Band [GHz]	*Measurement* S/N [dB]			
	RMS		Peak-to-peak	
	S_{21}	S_{12}	S_{21}	S_{12}
8.2-12.4	88.2	88.7	71.2	72.9
8.2-9.5	88.3	89.2	74.2	75.2
9.5-10.5	87.9	87.8	73.6	74.3
10.5-11.5	89.0	89.3	71.2	75.4
11.5-12.4	87.7	88.4	74.1	72.9

10 Hz; increasing with IF bandwidth) [13]. At 10 GHz, the output signal power at the reference plane was measured to -18.5 dBm, giving $S/N|_{\text{db}} \gtrsim 95.5$ dB; decreasing with increasing IF bandwidth. Therefore, for a 100 Hz IF bandwidth, $S/N|_{\text{db}} \gtrsim 88.5$ dB. This corresponds exactly to the independently extracted arithmetic average value from S_{21} and S_{12}, when based on the RMS approach across X-band carried out in this study, as shown in Table 6.5.

6.7 Conclusion

In this chapter, a technique based on renormalisation of S-parameters was presented to resolve the ambiguities in simultaneous transmittance and reflectance relationships, obtained from S-parameter measurements of a network, under a noisy measurement scenario. This technique was used to extract the complex dielectric properties of an fused deposition modelling (FDM) 3-D printed dielectric sample in a metal-pipe rectangular waveguide (MPRWG), based on the graphical method for extraction of dielectric properties. A noise resilience analysis was carried out for the graphical, renormalisation and Nicolson-Ross-Weir (NRW) techniques. It was found that both graphical and renormalisation methods correctly predicted the target value of n and κ within 5 dB of the root mean squared (RMS) error vector magnitude (EVM) value corresponding to the introduced additive white Gaussian noise. The modified NRW approach, performed similar to the graphical and renormalisation techniques, while, original NRW approach was the worse. Both NRW methods, however, do into account the conductivity of the waveguide walls and performed poorly under low-noise conditions. In this regard, both the graphical and renormalisation techniques are preferable to the NRW method, as the NRW method requires numerical solution to take into account losses in the waveguide walls. In addition, the output S/N ratio of a vector network analyser (VNA) operating in the X-band was also estimated from measurements of the thru section of an MPRWG.

6.8 Acknowledgements

Work presented in this chapter was done under the supervision of Prof. Stepan Lucyszyn and was published in Sun *et al.* [2]. In addition, Prof. Lucyszyn went over each and every word of the original draft, provided helpful feedback and suggested improvements which were invaluable to the work presented in this chapter. James Skinner at the U.K.'s National Physical Laboratory (NPL) measured the output signal power at the reference plane. Measurements at NPL were performed under the supervision and permission of Nick Ridler. Dr. Sun performed manual extraction using the graphical method; and also provided the data for noise resilience analysis for both the graphical

and Nicolson-Ross-Weir methods.

References

[1] J. Sun and S. Lucyszyn, "Extracting complex dielectric properties from reflection-transmission mode spectroscopy," *IEEE Access*, vol. 6, pp. 8302–8321, Mar. 2018.

[2] J. Sun, A. Dawood, W. J. Otter, N. M. Ridler, and S. Lucyszyn, "Microwave characterization of low-loss FDM 3-D printed ABS with dielectric-filled metal-pipe rectangular waveguide spectroscopy," *IEEE Access*, vol. 7, pp. 95455–95486, July 2019.

[3] R. K. Challa, D. Kajfez, V. Demir, J. R. Gladden, and A. Z. Elsherbeni, "Permittivity measurement with a non-standard waveguide by using TRL calibration and fractional linear data," *PIER*, vol. 2, pp. 1–13, 2008.

[4] P. I. Deffenbaugh, R. C. Rumpf, and K. H. Church, "Broadband microwave frequency characterization of 3-D printed materials," *IEEE Trans. Compon. Packag. Manuf. Technol.*, vol. 3, pp. 2147–2155, Dec. 2013.

[5] A. M. Nicolson and G. F. Ross, "Measurement of the intrinsic properties of materials by time-domain techniques," *IEEE Trans. Instrum. Meas.*, vol. 19, pp. 377–382, Nov. 1970.

[6] W. B. Weir, "Automatic measurement of complex dielectric constant and permeability at microwave frequencies," *Proc. IEEE*, vol. 62, pp. 33–36, Jan. 1974.

[7] J. J. Barroso and A. L. De Paula, "Retrieval of permittivity and permeability of homogeneous materials from scattering parameters," *Journal of Electromagnetic Waves and Applications*, vol. 24, no. 11-12, pp. 1563–1574, 2010.

[8] A. N. Vicente, G. M. Dip, and C. Junqueira, "The step by step development of NRW method," in *Proc. SBMO/IEEE MTT-S International Microwave and Optoelectronics Conference*, pp. 738–742, IEEE, Oct. 2011.

[9] A.-H. Boughriet, C. Legrand, and A. Chapoton, "Noniterative stable transmission/reflection method for low-loss material complex permittivity determination," *IEEE Trans. Microw. Theory Technol.*, vol. 45, pp. 52–57, Jan. 1997.

[10] Highest available signal-to-noise performance, delivering superior sensitivity and analytical performance: Technical Overview, Agilent Technologies INc., Publication Number SI-1353, Mar. 2011. Accessed: 72019. [Online]. Available: `https://www.agilent.com/cs/library/technicaloverviews/public/si-1353.pdf`.

[11] IRis-F1High-speed infrared spectrometer, IRsweep AG, 2018. Accessed: Mar. 07, 2019. [Online]. Available: http://cloudfront.irsweep.com/resources/IRsweep_IRisF1.pdf.

[12] MATLAB Functions. Accessed: 7 Mar. 2019. [Online]. Available: https://uk.mathworks.com/help/matlab/functions.html.

[13] Agilent PNA Microwave Network Analyzers: Data Sheet. Accessed: Mar. 07, 2019. [Online]. Available: http://literature.cdn.keysight.com/litweb/pdf/5989-7605EN.pdf.

Chapter 7

Terahertz Spectroscopy Using Surface Plasmon Excitation

7.1 Introduction

The Drude model can adequately describe the response of metals in a broad spectral domain but metals are not good candidates for surface plasmon excitation in the THz sub-spectrum due to high absorption. Semiconductors are ideal for THz plasmon excitation as their plasma frequency depends on the number of carriers n_{3D}. As n_{3D} can be easily altered by doping, semiconductors can be tailored to operate in the THz domain. The Drude model is fairly accurate for semiconductors in the THz range. Si is one semiconductor that is commonly used to study THz surface plasmons excitation as highly doped Si ($n_{3D} > 10^{17}$ cm^{-3}) can support THz surface plasmons.

Otter, at Imperial College London, in his PhD thesis [1] proposed a novel method for THz spectroscopy using plasmon excitation. Plasmons are excited on a silicon (Si) slab in the Otto configuration using the attenuated total reflection (ATR) scheme. The observed spectral response of reflected field shows a sharp dip at the crossover of prism and Si dispersion curves, due to surface plasmon excitation. This configuration can be used as a THz spectrometer as the observed spectrum is sensitive to changes in the dielectric constant of gap, gap size and the wavenumber along the interface that is dependent on the angle of incidence and material of prism. A material under test can be characterised using this technique by placing the sample in the gap and observing the change in reflected field at the detector.

Nazarov *et al.* [2] characterised highly doped Si samples through excitation of surface plasmons on Si samples underneath a prism using the ATR scheme. The peak of absorbance at the detector is shifted with a change in the material parameters of the sample. The shift in absorbance is highly

sensitive to the dielectric constant of the sample under test, and even slight changes in the dielectric constant of the sample can be detected [3]. The losses of the Si sample can be characterised by observing the decay in surface plasmons over a known length. More recently, the work by Poulin *et al.* [4] reviews some of the sensing techniques using surface plasmon excitation. They present an example of material characterisation of an unknown dielectric sample placed on a Si slab of known dielectric properties. While Nazarov *et al.* [2] used a glass prism in their work, sensing can be improved by using a prism with a high dielectric constant, such as Si.

The modelling aspects of the experimental set-up for THz spectroscopy through excitation of surface plasmons are considered in this chapter.

Three different modelling techniques are considered: (i) dispersion modelling by plotting dispersion curves; (ii) simplified modelling by treating the different media as semi-infinite planar slabs and; (iii) full wave modelling using FDTD and *COMSOL Multiphysics*®.

7.2 Dispersion Modelling

A plot of frequency versus the wavenumber (or propagation constant) is known as the dispersion curve. All real materials are frequency dispersive, which means that the material parameters ε and μ are functions of frequency. Some materials may exhibit little change in their material parameters over a certain range of frequencies and can be effectively modelled by constant values of ε and μ. The dispersion plot of such materials is a straight line over the frequency range of interest. For frequency-dispersive materials, the dispersion curve is not a straight line. In situations where electromagnetic energy travels between different media, a plot of dispersion curves of these media can give many insights, for example, the intersection of dispersion curves shows materials having similar wavenumbers and can represent electromagnetic excitation, absorption or reflection-less transmission between these media.

Figure 7.1(b) shows the SPP dispersion relationship of a heavily doped Si sample. The sample was n-type with a carrier concentration of $n_{3D} = 7.84 \times 10^{16}$ cm^{-3}, electron mobility $\mu = 797.194$ m^2/Vs, effective electron mass $m_{eff} = 0.26 m_e$, where m_e is the rest mass of the electron, and a dielectric constant of 11.64. The plasma frequency was calculated from (C.8) as $f_p = 4.9305$ THz and surface plasmon frequency as $f_{sp} = f_p/\sqrt{1+\varepsilon_r^{Si}} = 1.3868$ THz. Material parameters of available heavily doped Si samples are given in Table 7.1. The data was provided by Dr. Otter [1]. The dispersion curve of glass $\varepsilon_r = 2.25$ lies towards the right of the light line and intersects the SPP dispersion curve. The point of intersection shows that incident light from glass has the required wavenumber k (or momentum) to excite SPPs. This is the basis for the THz spectroscopy technique discussed

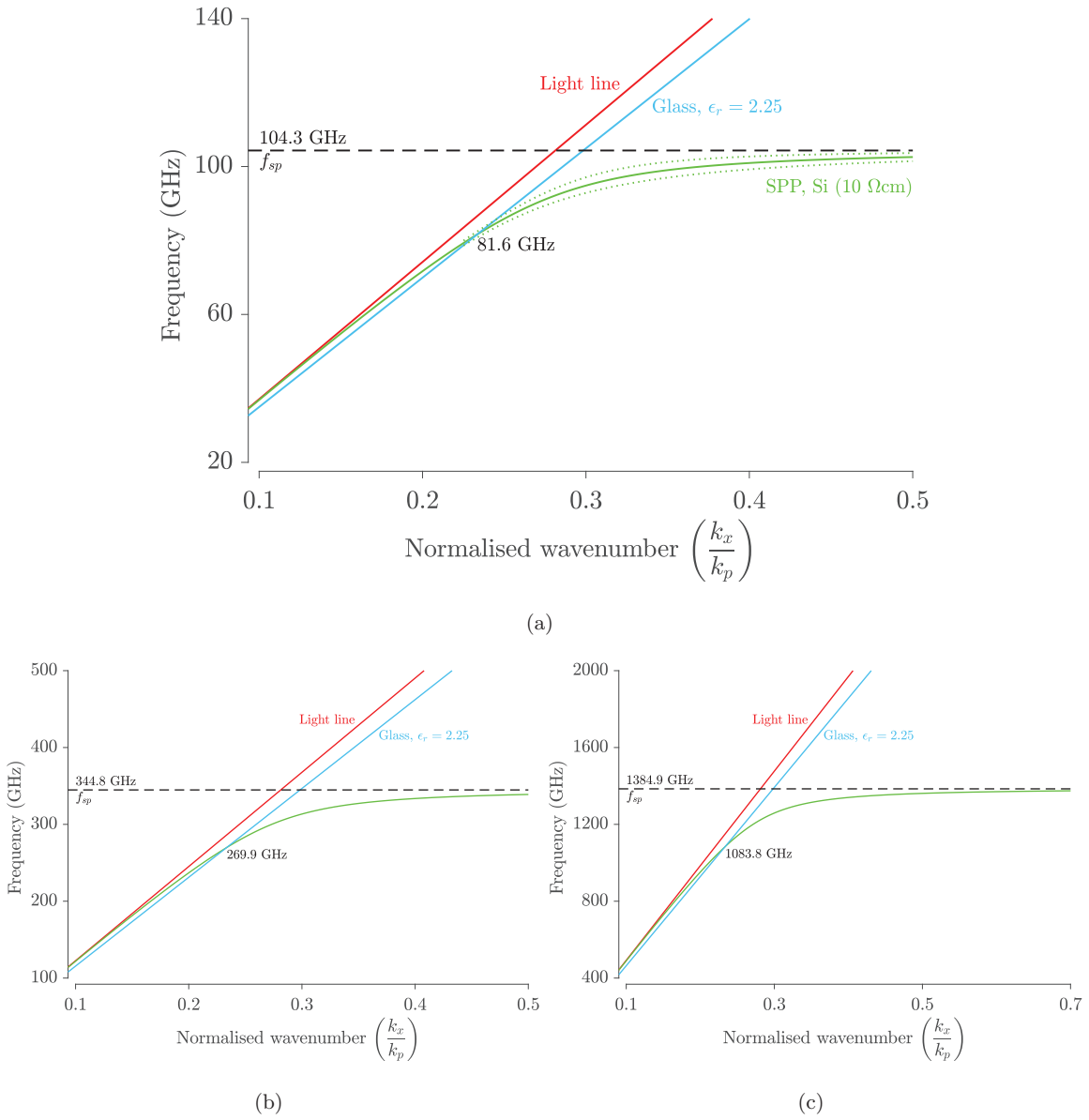


Figure 7.1: Frequency versus normalised wavenumber dispersion plots of surface plasmon polaritons (SPP) for n-type Si samples with resistivities: (a) 10 Ωcm; (b) 1 Ωcm; and (c) 0.1 Ωcm. The dispersion curves were computed using (1.8), where the dielectric was assumed to be air with Si sample underneath. The surface plasmon frequency f_{sp} is also indicated for the three samples, which is also the limiting value as the wavenumber increases. SPPs are excited where the dispersion curves, for glass and SPPs on Si, intersect. The dotted lines below and above the SPP dispersion curve, respectively, represent the odd and even SPP modes on a Si slab of thickness 525 μm, which were numerically computed using (3.32) and (3.33).

Table 7.1: Physical parameters of available n- and p-type heavily doped Si samples. Data reproduced from Otter [1].

Parameter	Type	Value		
Effective mass, m_{eff} (kg)	n	$0.26m_e$		
	p	$0.36m_e$		
Resistivity (Ωcm)	n	0.1	1	10
	p	0.1	1	10
Carrier density, n_{3D} (cm^{-3})	n	7.84×10^{16}	4.86×10^{15}	4.45×10^{15}
	p	2.77×10^{17}	1.46×10^{16}	1.34×10^{15}
Electron mobility, μ (m^2/Vs)	n	797.194	1286.008	1404.494
	p	225.632	428.082	466.418

earlier. Figure 7.1 shows dispersion curves of the glass prism plotted against 1 Ωcm and 0.1 Ωcm Si samples. In Fig. 7.1(a), dotted green lines depict even and odd surface plasmon modes which are excited on the Si slab because the thickness of the Si slab is comparable to plasmon wavelength. If a Si prism ($\varepsilon_r = 11.74$, $n = 3.426$) is used then the Si curve will now operate in the relatively flat portion of surface plasmon dispersion curve, as shown in Figs. 7.1 and 7.2. The resulting spectral response will be a sharp dip in the reflected wave due to absorption from surface plasmon excitation.

A prism made of a material with high dielectric constant will operate in the flatter portion of the surface plasmon dispersion curve, with the expected response having sharp spectral features. In contrast, for example, a prism made of glass will be operating in the portion of surface plasmon dispersion with steep slope and, therefore, the spectroscopic response for glass can vary over a very large frequency range. Most measurement systems are optimised to operate on a relatively narrow frequency band only; therefore, from a measurement perspective, it is not desirable to have a response that varies over a large frequency band. Also, the response of the dielectric prism can be assumed dispersionless in only a narrow frequency band. Hence, a prism with high dielectric constant and low loss, such as silicon, is more suited for spectroscopy as compared to glass.

7.3 Planar Media Reflection/Transmission Approach

As a second modelling approach, the experimental set-up was modelled by treating the prism, the air gap and the metal slab as planar media. The return loss of the set-up in Fig. 7.3 was then

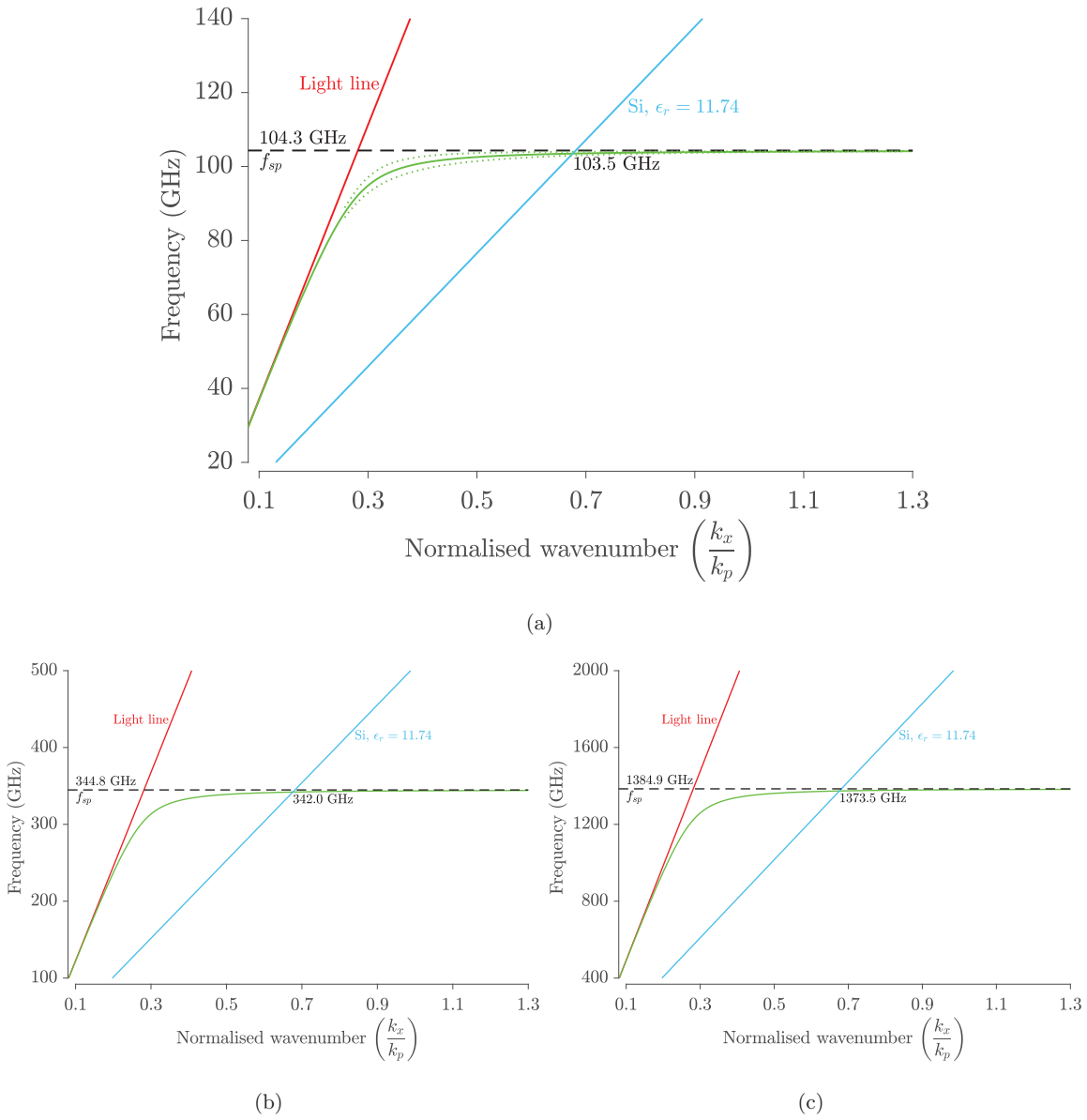


Figure 7.2: Frequency versus normalised wavenumber dispersion plots of surface plasmon polaritons (SPP) for n-type Si samples with resistivities: (a) 10 Ωcm; (b) 1 Ωcm; and (c) 0.1 Ωcm. The dispersion curves were computed using (1.8), where the dielectric was assumed to be air with Si sample underneath. The surface plasmon frequency f_{sp} is also indicated for the three samples, which is also the limiting value as the wavenumber increases. SPPs are excited where the dispersion curves, for Si prism and SPPs on Si slab, intersect. The dotted lines below and above the SPP dispersion curve, respectively, represent the odd and even SPP modes on a Si slab of thickness 525 μm, which were numerically computed using (3.32) and (3.33).

analysed, both, analytically and using *COMSOL Multiphysics*® simulation. The incident medium was prism and the transmitted medium was air, corresponding to the input and output port reference impedances.

The approach used here to compute the response of cascaded planar media, is to first compute the S-parameters of the individual layers, using (F.9) and (F.12), by treating them as independent Fabry-Pérot resonators with a known reference impedance, and then compute the overall response of the cascaded network. The response of all independent layers must have a common reference impedance, in order to satisfy the cascading condition. The obtained overall S-parameters were then renormalised to obtained the actual overall S-parameter response. In this case, the intrinsic impedance of the prism was used as the the common reference impedance when computing the response of individual layers and then, as a final step, the overall response was renormalised with the intrinsic impedances of the prism and that of air as the two reference impedances corresponding to the prism on the incident side and the air domain on the transmitted side, beyond the Si slab.

With the arrangement shown in Fig. 7.3, analytical and *COMSOL Multiphysics*® simulations were used to compute the return loss $20\log_{10}|S_{11}|$ by sweeping over the incident angle of an incoming electromagnetic plane wave and gap d_{gap} between prism and Si slab. For these simulations, a Si prism of relative permittivity $\varepsilon_r = 11.74$ ($n = 3.426$) was used.

For *COMSOL Multiphysics*® sumulations, the simulated geometry was terminated by a periodic input port (coloured cyan) at one end and perfect electric conductor (black) boundary at the other end parallel to the interface between planar media while Floquet periodic boundaries (green) were used to terminate the geometry along the sides normal to the interface between planar media. The x- and y-components of the propagation constants used to specify the Floquet periodic boundary for each medium i, given by k_{xi} and k_{yi}, were computed using (E.4)–(E.7) for each medium. Only the return loss S_{11} was considered with the *COMSOL Multiphysics*® simulations.

Figure 7.4(a) shows the analytically computed return loss $20\log_{10}|S_{11}|$ for the planar media arrangement, when d_{gap} is swept, in increments of 5 μm, with the prism made of Si and 10 Ωcm Si slab underneath. The angle of incidence θ_{inc} was kept fixed at 45°. Two distinct surface plasmon excitations could be clearly seen close to 103 GHz. These are the split even and odd modes which are excited on the either side of the Si slab. The result clearly corresponds to the theoretical prediction from the dispersion diagram shown in Fig. 7.2(a). For comparison, the numerically computed response from *COMSOL Multiphysics*® is plotted in Fig. 7.4(b), where d_{gap} was swept in increments of 25 μm and the frequency step was 0.01 GHz with $\theta_{inc} = 45°$.

Figure 7.5 shows a comparison between the analytical and numerical methods with $d_{gap} = 415$ μm.

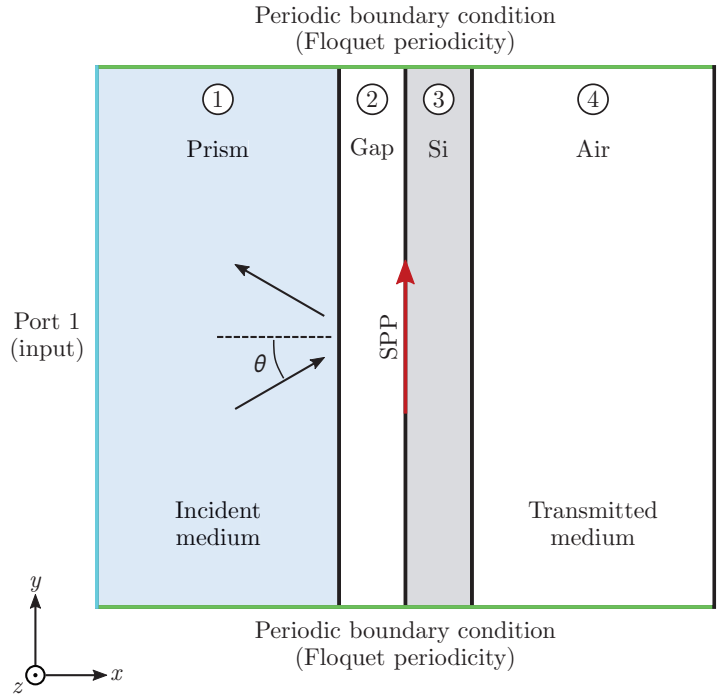


Figure 7.3: The Otto attenuated total reflection (ATR) scheme, for excitation of surface plasmon polaritons (SPP), depicted as a planar media reflection/transmission problem. The incident transverse electromagnetic (TEM) waves in the prism medium undergo total internal reflection at the side of prism adjacent to the gap between the prism and Si slab. The evanescent fields in the gap can have a wavenumber, parallel to the interface, that can excite SPPs on the surface of Si slab as shown by the red arrow. The Si slab is backed by air or free space. In the *COMSOL Multiphysics*® frequency domain solver, the incident TEM waves are excited at Port 1 with the specified incident angle θ_{inc}. The simulation domain at the top and bottom are truncated in Floquet boundary conditions, with the k_y and k_{xi} wavenumbers for the Floquet boundary computed from (E.6) and (E.7) for any medium i, respectively.

The *COMSOL Multiphysics*® response is shifted towards higher frequencies by about 0.15 GHz but, otherwise, shows good agreement with both analytical results presented earlier. The shift in frequency is due to the sensitive nature of plasmon excitation in a comparatively very narrow 0.1 GHz frequency band when using a finite mesh, consisting of 89600 rectangular elements, in *COMSOL Multiphysics*®. Also, it was found that using a coarse mesh shifts the response towards higher frequencies while a finer mesh shifts the response towards lower frequencies; suggesting that the finite mesh size contributes to disagreement with the analytical approach. In practice, with *COMSOL Multiphysics*®, a very fine mesh, consisting of 89600 rectangular elements, was used which could produce results in a reasonable amount of time. A still finer mesh might improve the agreement with the analytical method, but could take a prohibitively long time to simulate. Additionally, the mapped rectangular mesh used in *COMSOL Multiphysics*® had elements with non-uniform length along the direction of propagation x, with the mesh elements being finest close to the interface between any two media. The size of rectangular mesh elements was kept uniform along the vertical y-direction.

Figure 7.6 shows analytically computed return loss $20\log_{10}|S_{11}|$ plotted against frequency and swept angle of incidence, in increments of 0.25 degrees. Both odd (left) and even (right) mode plasmonic excitations are clearly visible. The response in Fig. 7.6 suggests that the optimal excitation occurs close to $\theta_{inc} = 45°$, with a 90° prism most suitable for SPP excitation.

The simulations were repeated for a 1 Ωcm Si slab, where Fig 7.8 shows a 2-D contour plot of analytically computed S_{11} against frequency and swept d_{gap}, in increments of 1.5 μm with the angle of incidence $\theta_{inc} = 45°$ kept constant. The return loss is minimum close to $d_{gap} = 160$ μm corresponding to optimal excitation of SPPs. Figure. 7.9 is a comparison of analytically and numerically computed return loss $20\log_{10}|S_{11}|$ for the 1 Ωcm Si slab with $d_{gap} = 160$ μm. Here, although the mesh resolution used in *COMSOL Multiphysics*® was comparable to the 10 Ωcm simulation; in terms of mesh elements per wavelength; however, there is much better agreement between the results from *COMSOL Multiphysics*® simulation and the analytical method, with the predicted plasmon resonance frequencies from both methods within 0.01 GHz of each other.

Figure 7.11 is a plot of normal H_z field from *COMSOL Multiphysics*® simulation showing surface plasmon excitation at 341.8 GHz. It can be observed in Fig. 7.11 that the evanescent x-component of the field does not penetrate too deep into the Si slab, and decays to less than 10% at a depth of 250 μm. Only one spectral dip is observed in the return loss response corresponding to a single surface plasmon excitation. The Si slab, in this case, can be approximated as a semi-infinite media as discussed earlier with the dispersion modelling approach. Figure 7.10 shows a plot of analytically

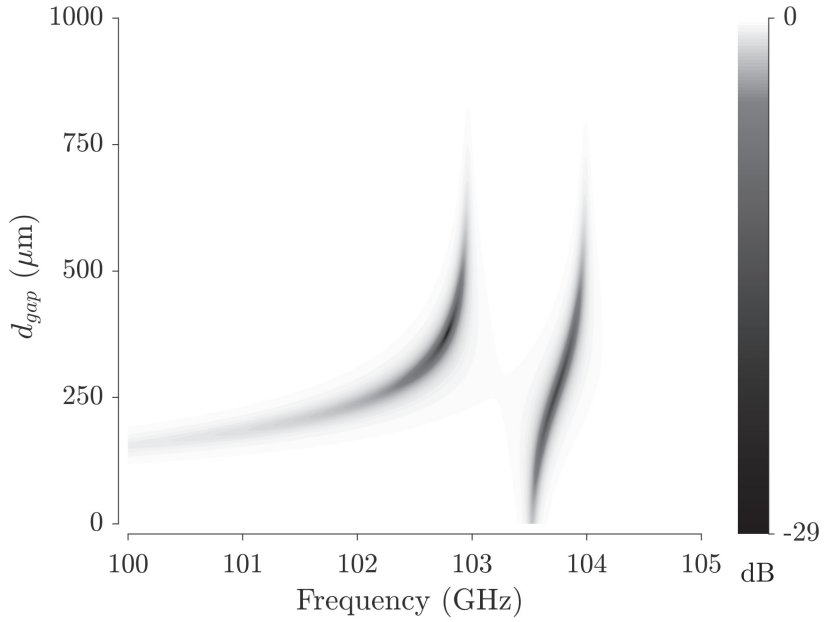
computed S_{11} against frequency and and angle of incidence, swept in increments of 0.25 degrees.

7.4 Full Wave Simulation Using *COMSOL Multiphysics*® and FDTD

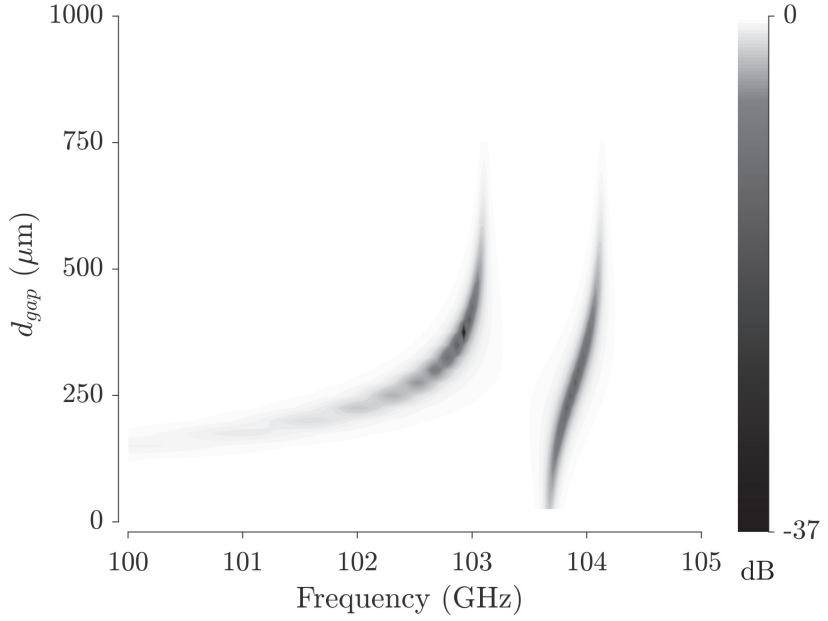
The set-up used for full-wave simulation is shown in Fig. 7.12. The prism is positioned, such that its shorter sides are aligned with the x- and y-axes. This is to ensure that ports are aligned with the shorter prism sides, as it is easier to define port excitation fields in both *COMSOL Multiphysics*® and FDTD if ports are parallel to any axis. Morveover, the ports are located close to the sides of the prism and not exactly on the prism. This is to match the actual intended experimental set-up in which the port could be a horn antenna or a waveguide placed close to the side of the prism. The Si sample was placed parallel to the diagonal prism side separated by an air gap. The whole arrangement is essentially a 2-D problem with the solution domain terminated by perfectly matched layer (PML) boundaries, to ensure that any radiated fields are absorbed and do not reflect back into the simulation space. Both, *COMSOL Multiphysics*® and FDTD use the same geometry set-up, however, it should be noted that while *COMSOL Multiphysics*® uses a frequency domain solver, FDTD is a time-domain method. The simulations were run for both 10 Ωcm and 1 Ωcm cases. For *COMSOL Multiphysics*® simulations, the specified mesh resolution was kept the same, while for the FDTD simulation the mesh resolution was doubled for the 1 Ωcm case. The shorter sides of the prism were 1.7 mm. It should be noted that, for 1 Ωcm case, the mesh consisted of slightly less elements owing to a decrease in d_{gap}.

The default meshing scheme in *COMSOL Multiphysics*® for 2-D problem uses triangular meshing elements. The meshed geometry consisted of 64,592 triangular mesh elements (for the 10 Ωcm case), as shown in Fig. 7.13. The meshing scheme used in FDTD consisted of rectangular mesh elements. The size of elements were non-uniform consisting of smaller elements for meshing the prism and Si slab with larger elements located at the edges of the simulation space including the PML regions. The FDTD mesh also used a non-uniform scheme with a total of 255,055 rectangular elements. The prism and slab were meshed using finer elements while the PML regions were mesh using coarser element. The meshed geometry is shown in Fig. 7.14.

The simulation was excited using Port 1 as shown in Fig. 7.12 and scattered fields were recorded at both Ports 1 and 2. For *COMSOL Multiphysics*®, a 'user defined' type of port was used with a 'slit' condition set as 'activated' and 'domain-backed' option selected. While *COMSOL Multiphysics*® is a frequency domain method which solves for a steady-state solution at a single



(a)



(b)

Figure 7.4: Plot of return loss $20\log_{10}|S_{11}|$ of the planar media problem depicted in Fig. 7.3, against frequency and gap between the prism and Si slab d_{gap} for the 10 Ωcm Si sample with $\theta_{inc} = 45°$: (a) analytical method; and (b) *COMSOL Multiphysics*® frequency domain solver. The odd (left) and even (right) mode surface plasmon excitations can be seen as sharp contours in the return loss plot. The return loss reaches a minimum for the odd and even modes close to $d_{gap} = 415$ μm and $d_{gap} = 270$ μm, respectively.

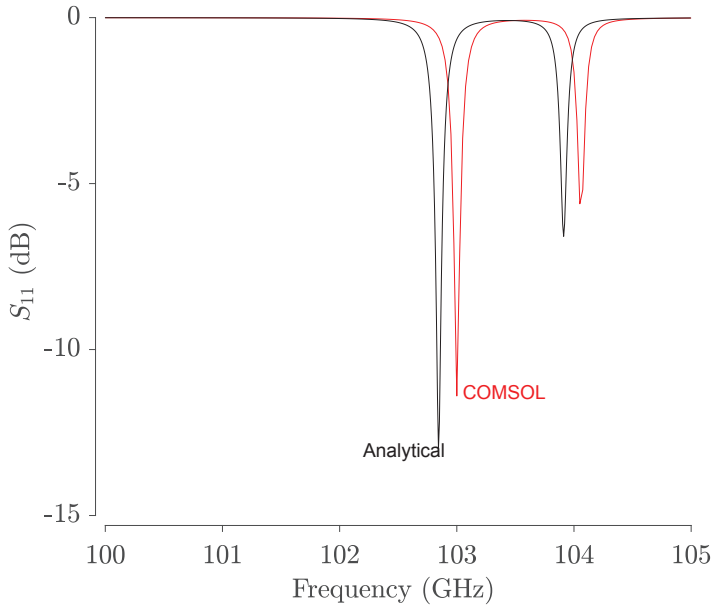


Figure 7.5: Comparison of return loss $20\log_{10}|S_{11}|$ plotted against frequency obtained from analytical method and *COMSOL Multiphysics*® simulation with gap between the prism and Si slab set as $d_{gap} = 415$ μm. The response shows odd (left) and even (right) mode surface plasmon modes excited on a Si slab of thickness 525 μm and 10 Ωcm resistivity. The *COMSOL Multiphysics*® response is shifted towards higher frequencies by about 0.15 GHz compared to the analytical method.

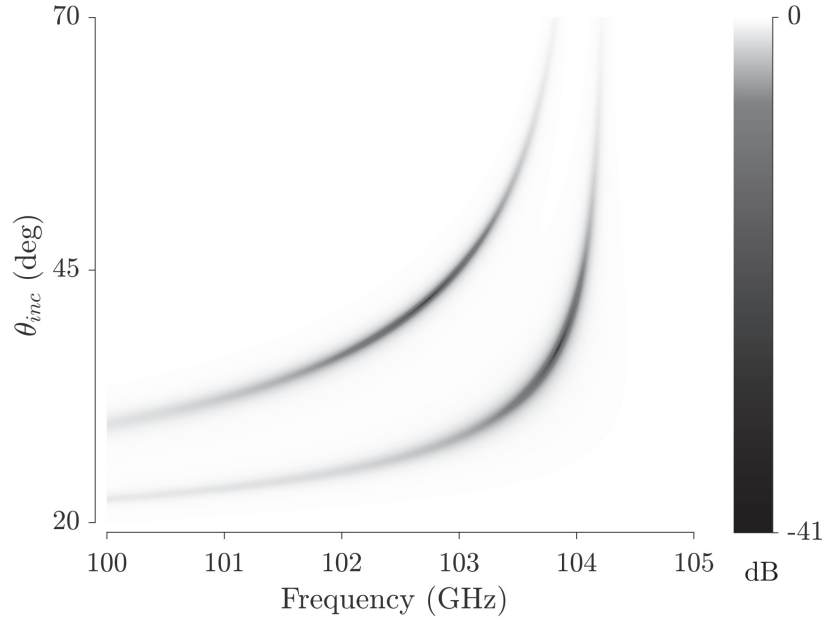
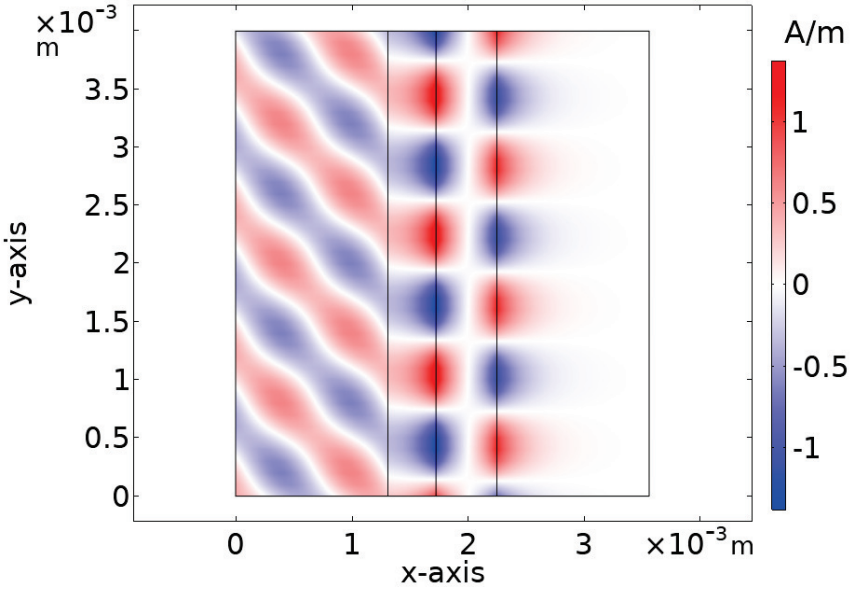
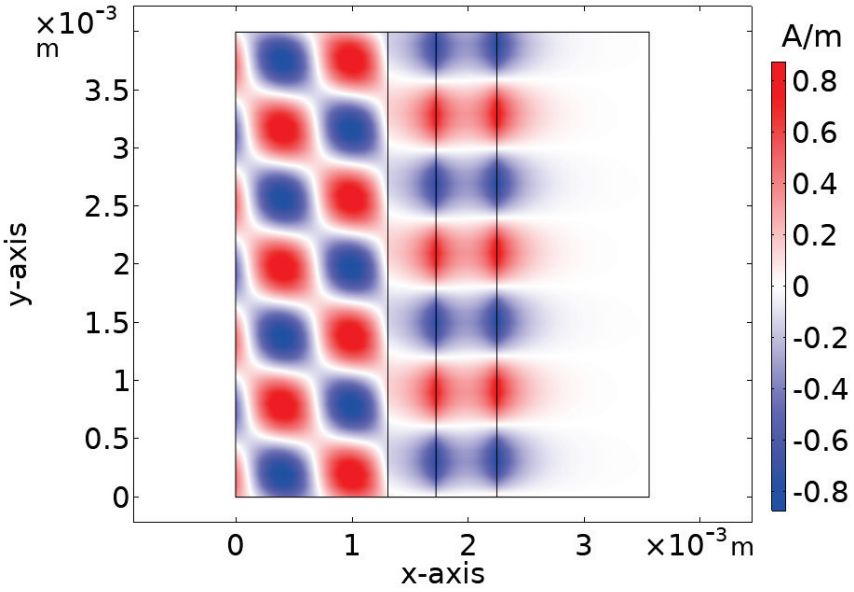


Figure 7.6: Plot of analytically computed return loss $20\log_{10}|S_{11}|$ against frequency and angle of incidence with $d_{gap} = 415$ μm. The response shows odd (left) and even (right) mode surface plasmon modes excited on a Si slab of thickness 525 μm and 10 Ωcm resistivity.



(a) 103 GHz



(b) 104.1 GHz

Figure 7.7: H_z magnetic field distributions of surface plasmons polaritons obtained from *COMSOL Multiphysics*® simulations for Si prism and 10 Ωcm Si slab at: (a) 103 GHz and; (b) 104.1 GHz. Odd and even mode surface plasmon excitations can be seen in (a) and (b), respectively, on both sides of the Si slab.

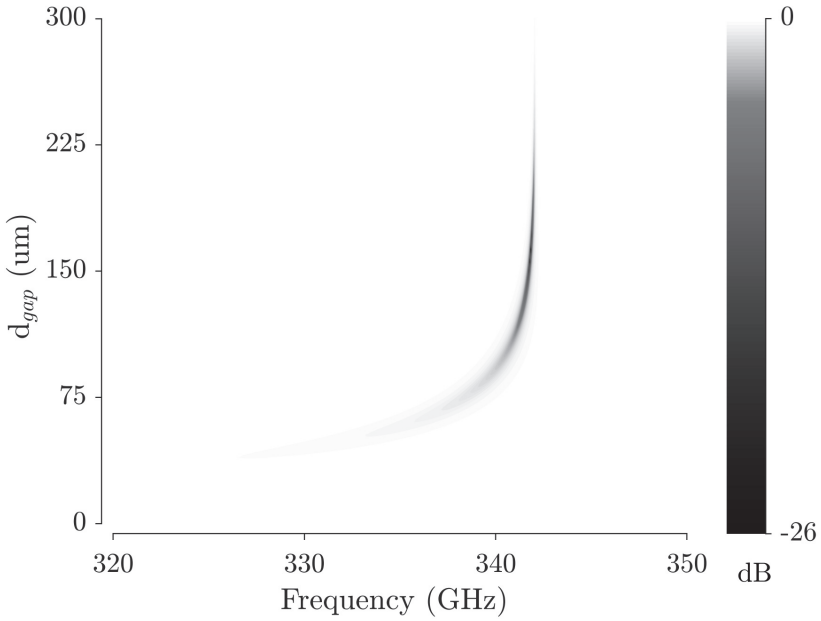


Figure 7.8: Contour plot of return loss $20\log_{10}|S_{11}|$ against frequency, and gap between the prism and Si slab d_{gap}, for the 1 Ωcm Si sample with $\theta_{inc} = 45°$. The optimal surface plasmon excitation occurs close to $d_{gap} = 160$ μm, where the return loss is minimum.

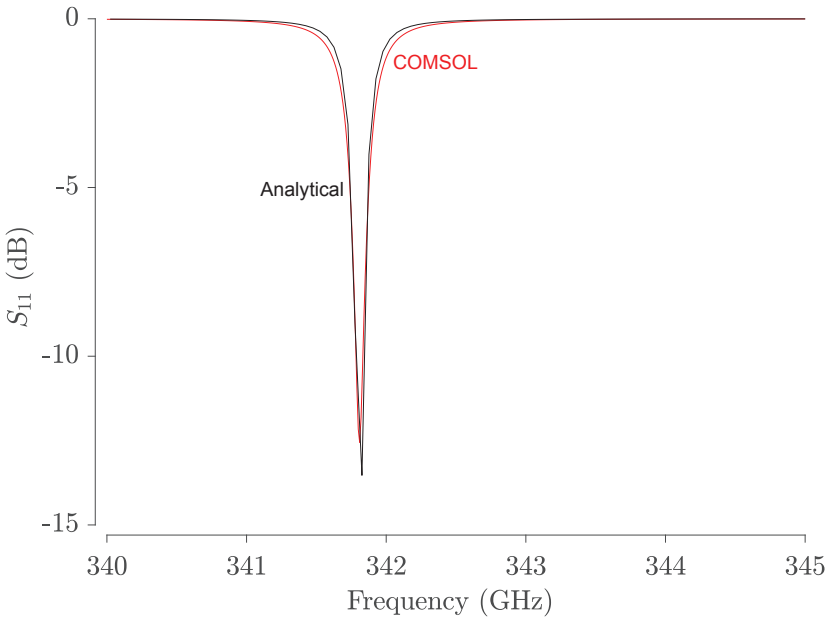


Figure 7.9: Comparison of return loss $20\log_{10}|S_{11}|$ plotted against frequency obtained from analytical method and *COMSOL Multiphysics*® simulation with gap between the prism and Si slab set as $d_{gap} = 160$ μm and $\theta_{inc} = 45°$. The predicted surface plasmon excitation from both methods is close to 341.8 GHz on a Si slab of thickness 525 μm and 1 Ωcm resistivity.

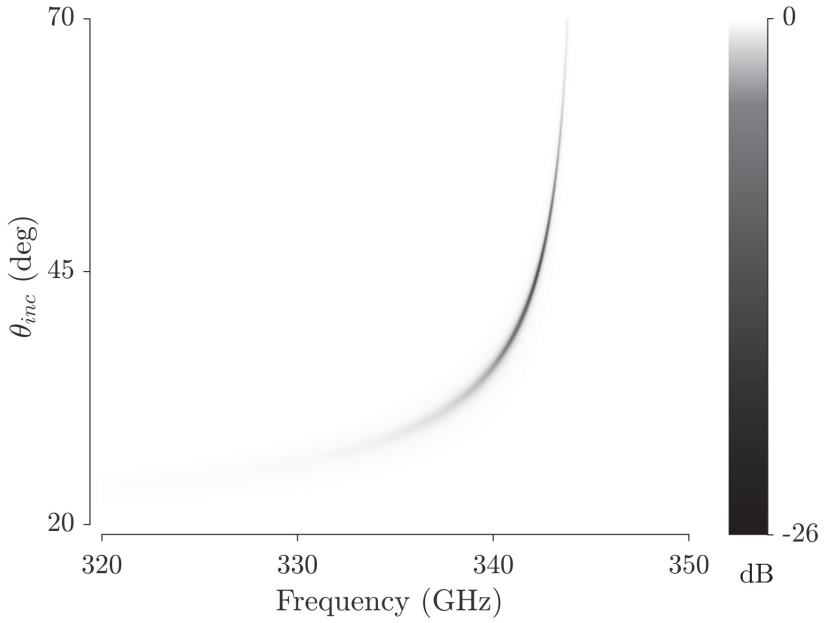


Figure 7.10: Analytically computed return loss $20\log_{10}|S_{11}|$ plotted against angle of incidence and frequency with $d_{gap} = 160$ μm. The return loss is minimum close to $\theta_{inc} = 45°$ corresponding to optimal surface plasmon excitation. The response tends to sharpen as θ_{inc} is increased.

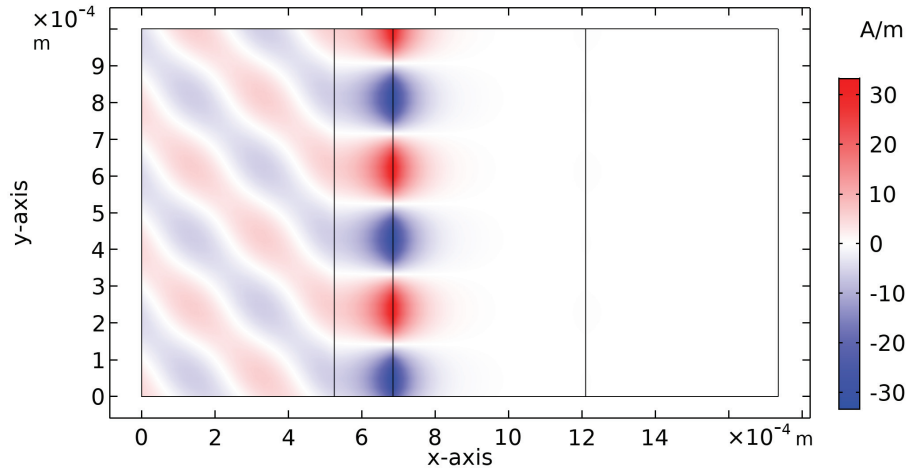


Figure 7.11: H_z magnetic field distributions of surface plasmon polaritons (SPP) obtained from *COMSOL Multiphysics*® simulations for Si prism and 1 Ωcm Si sample at 341.8 GHz. The excited SPPs reside on the surface of Si slab close to the prism. For analytical calculations, the Si slab can be approximated, in this case, as a semi-infinite media.

frequency, the FDTD method can be excited with a wide band time-domain pulse like a Gaussian pulse or Gaussian-derivative Ricker wavelet, to obtain the wide-band frequency response with a single run. *COMSOL Multiphysics*® was swept over a frequency range around the surface plasmon excitation frequency. The FDTD simulation was excited using a Gaussian-derivative Ricker wavelet source. The Ricker wavelet was generated by first using the MATLAB function *'gaussmf'* to generated the a Gaussian pulse and then taken the derivative of Gaussian pulse using the MATLAB *'diff'* function [5]. The excitation itself consisted only E_y component of electric field such that the electromagnetic wave propagates in $+x$ direction. A Gaussian profile was applied to E_y component for beam-shaping given by the mathematical expression,

$$E_y = E_{y0} e^{(y/2l_{side})^2} \tag{7.1}$$

where, E_{y0} is a constant set as 1 and l_{side} is the length of a shorter side of the prism which is also equal to the port width. Beam-shaping minimises reflections from the edges of the prism so that most of the energy is focused and projected in the centre of the prism.

7.4.1 Full-Wave Simulation Results

For full wave *COMSOL Multiphysics*® and FDTD simulations, electromagnetic waves are launched outside the prism from Port 1. The incident waves are partially reflected from the shorter side of prism, while the rest of the waves enter the prism and undergo total internal reflection from the diagonal, and are again partially reflected from the other side. The reflection and transmission of energy from the sides of the prism continue until the energy in the prism gradually escapes from the shorter sides and are recorded at the two ports. Some of the energy will excite plasmons on the Si slab and will appear as sharp spikes in the reflected response. The reflected response is the effective return loss $20\log_{10}|S_{11}^{eff}|$ where effective reflection coefficient is defined as,

$$20\log_{10}|S_{11}^{eff}| = 10\log_{10}(|S_{11}|^2 + |S_{21}|^2) \tag{7.2}$$

The normalised effective return loss $20\log_{10}|S_{11}^{eff}|$ from *COMSOL Multiphysics*® and FDTD simulations for 10 Ωcm and 1 Ωcm Si slab are plotted in Figs. 7.15 and 7.16, respectively. Both plots show excitation of plasmonic resonances with some additional resonant modes. For the 10 Ωcm case in Fig. 7.15, both *COMSOL Multiphysics*® and FDTD correctly predict odd and even mode surface plasmon excitations around 103 and 104 GHz with the *COMSOL Multiphysics*® response slightly shifted towards lower frequencies when compared to analytical calculations. For the 1 Ωcm case in Fig. 7.16, in addition to the expected resonance at around 342 GHz, an additional resonance

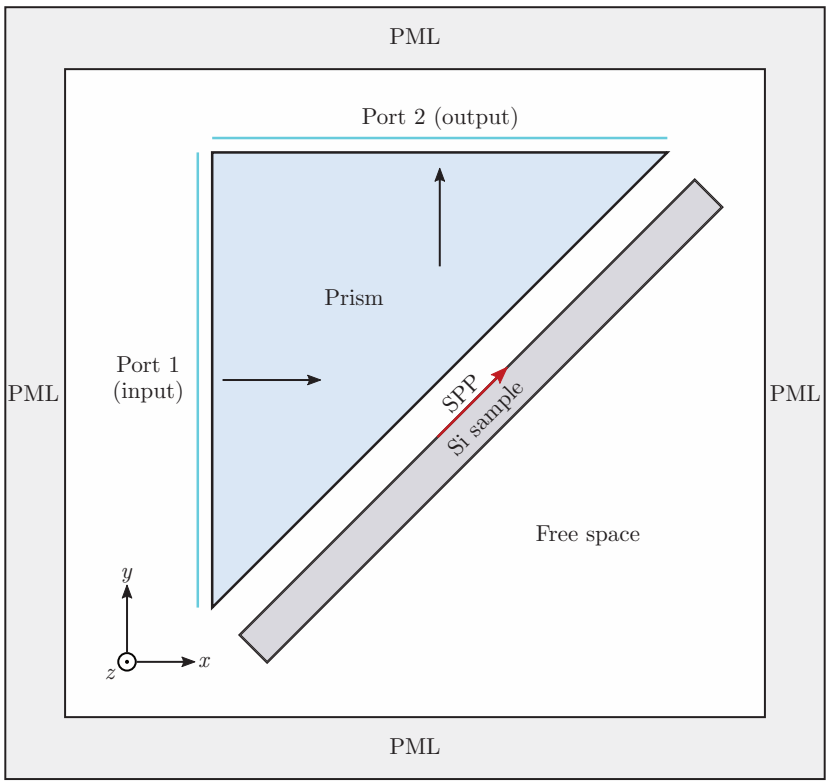
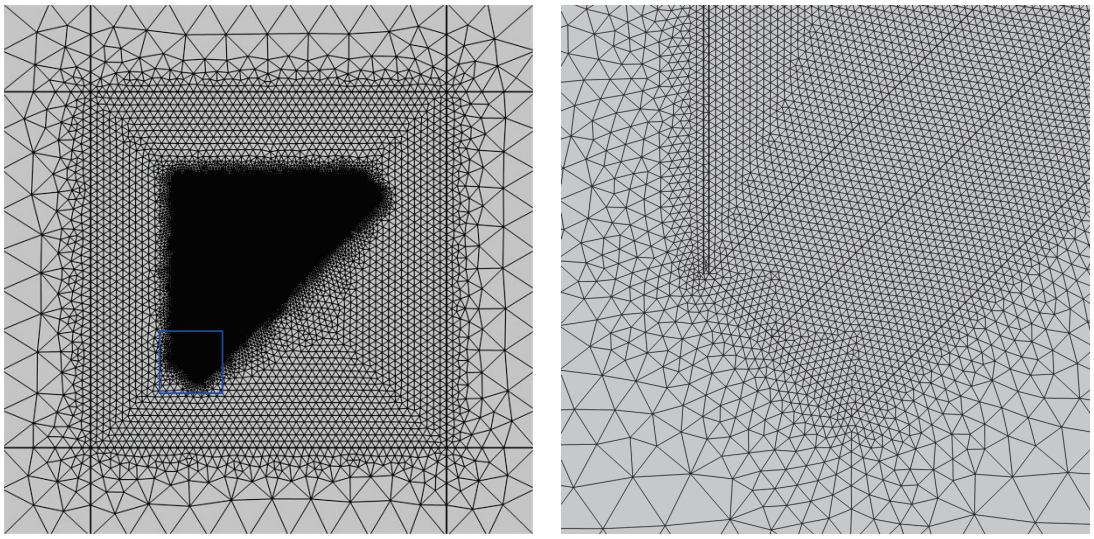


Figure 7.12: Simulated geometry showing prism, Si slab, ports and perfectly matched layer (PML) boundaries. A Ricker wavelet with a Gaussian profile is excited at Port 1, while Port 2 is used to record the transmitted fields. The evanescent component of the incident fields at the diagonal side of the prism excite surface plasmon polaritons on the Si slab. The whole simulation domain is terminated in PMLs to absorb any radiated fields.



(a) (b)

Figure 7.13: Non-uniform triangular meshing scheme used in *COMSOL Multiphysics*® with $d_{gap} = 415$ μm: (a) fully meshed geometry; (b) zoomed view of lower part of prism and Si slab. As seen in the zoomed view (b), the meshing is finest inside the prism, gap and the Si slab.



(a) (b)

Figure 7.14: Rectangular meshing scheme used in FDTD with $d_{gap} = 415$ μm: (a) fully meshed geometry; (b) zoomed view of lower part of prism and Si slab. With, rectangular meshing elements, the diagonal side of the prism and Si slab are approximated as a sawtooth.

can be observed above 342 GHz from both simulation techniques. Again, *COMSOL Multiphysics*® response is slightly shifted towards lower frequencies.

7.5 Spectroscopy of Material Sample

The experimental set-up described in this section can be used as a spectrometer by placing the dispersionless sample test material in the gap between prism and Si slab. The unknown dielectric constant of the sample test material can be determined from measurements by comparing against the spectral response of a material with known dielectric constant. As an example, Figs. 7.17 and 7.18 show the responses when the dielectric constant of a test material is varied between 2.30 and 2.35 in incremental steps of 0.01.

The effective return loss $20\log_{10}|S_{11}^{eff}|$ from full wave *COMSOL Multiphysics*® simulations for 10 Ωcm and 1 Ωcm Si slab are shown in Figs. 7.19 and 7.21, respectively, while FDTD results for 10 Ωcm and 1 Ωcm are shown in Figs. 7.20 and 7.22. Both, *COMSOL Multiphysics*® and FDTD results for 10 Ωcm (Figs. 7.19 and 7.20) predict the spectral location of surface plasmon resonances within 0.5 GHz. Morever, compared to the analytical results, the location of plasmon resonances are shifted towards lower frequencies in full wave simulations. For the 10 Ωcm Si slab, the spectral separation between the resonances computed from both, analytical and full wave simulations, is the same and is ∼0.08 GHz as shown in Figs. 7.19 and 7.20. For the 1 Ωcm Si slab, the spectral separation between the resonances computed from both, analytical and full wave simulations, is also same and is ∼0.35 GHz as shown in Figs. 7.21 and 7.22.

7.6 Conclusions

Surface plasmon excitation has a number of uses in the THz domain, especially for sensing and detection. Using the well-known attenuated total reflection configuration, a spectrometer design is proposed, making use of high resistivity Si slab. The proposed geometrical design is modelled using analytical and full-wave simulations that demonstrate surface plasmons excitation is dependent on the separation between the prism and the Si slab, and the dielectric constant of the material in the gap. Analytical modelling techniques consisted of dispersion modelling and analytical planar media modelling. Full-wave modelling included *COMSOL Multiphysics*® finite element based modelling that used a frequency domain solver and the finite-difference time domain (FDTD) method, which is a time-domain technique. The dispersion modelling technique was first used to predict the location of surface plasmon resonances using dispersion curves for prism and surface plasmon polaritons

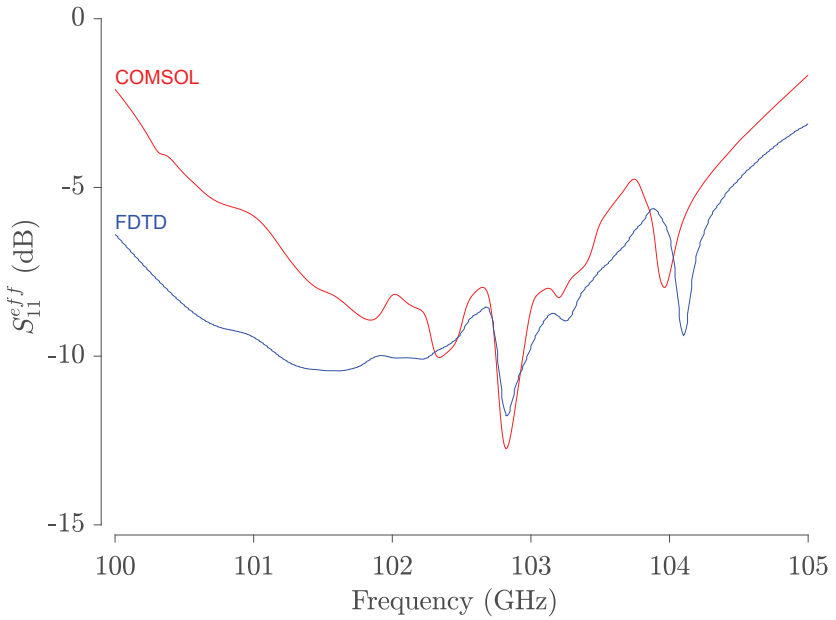


Figure 7.15: Effective return loss $20\log_{10}|S_{11}^{eff}|$ from full-wave *COMSOL Multiphysics*® and finite-difference time domain simulations for the 10 Ωcm Si slab with $d_{gap} = 415$ μm. The response from both solvers show odd and even excitation of surface plasmons close to 103 and 104 GHz, respectively.

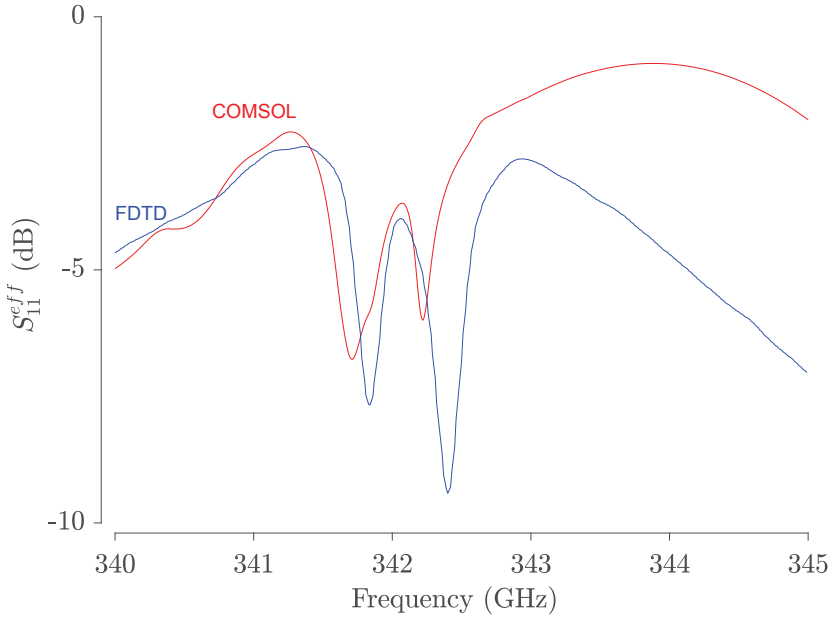


Figure 7.16: Effective return loss $20\log_{10}|S_{11}^{eff}|$ from *COMSOL Multiphysics*® and FDTD simulations for 1 Ωcm Si slab with $d_{gap} = 160$ μm. Unlike, analytical results, both full-wave solvers show two resonances in the observed response roughly centred around 342 GHz.

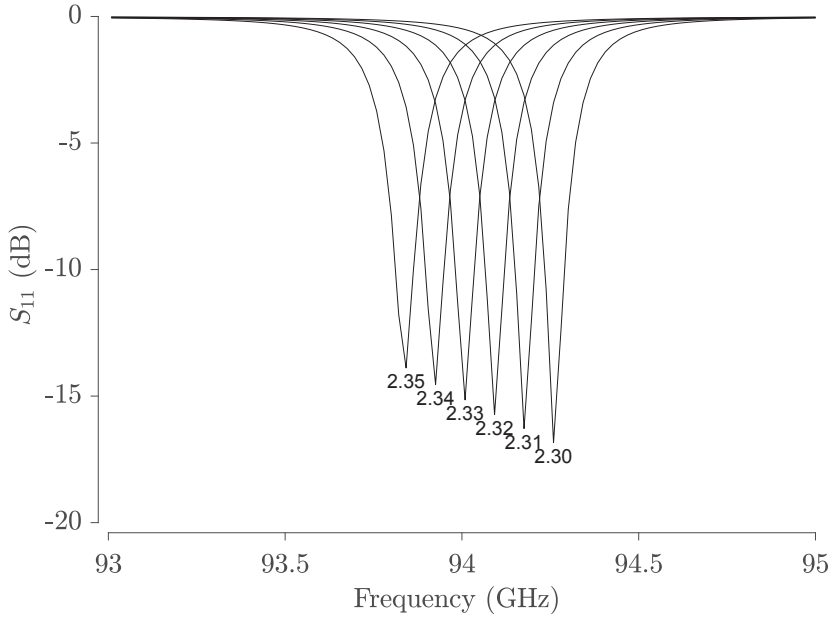


Figure 7.17: Analytically computed response $20\log_{10}|S_{11}|$ of a 750 μm thick test material having dielectric constant between 2.30 and 2.35 with 1 Ωcm Si slab. The surface plasmon resonance shifts by approximately 0.08 GHz if the dielectric constant changes by 0.01.

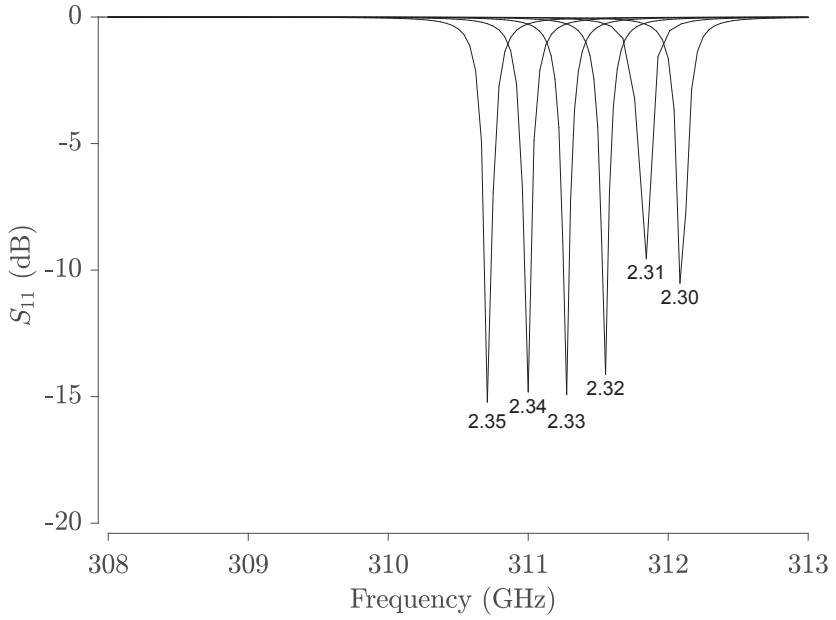


Figure 7.18: Analytically computed response $20\log_{10}|S_{11}|$ of a 300 μm thick test material having dielectric constant between 2.30 and 2.35 with 10 Ωcm Si slab. The surface plasmon resonance shifts by approximately 0.35 GHz if the dielectric constant changes by 0.01.

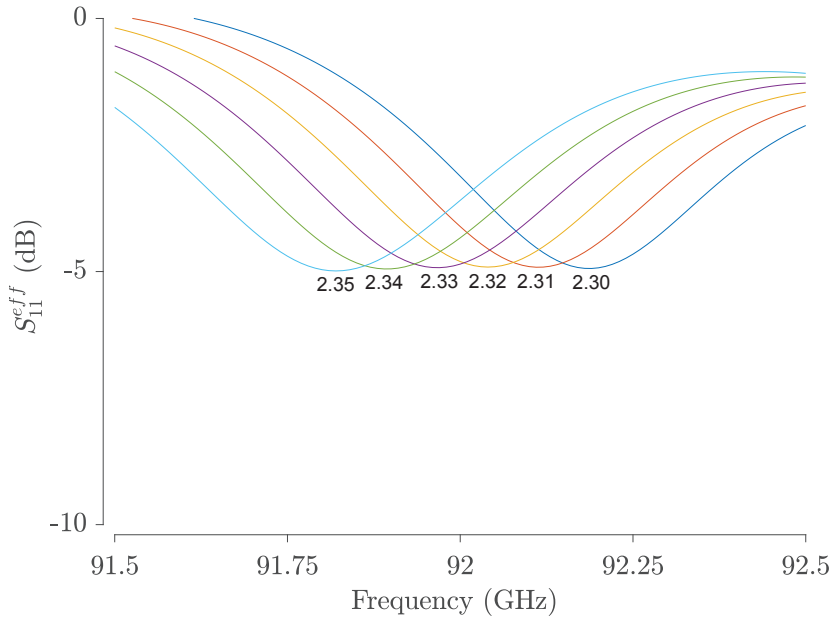


Figure 7.19: Effective return loss $20\log_{10}|S_{11}^{eff}|$ from full wave *COMSOL Multiphysics*® simulations for 10 Ωcm Si slab with $d_{gap} = 750$ μm. The surface plasmon resonance shifts by approximately 0.08 GHz if the dielectric constant changes by 0.01.

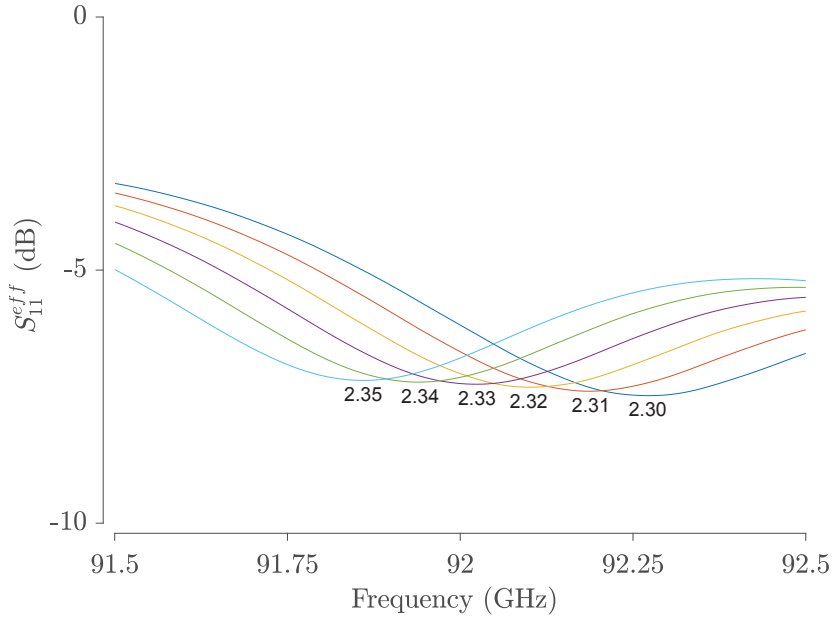


Figure 7.20: Effective return loss $20\log_{10}|S_{11}^{eff}|$ from full wave FDTD simulations for 10 Ωcm Si slab with $d_{gap} = 750$ μm. The surface plasmon resonance shifts by approximately 0.08 GHz if the dielectric constant changes by 0.01.

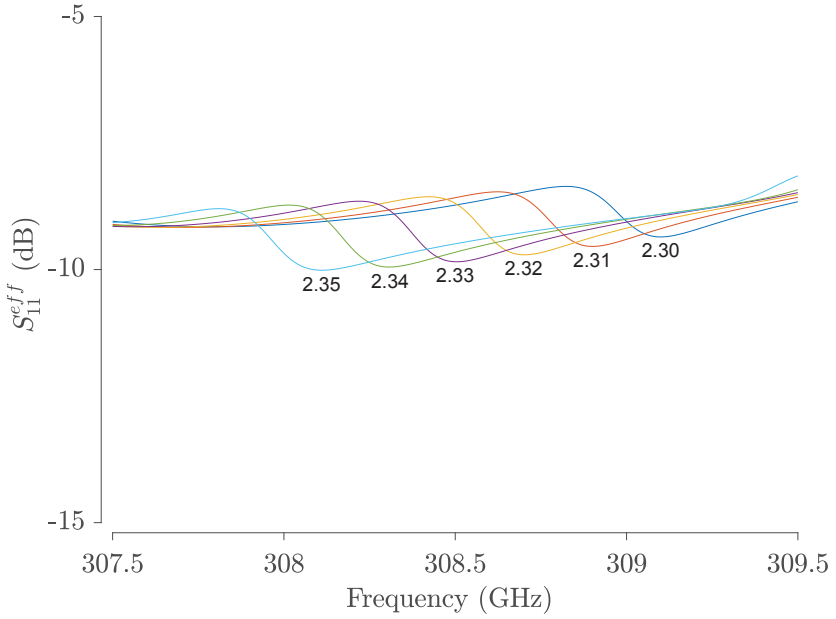


Figure 7.21: Effective return loss $20\log_{10}|S_{11}^{eff}|$ from full wave *COMSOL Multiphysics*® simulations for 1 Ωcm Si slab with $d_{gap} = 300$ μm. The surface plasmon resonance shifts by approximately 0.35 GHz if the dielectric constant changes by 0.01.

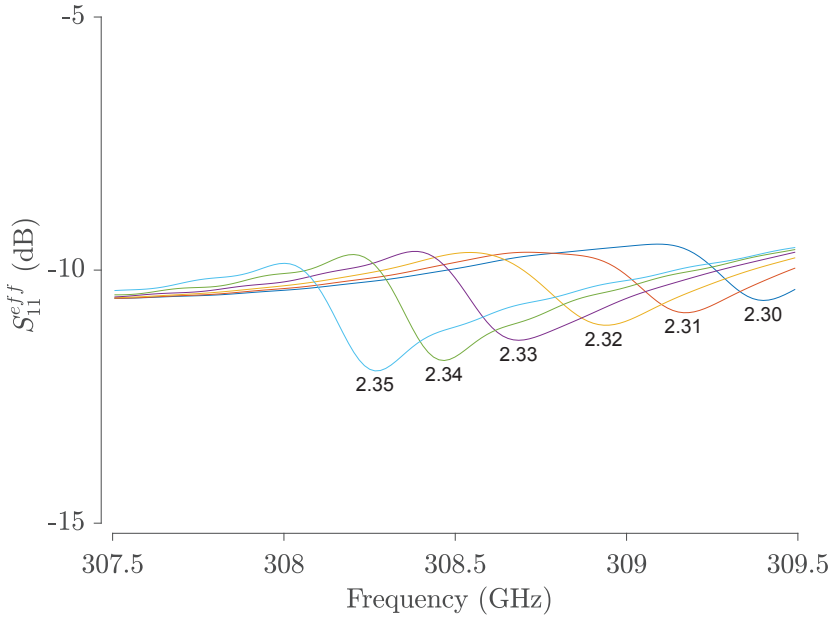


Figure 7.22: Effective return loss $20\log_{10}|S_{11}^{eff}|$ from full wave FDTD Multiphysics simulations for 1 Ωcm Si slab with $d_{gap} = 300$ μm. The surface plasmon resonance shifts by approximately 0.35 GHz if the dielectric constant changes by 0.01.

on a high resistivity Si slab. Next, a planar media approach was used to predict surface plasmon resonance using analytical method and full-wave *COMSOL Multiphysics*® solver. Next, the intended experimental set-up consisting of Si prism and a Si slab underneath the prism was simulated using the full-wave *COMSOL Multiphysics*® solver and the FDTD method. Both numerical approaches predicted excitation of surface plasmon resonances within 0.5 GHz in the worst case scenario. Finally, a material sample was used as a filler in the gap between the prism and Si slab. The dielectric constant of material was changed in steps of 0.01 which resulted in a shift in predicted surface plasmon resonances. With the 10 Ωcm Si slab, the shift in resonances was ∼0.08 GHz, whereas, for the 10 Ωcm Si slab, the shift in resonances was ∼0.35 GHz. The shift in surface plasmon resonances can be used to compare and predict the dielectric constant of an unknown sample against the response of a sample with known dielectric constant.

7.7 Acknowledgements

The work presented in this chapter is a continuation of the original work by Dr. William Otter [1]. This work was done under the supervision of Prof. Stepan Lucyszyn.

References

[1] W. J. Otter, *Technologies for terahertz frequency sensing*. PhD thesis, Imperial College London, 2015.

[2] M. M. Nazarov, A. P. Shkurinov, F. Garet, and J.-L. Coutaz, "Characterization of highly doped Si through the excitation of THz surface plasmons," *IEEE Trans. THz Sci. Technol.*, vol. 5, no. 4, pp. 680–686, 2015.

[3] S. Ekgasit, C. Thammacharoen, and W. Knoll, "Surface plasmon resonance spectroscopy based on evanescent field treatment," *Analytical Chemistry*, vol. 76, no. 3, pp. 561–568, 2004.

[4] M. Poulin, S. Giannacopoulos, and M. Skorobogatiy, "Surface wave enhanced sensing in the terahertz spectral range: Modalities, materials, and perspectives," *Sensors*, vol. 19, no. 24, p. 5505, 2019.

[5] MATLAB Functions. Accessed: 7 Mar. 2019. [Online]. Available: `https://uk.mathworks.com/help/matlab/functions.html`.

Chapter 8

Full-wave Modelling of Terahertz Frequency Plasmons in Two-Dimensional Electron Systems

8.1 Introduction

While models of terahertz frequency plasmons in two-dimensional electron systems (2-DES) are usually developed by reducing the number of spatial dimensions, fully three-dimensional models may be needed for the design and analysis of realistic structures. In this chapter, plasmons and magnetoplasmons observed in two recent experiments will be analysed using full-wave electromagnetic simulations. Here, agreement between the theoretical and the experimental results are demonstrated, and further device characteristics such as transmission, insertion loss, absorption, and field distributions are discussed. Then, a comparison of full-wave simulations with a two-dimensional model is carried out. Finally, approaches for increasing signal transmission and reducing insertion loss are discussed, with direct relevance for improving future experiments.

Two-dimensional electron systems are capable of supporting plasmons, which are slow electromagnetic waves caused by collective electron motion. In 2-DESs formed in III-V semiconductor heterostructures, plasmon frequencies typically lie in the microwave to terahertz frequency ranges. Terahertz plasmons are particularly attractive as they could be exploited in a range of practical devices; notably, terahertz sources and detectors.

Ever since the pioneering works of Dyakonov and Shur [**?**], one of the most commonly studied geometries for terahertz plasmon emitters and detectors is that based on the field-effect transistor [see Fig. 8.1(a)]. A 2-DES is terminated by two ohmic contacts, which allows application and

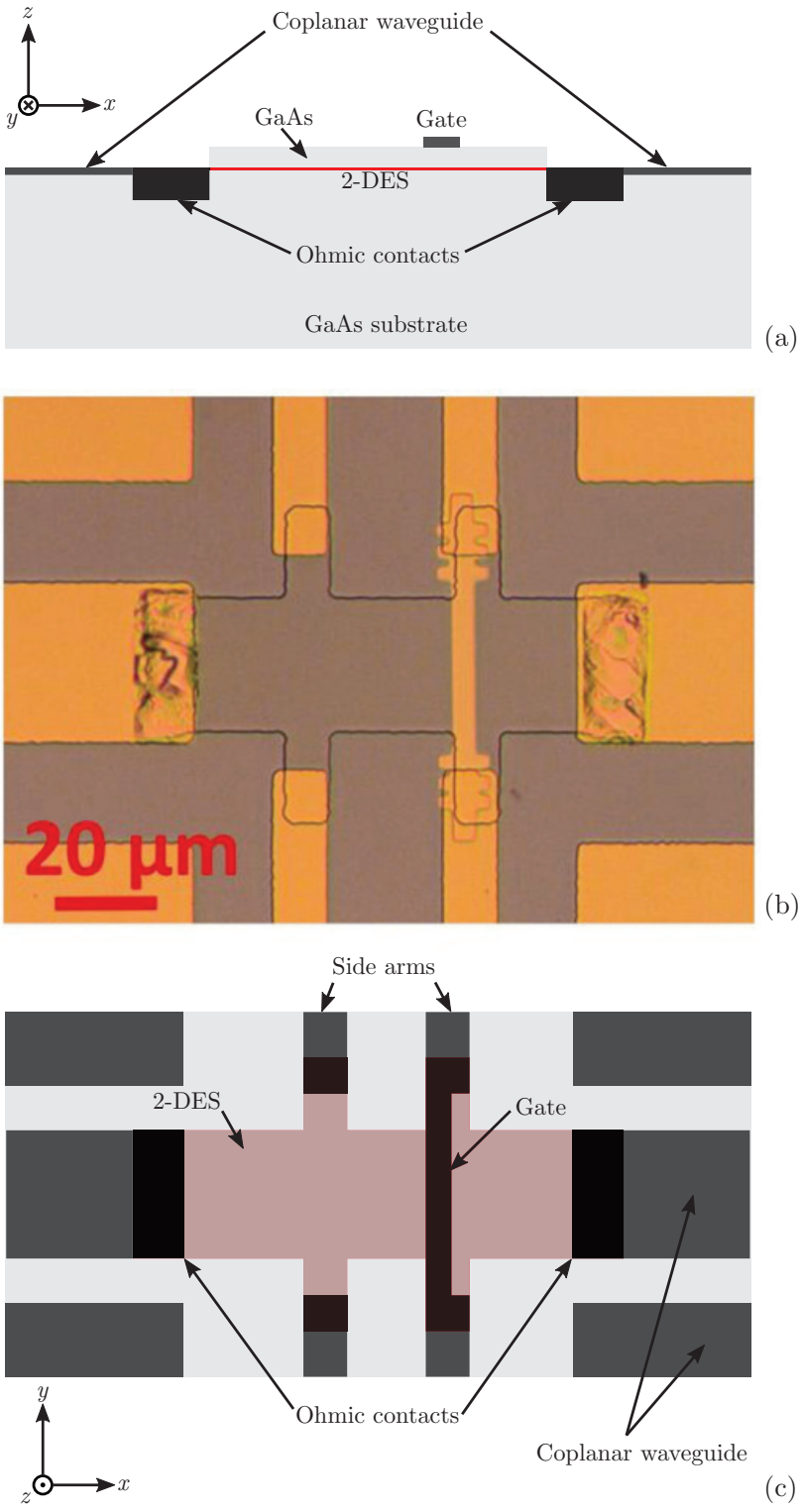


Figure 8.1: (a) Schematic side view of a 2-DES device used in experiments. The device geometry is inspired by the field-effect transistor; (b) Micrograph (adapted from Wu *et al.* [1]); and (c) schematic top view of the device used in experiments by Wu *et al.* The complex device geometry requires three-dimensional modelling. Figure reproduced from Dawood *et al.* [2].

detection of a DC voltage as well as the coupling-in and coupling-out of terahertz waves. Above the 2-DES is a gate, which controls the electron density in the 2-DES, and is frequently used for coupling into the free-space radiation. Variations of this basic structure have also been made, for example, in double-grating-gate devices [3].

Theoretical studies of such devices have been made predominantly with two-dimensional (2-D) models, in which the devices are assumed to be infinitely long in the y-direction [Fig. 8.1(a)]. Three-dimensional (3-D) models, however, may be needed to describe realistic devices, especially when agreement with experiment is sought. As an example, Figs. 8.1(b) and (c) show, respectively, a micrograph and a sketch of the device used by Wu *et al.* [1]. Several features that cannot be taken into account by a 2-D model stand out. First, the width of the 2-DES (25 μm in the y-direction) is smaller than its length (73 μm in the x-direction). Second, the 2-DES is connected at both ends to a coplanar waveguide (CPWG). Third, the 2-DES has a non-rectangular shape with four short stubs.

Full-wave numerical simulations are a natural choice for analysis of such structures and have been used in this study to:

(i) compare a full-wave 3-D electromagnetic model with the experiments by Wu *et al.* [1] on plasmon- (Section 8.3) and magneto-plasmon transmission (Section 8.4);

(ii) analyse the experimental devices beyond the available experimental data (Section 8.3);

(iii) compare the 3-D model with a two-dimensional model based on mode-matching (Sections 8.3 and 8.4);

(iv) design and model device geometries with improved characteristics (Section 8.6).

8.2 Device Structure and Modelling Considerations

Wu *et al.* formed a 2-DES in a GaAs/AlGaAs heterostructure grown by molecular beam epitaxy. The depth of the 2-DES was 75 nm [1]. It was found that slight variations of the permittivity, due to the detailed layer-structure, had little effect on the simulation results, and assumed that the substrate material was GaAs, with a relative permittivity of 12.4, see Fig. 8.1. The dc electron density in the 2-DES was $n_{2D} = 6.5 \times 10^{11}$ cm^{-2}. The electron scattering time was determined from dc conductivity measurements to be $\tau = 33$ ps. The device was formed by etching a mesa to have a length 73 μm and a width 25 μm. The mesa had four stubs around 10 μm wide and 7.5 μm long, each located around 15.5 μm from the ohmic contacts. The stubs were connected to four metal lines, two of which were shorted to form a gate above the 2-DES. It was found that including these

Table 8.1: Dimensions used in simulations (see Fig. 8.1). Table reproduced from Dawood *et al.* [2].

2-DES length, l	73 μm
2-DES width/width of center conductor, w	73 μm
2-DES depth/mesa height, h	75 nm
length of first ungated 2-DES section, l_{S1}	48.9 μm
length of second ungated 2-DES section, l_{S2}	19.7 μm
gate width/length of gated 2-DES section, l_g	4.4 μm
stub width, w_s	24 μm
stub length, l_s	11 μm
width of 2-DES side extension, w_e	14 μm
separation between left contact and stub, l_{t1}	16 μm
separation between stubs, l_{t2}	21.9 μm
separation between right contact and stub, l_{t3}	13.1 μm
CPWG gap, w_g	20 μm
width of waveguide ground plane, w_{cw}	15 μm
substrate thickness, t	50 μm
depth of ohmic contact, t_c	1250 nm
length of ohmic contact, l_c	12.5 μm

features into simulations was needed for full agreement with experiments. Two ohmic contacts of width 12.5 μm were formed, one at either end of the mesa. A metallic gate of width 4.4 μm was then deposited at a distance of 48.9 μm from the left ohmic contact. An LT-GaAs layer grown on the same substrate allowed Wu *et al* to form two photoconductive switches, one at each side of the device (not shown in Fig. 8.1), which were used for excitation and detection of picosecond-duration current pulses. The pulses were both delivered to and extracted from the 2-DES using two CPWGs, the centre conductors of which were connected to the ohmic contacts (see Fig. 8.1). A negative voltage applied to the gate relative to an ohmic contact depleted the 2-DES underneath the gate, and the relationship between the gate voltage and the electron density was found to be [2],

$$V_g = \left(\frac{n_{2D}}{\alpha_1}\right)^{\frac{1}{\gamma}} - \alpha_2 \tag{8.1}$$

where, V_g is in volts, n_{2D} is in cm^{-2}, $\alpha_1 = 5.3813 \times 10^{15}$ cm^{-2}, $\alpha_2 = 2.601$, and $\gamma = 0.2295$. In the experiments, the voltage typically varied between -0.4 and -2.4 V. Further details about the devices, experimental arrangement, and measurements can be found in Refs. [1], [4].

When describing semiconductor plasmons theoretically, one has to choose how to model electron dynamics (both in the 2-DES and at the junctions) and the electromagnetic fields. The full-wave simulations in this study are based on the standard Drude model based on Euler's hydrodynamic

equation of motion which, in the absence of dc magnetic fields, leads to an isotropic AC 2-D conductivity in the 2-DES of the form [2],

$$\sigma_{2D} = \frac{n_{2D}e^2}{j\omega m^* \left(1 + \frac{1}{j\omega\tau}\right)} \tag{8.2}$$

where, e is the electron charge, m^* is the effective electron mass and ω is the angular frequency. The full-wave simulations also use the full system of Maxwell's equations, which then dictate the boundary conditions.

The equations were solved using the RF module of the *COMSOL Multiphysics*® numerical package. The 2-DES was modelled using a surface current density defined by (8.2). The ohmic contacts, the CPWGs, and the gate were modelled as perfect conductors to reduce computational overhead. The whole structure was enclosed in a bounding box with dimensions $223 \times 100 \times 60$ μm^3. Two sides of the bounding box were used for the excitation and detection ports for the CPWGs, while the other sides were perfect electric conductors. The two outer (ground) conductors of the CPWGs were connected to a perfectly conducting box along the length of the structure. This ensured that the even CPWG mode was excited, which was found to couple well to plasmons in the experiments (rather than the slot-line mode, which did not) [1]. The waveguide sections to both sides of the 2-DES were 75 μm long. The central conductor of the waveguide was 30 μm wide, the gap between the conductors was 20 μm. The width of the outer conductors was 15 μm.

8.2.1 Excitation and Ports

In the model, a CPWG at either end was terminated in numeric ports. Numeric ports in *COMSOL Multiphysics*® compute the transverse 2-D field profile from boundary conditions imposed by the geometry of the modelled structure. The field profile is then used to excite an incident wave propagating perpendicular to the ports which simulates an infinitely long coplanar waveguide. In order to use numeric ports in *COMSOL Multiphysics*®, an additional 'study step' needs to be added before the actual simulation for each port. This step is called boundary mode analysis and computes the 2-D profile of the incident wave on the CPWG.

The transverse electric field profile of the even CPWG mode is shown in Fig. 8.2. The field profile was computed by solving Poisson's equation using the method of relaxation by employing the finite-difference discretisation scheme. The black lines indicate a PEC bounding box and the CPWG conductors. The field strength is stronger in the substrate (lower grey region) than in the air (upper white region). MATLAB code for computing the field profile is given in Appendix G.

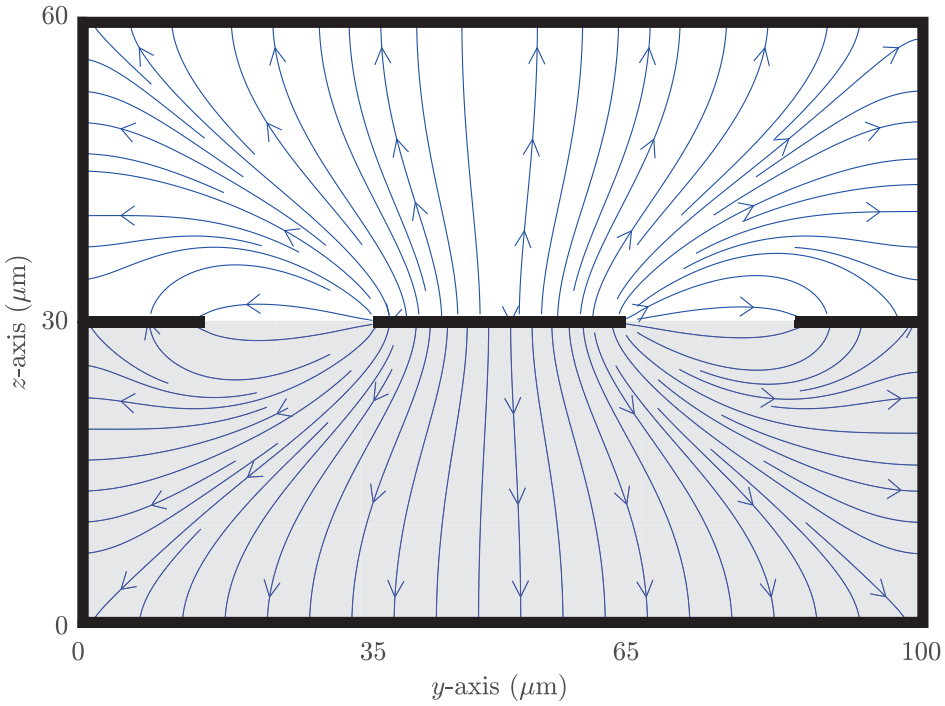


Figure 8.2: The transverse electric field profile of the even coplanar waveguide (CPWG) mode numerically computed from Laplace's equation, using a finite-difference scheme and method of relaxation. The thick black lines denote perfect electric conductor (PEC) boundaries and the CPWG conductors in the transverse plane. The lower half (shaded grey region) is GaAs substrate with the upper half (white region) is air. Fields are stronger in the GaAs region compared to air due to dielectric constant of GaAs being greater than air. With the even CPWG mode, the side conductors or ground planes of the CPWG must be maintained at the sample potential while the centre conductor is at a different potential. This is ensured by connecting the outer ground planes with the bounding PEC box.

8.2.2 Meshing

It should be noted that the depth of the AlGaAs layer (70 nm) and thickness of the 2-DES layer (simulated as a boundary condition) are very small compared to the height of the GaAs substrate (30 μm). It is not possible to use uniform meshing as the size of mesh will be prohibitively large. Along the height of the structure, meshing should be finer near the 2-DES and coarser at the PEC boundaries. Along the length of the 2-DES, meshing should be finest in the gated region, relatively fine in the ungated regions and coarser along the CPWG. Along the width, meshing needs to be fine at the edges of the 2-DES. A general rule of thumb is to ensure that there are at least 5 elements per wavelength in the longitudinal direction.

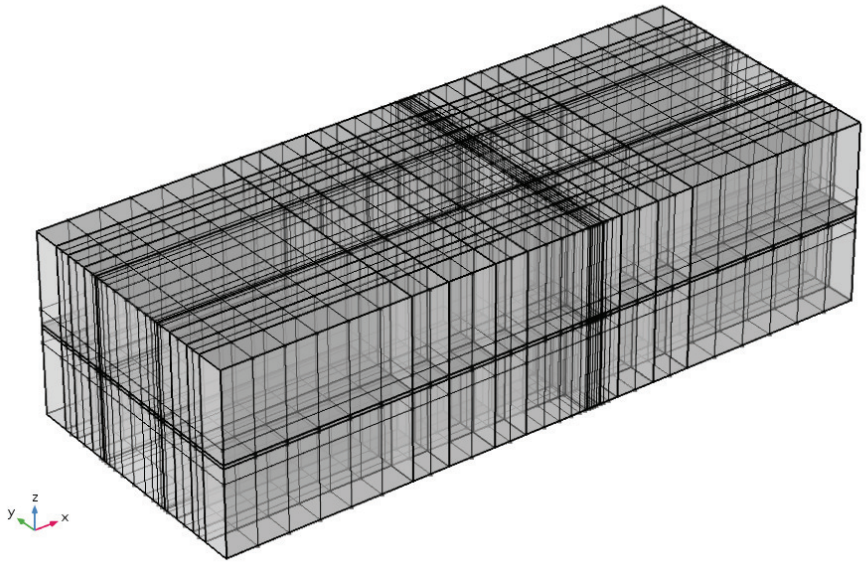


Figure 8.3: Meshed model in *COMSOL Multiphysics*® illustrating the non-uniform meshing scheme with cubic elements. Along the longitudinal direction, meshing is finest in the gated region, while the ungated 2-DES and coplanar waveguide sections have coarse meshing. Along the vertical direction meshing is finest close to the 2-DES and AlGaAs layer with a total of 8 meshing elements in the z-direction. Along the y-direction, meshing is finest at the edges of the 2-DES.

In *COMSOL Multiphysics*®, the default tetrahedral meshing scheme is inefficient for a 2-DES device geometry, as it tends to mesh densely at corners where a coarser meshing will be sufficient. Since the structure consists of straight boundaries, the best scheme is non-uniform, mapped meshing with cubic elements as shown in Fig. 8.3.

8.3 Comparison with Experiments: Gate-Modulation Signals

In the experiments, picosecond current pulses from a photoconductive switch were injected into one of the coplanar waveguides.They are then passed through the 2-DES and coupled into the waveguide at the other side of the 2-DES. This waveguide was connected to a second switch, where the transmitted pulses were detected. To increase the signal-to-noise ratio of the detected signals, a gate-modulation technique was used. The gate voltage was periodically modulated by a weak signal around a stationary value, which allowed Wu *et al.* to employ lock-in detection. As a result, the detected signals were proportional to the absolute value of the derivative of the transmission coefficient with respect to the gate voltage. Figure 8.4(a) shows, as a colour plot, the experimentally

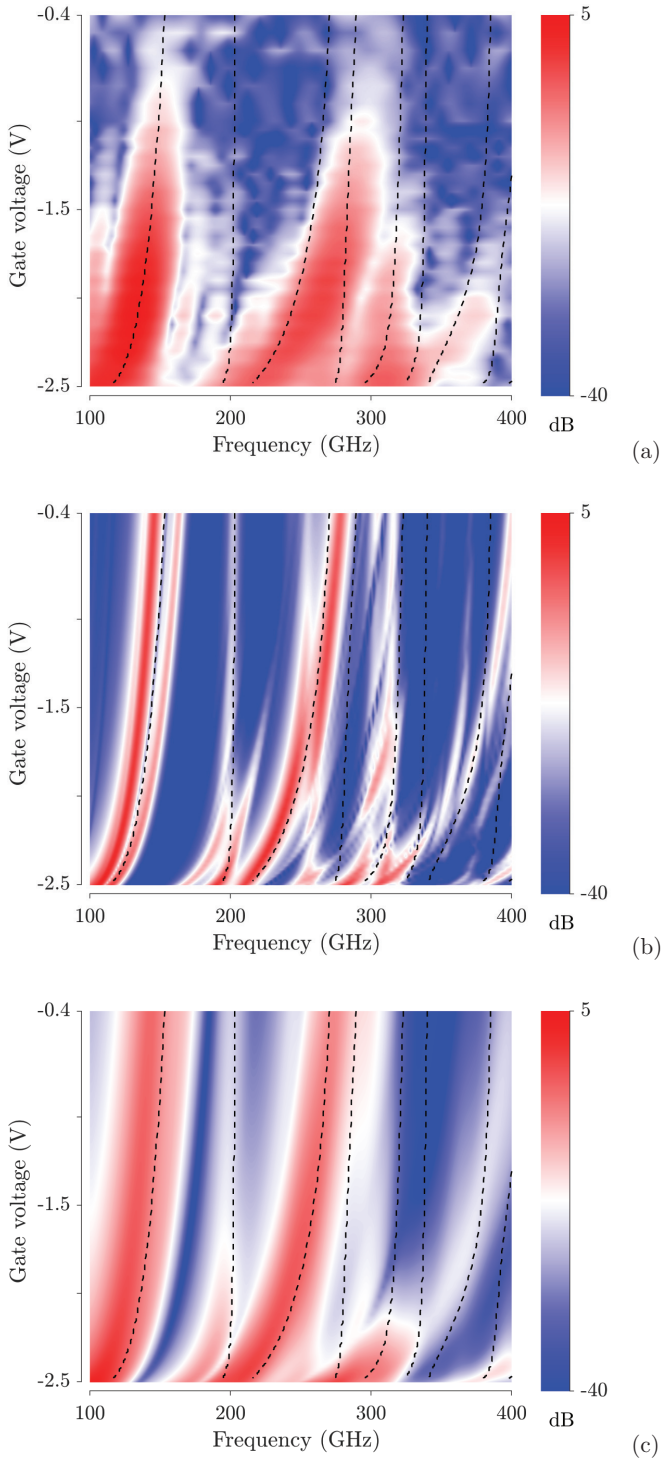


Figure 8.4: (a) Measured gate modulation signals (data taken from Wu *et al.* [1]), compared with *COMSOL Multiphysics*® models having with $\tau = 33$ ps (b) and with $\tau = 7$ ps (c). The lower value of τ provides better agreement with experiment. The dashed lines show positions of plasmon resonances calculated by a two-dimensional modal technique. Figure reproduced from Dawood *et al.* [2].

measured signals in the frequency range 100-400 GHz and for a range of gate voltages. The lines superimposed on the plot show the positions of the resonances calculated by a 2-D mode-matching technique as reported previously in Sydoruk *et al.* [5].

In the simulations, the even CPWG mode was excited in the left coplanar waveguide section at a single frequency and the transmitted signal was observed at the opposite end of the right CPWG section. The process was repeated for a range frequencies and electron densities. The simulations are performed in the frequency domain with the same excitation power at every frequency. The experimental excitation power, however, varied with frequency (as reported in Wu *et al.* [1]. To allow direct comparison between the simulations and the experiments, simulation results were scaled assuming an exponential decay of the excitation power with frequency. Then the derivative of the transmission with respect to the gate voltage was calculated using (8.1).

Figure 8.4(b) shows the simulated gate-modulation signals for $\tau = 33$ ps, the value obtained from DC conductivity measurements. The simulated resonances are clearly narrower than the experimentally observed ones, indicating higher losses in the experiment than predicted from the DC value of the scattering time. Such reduction of the quality factors of the experimental terahertz resonances were observed in a number of other experiments which used different 2-DES geometries, and excitation and detection techniques. For example, Popov *et al.* [6] found that the value of τ needed to fit the absorption measurements in a grid-gated field-effect transistor was lower than the value predicted from the DC conductivity by roughly an order of magnitude. El Fatimy *et al.* [7] reported that a plasmon resonance in a high-electron-mobility transistor measured experimentally had the quality factor 3 and was lower than the value of 13 expected from the measurements of DC mobility. A number of explanations for the apparent reduction of the value of τ were proposed, such as different relaxation mechanisms involved at DC and THz frequencies [8], ballistic transport and viscosity [7], leakage of gated plasmons into ungated regions and oblique modes [9]. No explanation appears so far to have gained wide acceptance. The 3-D model presented in this study, however, directly takes into account interaction of plasmons in the gated and ungated regions as well as the plasmon field distribution both along and across the device, and so it is unlikely that plasmon leakage and oblique modes are responsible for the difference between Figs. 8.4(a) and (b). Following other authors, therefore, τ is treated as a phenomenological parameter in this study, and the calculations were repeated for a number of lower values of τ. It was found that the best agreement between the experiments and the simulations was at $\tau = 7$ ps, as shown in Fig. 8.4(c).

Three strong features can be seen both in the theoretical and experimental plots. The first one starts at around 100 GHz for the lowest value of the gate voltage. The second starts at

200 GHz. The third lies around 300 GHz, and is strong only for low values of the gate voltage. The experimental features are shifted to the higher frequencies compared to the theoretical ones. A possible reason for the shift is the approximate nature of (8.1) that was used to estimate the gate voltage from the theoretical values of the concentration. In the experiments, the gate voltage was measured directly. The maximum amplitudes of the experimental and modelled signals decrease with increasing frequency and with decreasing gate voltage. There are, however, differences in the relationships between the amplitudes of the peaks between the experiment and the simulations. It may be due to the complex shape of the excitation spectrum, which was not fully reproduced in the simulations.

8.4 Beyond Experiment: Transmission, Reflection, Absorption and Field Profiles

The use of the gate-modulation technique in the experiments was dictated by the need to increase the signal-to-noise ratio and eliminate direct cross-talk between the components on either side of the 2-DES. In addition, the picosecond pulses used in the experiments delivered less power at higher frequencies, leading to weaker plasmon excitation.

Numerical simulations are free from these constraints, however, and allow analysis of the device across a wide parameter space. The colour plot in Fig. 8.5(a) shows the simulated transmission (S_{21}) coefficient for $\tau = 7$ ps (as before, the dashed lines are the resonances calculated by the 2-D model). More resonances can now be seen than in the gate-modulation plot of Fig. 8.4(c). This is because the resonances that depend weakly on the gated electron density are no longer suppressed, and the excitation amplitude is kept constant at all frequencies.

Figure 8.5(b) shows the transmission (S_{21}, black line) at a single value of the gate voltage, $V_g = -2$ V. It also shows the reflection (S_{11}) and the absorption coefficients (blue and red lines, respectively), the latter calculated as $1 - S_{21} - S_{11}$. The reflection and absorption of the signal dominate, and the transmitted signal does not exceed -25 dB. The transmission plot shows five resonances at 126, 192, 249, 300, and 358 GHz. To explain their nature, Fig. 8.6 shows the longitudinal (x-) component of the electric field, first, as contour plots in the plane of the 2-DES (left column) and, second, across the middle of the 2-DES (right column).

At the lowest-frequency resonance of 126 GHz, only the gated section of the 2-DES is excited strongly and evenly across the width of the 2-DES (y-direction). It has a single peak along the length (x-direction) of the gated section, which fits roughly a half of a plasmon wavelength. This is,

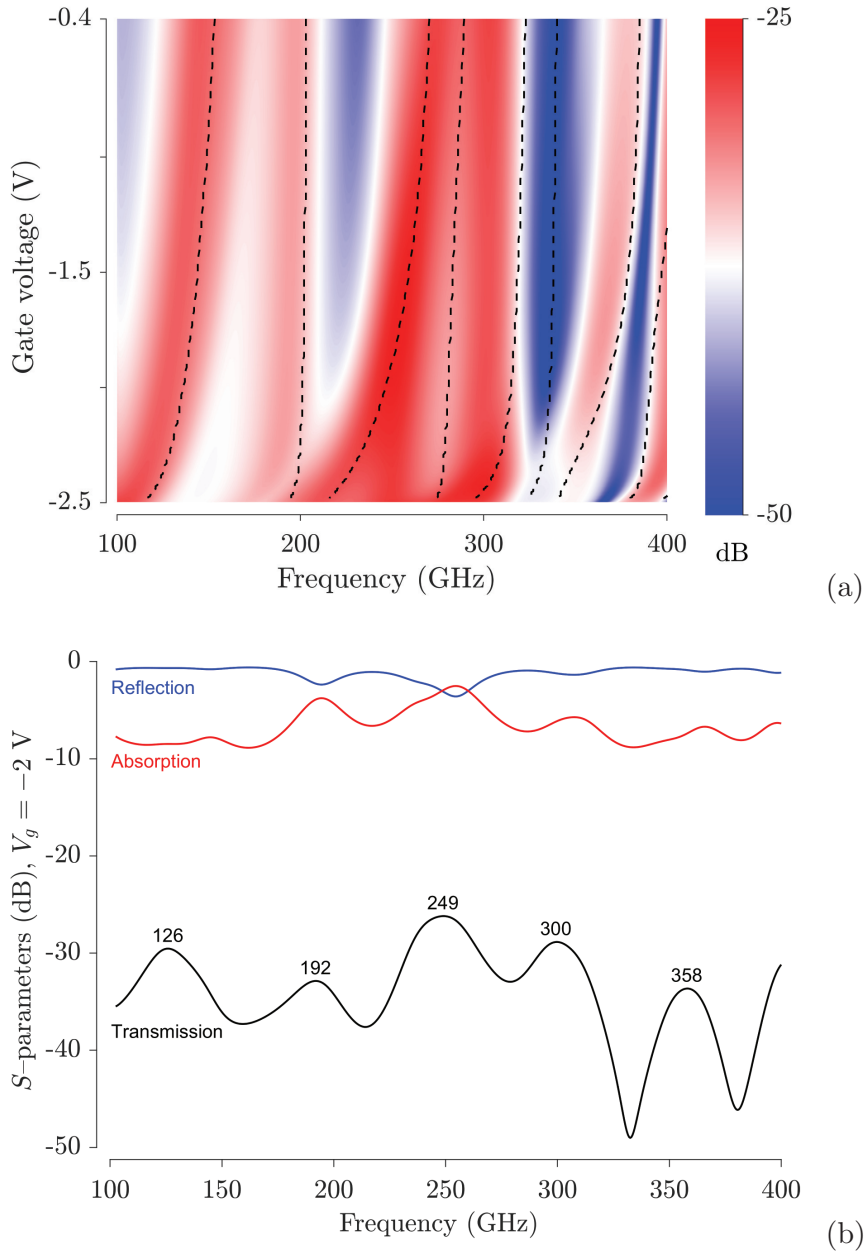


Figure 8.5: (a) Modelled true transmission ($20\log_{10}|S_{21}|$) for a range of gate voltages; and (b) transmission, reflection and absorption at a gate voltage of -2 V in the device. The absorption and reflection dominate, and the transmission does not exceed -25 dB. The spectral location of resonances are indicated with the transmission plot in (b). Figure reproduced from Dawood *et al.* [2].

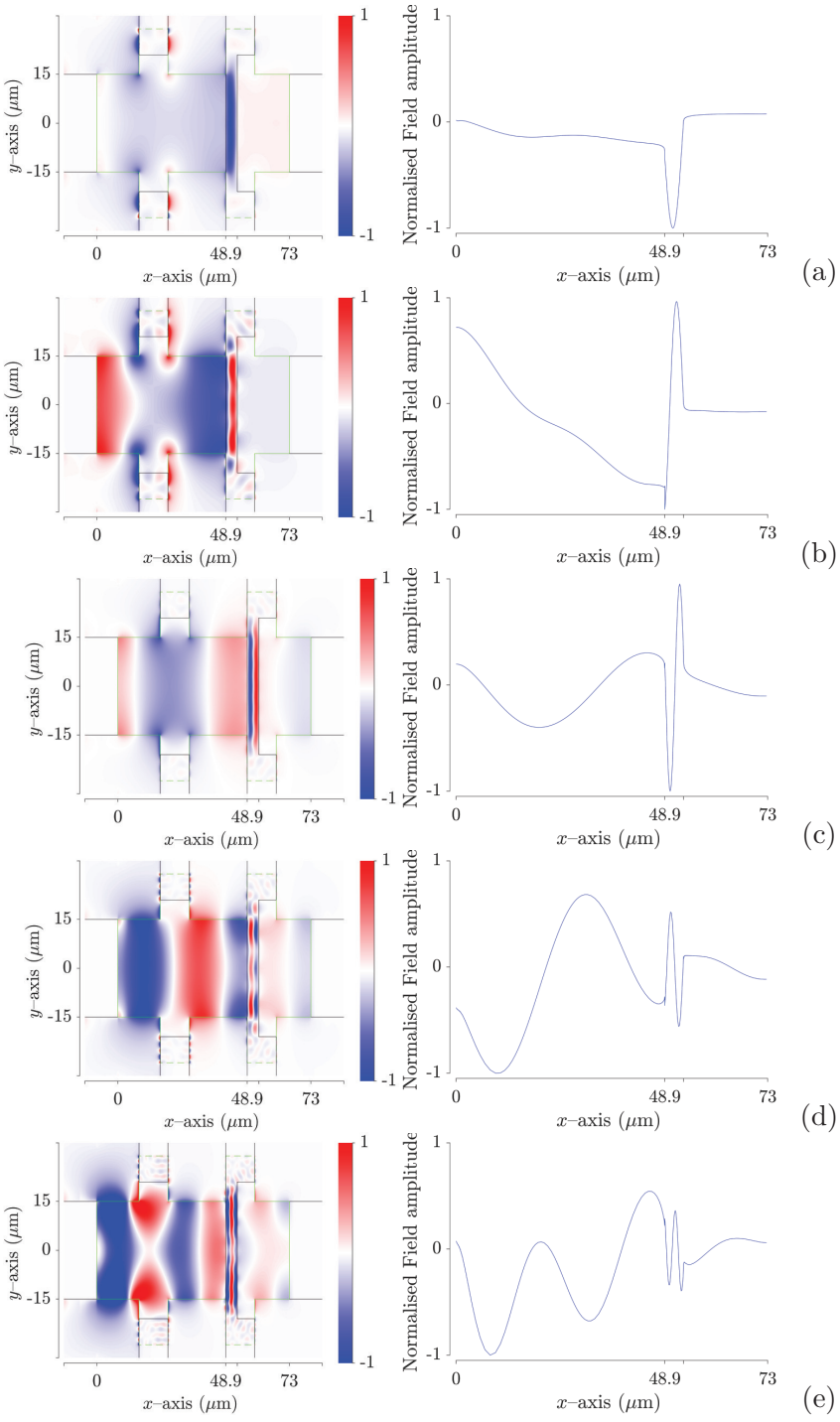


Figure 8.6: Distributions of the longitudinal component of the electric field on the 2-DES. The frequencies correspond to the transmission peaks in Fig. 8.5. The left panels present the top view, the right panels present the field calculated along a line across the middle of the 2-DES. The first three resonances appear to be predominantly longitudinal excitations; the last two-resonances show transverse excitations and excitations at the edges of the 2-DES. Figure reproduced from Dawood *et al.* [2].

therefore, the first longitudinal gated-section resonance, and its position agrees well with the 2-D calculation shown by dashed lines in Fig. 8.5(a).

With the second resonance at 192 GHz, the longer (left hand side) ungated section of the 2-DES is excited in addition to the gated section. In the ungated section, the field maximum and minimum are reached at the opposite ends, and the field has a distorted half-wavelength pattern. The excitation amplitudes are higher at the 2-DES edges, suggesting excitation of edge plasmons. The field in the gated portion of the 2-DES is non-uniform across the width of the 2-DES, showing both longitudinal and transverse plasmon excitation. The resonance position agrees well with the 2-D calculation [see dashed line in Fig. 8.5(a)] which suggests that this resonance corresponds to the first-order longitudinal resonance of the long section of the 2-DES.

The third resonance, at 249 GHz, shows strong excitation of both the gated and the long ungated sections, each fitting around one plasmon wavelength. Even though the edges of the ungated section are also excited, it appears to be a predominantly longitudinal resonance that is a result of an interaction between the gated and the long ungated sections. The nature of the resonance is confirmed, again, by the good agreement with the 2-D model seen from Fig. 8.5(a).

The fields of the final two resonances, at 300 and 358 GHz, are strongly non-uniform across the width of the different 2-DES sections. The gated 2-DES shows both longitudinal and transverse plasmon excitation, with multiple field minima and maxima along x- and y-directions. The long and short ungated 2-DESs are excited strongly at the edges. As can be expected, the 2-D calculations fail to predict the position of these two resonances.

8.5 Comparison with Experiments: Magnetoplasmons

Using the same device and technique, Wu *et al.* detected magnetoplasmon resonances in a magnetic field applied perpendicular to the plane of the 2-DES [4]. The colour plot in Fig. 8.7(a) shows the measured gate-modulation signals. The gate voltage was -2 V, and the magnetic field varied between 0 and 0.4 T. The dashed black lines show the position of 2-D resonances found by the mode-matching technique. The red line is the cyclotron resonance.

In the presence of a DC magnetic field B_0, pointing in the positive z-direction, the 2-D Drude conductivity in the 2-DES becomes anisotropic. The current density, $\mathbf{J}$, can then be expressed as [2],

$$\begin{bmatrix} J_x \\ J_y \end{bmatrix} = \begin{bmatrix} en_{2D}v_x \\ en_{2D}v_y \end{bmatrix} = \begin{bmatrix} \sigma_{xx} & \sigma_{xy} \\ \sigma_{yx} & \sigma_{yy} \end{bmatrix} \begin{bmatrix} E_x \\ E_y \end{bmatrix} \tag{8.3}$$

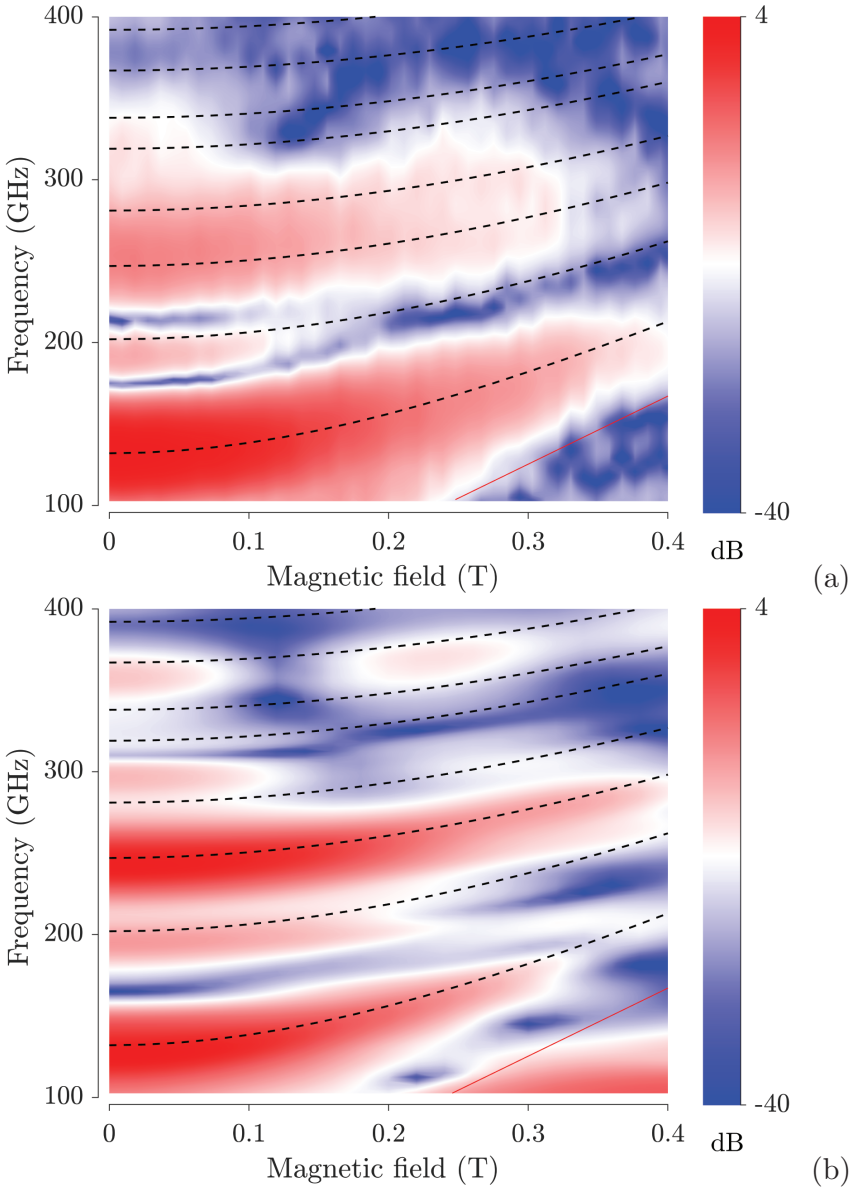


Figure 8.7: (a) Measured (data taken from Wu *et al.*[4]); and (b) simulated gate-modulation signals for magneto-plasmons. The dashed lines are the predicted resonances from the 2-D modal technique. The red line indicates the cyclotron frequency. Theory and experiment agree for features between 100 and 300 GHz. Figure reproduced from Dawood *et al.* [2].

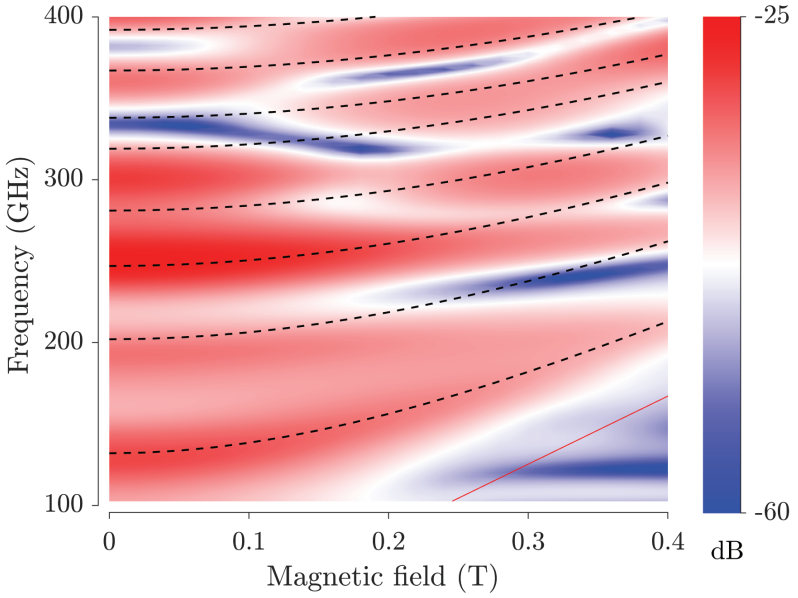


Figure 8.8: Simulated true transmission ($20\log_{10}|S_{21}|$) from *COMSOL Multiphysics*® frequency domain solver for the same structure. The dashed lines show positions of the resonances predicted by the 2-D modal technique. Figure reproduced from Dawood *et al.* [2].

where,

$$\sigma_{xx} = \frac{e^2 n_{2D}\left(j\omega m + \frac{m}{\tau}\right)}{\left(j\omega m + \frac{m}{\tau}\right)^2 + e^2 B_0^2} \tag{8.4}$$

$$\sigma_{xy} = \frac{e^3 n_{2D} B_0}{\left(j\omega m + \frac{m}{\tau}\right)^2 + e^2 B_0^2} \tag{8.5}$$

$$\sigma_{yx} = \frac{-e^3 n_{2D} B_0}{\left(j\omega m + \frac{m}{\tau}\right)^2 + e^2 B_0^2} \tag{8.6}$$

$$\sigma_{yy} = \frac{e^2 n_{2D}\left(j\omega m + \frac{m}{\tau}\right)}{\left(j\omega m + \frac{m}{\tau}\right)^2 + e^2 B_0^2} \tag{8.7}$$

Figure 8.7(b) shows the gate-modulation signals simulated using (8.3)–(8.7). The agreement with the experiment is good for the features lying between 100 and 300 GHz. As before, the difference in the relative strength of the measured and simulated resonances can be attributed to the spectrum of the excitation pulses. Some of the resonances modelled above 300 GHz do not show in the measurements, possibly because the excitation signals were weak. On the other hand, the experimental resonance lying below 100 GHz for weak magnetic fields does not show in the modelled results. To the right of the cyclotron line, the simulations predict a strong signal but only a faint feature can be seen in the measurements.

While Figs. 8.7(a) and (b) showed the gate-modulation signals, Fig. 8.8 shows the simulated true transmission coefficient. The maximum transmission does not exceed −25 dB for all values of the magnetic field. The behaviour of the lowest resonance with the magnetic field agrees well with the prediction of the 2-D model. The next two resonances agree well with the 2-D model at low magnetic field. They do not follow, however, the parabolic behaviour of the 2-D curves, and it leads to a discrepancy between the 3-D simulation and the 2-D model at higher fields. As can be expected from the results for zero magnetic field discussed above, the full-wave 3-D simulations and the 2-D model disagree in their predictions of the resonance positions. This disagreement is attributed to the excitation of edge plasmons and of transverse plasmons (with non-trivial component of the wavenumber in the y-direction), both of which are not taken into account by the 2-D model.

8.6 Improving Device Performance

The simulated transmission for the experimental device did not exceed –25 dB, as shown in Figs. 8.5 and 8.8. Such a low value is due to two factors: high plasmon absorption in the 2-DES, and high signal reflection between the 2-DES and the coplanar waveguides [Fig. 8.5(b)]. The plasmon loss could be reduced by shortening the length of the 2-DES. The high insertion loss can be attributed to the dissimilar field distributions in the 2-DES and the coplanar waveguides. The even mode supported by the coplanar waveguide is a quasi-TEM mode whose field is concentrated in the gaps between the centre and the ground conductors. On the other hand, plasmons are TM modes whose field is concentrated around the 2-DES. Rearranging the waveguide electrodes to create a high electric field along the 2-DES is, therefore, likely to improve the coupling. It can be done by connecting the gate and the ground electrodes via a capacitor (which will decouple the gate and the ground at DC allowing voltages to be applied to the gate).

A possible device is shown schematically in Fig. 8.9. The length of the gated section here is 4 μm, and the ungated sections have been both reduced to 2 μm. The device width remains 30 μm. Figure 8.10(a) shows the simulated transmission for a range of voltages, and Fig. 8.10(b) shows the transmission, reflection and absorption for the gate voltage of −2 V. Improvements can be seen upon comparing Fig. 8.10 for the new device to Fig. 8.5 for the original experimental device. The maximum transmission has increased by over 20 dB for the peak at 165 GHz. The insertion loss has also decreased by a similar amount. The observed three resonances correspond to the excitation of the longitudinal gated plasmons, as can be seen from the field distributions shown in Fig. 8.11 for $V_g = -2$ V at 164, 272 and 393 GHz. The peak frequencies are close to the three lowest resonant frequencies of longitudinal gated plasmons (144, 279, and 407 GHz) assuming an integer number of

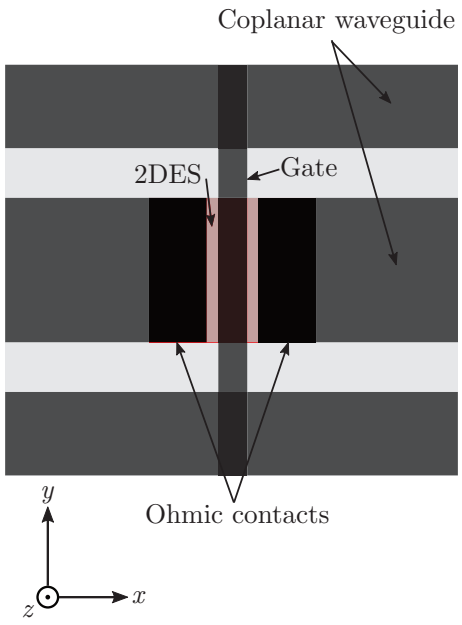


Figure 8.9: Top view of the device with improved characteristics. A shorter overall length reduces absorption in the 2-DES channel (shaded red), whereas, connecting the gate and the ground planes of the coplanar waveguides provides better coupling between the 2-DES and the waveguides. Figure reproduced from Dawood *et al.* [2].

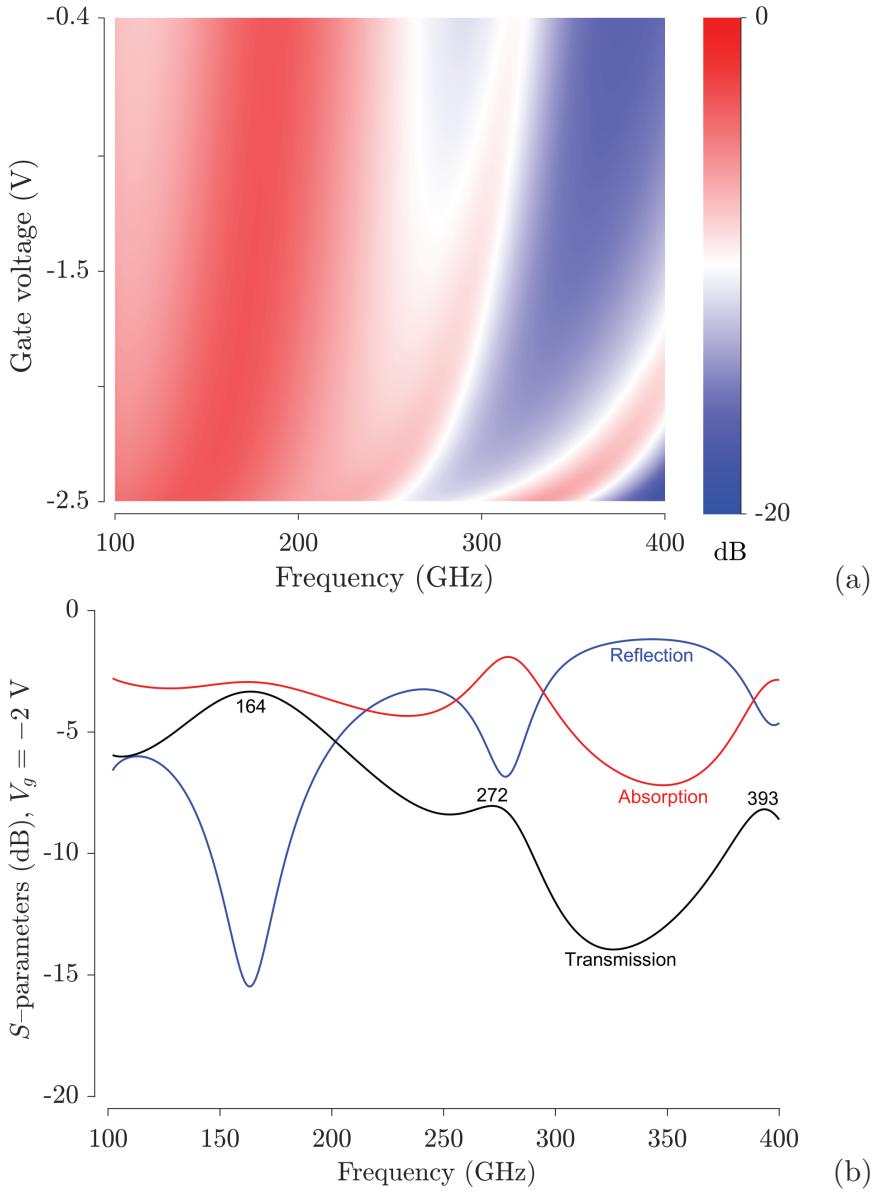


Figure 8.10: Simulated transmission (a) as a function of gate voltage; and (b) the transmission, reflection, and absorption characteristics at a gate voltage of −2 V for the device of Fig. 8.9. At 164 GHz, the transmission is around −3 dB, and the insertion loss is below −15 dB. Figure reproduced from Dawood *et al.* [2].

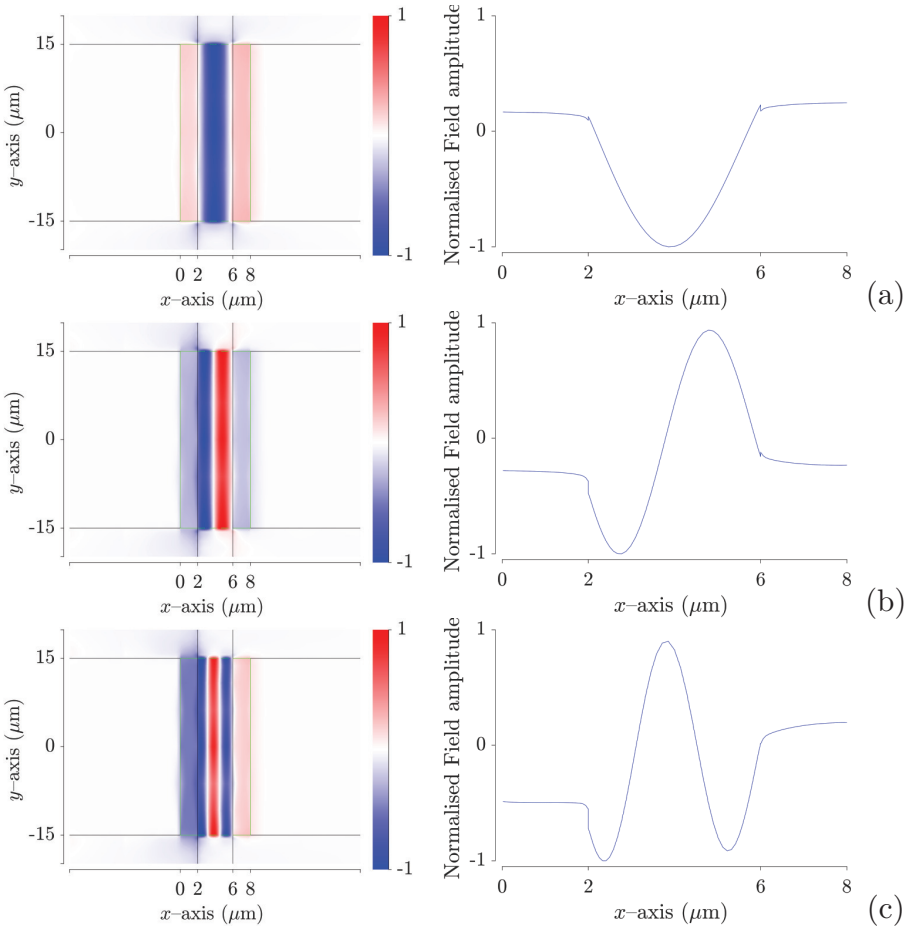


Figure 8.11: Longitudinal component of the electric field on the 2-DES at the three transmission peaks shown in Fig. 8.10 at 164, 272 and 393 GHz. The left panels present the top view, the right panels present the field calculated along a line across the middle of the 2-DES. At all frequencies, only longitudinal plasmons are excited. Figure reproduced from Dawood *et al.* [2].

plasmon wavelengths in the gated section.

8.7 Modelling Losses in the Device Structure

As discussed in Section 8.3, several different mechanisms for a decrease in effective value of τ have been discussed in different publications. It was interesting to explore the different loss mechanisms using the full-wave solver. Within the limited scope of this work, only the following loss mechanisms were studied independently: (i) losses from edges of the 2-D channel; (ii) losses due to the substrate; and (iii) losses due to ohmic contacts.

8.7.1 Modelling 2-DES Edge Losses

One possible sources of losses, suggested by Dr. Sydoruk, was that the losses in the 2-DES channel might be non-uniform in the transverse direction. Plasmons travelling at the edges of the 2-DES might be experiencing more losses compared to those in the centre of the channel. The lossy profile chosen for the simulation is shown in Fig. 8.12, where the value of τ is varied along the y-direction. The value of τ was varied between 50 ps, occurring at the centre of the 2-DES, and 5 ps, occurring at the edges of the 2-DES. The gate modulation signal with this lossy profile is shown in Fig. 8.13 which shows broadening of resonance compared with the case when there were no edge losses.

8.7.2 Modelling Substrate Losses

The second loss mechanism studied, was to introduce substrate losses. For this, the effective permittivity of GaAs substrate was set as $\tilde{\varepsilon}_{reff} = \varepsilon_r' - j\varepsilon_r'' = 12.8 - j0.5$ inside *COMSOL Multiphysics*®, where $\tau = 33$ ps. The plot of computed gate modulation signal is shown in Fig. 8.14.

8.7.3 Modelling Losses in Ohmic Contacts

At THz frequencies, the ohmic contacts might not act as perfect conductors and can contribute to losses. The losses in ohmic contacts were modelled by using the classical skin effect model (A.20) inside *COMSOL Multiphysics*®, where ε_r was set as 1 and the bulk DC conductivity of ohmic contacts were fixed at $\sigma = 5000$ S/m, where $\tau = 33$ ps. The plot of gate modulation with these parameters is shown in Fig. 8.15.

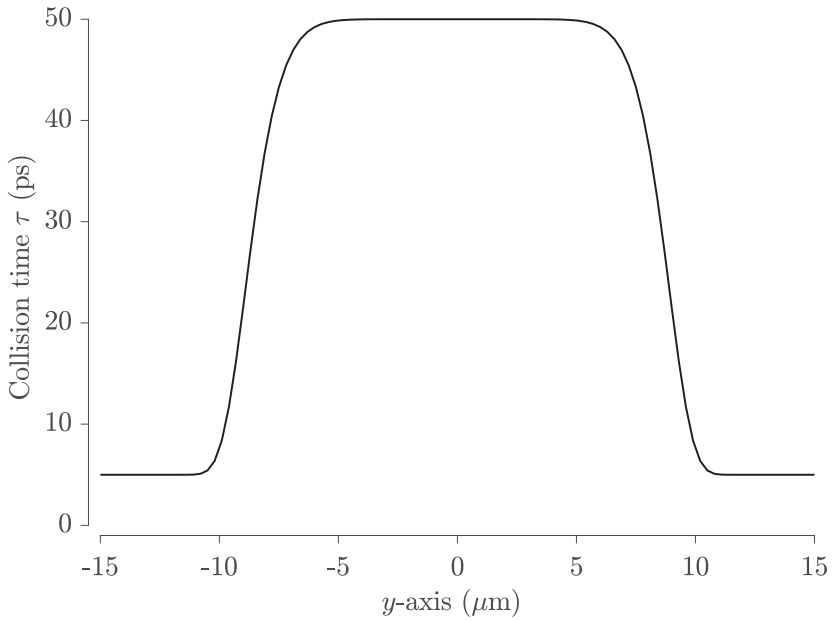


Figure 8.12: Lossy τ profile in the transverse direction along the 2-DES channel. The 2-DES lies at $-15 < y < 15$ μm. The profile introduces edge losses in the 2-DES channel.

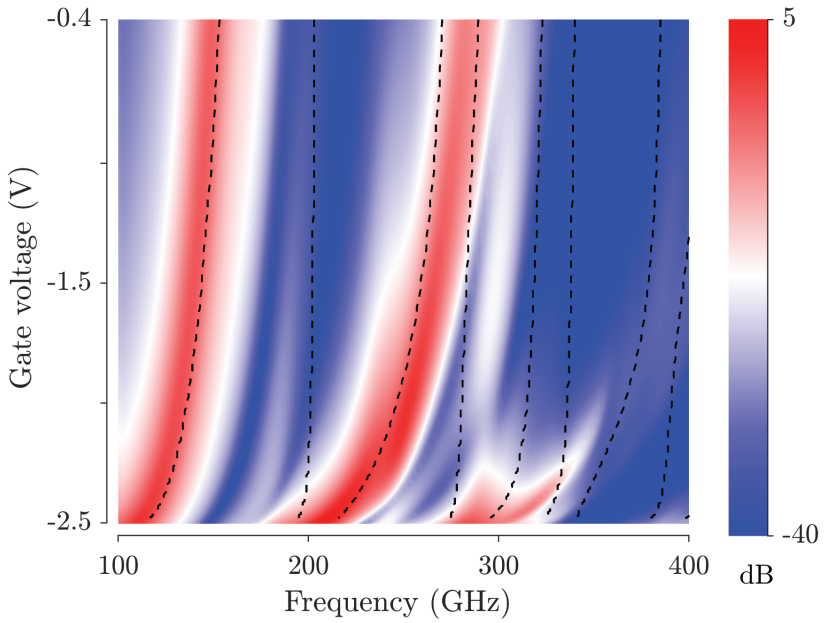


Figure 8.13: Plot of gate modulation signal with the lossy profile shown in Fig. 8.12. The dashed lines show predicted resonances from the 2-D modal technique. Adding edge losses broadens the resonances obtained from simulation.

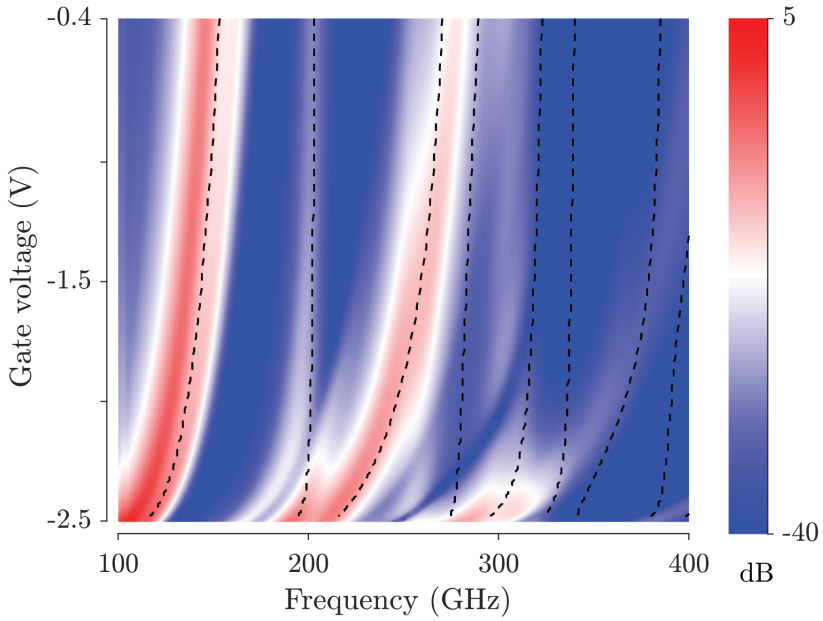


Figure 8.14: Plot of gate modulation signal with substrate losses and $\tau = 33$ ps. The dashed lines show predicted resonances from the 2-D modal technique. With substrate losses, the resonances obtained from simulation are broadened.

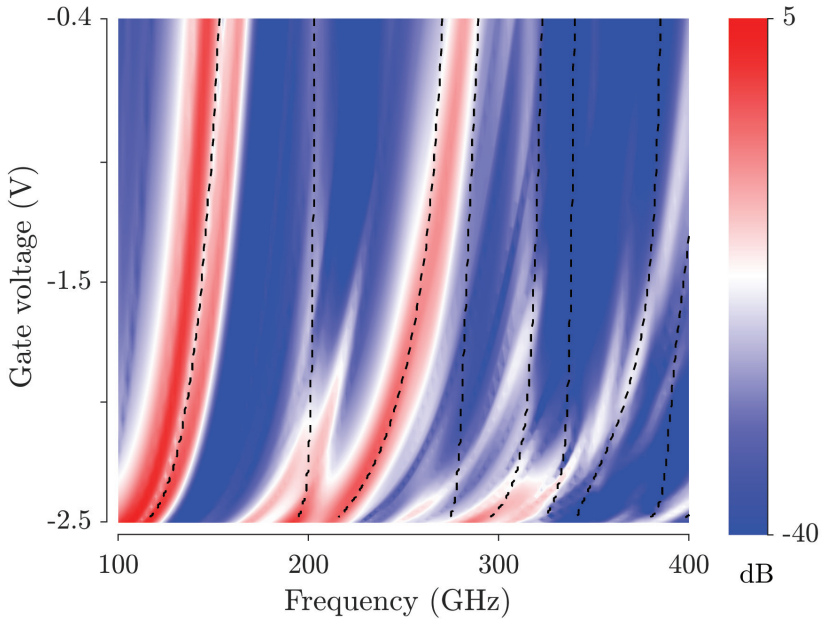


Figure 8.15: Plot of gate modulation signal taking into account ohmic losses in contacts with $\tau = 33$ ps. The dashed lines show predicted resonances from the 2-D modal technique. Some of the resonances are broadened while some sharp resonances can also be observed.

8.8 Conclusions

A full-wave three-dimensional model of the experimental devices showed agreement with the experimental results obtained by gate-modulation, both for plasmons and magnetoplasmons. This model was used to analyse device characteristics that could not be directly measured in experiments, such as the true transmission, reflection, and absorption, as well as to study the field distributions at the transmission maxima. The predictions of the fully three-dimensional model were also compared with a two-dimensional model based on modal expansions. While the frequencies of some plasmon resonances could be explained equally well by both approaches, the full-wave simulations showed additional resonances that can be attributed to plasmon excitation across and at the edges of the device. The calculations in this study predicted the transmission in the experimental devices to be below -25 dB, in part due to the high plasmon reflection, and in part due to high insertion loss. By reducing the length of the ungated sections and modifying the coupling geometry between the 2-DES and the coplanar waveguides, a device was proposed in which the maximum transmission increased by 20 dB. In addition, different mechanisms for losses were also studied using extended simulations. The different losses considered were, edge losses at the 2-DES channel, losses from the substrate and losses in the ohmic contacts.

8.9 Acknowledgements

The work presented in this chapter was done under the supervision of Dr. Oleksiy Sydoruk and was published as Dawood *et al.* [2]. Additionally, Dr. Sydoruk went through each and every word of the original draft, provide helpful feedback and suggested improvements which were invaluable to this thesis. This chapter heavily draws on the original experimental work by Wu *et al.* [1].

References

[1] J. Wu, A. S. Mayorov, C. D. Wood, D. Mistry, L. Li, W. Muchenje, M. C. Rosamond, L. Chen, E. H. Linfield, A. G. Davies, and J. E. Cunningham, "Excitation, detection, and electrostatic manipulation of terahertz-frequency range plasmons in a two-dimensional electron system," *Sci. Rep.*, vol. 5, 2015.

[2] A. Dawood, J. Wu, C. Wood, L. Li, E. Linfield, A. Davies, J. Cunningham, and O. Sydoruk, "Full-wave modelling of terahertz frequency plasmons in two-dimensional electron systems," *J. Phys. D: Appl. Phys.*, vol. 52, no. 21, pp. 1–10, 2019.

[3] T. Otsuji, Y. M. Meziani, T. Nishimura, T. Suemitsu, W. Knap, E. Sano, T. Asano, and V. V. Popov, "Emission of terahertz radiation from dual grating gate plasmon-resonant emitters fabricated with InGaP/InGaAs/GaAs material systems," *J. Phys. Condens. Matter*, vol. 20, pp. 384206–384211, 2008.

[4] J. Wu, O. Sydoruk, A. S. Mayorov, C. D. Wood, D. Mistry, L. Li, E. H. Linfield, A. G. Davies, and J. E. Cunningham, "Time-domain measurement of terahertz frequency magnetoplasmon resonances in a two-dimensional electron system by the direct injection of picosecond pulsed currents," *Appl. Phys. Lett.*, vol. 108, no. 9, 2016.

[5] O. Sydoruk, J. Wu, A. Mayorov, C. Wood, D. Mistry, and J. Cunningham, "Terahertz plasmons in coupled two-dimensional semiconductor resonators," *Phys. Rev. B*, vol. 92, 2015.

[6] V. V. Popov, O. V. Polischuk, T. V. Teperik, X. G. Peralta, S. J. Allen, N. J. M. Horing, and M. C. Wanke, "Absorption of terahertz radiation by plasmon modes in a grid-gated double-quantum-well field-effect transistor," *J. Appl. Phys.*, vol. 94, no. 5, pp. 3556–3562, 2003.

[7] A. El Fatimy, F. Teppe, N. Dyakonova, W. Knap, D. Seliuta, G. Valušis, A. Shchepetov, Y. Roelens, S. Bollaert, A. Cappy, *et al.*, "Resonant and voltage-tunable terahertz detection in InGaAs/InP nanometer transistors," *Appl. Phys. Lett.*, vol. 89, no. 13, p. 131926, 2006.

[8] R. E. Tyson, R. J. Stuart, H. P. Hughes, J. E. F. Frost, D. A. Ritchie, G. A. C. Jones, and C. Shearwood, "Non-linear doppler shift of the plasmon resonance in a grating-coupled drifting 2DEG," *Int. J. Infrared Milli*, vol. 14, pp. 1237–1249, 1993.

[9] A. Shchepetov, C. Gardès, Y. Roelens, A. Cappy, S. Bollaert, S. Boubanga-Tombet, F. Teppe, D. Coquillat, S. Nadar, N. Dyakonova, *et al.*, "Oblique modes effect on terahertz plasma wave

resonant detection in InGaAs/InAl as multichannel transistors," *Appl. Phys. Lett.*, vol. 92, no. 24, p. 242105, 2008.

Chapter 9

Conclusions

The first chapter was a review of current trends in terahertz (THz) technology and state-of-the-art research in plasmonics, with an emphasis on modelling aspects. A finite-difference time domain (FDTD) code was developed in-house to model problems related to plasmonics. The FDTD code was used to model 2-D plasmons in a two-dimensional electron system (2-DES); local plsamonic oscillations on a gold nanosphere when subjected to an incident electromagnetic (EM) wave; and a lossy spherical cavity resonator. The FDTD code was further improved to incorporate coordinate-independent, non-uniform meshing scheme.

A comprehensive review of travelling waves, pseudo waves and power waves in microwave theory was presented in Chapter 2. Generalised scattering parameters based on the voltage/pseudo-wave and power-wave definitions were discussed and generalised n-port interconversion between S- and S_p-parameters was derived. One- and two-port network models were presented for lossy two- and three-media reflection/transmission problems. It was demonstrated that conventional S-parameters cannot be used directly to compute power if reference port impedance is complex. Additionally, generalised direct conversion formulas for interconversion between two-port network parameters were derived that are valid for arbitrary reference port impedances.

A two-media lossy Fabry-Pérot resonator was analysed in Chapter 3. The complex eigenfrequency of a Fabry-Pérot resonator was computed using analytical and numerical methods as the walls of the resonator were transformed from perfect electric conductor (PEC) to free space. It was found that numerical solvers fail to correctly predict the complex eigenfrequency as the resonator becomes too lossy.

Chapter 4 reviewed the concept of excitation of Fabry-Pérot eigenmodes in dielectric-filled metal-pipe rectangular waveguide (MPRWG). It was argued that due to the 3-D printing process, voids and inhomogeneities in 3-D printed dielectric samples excited ‘open-box’ mode resonances.

Rigorous analytical, as well as, numerical methods were used to analyse these eigenmodes, and the predicted eigenfrequencies showed good agreement with the observed spectral location of eigenmode frequencies from measurements. A numerical technique for accurate prediction and excitation of open-box resonances in a dielectric-filled waveguide was proposed. According to this technique, the permittivity of the dielectric sample was defined as an in-homogeneous and anisotropic tensor. The predicted spectral location of open-box mode resonances were within 0.01 GHz of those computed from the analytical method, making this new technique a useful tool in accurate numerical analysis of open-box mode resonances.

Based on the theory developed in Chapter 4 for analysis of 'open-box' modes in dielectric-filled MPRWG, Chapter 5 explored excitation of natural Fabry-Pérot modes in dielectric-filled parallel-plate and circular waveguides using numerical and analytical techniques. The predicted open-box resonances from numerical simulations were within 0.02 GHz of those computed from the analytical method.

In Chapter 6, a novel S-parameter renormalisation technique for resolving ambiguities in reflectance and transmittance of a two-port network, with noisy measurements, was reviewed. In addition, a method for estimation of vector network analyser (VNA) output signal-to-noise (S/N) ratio was also reviewed. Also, noise analysis of measured output thru response of a VNA set-up was undertaken for the first time and it was revealed that the estimated S/N ratio came out to be 88.5 dB, which coincided with the measured value.

Chapter 7 introduced a technique for spectroscopic characterisation of a dielectric sample by exciting surface plasmons on a plasmonic material like high resistivity Si, which was placed underneath a Si prism. When the prism was subject to an incident EM wave, surface plasmons were excited on the Si slab, where the frequency of excitation could be determined from the intersection of plasmon and Si prism dispersion curves. The proposed experimental set-up was modelled using three different strategies, including dispersion modelling, as a planar n-layer media, and full-wave numerical modelling using the FDTD technique and *COMSOL Multiphysics*® frequency domain solver. The numerical modelling strategies predicted spectral location of plasmon resonances within 0.5 GHz of each other in the worst case scenario.

In Chapter 8, full-wave *COMSOL Multiphysics*® frequency domain simulations were used to study 2-D plasmon propagation in an experimental device operating close to the THz band. The full-wave simulations predicted a high energy loss as plasmons propagated along the 2-D channel. It was found that by reducing channel length, transmission could be improved by as much as 20 dB. The simulations were repeated with an applied magnetic field normal to the channel with the

simulated gate modulation voltage showing good agreement with the experimental results.

Journal Publications

1. **A. Dawood**, J. Wu, C. Wood, L. H. Li, E. H. Linfield, A. G. Davies, J. Cunningham, O. Sydoruk, "Full-wave modelling of terahertz frequency plasmons in two-dimensional electron systems," *J. Phys. D: Appl. Phys.*, pp. 1–10, Mar. 2019.

2. J. Sun, **A. Dawood**, W. J. Otter, N. M. Ridler, and S. Lucyszyn, "Microwave characterization of low-loss FDM 3-D printed ABS with dielectric-filled metal-pipe rectangular waveguide spectroscopy," *IEEE Access*, vol. 7, pp. 95455–95486, July 2019.

Conferences

A. Dawood, O. Sydoruk, "Excitation of terahertz plasmons in two-dimensional electron channels by coupling to coplanar waveguides," 7^{th} *International Conference on Optical Terahertz Science and Technology (OTST)*, University College London, Apr. 2017.

Appendix A

Fundamental Forces and Maxwell's Equations

A.1 Fundamental Forces

According to classical physics there are four fundamental forces in nature. These are in decreasing strength as follows:

(i) strong nuclear,

(ii) electromagnetic,

(iii) weak nuclear and

(iv) gravity.

Strong and weak nuclear forces are present inside the nucleus of an atom, gravity as experienced by us in our daily lives is well-known, while electromagnetic forces are due to interaction of charges.

A.2 Maxwell's Equations

Electromagnetic theory is the study of electromagnetic phenomena due to electromagnetic forces. The fundamental laws in electromagnetic theory were developed and well established more than a hundred years ago in the late 19^{th} century and became known as *Maxwell's equations*. Maxwell's equations represent the fundamental unification of electric and magnetic force [1]. The fundamental integral form of Maxwell's equations are,

$$\oint_L \bar{\mathcal{E}} \cdot d\boldsymbol{l} = -\int_S \frac{\partial \bar{\mathcal{B}}}{\partial t} \cdot d\boldsymbol{S} \tag{A.1}$$

$$\oint_L \bar{\mathcal{H}} \cdot d\boldsymbol{l} = \int_S \frac{\partial \bar{\mathcal{D}}}{\partial t} \cdot d\boldsymbol{S} + \int_S \bar{\mathcal{J}} \cdot d\boldsymbol{S} \tag{A.2}$$

$$\oint_S \bar{\mathcal{D}} \cdot d\boldsymbol{S} = \int_v \rho_v dv = q_{enc} \tag{A.3}$$

$$\oint_S \bar{\mathcal{B}} \cdot d\boldsymbol{S} = 0 \tag{A.4}$$

Equations (A.1)–(A.4) are known as Faraday's Law, Ampere's Law, Gauss's Law and Gauss's Law for magnetism, respectively. The differential form of Maxwell's equations in time-domain are ,

$$\nabla \times \bar{\mathcal{E}} = -\frac{\partial \bar{\mathcal{B}}}{\partial t} \tag{A.5}$$

$$\nabla \times \bar{\mathcal{H}} = \frac{\partial \bar{\mathcal{D}}}{\partial t} + \bar{\mathcal{J}} \tag{A.6}$$

$$\nabla \cdot \bar{\mathcal{D}} = -\rho_V \tag{A.7}$$

$$\nabla \cdot \bar{\mathcal{B}} = 0 \tag{A.8}$$

where, $\bar{\mathcal{E}}$ is the electric field in V/m, $\bar{\mathcal{H}}$ is the magnetic field in A/m, $\bar{\mathcal{D}}$ is the electric flux density in C/m^2, $\bar{\mathcal{B}}$ is the magnetic flux density in tesla, $\bar{\mathcal{J}}$ is the electric current density in A/m^2 and ρ_V is the volume charge density in C/m^3. Here, the time-varying field quantities are denoted by slanted letters. The constitutive relations are,

$$\bar{\mathcal{D}} = \varepsilon \bar{\mathcal{E}} \tag{A.9}$$

$$\bar{\mathcal{B}} = \mu \bar{\mathcal{H}} \tag{A.10}$$

$$\bar{\mathcal{J}} = \sigma \bar{\mathcal{E}} \tag{A.11}$$

where, $\varepsilon = \varepsilon_r \varepsilon_0$ and $\mu = \mu_r \mu_0$ are the permittivity and permeability; σ is the conductivity in S/m; ε_r and μ_r are the relative permittivity and relative permeability, respectively; and, ε_0 and μ_0 are the permittivity and permeability of free space, respectively. At an interface between two different media, the normal components of $\bar{\mathcal{D}}$ and $\bar{\mathcal{B}}$ must be continuous, while the tangential components of $\bar{\mathcal{E}}$ and $\bar{\mathcal{H}}$ must be continuous. These are known as the boundary conditions. Along with the constitutive relations and boundary conditions, Maxwell's equations completely describe electromagnetic phenomenon.

A.3 Complex Phasor Form of Maxwell's Equations and Classical Skin Effect Model

Phasors are the steady-state frequency-domain transformation of sinusoidal time-domain functions. Assuming time dependence of the form $e^{j\omega t}$ and making the substitution $d/dt = j\omega$, Maxwell's

equations in the complex phasor form can be written as,

$$\nabla \times \mathbf{E} = -j\omega\mu\mathbf{H} \tag{A.12}$$

$$\nabla \times \mathbf{H} = j\omega\varepsilon\mathbf{E} + \mathbf{J} = (\sigma + j\omega\varepsilon)\mathbf{E} \tag{A.13}$$

Here, the phasor fields are represented by straight bold-face letters. Also, the material parameters μ, ε and σ may be frequency-dependent, complex or tensor quantities and can be expressed as,

$$\tilde{\mu}(\omega) = \mu' - j\mu'' = \tilde{\mu}_r(\omega)\mu_0 \tag{A.14}$$

$$\tilde{\varepsilon}(\omega) = \varepsilon' - j\varepsilon'' = \tilde{\varepsilon}_r(\omega)\varepsilon_0 \tag{A.15}$$

$$\tilde{\sigma}(\omega) = \sigma' - j\sigma'' \tag{A.16}$$

The imaginary terms μ'' and ε'' denote quadrature response losses due to magnetic and electric polarisations, respectively, while conduction losses are due to σ. Most lossy materials are non-magnetic and the losses are generally due to both, electric polarisation and conduction. In dielectrics, polarisation losses are dominant, while in metals, the losses are mainly due to conduction. Where the material parameters are anisotropic, these can be expressed as a 3×3 tensor given by,

$$\varepsilon = \begin{bmatrix} \varepsilon_{xx} & \varepsilon_{xy} & \varepsilon_{xz} \\ \varepsilon_{yx} & \varepsilon_{yy} & \varepsilon_{yz} \\ \varepsilon_{zx} & \varepsilon_{zy} & \varepsilon_{zz} \end{bmatrix} \tag{A.17}$$

An effective complex permittivity function can be defined, which includes the effect of both, polarisation and conduction losses. In material characterisation, for example, only the effective permittivity is observed, containing the effects of polarisation and conduction losses. From (A.13),

$$\begin{aligned} \nabla \times \mathbf{H} &= j\omega\tilde{\varepsilon}\mathbf{E} + \mathbf{J} \\ &= j\omega\tilde{\varepsilon}\mathbf{E} + \sigma\mathbf{E} \\ &= j\omega\left(\tilde{\varepsilon} + \frac{\sigma}{j\omega}\right)\mathbf{E} \\ &= j\omega\tilde{\varepsilon}_{eff}\left(\omega\right)\mathbf{E} \\ &= j\omega\tilde{\varepsilon}_{reff}\left(\omega\right)\varepsilon_0\mathbf{E} \end{aligned} \tag{A.18}$$

where, the effective relative permittivity can be expressed as,

$$\tilde{\varepsilon}_{reff}\left(\omega\right) = \tilde{\varepsilon}_r\left(\omega\right) + \frac{\sigma}{j\omega\varepsilon_0} = \varepsilon'_{reff} - j\varepsilon''_{reff} \tag{A.19}$$

For dielectrics (or insulators), $\sigma \ll 0$ and the term $\sigma/j\omega\varepsilon_0$ can be neglected. Losses in dielectrics are mainly due to polarisation and represented by the term $\varepsilon'' = 0$. For metals, $\sigma \gg 0$ and

polarisation losses can be neglected compared to conduction losses, and the frequency-dependent effective complex relative permittivity, can expressed as,

$$\tilde{\varepsilon}_{reff}(\omega) = \varepsilon_r + \frac{\sigma}{j\omega\varepsilon_0} \tag{A.20}$$

Equation (A.19) is known as the classical skin effect model.

Appendix B

Effective Complex Dielectric Function and Refractive Index

The effective complex dielectric function is fundamentally related to Maxwell's equations. In practical situations, often the sources of losses cannot be separated. In such a cases it is convenient to define an effective complex dielectric function which characterises the effective response of a material.

The imaginary part of complex dielectric function only exists when there is a loss, but both, real and imaginary parts contribute to loss in this case. So, it is difficult to find any physical meaning from the real and imaginary parts of the effective complex dielectric function.

The complex refractive index is physically more meaningful as it quantifies both phase velocity and loss. The real part of the complex refractive index is related to the phase velocity of an electromagnetic (EM) wave in a medium, while the imaginary part denotes losses in the medium. The complex refractive index is expressed as,

$$\tilde{n} = n + j\kappa = \pm\sqrt{\tilde{\mu}_{reff}\tilde{\varepsilon}_{reff}} \tag{B.1}$$

where, n is the refractive index and κ is the extinction coefficient. For a non-magnetic material ($\tilde{\mu}_{reff} = 1$), the complex effective relative permittivity and the complex refractive index can be inter-converted using the following formulas,

Conversion from $\tilde{\varepsilon}$ to $\tilde{n}$

$$n + j\kappa = \pm\sqrt{\varepsilon'_{reff} + j\varepsilon''_{reff}} \tag{B.2}$$

Conversion from $\tilde{n}$ to $\tilde{\varepsilon}$

$$\varepsilon'_{reff} = n^2 - \kappa^2. \tag{B.3}$$

$$\varepsilon''_{reff} = 2n\kappa. \tag{B.4}$$

Appendix C

Drude Model

The Drude Model, named after Paul Drude, describes the response of a collection of charges or ions (known to physicists as plasma) when subjected to an electric field. The Drude model can be applied to metals, which contain an abundance of free electrons. For many metals and semiconductors, this model is an excellent approximation of the electromagnetic response of these materials over a wide range of frequencies, including the THz domain. Consider an electron of charge e in an external electric field of strength E, where $\mathbf{E} = E\hat{a}_E$, as shown in Fig. C.1. The electron will experience a force eE opposite to the applied electric field and a drag force mv/τ in the direction of the applied electric field. Under equilibrium, the forces on the electron can be written as,

$$m\frac{d\mathbf{v}}{dt} = e\mathbf{E} - \frac{m\mathbf{v}}{\tau} \tag{C.1}$$

where, e is the charge in C, v is the velocity of electron in m/s, m is the mass of electron in kg and τ is the relaxation (or collision) time. In the complex phasor domain, d/dt can be replaced with $j\omega$

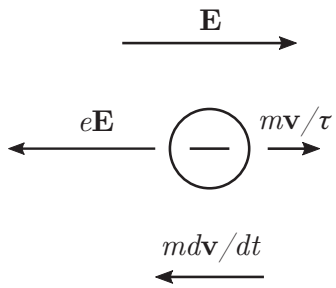


Figure C.1: Forces on an electron in the presence of electric field. $\mathbf{E}$ is an externally applied electric field, $e\mathbf{E}$ is the force on electron due to $\mathbf{E}$, $m\mathbf{v}/\tau$ is the damping force and $md\mathbf{v}/dt$ is the resultant force.

assuming a time dependence of the form $e^{+j\omega t}$.

$$j\omega mv = eE - \frac{mv}{\tau} \tag{C.2}$$

Solving for v,

$$v = \frac{eE}{j\omega m\left(1 + \frac{1}{j\omega\tau}\right)} \tag{C.3}$$

The current density due to n_{3D} number of electrons in a volume V, all moving with an average velocity v is then,

$$J = env = \frac{n_{3D}e^2E}{j\omega m\left(1 + \frac{1}{j\omega\tau}\right)} \tag{C.4}$$

From the constitutive relationship (A.11),

$$\tilde{\sigma}(\omega) = \frac{n_{3D}e^2}{j\omega m\left(1 + \frac{1}{j\omega\tau}\right)} \tag{C.5}$$

This is the expression for the complex Drude conductivity. Note that, $\tilde{\sigma}$ is expressed as a function of angular frequency ω. Substituting $\tilde{\sigma}$ in (A.20),

$$\tilde{\varepsilon}_{reff}(\omega) = \varepsilon_r - \frac{\frac{n_{3D}e^2}{m\varepsilon_0}}{\omega^2\left(1 + \frac{1}{j\omega\tau}\right)} \tag{C.6}$$

where, ε_r may appear as $\varepsilon_{r\infty}$ in some texts and is known as the high frequency relative permittivity such that, $\varepsilon_{r\infty} = \lim_{\omega\to\infty} \tilde{\varepsilon}_r(\omega)$. The angular plasma frequency is defined as,

$$\omega_p = \sqrt{\frac{n_{3D}e^2}{m\varepsilon_0}} \tag{C.7}$$

the complex effective relative permeability can be written as,

$$\tilde{\varepsilon}_{reff}(\omega) = \varepsilon_r - \frac{\omega_p^2}{\omega^2\left(1 + \frac{1}{j\omega\tau}\right)} \tag{C.8}$$

An alternate form of (C.8) is,

$$\tilde{\varepsilon}_{reff}(\omega) = \varepsilon_r - \frac{\omega_p^2}{\omega\left(\omega - j\breve{\gamma}\right)} \tag{C.9}$$

where, $\breve{\gamma} = 1/\tau$ is the damping factor. Drude model for loss-less case is,

$$\varepsilon_{reff}(\omega) = \varepsilon_r - \frac{\omega_p^2}{\omega^2} \tag{C.10}$$

When $\omega\tau \ll \omega_p$, the real part of ε_{reff} is a large negative number and the material acts as a good conductor, reflecting most of the electromagnetic waves. At frequencies close to ω_p the material starts to act like a semiconductor. For $\omega\tau \gg \omega_p$ the material behaves like a dielectric allowing electromagnetic waves to pass through it without significant losses.

Appendix D

The Equation of Plane Wave in Unbounded Medium

From Maxwell's equations, the wave equation can be derived as [2],

$$\nabla^2 \mathbf{E} + k^2 \mathbf{E} = 0 \tag{D.1}$$

The solution to this wave equation, assuming the wave is travelling in an unbounded medium with a positive time dependence $e^{+j\omega t}$, is of the form,

$$\mathbf{E} = \mathbf{E}_0 e^{-j\mathbf{k}\cdot\mathbf{r}} \tag{D.2}$$

Here, $\mathbf{k} = k_x\hat{x} + k_y\hat{y} + k_z\hat{z}$ is a vector in the direction of propagation, $\mathbf{E}_0$ is perpendicular to $\mathbf{k}$ and $\mathbf{r} = x\hat{x} + y\hat{y} + z\hat{z}$ is the position vector. Equation (D.2) is the generalised expression of a plane wave. Here, $|\mathbf{k}| = k = \omega\sqrt{\tilde{\mu}_{reff}\tilde{\varepsilon}_{reff}}$ is the wavenumber with units rad/m. A solution to (D.1) exists when $k^2 = k_x^2 + k_y^2 + k_z^2$ is satisfied. If the wavenumber k is complex then it can be written as a sum of its real and imaginary parts.

$$k = \beta - j\alpha \tag{D.3}$$

where,

$$\alpha = 2k_0\kappa = \frac{2\omega}{c_0}\kappa \tag{D.4}$$

Here, α is the attenuation constant and expressed as Nepers per metre (Np/m); β is known as phase constant and expressed as radians per metre (rad/m).

Assuming the electric field is linearly polarised along $\hat{y}$, a plane wave propagating in the $+x$-direction can be written as,

$$\mathbf{E} = E_0 e^{-\alpha x} e^{-j\beta x}\hat{y} \tag{D.5}$$

The magnetic field is given by,

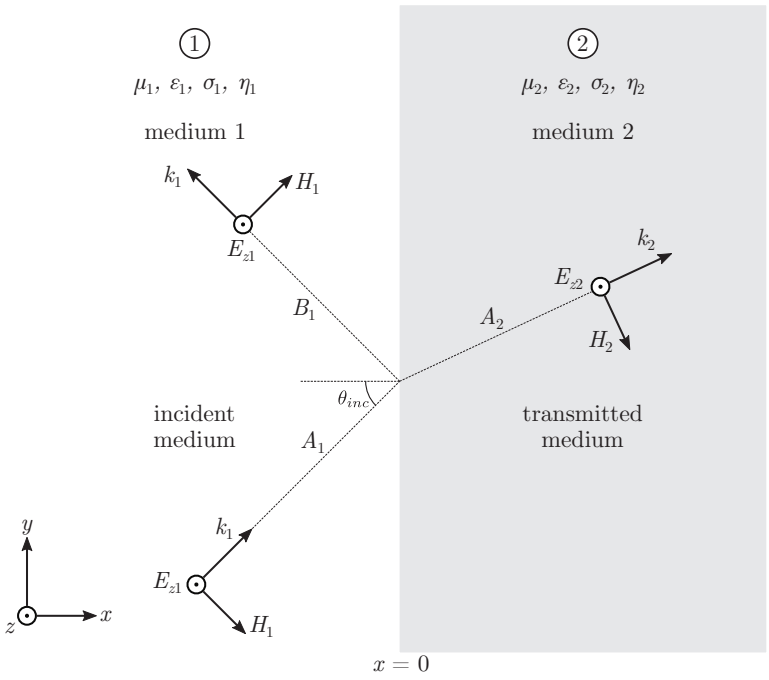
$$\mathbf{H} = \frac{E_0}{\eta} e^{-\alpha x} e^{-j\beta x} \hat{z} \tag{D.6}$$

where, $\eta = \sqrt{\tilde{\mu}_{eff}/\tilde{\varepsilon}_{eff}}$ is the intrinsic impedance of the medium in which the EM wave is travelling. **E**, **H** and **k** satisfy a right-handed relationship, where $\hat{e} \times \hat{h} = \hat{k}$, $\hat{e}$ and $\hat{h}$ being unit vectors along **E** and **H**, respectively.

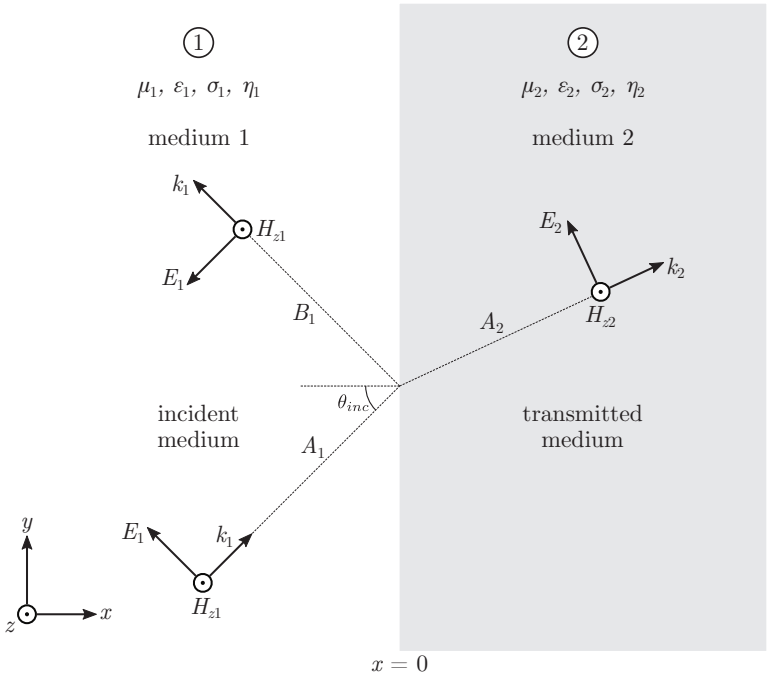
Appendix E

Electric Field Reflection and Transmission Coefficients Due to a Plane Wave Reflection and Transmission at an Interface Between Two Media

The plane wave reflection and transmission at an interface (or boundary) between two different media can be treated as two special cases, namely transverse electric (TE) or transverse magnetic (TM) polarisations. TE and TM polarised EM waves are also known as s- or p-polarised waves, respectively. In the case of TE polarisation, the electric field is transverse (or perpendicular) to the plane of incidence, which is the xy-plane as shown in Fig. E.1(a). Similarly, in the case of TM polarisation, the magnetic field is normal (or electric field is parallel) to the plane of incidence as shown in Fig. E.1(b). Writing incident fields in medium i with coefficients A_i and reflected fields



(a)



(b)

Figure E.1: Illustration of transverse electromagnetic (TEM) wave obliquely incident at an interface between two media making an angle θ_{inc} with the normal: (a) transverse electric (TE or s-polarisation); and (b) transverse magnetic (TM or p-polarisation). The coefficients A_i are the amplitudes of incident transverse field components in medium i while, the coefficients B_i are the amplitudes of reflected transverse field components in medium i.

with coefficients B_i, following equations are obtained for the TM case,

$$H_z = \begin{cases} \left(A_1 e^{-jk_{x1}x} + B_1 e^{jk_{x1}x}\right) e^{-jk_{y1}y} & x \leq 0 \\ A_2 e^{-jk_{x2}x} e^{-jk_{y2}y} & x > 0 \end{cases} \tag{E.1}$$

$$E_x = \begin{cases} \frac{k_{y1}}{\omega\varepsilon_1}\left(-A_1 e^{-jk_{x1}x} - B_1 e^{jk_{x1}x}\right) e^{-jk_{y1}y} & x \leq 0 \\ \frac{k_{y2}}{\omega\varepsilon_2} A_2 e^{-jk_{x2}x} e^{-jk_{y2}y} & x > 0 \end{cases} \tag{E.2}$$

$$E_y = \begin{cases} \frac{k_{x1}}{\omega\varepsilon_1}\left(A_1 e^{-jk_{x1}x} - B_1 e^{jk_{x1}x}\right) e^{-jk_{y1}y} & x \leq 0 \\ \frac{k_{x2}}{\omega\varepsilon_2} A_2 e^{-jk_{x2}x} e^{-jk_{y2}y} & x > 0 \end{cases} \tag{E.3}$$

The unbounded wavenumber in medium i is,

$$k_i = \omega\sqrt{\mu_i\varepsilon_i} = \frac{\omega}{c}\sqrt{\mu_{ri}\varepsilon_{ri}} \tag{E.4}$$

Here, μ_{ri} and ε_{ri} are the relative permeability and relative permittivity of medium i, respectively. If medium i is conductive then ε_{ri} will be complex and given by (A.19). From boundary conditions, the tangential component of wavenumber is continuous across an interface,

$$k_{y1} = k_{y2} = k_y \tag{E.5}$$

with,

$$k_{y1} = k_1 \sin(\theta_{inc}) \tag{E.6}$$

The normal component of wavenumber in medium i is then,

$$k_{xi}^2 = k_i^2 - k_y^2 \tag{E.7}$$

From boundary conditions, the tangential field components must be continuous across the interface. For H_z,

$$A_1 + B_1 = A_2 \tag{E.8}$$

Similarly for E_y,

$$\frac{k_{x1}}{\omega\varepsilon_1}(A_1 - B_1) = \frac{k_{x2}}{\omega\varepsilon_2} A_2. \tag{E.9}$$

Writing in matrix form,

$$\begin{bmatrix} 1 & 1 & -1 \\ \frac{k_{x1}}{\omega\varepsilon_1} & -\frac{k_{x1}}{\omega\varepsilon_1} & \frac{k_{x2}}{\omega\varepsilon_2} \end{bmatrix} \begin{bmatrix} A_1 \\ B_1 \\ A_2 \end{bmatrix} = \begin{bmatrix} 0 \\ 0 \\ 0 \end{bmatrix} \tag{E.10}$$

Solving for B_1 and A_2 in terms of A_1,

$$B_1 = \frac{\varepsilon_2 k_{x1} - \varepsilon_1 k_{x2}}{\varepsilon_2 k_{x1} + \varepsilon_1 k_{x2}} A_1 \tag{E.11}$$

and,

$$A_2 = \frac{2\varepsilon_2 k_{x1}}{\varepsilon_2 k_{x1} + \varepsilon_1 k_{x2}} A_1 \tag{E.12}$$

which are the electric field reflection and transmission coefficients, and are defined as,

$$\Gamma = \left.\frac{B_1}{A_1}\right|_{B_2=0} \rightarrow B_1 \quad \text{with} \quad A_1 = 1 \tag{E.13}$$

and,

$$T = \left.\frac{A_2}{A_1}\right|_{B_2=0} \rightarrow A_2 \quad \text{with} \quad A_1 = 1 \tag{E.14}$$

The electric field reflection and transmission coefficients can be expressed as, [2],

$$\Gamma = \frac{1 - \zeta_e}{1 + \zeta_e} \tag{E.15}$$

and,

$$T = \frac{2}{1 + \zeta_e} \tag{E.16}$$

where,

$$\zeta_e = \frac{\mu_2 k_{x1}}{\mu_1 k_{x2}} \tag{E.17}$$

The electric field reflection and transmission coefficients for the TE incidence are obtained in a similar manner and given by,

$$\Gamma = \frac{1 - \zeta_m}{1 + \zeta_m} \tag{E.18}$$

and,

$$T = \frac{2}{1 + \zeta_m} \tag{E.19}$$

where,

$$\zeta_m = \frac{\varepsilon_1 k_{x2}}{\varepsilon_2 k_{x1}} \tag{E.20}$$

Appendix F

Plane Wave Reflection and Transmission For Planar Three-Layer Media

The plane wave reflection and transmission for the planar three-media case, like two-media case, can be considered either as TM or TE incidence. Figure F.1(b) shows a TM wave obliquely incident on three-layer media. Medium 2, which is just a slab, is flanked by semi-infinite media on either side. It is assumed that the incident and transmitted media have the same material parameters, i.e., $\mu_{r1} = \mu_{r3}$, $\varepsilon_{r1} = \varepsilon_{r3}$, $\sigma_1 = \sigma_3$ and $\eta_1 = \eta_3$. Writing equations for the TM incidence, the electric and magnetic fields in the three media can be written as,

$$H_z = \begin{cases} \left(A_1 e^{-jk_{x1}x} + B_1 e^{jk_{x1}x}\right) e^{-jk_y y} & x \leq 0 \\ \left(A_2 e^{-jk_{x2}x} + B_2 e^{jk_{x2}x}\right) e^{-jk_y y} & 0 < x \leq l \\ A_3 e^{-jk_{x1}(x-l)} e^{-jk_y y} & x > l \end{cases} \tag{F.1}$$

$$E_x = \begin{cases} \dfrac{k_y}{\omega\varepsilon_1}\left(-A_1 e^{-jk_{x1}x} - B_1 e^{jk_{x1}x}\right) e^{-jk_y y} & x \leq 0 \\ \dfrac{k_y}{\omega\varepsilon_2}\left(-A_2 e^{-jk_{x2}x} - B_2 e^{jk_{x2}x}\right) e^{-jk_y y} & 0 < x \leq l \\ \dfrac{k_y}{\omega\varepsilon_1} A_3 e^{-jk_{x1}(x-l)} e^{-jk_y y} & x > l \end{cases} \tag{F.2}$$

$$E_y = \begin{cases} \dfrac{k_{x1}}{\omega\varepsilon_1}\left(A_1 e^{-jk_{x1}x} - B_1 e^{jk_{x1}x}\right) e^{-jk_y y} & x \leq 0 \\ \dfrac{k_{x2}}{\omega\varepsilon_2}\left(A_2 e^{-jk_{x2}x} - B_2 e^{jk_{x2}x}\right) e^{-jk_y y} & 0 < x \leq l \\ \dfrac{k_{x1}}{\omega\varepsilon_1} A_3 e^{-jk_{x1}(x-l)} e^{-jk_y y} & x > l \end{cases} \tag{F.3}$$

The unbounded wavenumber in medium i is,

$$k_i = \omega\sqrt{\mu_i\varepsilon_i} = \frac{\omega}{c}\sqrt{\mu_{ri}\varepsilon_{ri}} \tag{F.4}$$

Here, μ_{ri} and ε_{ri} are the relative permeability and relative permittivity of medium i, respectively. If medium i is conductive then ε_{ri} will be complex and given by (A.19). From boundary conditions, the tangential component of wavenumber is continuous across an interface,

$$k_{y1} = k_{y2} = k_{y3} = k_y \tag{F.5}$$

with,

$$k_{y1} = k_1 \sin(\theta_{inc}) \tag{F.6}$$

The normal component of wavenumber in medium i is then,

$$k_{xi}^2 = k_i^2 - k_y^2 \tag{F.7}$$

Here, the reference plane for coefficients A_1, B_1, A_2 and B_2 is the plane $x = 0$, while the reference plane for coefficient A_3 is $x = l$. Applying boundary conditions $H_{z1}(x = 0) = H_{z2}(x = 0)$, $E_{y1}(x = 0) = E_{y2}(x = 0)$, $H_{z2}(x = l) = H_{z3}(x = l)$, $E_{y2}(x = l) = E_{y3}(x = l)$ and after some algebraic manipulations, the following matrix system is obtained,

$$\begin{bmatrix} 1 & 1 & -1 & -1 & 0 \\ \dfrac{k_{x1}}{\omega\varepsilon_1} & -\dfrac{k_{x1}}{\omega\varepsilon_1} & -\dfrac{k_{x2}}{\omega\varepsilon_2} & \dfrac{k_{x2}}{\omega\varepsilon_2} & 0 \\ 0 & 0 & e^{-jk_{x2}l} & e^{jk_{x2}l} & -1 \\ 0 & 0 & \dfrac{k_{x2}}{\omega\varepsilon_2}e^{-jk_{x2}l} & -\dfrac{k_{x2}}{\omega\varepsilon_2}e^{jk_{x2}l} & -\dfrac{k_{x1}}{\omega\varepsilon_1} \end{bmatrix} \begin{bmatrix} A_1 \\ B_1 \\ A_2 \\ B_2 \\ A_3 \end{bmatrix} = \begin{bmatrix} 0 \\ 0 \\ 0 \\ 0 \end{bmatrix} \tag{F.8}$$

After some algebraic manipulations following is obtained,

$$\frac{B_1}{A_1} = \frac{\left(1 - e^{-2jk_{x2}l}\right)(1-\zeta)(1+\zeta)}{(1+\zeta)^2 - e^{-2jk_{x2}l}(1-\zeta)^2} \tag{F.9}$$

$$\frac{A_2}{A_1} = \frac{-2(1+\zeta)}{(1+\zeta)^2 - e^{-2jk_{x2}l}(1-\zeta)^2} \tag{F.10}$$

$$\frac{B_2}{A_1} = \frac{-2e^{-2jk_{x2}l}(1-\zeta)}{(1+\zeta)^2 - e^{-2jk_{x2}l}(1-\zeta)^2} \tag{F.11}$$

$$\frac{A_3}{A_1} = \frac{4\zeta e^{-jk_{x2}l}}{(1+\zeta)^2 - e^{-2jk_{x2}l}(1-\zeta)^2} \tag{F.12}$$

with generalised coefficients,

$$\zeta = \begin{cases} \dfrac{\varepsilon_1 k_{x2}}{\varepsilon_2 k_{x1}} & \text{TM} \\ \dfrac{\mu_2 k_{x1}}{\mu_1 k_{x2}} & \text{TE} \end{cases} \tag{F.13}$$

Where, the electric field reflection and transmission coefficients are defined as,

$$\Gamma = \left.\frac{B_1}{A_1}\right|_{B_2=0} \rightarrow B_1 \quad \text{with} \quad A_1 = 1 \tag{F.14}$$

and,

$$T = \left.\frac{A_2}{A_1}\right|_{B_2=0} \rightarrow A_2 \quad \text{with} \quad A_1 = 1 \tag{F.15}$$

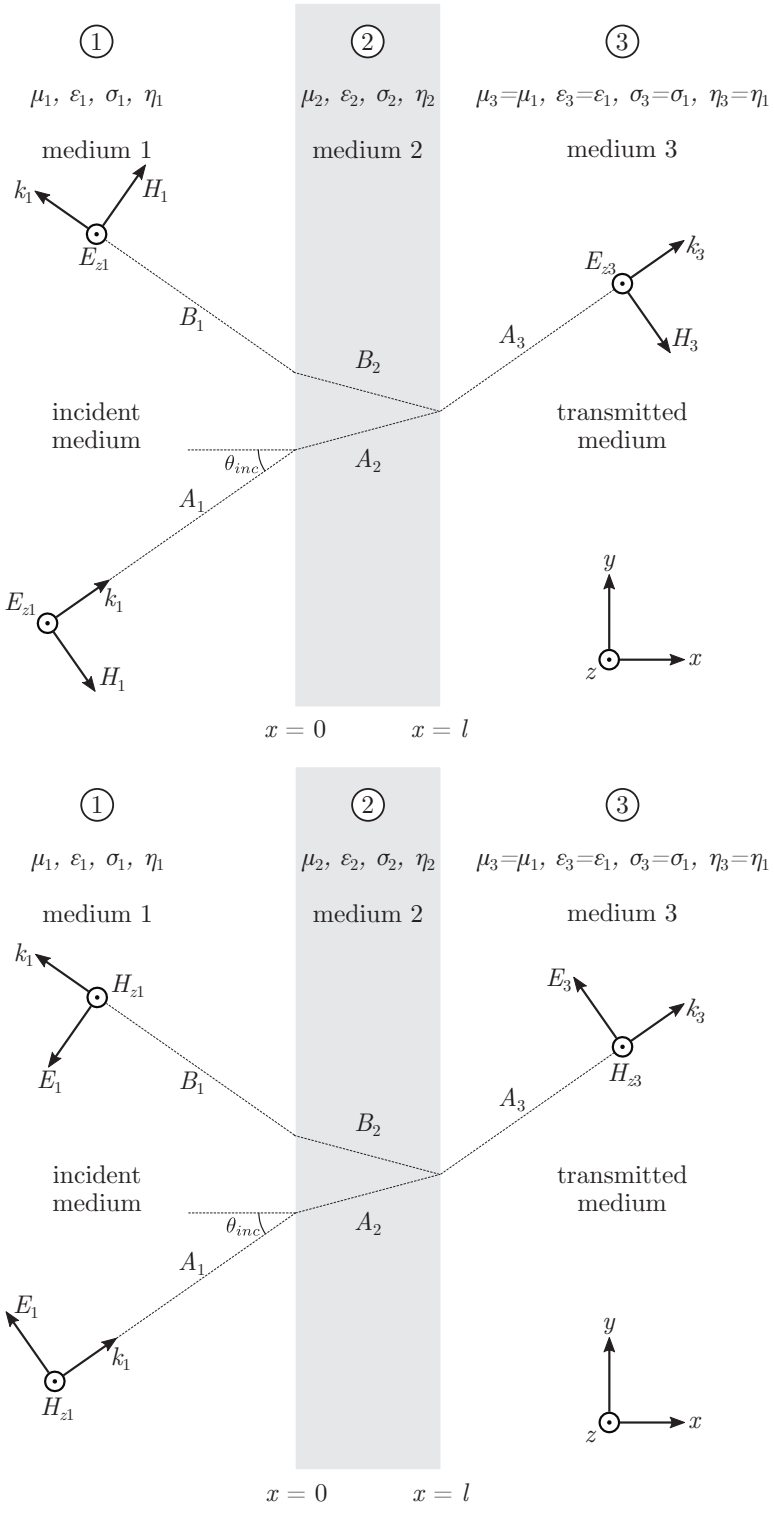


Figure F.1: Illustration of transverse electromagnetic (TEM) wave obliquely incident on a planar three-layer media making an angle θ_{inc} with the normal: (a) transverse electric (TE or s-polarisation); and (b) transverse magnetic (TM or p-polarisation). The coefficients A_i are the amplitudes of incident transverse field components in medium i while, the coefficients B_i are the amplitudes of reflected transverse field components in medium i. The slab is of thickness l.

Appendix G

MATLAB Code to Compute Coplanar Waveguide Mode Profile

```
% Solves Poisson's equation in 2-D to compute electric field mode profile.
clc
clear all

MaxTime = 1000; % Iterations
SizeX = 101;
SizeY = 61;
SourceX = ceil(SizeX/2);
SourceY = ceil(SizeY/2);

DomainX = 300e-3;
DomainY = 300e-3;
er_sub = 12.4;
e0 = 8.854187817e-12;
u0 = 1.256637061e-6;
c = 299792458;
eta0 = 376.73031346177;
deltax = DomainX/SizeX;
deltay = DomainY/SizeY;

V = zeros(SizeX,SizeY);
Ex = zeros(SizeX,SizeY);
Ey = zeros(SizeX,SizeY);
eps = e0*ones(SizeX,SizeY);
eps(:,1:round(SizeY/2)) = er_sub.*eps(:,1:round(SizeY/2));

q = zeros(SizeX,SizeY);
Wg = round(15);
Wc = round(15);
% ========== Initialising boundary conditions ==========
% Fixed potential on centre conductor and ground
V(1:Wg,round(SizeY/2)) = -1;
V(SizeX-Wg+1:SizeX,round(SizeY/2)) = -1;
V(1,:) = -1;
V(SizeX,:) = -1;
V(:,1) = -1;
V(:,SizeY) = -1;
V(round(SizeX/2)-Wc:round(SizeX/2)+Wc,round(SizeY/2)) = 1;
```

```
% ========================================================
S=V;
i = 2:SizeX-1;
j = 2:SizeY-1;

for t = 1:MaxTime
V(i,j) = (deltay^2*(V(i+1,j)+V(i-1,j))+deltax^2*(V(i,j+1)+V(i,j-1))+q(i,j)./(
    deltax^2*deltay^2*eps(i,j)))/(2*deltax^2+2*deltay^2);
% ================= Boundary conditions ================
% Fixed potential on centre conductor and ground
V(1:Wg,round(SizeY/2)) = -1;
V(SizeX-Wg+1:SizeX,round(SizeY/2)) = -1;
V(1,:) = -1;
V(SizeX,:) = -1;
V(:,1) = -1;
V(:,SizeY) = -1;
V(round(SizeX/2)-Wc:round(SizeX/2)+Wc,round(SizeY/2)) = 1; % centre conductor
% ========================================================
end
% ================ Data ==============
[Ex, Ey] = gradient ( -V', deltax, deltay );
y = 2.5e15:0.1e15:6.5e15;
a1 = 5.3813 * 10^(11+4);
a2 = 2.6010;
gamma = 0.2295;
x = (y./a1).^(1./gamma)-a2;

x1 = x;
y1 = y;
DName1 = 'abc';
Colour1 = 'b';

x_label = '$y$-axis ($\mu$m)';
y_label = '$z$-axis ($\mu$m)';
% ====================================

figure301 = figure(1);
clf
FontName = 'CMU Serif';
FontSize = 12;
FontWeight = 'normal';
FontWeightLabel = 'normal';
FontSizeLabel = 12;
LineWidth = 1;
[x,y]=meshgrid(0:SizeX-1,0:SizeY-1);
streamslice(x,y,Ex,Ey,1,'arrows','cubic')
hold on
plot([0 15],[30 30],'LineWidth',5.0,'Color',[0 0 0])
plot([35 65],[30 30],'LineWidth',5.0,'Color',[0 0 0])
plot([85 100],[30 30],'LineWidth',5.0,'Color',[0 0 0])

set(gca, 'FontSize',FontSize,'FontWeight',FontWeight,'TickLabelInterpreter', '
    latex');
grid on
xlim([0,100])
ylim([0,60])
xlabel(x_label,'FontSize', FontSizeLabel,'FontWeight', FontWeightLabel,'FontName',
    FontName,'interpreter','latex');
ylabel(y_label,'FontSize', FontSizeLabel,'FontWeight', FontWeightLabel,'FontName',
    FontName,'interpreter','latex');
grid off
```

```
xticks_loc = [0 35 65 100];
xtick_labels = cellstr(num2str(xticks_loc'))';
yticks_loc = [0 30 60];
ytick_labels = cellstr(num2str(yticks_loc'))';
xticks(xticks_loc);
xticklabels(xtick_labels);
yticks(yticks_loc);
yticklabels(ytick_labels);
annotation(gcf,'rectangle',[0.0831428571428571 0.111904761904762 0.900785714285714
    0.433333333333333],'Color','none','FaceColor',[0 0 0],'FaceAlpha',0.1);
annotation(gcf,'rectangle',[0.0857142857142857 0.116666666666667 0.894642857142857
    0.852380952380952],'LineWidth',5);
ax = gca; ax.Units = 'pixels'; outerpos = ax.OuterPosition; ti = ax.TightInset; ti
    (ti < 0.1) = 0.15; left = outerpos(1) + ti(1); bottom = outerpos(2) + ti(2);
    ax_width = outerpos(3) - ti(1) - ti(3); ax_height = outerpos(4) - ti(2) - ti(4)
    ; ax.Position = [left bottom ax_width ax_height]; fig = gcf; fig.Units = '
    pixels'; fig.PaperPositionMode = 'auto'; fig_pos = fig.PaperPosition; fig.
    PaperSize = [fig_pos(3) fig_pos(4)];
```

Appendix H

Two-port network conversions between S, Z, Y, h, ABCD and T parameters

Table H.1: Conversion from S to Z, Y, h, ABCD and T parameters.

$Z_{11} = -\frac{Z_{ref1}}{2}\frac{S_{11} - S_{22} - \Delta S + 1}{S_{11} + S_{22} - \Delta S - 1}$	$Z_{12} = -\check{k}_2 Z_{ref2}\frac{S_{12}}{S_{11} + S_{22} - \Delta S - 1}$
$Z_{21} = -\check{k}_1 Z_{ref1}\frac{S_{21}}{S_{11} + S_{22} - \Delta S - 1}$	$Z_{22} = \frac{Z_{ref2}}{2}\frac{S_{11} - S_{22} + \Delta S - 1}{S_{11} + S_{22} - \Delta S - 1}$
$Y_{11} = -\frac{1}{2Z_{ref1}}\frac{S_{11} - S_{22} + \Delta S - 1}{S_{11} + S_{22} + \Delta S + 1}$	$Y_{12} = -\frac{\check{k}_2}{Z_{ref1}}\frac{S_{12}}{S_{11} + S_{22} + \Delta S + 1}$
$Y_{21} = -\frac{\check{k}_1}{Z_{ref2}}\frac{S_{21}}{S_{11} + S_{22} + \Delta S + 1}$	$Y_{22} = \frac{1}{2Z_{ref2}}\frac{S_{11} - S_{22} - \Delta S + 1}{S_{11} + S_{22} + \Delta S + 1}$
$h_{11} = -\frac{Z_{ref1}}{2}\frac{S_{11} + S_{22} + \Delta S + 1}{S_{11} - S_{22} + \Delta S - 1}$	$h_{12} = -\check{k}_2\frac{S_{12}}{S_{11} - S_{22} + \Delta S - 1}$
$h_{21} = \frac{\check{k}_1 Z_{ref1}}{Z_{ref2}}\frac{S_{21}}{S_{11} - S_{22} + \Delta S - 1}$	$h_{22} = \frac{1}{2Z_{ref2}}\frac{S_{11} + S_{22} + \Delta S - 1}{S_{11} - S_{22} + \Delta S - 1}$
$A = \frac{\check{k}_2}{\check{k}_1}\frac{S_{11} - S_{22} - \Delta S + 1}{4S_{21}}$	$B = \frac{\check{k}_2 Z_{ref2}}{\check{k}_1}\frac{S_{11} + S_{22} + \Delta S + 1}{4S_{21}}$
$C = -\frac{\check{k}_2}{\check{k}_1 Z_{ref1}}\frac{S_{11} + S_{22} - \Delta S - 1}{4S_{21}}$	$D = -\frac{\check{k}_2 Z_{ref2}}{\check{k}_1 Z_{ref1}}\frac{S_{11} - S_{22} + \Delta S - 1}{4S_{21}}$
$T_{11} = \frac{1}{S_{21}}$	$T_{12} = -\frac{S_{22}}{S_{21}}$
$T_{21} = \frac{S_{11}}{S_{21}}$	$T_{22} = -\frac{\Delta S}{S_{21}}$

Table H.2: Conversion from Z to S, Y, h, ABCD and T parameters.

$S_{11} = \frac{Z_{11}Z_{ref2} - Z_{22}Z_{ref1} + Z_{11}Z_{22} - Z_{12}Z_{21} - Z_{ref1}Z_{ref2}}{Z_{11}Z_{ref2} + Z_{22}Z_{ref1} + Z_{11}Z_{22} - Z_{12}Z_{21} + Z_{ref1}Z_{ref2}}$	$S_{12} = \frac{2Z_{ref1}}{\check{k}_2} \frac{Z_{12}}{Z_{11}Z_{ref2} + Z_{22}Z_{ref1} + Z_{11}Z_{22} - Z_{12}Z_{21} + Z_{ref1}Z_{ref2}}$
$S_{21} = \frac{2Z_{ref2}}{\check{k}_1} \frac{Z_{21}}{Z_{11}Z_{ref2} + Z_{22}Z_{ref1} + Z_{11}Z_{22} - Z_{12}Z_{21} + Z_{ref1}Z_{ref2}}$	$S_{22} = -\frac{Z_{ref2}Z_{11} - Z_{ref1}Z_{22} - Z_{11}Z_{22} + Z_{12}Z_{21} + Z_{ref1}Z_{ref2}}{Z_{11}Z_{ref2} + Z_{22}Z_{ref1} + Z_{11}Z_{22} - Z_{12}Z_{21} + Z_{ref1}Z_{ref2}}$
$Y_{11} = \frac{Z_{22}}{\Delta Z}$	$Y_{12} = -\frac{Z_{12}}{\Delta Z}$
$Y_{21} = -\frac{Z_{21}}{\Delta Z}$	$Y_{22} = \frac{Z_{11}}{\Delta Z}$
$h_{11} = \frac{\Delta Z}{Z_{22}}$	$h_{12} = \frac{Z_{12}}{Z_{22}}$
$h_{21} = -\frac{Z_{21}}{Z_{22}}$	$h_{22} = \frac{1}{Z_{22}}$
$A = \frac{Z_{11}}{Z_{21}}$	$B = \frac{\Delta \mathrm{Z}}{Z_{21}}$
$C = \frac{1}{Z_{21}}$	$D = \frac{Z_{22}}{Z_{21}}$
$T_{11} = \frac{\check{k}_1}{2\check{k}_2 Z_{ref2}} \frac{Z_{11}Z_{ref2} + Z_{22}Z_{ref1} + Z_{11}Z_{22} - Z_{12}Z_{21} + Z_{ref1}Z_{ref2}}{Z_{21}}$	$T_{12} = \frac{\check{k}_1}{2\check{k}_2 Z_{ref2}} \frac{Z_{11}Z_{ref2} - Z_{22}Z_{ref1} - Z_{11}Z_{22} + Z_{12}Z_{21} + Z_{ref1}Z_{ref2}}{Z_{21}}$
$T_{21} = \frac{\check{k}_1}{2\check{k}_2 Z_{ref2}} \frac{Z_{11}Z_{ref2} - Z_{22}Z_{ref1} + Z_{11}Z_{22} - Z_{12}Z_{21} - Z_{ref1}Z_{ref2}}{Z_{21}}$	$T_{22} = \frac{\check{k}_1}{2\check{k}_2 Z_{ref2}} \frac{Z_{11}Z_{ref2} + Z_{22}Z_{ref1} - Z_{11}Z_{22} + Z_{12}Z_{21} - Z_{ref1}Z_{ref2}}{Z_{21}}$

Table H.3: Conversion from Y to S, Z, h, ABCD and T parameters.

$S_{11} = -\frac{Y_{11}Z_{ref1} - Y_{22}Z_{ref2} + \Delta Y Z_{ref1}Z_{ref2} - 1}{Y_{11}Z_{ref1} + Y_{22}Z_{ref2} + \Delta Y Z_{ref1}Z_{ref2} + 1}$	$S_{12} = \frac{2Z_{ref1}^2}{\check{k}_2} \frac{Y_{12}}{Y_{11}Z_{ref1} + Y_{22}Z_{ref2} + \Delta Y Z_{ref1}Z_{ref2} + 1}$
$S_{21} = -\frac{2Z_{ref2}^2}{\check{k}_1} \frac{Y_{21}}{Y_{11}Z_{ref1} + Y_{22}Z_{ref2} + \Delta Y Z_{ref1}Z_{ref2} + 1}$	$S_{22} = \frac{Y_{11}Z_{ref1} - Y_{22}Z_{ref2} - \Delta Y Z_{ref1}Z_{ref2} + 1}{Y_{11}Z_{ref1} + Y_{22}Z_{ref2} + \Delta Y Z_{ref1}Z_{ref2} + 1}$
$Z_{11} = \frac{Y_{22}}{\Delta Y}$	$Z_{12} = -\frac{Y_{12}}{\Delta Y}$
$Z_{21} = -\frac{Y_{21}}{\Delta Y}$	$Z_{22} = \frac{Y_{11}}{\Delta Y}$
$h_{11} = \frac{1}{Y_{11}}$	$h_{12} = -\frac{Y_{12}}{Y_{11}}$
$h_{21} = \frac{Y_{21}}{Y_{11}}$	$h_{22} = \frac{\Delta Y}{Y_{11}}$
$A = -\frac{Y_{22}}{Y_{21}}$	$B = -\frac{1}{Y_{21}}$
$C = -\frac{\Delta Y}{Y_{21}}$	$D = -\frac{Y_{11}}{Y_{21}}$
$T_{11} = -\frac{\check{k}_1}{2\check{k}_2 Z_{ref2}^2} \frac{Y_{11}Z_{ref1} + Y_{22}Z_{ref2} + \Delta Y Z_{ref1}Z_{ref2} + 1}{Y_{21}}$	$T_{12} = \frac{\check{k}_1}{2\check{k}_2 Z_{ref2}^2} \frac{Y_{11}Z_{ref1} - Y_{22}Z_{ref2} - \Delta Y Z_{ref1}Z_{ref2} + 1}{Y_{21}}$
$T_{21} = \frac{\check{k}_1}{2\check{k}_2 Z_{ref2}^2} \frac{Z_{ref1}Y_{11} - Z_{ref2}Y_{22} + \Delta Y Z_{ref1}Z_{ref2} - 1}{Y_{21}}$	$T_{22} = -\frac{\check{k}_1}{2\check{k}_2 Z_{ref2}^2} \frac{Y_{11}Z_{ref1} + Y_{22}Z_{ref2} - \Delta Y Z_{ref1}Z_{ref2} - 1}{Y_{21}}$

Table H.4: Conversion from h to S, Z, Y, ABCD and T parameters.

$S_{11} = \frac{h_{11} - h_{22}Z_{ref1}Z_{ref2} + \Delta h Z_{ref2} - Z_{ref1}}{h_{11} + h_{22}Z_{ref1}Z_{ref2} + \Delta h Z_{ref2} + Z_{ref1}}$	$S_{12} = \frac{2Z_{ref1}}{\check{k}_2} \frac{h_{12}}{h_{11} + h_{22}Z_{ref1}Z_{ref2} + \Delta h Z_{ref2} + Z_{ref1}}$
$S_{21} = -\frac{2Z_{ref2}^2}{\check{k}_1} \frac{h_{21}}{h_{11} + h_{22}Z_{ref1}Z_{ref2} + \Delta h Z_{ref2} + Z_{ref1}}$	$S_{22} = \frac{h_{11} - h_{22}Z_{ref2}Z_{ref1} - \Delta h Z_{ref2} + Z_{ref1}}{h_{11} + h_{22}Z_{ref1}Z_{ref2} + \Delta h Z_{ref2} + Z_{ref1}}$
$Z_{11} = \frac{\Delta h}{h_{22}}$	$Z_{12} = \frac{h_{12}}{h_{22}}$
$Z_{21} = -\frac{h_{21}}{h_{22}}$	$Z_{22} = \frac{1}{h_{22}}$
$Y_{11} = \frac{1}{h_{11}}$	$Y_{12} = -\frac{h_{12}}{h_{11}}$
$Y_{21} = \frac{h_{21}}{h_{11}}$	$Y_{22} = \frac{\Delta h}{h_{11}}$
$A = -\frac{\Delta h}{h_{21}}$	$B = -\frac{h_{11}}{h_{21}}$
$C = -\frac{h_{22}}{h_{21}}$	$D = -\frac{1}{h_{21}}$
$T_{11} = -\frac{\check{k}_1}{2\check{k}_2 Z_{ref2}^2} \frac{h_{11} + h_{22}Z_{ref1}Z_{ref2} + \Delta h Z_{ref2} + Z_{ref1}}{h_{21}}$	$T_{12} = \frac{\check{k}_1}{2\check{k}_2 Z_{ref2}^2} \frac{h_{11} - h_{22}Z_{ref1}Z_{ref2} - \Delta h Z_{ref2} + Z_{ref1}}{h_{21}}$
$T_{21} = -\frac{\check{k}_1}{2\check{k}_2 Z_{ref2}^2} \frac{h_{11} - h_{22}Z_{ref1}Z_{ref2} + \Delta h Z_{ref2} - Z_{ref1}}{h_{21}}$	$T_{22} = \frac{\check{k}_1}{2\check{k}_2 Z_{ref2}^2} \frac{h_{11} + h_{22}Z_{ref1}Z_{ref2} - \Delta h Z_{ref2} - Z_{ref1}}{h_{21}}$

Table H.5: Conversion from ABCD to S, Z, Y, h and T parameters.

$S_{11} = \frac{AZ_{ref2} + B - CZ_{ref1}Z_{ref2} - DZ_{ref1}}{AZ_{ref2} + B + CZ_{ref1}Z_{ref2} + DZ_{ref1}}$	$S_{12} = \frac{2Z_{ref1}}{\check{k}_2} \frac{AD - BC}{AZ_{ref2} + B + CZ_{ref1}Z_{ref2} + DZ_{ref1}}$
$S_{21} = \frac{2Z_{ref2}}{\check{k}_1} \frac{1}{AZ_{ref2} + B + CZ_{ref1}Z_{ref2} + DZ_{ref1}}$	$S_{22} = \frac{-AZ_{ref2} + B - CZ_{ref2}Z_{ref1} + DZ_{ref1}}{AZ_{ref2} + B + CZ_{ref1}Z_{ref2} + DZ_{ref1}}$
$Z_{11} = \frac{A}{C}$	$Z_{12} = \frac{AD - BC}{C}$
$Z_{21} = \frac{1}{C}$	$Z_{22} = \frac{D}{C}$
$Y_{11} = \frac{D}{B}$	$Y_{12} = -\frac{AD - BC}{B}$
$Y_{21} = -\frac{1}{B}$	$Y_{22} = \frac{A}{B}$
$h_{11} = \frac{B}{D}$	$h_{12} = \frac{AD - BC}{D}$
$h_{21} = -\frac{1}{D}$	$h_{22} = \frac{C}{D}$
$T_{11} = \frac{\check{k}_1}{2\check{k}_2 Z_{ref2}} \left(AZ_{ref2} + B + CZ_{ref1}Z_{ref2} + DZ_{ref1}\right)$	$T_{12} = \frac{\check{k}_1}{2\check{k}_2 Z_{ref2}} \left(AZ_{ref2} - B + CZ_{ref1}Z_{ref2} - DZ_{ref1}\right)$
$T_{21} = \frac{\check{k}_1}{2\check{k}_2 Z_{ref2}} \left(AZ_{ref2} + B - CZ_{ref1}Z_{ref2} - DZ_{ref1}\right)$	$T_{22} = \frac{\check{k}_1}{2\check{k}_2 Z_{ref2}} \left(AZ_{ref2} - B - CZ_{ref1}Z_{ref2} + DZ_{ref1}\right)$

Table H.6: Conversion from T to S, Z, Y, h and ABCD parameters.

$S_{11} = \dfrac{T_{21}}{T_{11}}$	$S_{12} = \dfrac{\Delta T}{T_{11}}$
$S_{21} = \dfrac{1}{T_{11}}$	$S_{22} = -\dfrac{T_{12}}{T_{11}}$
$Z_{11} = \dfrac{Z_{ref1}}{2}\dfrac{T_{11}+T_{21}+T_{12}+T_{22}}{T_{11}+T_{12}-T_{21}-T_{22}}$	$Z_{12} = \check{k}_2 Z_{ref2}\dfrac{\Delta T}{T_{11}+T_{12}-T_{21}-T_{22}}$
$Z_{21} = \check{k}_1 Z_{ref1}\dfrac{1}{T_{11}+T_{12}-T_{21}-T_{22}}$	$Z_{22} = \dfrac{Z_{ref2}}{2}\dfrac{T_{11}-T_{12}-T_{21}+T_{22}}{T_{11}+T_{12}-T_{21}-T_{22}}$
$Y_{11} = \dfrac{1}{2Z_{ref1}}\dfrac{T_{11}-T_{12}-T_{21}+T_{22}}{T_{11}-T_{12}+T_{21}-T_{22}}$	$Y_{12} = -\dfrac{\check{k}_2}{Z_{ref1}}\dfrac{\Delta T}{T_{11}-T_{12}+T_{21}-T_{22}}$
$Y_{21} = -\dfrac{\check{k}_1}{Z_{ref2}}\dfrac{1}{T_{11}-T_{12}+T_{21}-T_{22}}$	$Y_{22} = \dfrac{1}{2Z_{ref2}}\dfrac{T_{12}+T_{22}+T_{11}+T_{21}}{T_{11}-T_{12}+T_{21}-T_{22}}$
$h_{11} = \dfrac{Z_{ref1}}{2}\dfrac{T_{11}-T_{12}+T_{21}-T_{22}}{T_{11}-T_{12}-T_{21}+T_{22}}$	$h_{12} = \check{k}_2\dfrac{\Delta T}{T_{11}-T_{12}-T_{21}+T_{22}}$
$h_{21} = -\dfrac{\check{k}_1 Z_{ref1}}{Z_{ref2}}\dfrac{1}{T_{11}-T_{12}-T_{21}+T_{22}}$	$h_{22} = \dfrac{1}{2Z_{ref2}}\dfrac{T_{11}+T_{12}-T_{21}-T_{22}}{T_{11}-T_{12}-T_{21}+T_{22}}$
$A = \dfrac{\check{k}_2}{4\check{k}_1}(T_{11}+T_{12}+T_{21}+T_{22})$	$B = \dfrac{\check{k}_2 Z_{ref2}}{4\check{k}_1}(T_{11}+T_{21}-T_{12}-T_{22})$
$C = \dfrac{\check{k}_2}{4\check{k}_1 Z_{ref1}}(T_{11}-T_{21}+T_{12}-T_{22})$	$D = \dfrac{\check{k}_2 Z_{ref2}}{4\check{k}_1 Z_{ref1}}(T_{11}-T_{21}-T_{12}+T_{22})$

Table H.7: Conversion between two-port S- and S_p-parameters.

$S_{p11} = \dfrac{1}{Z_{ref1}}\left[Re\left\{Z_{ref1}\right\}S_{11} + Im\left\{Z_{ref1}\right\}\right]$	$S_{p12} = \dfrac{\check{k}_2\check{k}_{p1}Re\left\{Z_{ref1}\right\}}{\check{k}_1\check{k}_{p2}}S_{12}$
$S_{p21} = \dfrac{\check{k}_1\check{k}_{p2}Re\left\{Z_{ref2}\right\}}{\check{k}_2\check{k}_{p1}}S_{21}$	$S_{p22} = \dfrac{1}{Z_{ref2}}\left[Re\left\{Z_{ref2}\right\}S_{22} + Im\left\{Z_{ref2}\right\}\right]$

Appendix I

MATLAB Code to Compute Fabry-Pérot Eigenmodes in Parallel-Plate Waveguide

```
% Fabry-Perot eigenmodes of dielectric-filled parallel-plate waveguide
clc
sUnit = 1e-3; sUnitname = 'mm';
fUnit = 1e9; fUnitname = 'GHz';

f0 = (8.2:0.01:12.4).*fUnit;
w0 = 2.*pi.*f0;
m = 1; % mode number

a = 22.86*sUnit;
l = 9.626*sUnit;

e0 = 8.854187817e-12;
u0 = 1.256637061e-6;
c  = 299792458;

er_d_inf = 2.325;
sig_d = 0;
mu_d = u0;
tandelta = 0.001973;
ert = 1;
ertt = tandelta;
e_d = er_d_inf.*(ert+1j.*ertt);

kc = m.*pi./a;
e1 = e0;
u1 = u0;
e2 = e_d*e0;
u2 = u0;
g1 = 1j.*sqrt(w0.^2.*e1.*u1-kc.^2);
g2 = 1j.*sqrt(w0.^2.*e2.*u2-kc.^2);
ze = (u1.*1j.*sqrt(w0.^2.*e2.*u2-kc.^2))./(u2.*1j.*sqrt(w0.^2.*e1.*u1-kc.^2));
zm = (e2.*1j.*sqrt(w0.^2.*e1.*u1-kc.^2))./(e1.*1j.*sqrt(w0.^2.*e2.*u2-kc.^2));
P  = 1j.*sqrt(w0.^2.*e2.*u2-kc.^2).*l;

f0 = 5*fUnit:0.25*fUnit:15*fUnit;
% TE
sol1 = zeros(1,length(f0)); % Odd   :(1+z)-exp(-P).*(1-z)
sol2 = zeros(1,length(f0)); % Even  :(1+z)+exp(-P).*(1-z)
% TM
```

```
sol3 = zeros(1,length(f0)); % Odd   :(1+z)-exp(-P).*(1-z)
sol4 = zeros(1,length(f0)); % Even  :(1+z)+exp(-P).*(1-z)
for i=1:length(f0)
    syms w0
    %sol_wI = vpasolve(exp(-1j*w0*sqrt(mu_d*e_d)*a/2)+exp(1j*w0*sqrt(mu_d*e_d)*a
        /2)==0,w0,2*pi*f0)/2/3.1415/1e9
    sol_wI1 = vpasolve((1+(u1.*1j.*sqrt(w0.^2.*e2.*u2-kc.^2))./(u2.*1j.*sqrt(w0
        .^2.*e1.*u1-kc.^2)))-exp(-1j.*sqrt(w0.^2.*e2.*u2-kc.^2).*l).*(1-(u1.*1j.*
        sqrt(w0.^2.*e2.*u2-kc.^2))./(u2.*1j.*sqrt(w0.^2.*e1.*u1-kc.^2)))==0,w0,2*pi
        *f0(i))/2/3.1415/1e9;
    if sol_wI1 > 0
        sol1(1,i) = double(sol_wI1);
    end
    sol_wI2 = vpasolve((1+(u1.*1j.*sqrt(w0.^2.*e2.*u2-kc.^2))./(u2.*1j.*sqrt(w0
        .^2.*e1.*u1-kc.^2)))+exp(-1j.*sqrt(w0.^2.*e2.*u2-kc.^2).*l).*(1-(u1.*1j.*
        sqrt(w0.^2.*e2.*u2-kc.^2))./(u2.*1j.*sqrt(w0.^2.*e1.*u1-kc.^2)))==0,w0,2*pi
        *f0(i))/2/3.1415/1e9;
    if sol_wI2 > 0
        sol2(1,i) = double(sol_wI2);
    end
    sol_wI3 = vpasolve((1+(e2.*1j.*sqrt(w0.^2.*e1.*u1-kc.^2))./(e1.*1j.*sqrt(w0
        .^2.*e2.*u2-kc.^2)))-exp(-1j.*sqrt(w0.^2.*e2.*u2-kc.^2).*l).*(1-(e2.*1j.*
        sqrt(w0.^2.*e1.*u1-kc.^2))./(e1.*1j.*sqrt(w0.^2.*e2.*u2-kc.^2)))==0,w0,2*pi
        *f0(i))/2/3.1415/1e9;
    if sol_wI3 > 0
        sol3(1,i) = double(sol_wI3);
    end
    sol_wI4 = vpasolve((1+(e2.*1j.*sqrt(w0.^2.*e1.*u1-kc.^2))./(e1.*1j.*sqrt(w0
        .^2.*e2.*u2-kc.^2)))-exp(-1j.*sqrt(w0.^2.*e2.*u2-kc.^2).*l).*(1-(e2.*1j.*
        sqrt(w0.^2.*e1.*u1-kc.^2))./(e1.*1j.*sqrt(w0.^2.*e2.*u2-kc.^2)))==0,w0,2*pi
        *f0(i))/2/3.1415/1e9;
    if sol_wI4 > 0
        sol4(1,i) = double(sol_wI4);
    end
end
[flipud(sort(sol1)') flipud(sort(sol2)') flipud(sort(sol3)') flipud(sort(sol4)')]
```

References

[1] D. J. Griffiths, *Introduction to electrodynamics*. Upper Saddle River, NJ: Prentice Hall, 3rd ed., 2008.

[2] L. Solymar and E. Shamonina, *Waves in metamaterials*. Oxford University Press, 2009.

[3] D. Youla, "On scattering matrices normalized to complex port numbers," *Proc. Inst. Radio Engineers*, vol. 49, no. 7, p. 1221, 1961.

[4] K. Kurokawa, "Power waves and the scattering matrix," *IEEE Trans. Microw. Theory Techn.*, vol. 13, pp. 194–202, Mar. 1965.

[5] R. B. Marks and D. F. Williams, "A general waveguide circuit theory," *J. Res. Nat. Inst. Stand. Technol.*, vol. 97, no. 5, pp. 533–562, 1992.

[6] S. Amakawa, "Scattered reflections on scattering parameters –Demystifying complex-referenced S parameters–," *IEICE Trans. Electron.*, vol. 99, no. 10, pp. 1100–1112, 2016.

Index

attenuated total reflection (ATR), 6, 156
attenuation constant, 78, 218

cavity resonator, 59
characteristic impedance, 21, 29
    normalised, 29
    of MPRWG, 79
    power-current definition, 29
    power-voltage definition, 29
    transmission line, 26
    voltage-current definition, 29
classical skin effect model, 213
complex conjugate impedance matching, 23
conductivity
    complex, 212
Courant stability condition, 12
cut-off frequency
    air-filled MPRWG, 79

de-embedding of S-parameters, 96
dielectric constant, 79
    conversion to refractive index, 214
    effective, 214
dispersion
    gated 2-D plasmons, 8
    plasmon, 5
    ungated 2-D plasmons, 8
dispersion curve, 157
Drudé conductivity, 217
Drudé model, 216
    FDTD, 11

eigenfrequency
    complex, 15, 62

Fabry-Pérot
    eigenmode, 106, 107
        in circular waveguide, 112
        in parallel-plate waveguide, 107
    resonance frequency, 81
    resonator, xiii
        eigenvlue solution, 63
        general solution, 60
        inverse, 68
        lossy, 64
Fabry-Pérot resonance
    Q-factor, 88
FDTD tecnhique, 10
Floquet boundary condition, 161
Fourier transform, 15
frequency dispersion, 157

grating coupler, 8
guided-wave media, 21
guided-wavelength
    complex, 80

high electron mobility transitor (HEMT), 8

intrinsic impedance, 219

loss tangent, 79
    electric, 79

matrix renormalisation, 25
Maxwell's equations
    boundary conditions, 211
    complex phasor form, 211
    differential form, 211
    integral form, 210

natural frequency, 62
NRW method, 132

open-box mode
    in parallel-plate waveguide, 107, 112
open-box modes, 87
    analyticall modelling, 96

perfectly matched layer (PML), 164
permeability
    complex, 79, 212
    free space, 79
permittivity
    complex, 79, 212
    effective, 212
    free space, 79

frequency dependent, 213
tensor, 212
perturbation model, 16
phase constant, 78, 218
complex, 80
phase velocity, 214
plane wave, 218
plasma frequency, 217
plasmonics, 2
plasmons
2-D, 8
bulk, 3
surface, 5
polarisation (TE or TM), 220
power wave, 22
propagating mode, 21
propagation constant, 48, 63, 80
circular waveguide, 116
complex, 78
transmission line, 26
variational modelling, 78
pseudo wave, 22

Q-factor
Fabry-Pérot resonance, 88
unloaded, 62, 86
Q-factor modelling, 86

reference impedance, 22
reflection and transmission coefficient
three-media, 224
two-media, 220
reflection coefficient, 24
electric field, 223
exceeding unity, 25
Fresnel, 24
power-wave, 32
voltage, 26
voltage-wave, 32
refractive index, 79, 214
conversion to dielectric constant, 215
relative permittivity
high frequency, 49, 217
renormalisation, 22
of scattering parameters, 40
renormalisation method, 129
Ricker wavelet, 170

S_I-parameters, 34
S- and S_P-parameter interconversion, 44
S-parameters, 34
1-D Fabry-Pérot resonator, 49, 64
circular waveguide, 116
de-embedding, 85, 96
NRW method, 136
signal flow graph, 49
slit condition in *COMSOL Multiphysics*®, 164
spherical resonator, 15
surface impedance, 79
surface plasmon frequency, 157
surface plasmons, 3

TE_z and TM_z arrangement of nodes in FDTD, 10
telegraphers' equations, 26
transmission coefficient
electric field, 223
transmission line model
Fabry-Pérot resonator, 49
travelling waves, 22, 30
two-dimensional electron system (2-DES), 8
two-port network
cascading, 38
generalised, 32
three-layer media, 46
two-layer media, 45
two-port network parameters
interconversion between, 36

voltage wave, 21, 22

wave impedance, 21, 79
wave number, 80
waveguides as transmission lines, 27
wavelength, 80
wavenumber, 218, 222

zero-order power propagation model, 52